Exploring the potential of acoustic energy transfer

Document Version:
Publisher's PDF, also known as Version of Record (includes final page, issue and volume numbers)

Please check the document version of this publication:

• A submitted manuscript is the version of the article upon submission and before peer-review. There can be important differences between the submitted version and the official published version of record. People interested in the research are advised to contact the author for the final version of the publication, or visit the DOI to the publisher's website.
• The final author version and the galley proof are versions of the publication after peer review.
• The final published version features the final layout of the paper including the volume, issue and page numbers.

Link to publication

Download date: 04. Oct. 2023

Exploring the potential of acoustic energy transfer

Maurice G. L. Roes

Exploring the potential of acoustic energy transfer

PROEFSCHRIFT

ter verkrijging van de graad van doctor aan de Technische Universiteit Eindhoven, op gezag van de rector magnificus prof. dr. ir. F. P. T. Baaijens, voor een commissie aangewezen door het College voor Promoties, in het openbaar te verdedigen op woensdag 25 november 2015 om 16:00 uur.

door

Maurice Gijsbert Lodewijk Roes

geboren te Breukelen

Dit proefschrift is goedgekeurd door de promotor. De samenstelling van de promotiecommissie is als volgt:

voorzitter:	prof. dr. ir. A. C. P. M. Backx
1^e promotor:	prof. dr. E. A. Lomonova
copromotoren:	dr. J. L. Duarte
	ir. M. A. M. Hendrix
leden:	prof. dr. ir. R. M. Aarts
	prof. dr. mont. M. Kupnik (TU Darmstadt)
	prof. dr. ir. I. Lopez Arteaga
	prof. E. M. Yeatman (Imperial College London)

Het onderzoek dat in dit proefschrift wordt beschreven is uitgevoerd in overeenstemming met de TU/e Gedragscode Wetenschapsbeoefening.

Summary

Exploring the potential of acoustic energy transfer

———————————

A HANDFUL OF METHODS for the contactless transfer of energy are available nowadays. The most common of these is the use of inductively coupled coils, which is already being used extensively in various consumer electronics and in industrial applications. Less commonly encountered species of contactless energy transfer (CET) include capacitive coupling, far-field electromagnetic, optical, and, as a very recent development, acoustic systems. The last-mentioned form is the main topic of this thesis.

Acoustic energy transfer, or AET, is a method of contactless energy transfer that makes use of sound waves as an intermediate energy carrier to transfer energy. A transmitter converts electrical energy into vibrations, which are successively radiated as a pressure wave. The medium which it propagates in can be of a gaseous, fluid or a solid nature. A receiver at a point along the path of the sound wave extracts the energy from the wave and converts it back into electrical energy. Unlike inductively coupled CET, acoustic energy transfer can transfer energy at a high efficiency over distances that are large in comparison to the transmitter and receiver sizes, owing to the high directivity of the transmitter. The efficiency of inductive CET drops off sharply when the distance becomes larger than the coil diameter. Acoustic energy transfer has the additional advantage of not relying on electromagnetic fields for the propagation of energy. Therefore it is ideally suited in situations where these fields are undesirable; for instance in hazardous environments, in direct vicinity of metallic objects, or in environments where the presence of strong electromagnetic fields is a health and safety issue.

This thesis is aimed at creating understanding of the workings of acoustic energy transfer in air. It starts from basic sound wave theory and through experiments works its way forward. Its main purpose lies in providing an exploratory overview of the subject, pointing out the main features, chances and limitations of the approach.

It investigates a number of peculiarities of the system and describes various paths that have been followed in the pursuit of optimised system performance. Topics that are covered are the theoretical limit to the energy transfer efficiency, determination of losses, modelling of effects that are encountered during measurements, and design and implementation of impedance adaptation measures for transducers.

A model based on diffraction and attenuation predicts that energy transfer over a distance of one metre is possible at an efficiency of 65 %, when the diameter of the transmitter and receiver is limited to 20 cm. Optimal electrical loading conditions, derived from this model, indicate that the receiving element has an efficiency of 50 % when maximum output power is desired. Even when these transducer losses are included in the model, acoustic energy transfer still performs at least five to ten times better in terms of efficiency than an inductively coupled system of the same dimensions.

Experiments, in which a maximum output power of 40 mW was demonstrated, reveal the occurrence, influence and importance of reflections on the energy transfer of an AET system. Reflections greatly boost the output power, but only at distinct distances from the transmitter, thereby preventing free placement of the receiving element. These reflections are modelled both by means of finite element modelling, and with a transmission line model in which a lumped element attenuation coefficient is used to account for spreading of the sound wave and absorption in the medium.

Impedance matching of the transmitting and receiving transducers to the medium is investigated as a means for increasing the output power and reducing the influence of reflections on the energy transfer. Two methods of impedance adaptation are considered in this thesis. Stepped-exponential horns were designed, optimised and constructed for both the transmitting and receiving transducers. Resonance in the horns is used to obtain large impedance transformation ratios. Experiments show that the horns increase the output power by a factor 3.1 and the efficiency by a factor 7.5 at 10 cm distance between the transmitter and the receiver. However, the modelled response deviates significantly from the measured behaviour. A second impedance adaptation measure was found in radiating surface enlargement. It is applied to bolt-clamped Langevin transducers in the form of aluminium plates that can be screwed onto the transducer. It was found that the plates do not increase the output power. Experiments also revealed significant nonlinearity of the transducer output with respect to the driving voltage, resulting in chaotic behaviour. A maximum output power of 36.3 mW was measured. It can be shown that optimal positioning of the transmitter is possible based on measurements of its electrical impedance.

This thesis shows that acoustic energy transfer through air is feasible. Achieved

power levels are adequate for small systems such as sensors, MEMS, et cetera, but are insufficient for implementation in more power hungry applications such as actuators or wireless charging. The transducers are the restricting factor. Transducer modelling is shown to be of critical importance for accurate acoustic energy transfer performance, since it is the element that connects the electrical, mechanical and acoustic domains.

Contents

1 Conventions

S EVERAL conventions have been adopted in this thesis, some of which will be familiar to the reader, while others may not be so obvious at first glance. To avoid any ambiguity in meaning and understanding of notations and symbols, the notational conventions that are employed are discussed in this chapter. A complete list of symbols and notation is added in Appendix A at page 169 for the reader's reference, in which all symbols and notation are grouped in tables for easy reference.

1.1 Symbols

Considering that the work described in this dissertation deals with two different domains of engineering, i.e. the electrical and the mechanical or acoustical domain, there will inevitably be some overlap in the traditional symbol definitions of certain quantities. For example, both mechanical speed and electrical voltage are normally indicated with a small v or the capital V. To allow a distinction between the two variables to be made, in this thesis voltages are always indicated with a v and the mechanical speed is expressed as u. Likewise, pressure is represented by a small p, and pressure amplitude by P, not to be confused with power, which will always be indicated with a capital Π.

As mentioned earlier, the reader is kindly referred to Appendix A in case of any doubt with respect to the meaning of certain variables or parameters.

1.2 Acoustic impedance

Although the concept of impedance was introduced by Oliver Heaviside in 1886, it was only in 1919 that the term was first used in connection with acoustic problems by Arthur Webster [128]. While originally the term 'impedance' implied a quantity that impedes or restricts current flow, a more accurate description would be that impedance impedes the flow of *energy*. This broader definition allows the concept to be used in acoustics just as well as in electric problems.

Although Webster originally proposed to define the acoustic impedance as the ratio of the excess pressure p to the volume displacement X in the medium; $Z^a = p/X$, this definition is far from definite. Most works on acoustics define acoustic impedance as pressure divided by volume velocity (for example [58, 85, 120]) although other definitions exist, such as pressure divided by particle velocity (e.g. [57, 69]). Lastly, the *radiation impedance* of a vibrating object is typically defined in the same manner as a mechanical impedance, that is, as the ratio of force to velocity.

Obviously, each of these definition has its own merits. Electing the volume velocity to be an equivalent of current allows to make use of continuity relationships. Choosing force, on the other hand, as equivalent of voltage and velocity for current means that the power relationship of the equivalent circuit is maintained. Moreover, this choice has the advantage that it is the definition of mechanical impedance, which conveniently expresses the radiation impedance of a loudspeaker for example. In this dissertation, however, acoustic impedance is defined as the quotient of pressure and particle velocity. Since this work uses the excess pressure and particle velocity as principal acoustical quantities, it is only logical to choose these quantities as equivalents for voltage and current respectively. Moreover, specific acoustic impedance of a medium has the same definition [58]. The resulting unit of acoustic impedance is $\mathrm{N\,s/m^3}$, for which often the Rayleigh or rayl unit is used.

1.3 Mathematical notation

Vectors represent quantities that do not only have a magnitude, but that also have a direction. This directional dependency is indicated in this thesis by an arrow above the symbol, so as to be able to distinguish them from scalar quantities, for example the vector $\vec{x}$, as opposed to the scalar x.

Special spatial derivatives of vector fields such as the gradient, divergence and curl are denoted using ∇, the 'nabla' or 'del' operator. It is defined in the Euclidian space with coordinates $(x_1, x_2, \ldots, x_n)$ and unit vectors $\hat{x}_1, \hat{x}_2, \ldots \hat{x}_n$ in the corresponding

directions, as

$$\nabla = \sum_{i=1}^{n} \hat{x}_i \frac{\partial}{\partial x_i} \, . \tag{1.1}$$

For a standard three-dimensional Cartesian coordinate system with unit vectors $\hat{x}$, $\hat{y}$ and $\hat{z}$ this would be

$$\nabla = \hat{x} \frac{\partial}{\partial x} + \hat{y} \frac{\partial}{\partial y} + \hat{z} \frac{\partial}{\partial z} \, . \tag{1.2}$$

According to this notation, the gradient of a scalar field s, and the divergence and curl of a vector field $\vec{v} = v_x \hat{x} + v_y \hat{y} + v_z \hat{z}$ are respectively given by

$$\nabla s = \frac{\partial s}{\partial x} \hat{x} + \frac{\partial s}{\partial y} \hat{y} + \frac{\partial s}{\partial z} \hat{z} \tag{1.3a}$$

$$\nabla \cdot \vec{v} = \frac{\partial v_x}{\partial x} + \frac{\partial v_y}{\partial y} + \frac{\partial v_z}{\partial z} \tag{1.3b}$$

$$\nabla \times \vec{v} = \left(\frac{\partial v_z}{\partial y} - \frac{\partial v_y}{\partial z} \right) \hat{x} + \left(\frac{\partial v_x}{\partial z} - \frac{\partial v_z}{\partial x} \right) \hat{y} + \left(\frac{\partial v_y}{\partial x} - \frac{\partial v_x}{\partial y} \right) \hat{z} \tag{1.3c}$$

Lastly, complex quantities are denoted by means of a bar notation, for example $\bar{a} = \alpha + j\beta$. Complex variables are frequently used throughout this thesis to represent harmonically varying quantities.

2 Introduction

ENERGY is a truly elusive physical property. It is something that cannot be observed directly, although one can observe the effects energy brings about—it can be felt as heat, experienced as velocity, seen and heard as lightning and thunder, or the crashing of waves onto the shore. This is probably the main reason for many people finding it so fascinating a concept. It is shrouded in a bit of magic and mystery, in a world that is thoroughly dissected, classified and (arguably) largely understood.

Energy is often described as the ability of a system to perform work. Now work is a much more comprehensible concept for most people. Mechanical work is performed when a force is exerted on an object in order to move it. More precisely: the product of the force in the direction of the movement, multiplied by the distance travelled, equals the mechanical work done.

Energy exists in many forms: electrical, mechanical, thermal, nuclear, magnetic, gravitational, chemical, et cetera. Mankind has used many of these forms of energy throughout history. Mechanical, thermal and chemical energy have long been the energies of choice. Starting with the industrial revolution the use of energy skyrocketed, and has continued its growth ever since. The advent of the electrical era, starting from around the mid-1880s, brought a whole new source of energy within reach of the common man. It meant constantly available lighting without the

---

This chapter is based on [96] and [97].

disadvantages of fire hazard, smell and smoke, all at the command of a button. Numerous applications would follow, leading to the present day world were electrical energy plays such a vital role that the whole society would collapse if the power system were to fail. Man embraced electricity as its main energy carrier, not only in his home, but for his portable devices as well. The amount of comfort and luxury experienced because of this choice is unrivalled throughout history.

One of the inherent drawbacks of electricity, albeit a negligible one in most cases, is the fact that a physical connection is necessary for the electrical energy to propagate. Wire connections are a necessity for electric currents to flow efficiently from one point to the other. As a result, copper must have never been in so high a demand since the end of the bronze age around 1200BCE, relatively speaking. The requirement of a physical connection can be somewhat alleviated through the use of a battery as a power source, as is extremely common nowadays in portable devices, such as mobile phones, cameras, laptop computers, et cetera. Recharging of these batteries, however, still requires a connection to another source of electrical energy. Contactless energy transfer (CET) has been envisaged by many to overcome the necessity of a physical connection between an electrical energy source on one hand, and an electrical device on the other hand. Some even dreamt dreams as bold as powering a whole world wirelessly [1].

There are many applications were a physical connection between a device and a power source is impractical or even impossible. In other cases it may only be a matter of convenience. Contactless energy transfer is used to charge the batteries of mobile devices or vehicles [119, 126], it is used in industry to power actuators in which the disturbance force introduced by a cable slab is undesired [23, 118], it can be used to charge implants without surgical intervention [25, 88], or it can be used to power sensor networks [55].

2.1   Background

2.1.1   Contactless energy transfer

A handful of methods for the contactless transfer of energy are available nowadays. The most common of these is the use of inductively coupled coils, a coreless transformer if you will, which is being used already in various consumer electronics and in industrial applications. Less commonly encountered species of CET include capacitive coupling, far-field electromagnetic, optical, and, as a very recent development, acoustic systems. The last-mentioned form is the main topic of this thesis. Figure 2.1 schematically depicts the working area of these methods of contactless energy
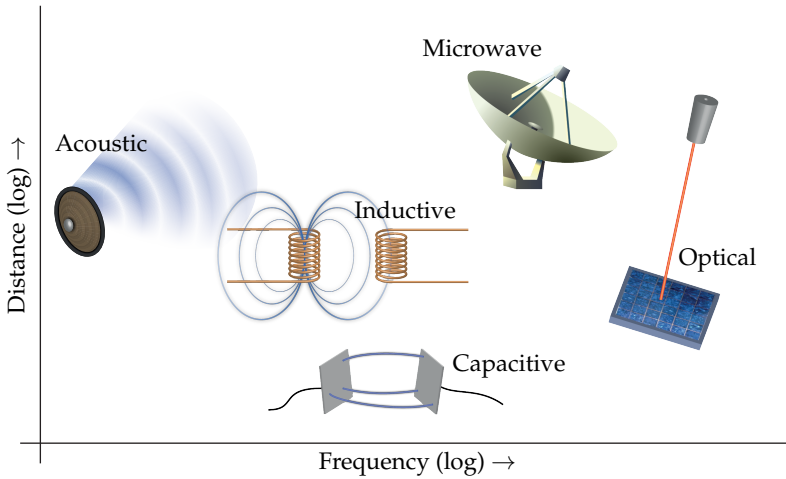
Figure 2.1 A very schematic survey of common CET methods shows that each has its own area of application in terms of distance and frequency. Acoustic energy transfer covers the medium distance, low frequency region.

transfer. This is image is meant to serve purely illustrative purposes, and should not be considered as a factual classification. In practice there will be some overlap in working area between methods, as well as systems that operate in completely different areas. Optimal performance, however, is approximately attained in the areas indicated in the graph.

Inductive CET has been receiving considerable attention lately. It is used both in consumer applications, such as mobile device charging [119,126], and in industrial applications [40,118]. Recent publications relate of systems delivering energy over distances up to 2 m at high efficiencies [53,68,107]. These systems are a very exciting development, as they seem to promise unlimited freedom of movement, allowing any device to be powered anywhere. There are unfortunately a number of drawbacks to inductive CET. The distance that can be crossed with inductive CET at a reasonable efficiency is of the same order of magnitude as (or smaller than) the size of the transmitter and receiver [84,127]. Large distances result in low coupling between the transmitter and receiver coils, requiring large reactive currents. These currents in turn cause high conduction losses. Furthermore, these systems are often driven at frequencies ranging from hundreds of kHz to several MHz, causing high switching losses in the driving power electronics.

Capacitively coupled CET is used far less often, which is largely due to the limited distance that can be crossed with it. This is a consequence of the inverse proportion-

ality of the capacitance with the distance, requiring high voltages and frequencies for the transfer of a reasonable amount of energy. High voltages lead to difficulties in prevention of electric breakdown. The advantage of capacitively coupled contactless energy lies in the nature of the electric field, which, unlike the magnetic field used in inductive CET, is much more constrained between the metal plates. As such there are less electromagnetic compatibility issues to be expected [55]. The high frequencies, on the other hand, may completely negate this advantage.

Far-field electromagnetic (EM) energy transfer, [16, 28, 81], often called RF energy transfer or microwave energy transfer, is used occasionally for contactless energy transfer as well. In contrast to inductive and capacitive energy transfer, far-field CET, as the name implies, uses a radiative electromagnetic field to convey energy. Hence microwaves and directional antennas have to be used. Both the transmitter and receiver size will at least be of the order of a wavelength, if they are to have a certain directivity. Consequently, when system dimensions lie in the centimetre range, frequencies of the order of 10 GHz are necessary. Rectification of these high frequency waves at the receiving end can be achieved at high efficiencies of 80 %– 90 % [81], but generation of the microwaves is much more difficult, especially when a solid-state RF generator is used.

Optical energy transmission uses the same principle as far-field EM but here the wavelengths lie in (or near) the visible spectrum. Lasers can be used to generate the optical beam, and photovoltaic diodes can take care of the conversion back to electrical energy [28, 93, 104]. So far, in both conversion steps between 40 and 50 % of energy is lost [28]. Furthermore, the possible risks and hazards involved in the use of high power laser beams should not be underestimated [45, 104].

2.1.2 Acoustic energy transfer

All of the previously described methods rely on electromagnetic fields for the transfer of energy. One can divide them into energy transfer based on radiative (microwave and optical CET) and nonradiative fields (inductive and capacitive CET). The former type of energy transfer is not restricted to the use of electromagnetic waves alone; any type of wave can be used for this purpose. The transport of energy by sound waves instead of EM waves lies at the basis of acoustic energy transfer (AET).

The basic structure of an acoustic energy transfer (AET) system is depicted in figure 2.2; a power amplifier supplies electrical energy to a transmitting transducer, which converts it into mechanical vibrations. The transmitter is coupled to a medium, in which it generates a pressure wave. A receiving transducer, positioned at a point along the path of the sound wave, converts the motion caused by the sound wave back into electrical energy. A rectifier and a capacitor provide a usable steady DC
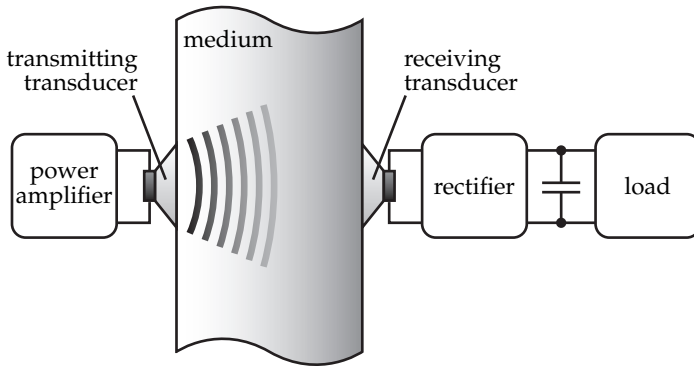
Figure 2.2   An acoustic energy transfer system consists of a transmitting transducer that generates sound waves in a medium, and a receiving transducer that converts them back to electrical energy.

voltage that powers a load. The medium can be anything ranging from air to human tissue or a solid; in principle any material that will propagate a pressure wave will do.

Acoustic energy in its purest form is used in various applications, such as ultrasonic cleaning, medical ultrasonography, nondestructive testing, distance measurement (e.g. sonar), therapeutic ultrasound, ultrasonic welding, et cetera. These applications are different from acoustic energy transfer in that they directly use the acoustic energy for a specific purpose, without converting it back to electrical energy. Somewhat closer related to AET are piezoelectric energy harvesting and piezoelectric transformers. Energy harvesters make use of available (vibrational) energy to generate electricity, and could be considered to be a non-driven AET system. Piezoelectric transformers convert electric energy into vibrations, with the inverse process taking place at the secondary side, which is the essence of AET. However, it lacks the spatial separation of the transmitter and receiver that is desired for a contactless energy transfer system. The ceramic of such a transformer is transmitter, receiver and medium, all in one.

One of the advantages of acoustic energy transfer, in comparison to CET based on electromagnetic fields, lies in the much lower speed of propagation c of pressure waves in air with respect to the electromagnetic propagation velocity c_{EM}. Therefore, the sound waves have a smaller wavelength for a given frequency than their electromagnetic counterpart. This in turn means that the transmitter and receiver can be a factor c_{EM}/c smaller for a given directionality of the transmitter [25]. Alternatively, if the desired transmitter and receiver dimensions are given (as is usually the case), then the frequency that is used in an AET system can be a factor c_{EM}/c smaller than that of the electromagnetic system, while still achieving the same directionality.

Accordingly, losses in the driving power electronics will be much lower. The design of the electronics can be kept considerably simpler as well. Furthermore, because acoustic energy transfer, in contrast to all other discussed methods, does not rely on electromagnetic fields for the propagation of energy, it is ideally suited for situations where these fields are undesired, for instance in hazardous environments, in direct vicinity of metallic objects, or environments where the presence of strong electromagnetic fields is a health and safety issue.

2.1.3 Acoustic energy transfer versus inductive CET

The major competitor for acoustic energy transfer is of course inductively coupled CET, being the *de facto* standard at this moment. Well designed systems can reach total energy transfer efficiencies, including electronics, of over 95 %. However, when the distance between the transmitter and receiver becomes much larger than their radii, the efficiency of inductive CET decreases rapidly [127]. Mur-Miranda *et al.* [84] presented a simplified model of inductive contactless energy transfer that indicates that the efficiency decreases with the sixth power of distance. The model by Waffenschmidt and Staring [127] shows that the efficiency of an inductively coupled system can be very high, even when using coils that have a low quality factor, but only up to a certain distance. The graphs of efficiency versus distance that they present in their paper show a relatively flat efficiency curve up to a bending point, after which the efficiency drops sharply.

Acoustic energy transfer performs much better in this respect [25,78,98] and can be a good alternative when inductive CET falls short. It benefits from the focusing ability of sound waves. The energy contained in the waves can therefore stay confined to a narrow beam, without too much divergence. In the ideal case the sound beam does not diverge at all, and the only losses in the propagation are due to absorption by the medium. Chapter 4 will go into more detail about modelling of the losses in an AET system and derivation of a theoretical limit to the energy transfer efficiency.

Figure 2.3 shows an example of how acoustic energy transfer is able to outperform inductive CET. The two methods are compared based on the celebrated paper by Kurs *et al.* [68]. The paper describes an inductive energy transfer system using two self-resonant coils of 30 cm radius, which were used to transfer 60 W over a distance of more than 2 m at an efficiency of 40 %. The measured energy transfer efficiencies are indicated by the black dots in figure 2.3. As can be seen, they correspond quite well to the theoretical limit, reproduced from [127]. The point where the measured efficiency starts to decrease occurs at a higher distance between the coils, but the drop in efficiency is just as sharp as predicted by Waffenschmidt and Staring.
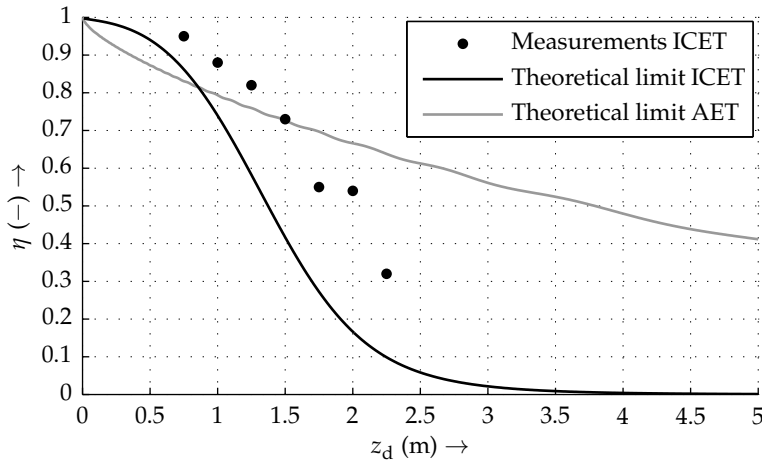
Figure 2.3   The measured efficiency η versus distance z_d of an inductive CET system from [68] shows a good resemblance with the theoretical limit from [127]. For larger distances the theoretical efficiency limit of an AET system of the same dimensions is much higher.

The theoretical efficiency limit for an acoustic energy transfer system[1] of the same dimensions (i.e. a transmitter and receiver radius of 30 cm) shows the advantage that AET has at larger distances. The efficiency decreases much more gradually, and outperforms the inductive system when the distance becomes greater than 1.5 m. A typical operating frequency of 20 kHz was assumed for the AET system. The efficiency of the AET system will be even higher when the frequency is optimised for each distance.

This example illustrates the much reduced dependency on distance of acoustic energy transfer in comparison to inductive energy transfer. AET is therefore a good alternative whenever the distance to be crossed is larger than the size of the transmitter and the receiver.

2.2   Research on AET

Acoustic energy transfer is not a new concept. The first application of AET dates back thirty years, to 1985, when Cochran *et al.* described a piezoelectric implant used for osteogenesis [19]. Their implant was a bit different from what was common at that time, as it could be powered by a low intensity ultrasound source, making it the

---

[1]This efficiency limit is discussed in chapter 4.

first application of AET. After this publication it was silent for a long time around the topic of AET. There was still only a handful of publications available on acoustic energy transfer at the time of the start of the research that is described in this thesis. At the present moment, however, the subject is starting to gain some momentum, and the number of publications on the topic slowly but steadily increases. Many research groups in various parts of the world picked up the research topic, not in the least due to publications of the author, notably [97].

Examining the limited amount of literature that exists on acoustic energy transfer, one can divide all publications into three groups on the basis of the propagation medium that they use: fluid, metal, or air. The first two groups are by far the largest, while the number of publications on acoustic energy transfer through air is fairly limited.

Fluid medium or tissue

Many publications on acoustic energy transfer deal with biomedical applications, where it is either used to power implants [9,25,54,70,72,73,78,80,88–91,108–112,114, 115], or the energy of the ultrasonic wave is used directly for the intended purpose without intermediate conversion to electrical energy [19,26,27].

At the moment batteries make up the largest part of the volume of an implant [25]. In an attempt to miniaturise the implants, wireless energy transfer is proposed, so that the battery capacity can be reduced. An additional advantage of implant charging by means of CET is that recharging is rendered a less invasive procedure. Acoustic energy transfer is a good alternative to inductive CET in this case because of the absence of electromagnetic fields and the possibility of using a miniature receiver. Besides *in vitro* experiments, a number of authors have already shown the feasibility of biomedical AET with *in vivo* experiments [70,78].

As the characteristic impedance of tissue is very comparable to that of water, of-tentimes experiments are conducted in a fluid medium, instead of using actual tissue. The frequencies that are used in most publications lie in the megahertz range (0.5–2.25 MHz). Ozeri *et al.* explain that the choice of frequency for a biomedical AET system is a trade-off between attenuation losses, diffraction losses, and additionally the receiving transducer's thickness [88].

The maximum efficiency that was measured in these publications is 39.1 % [90]. The power levels that are used are quite low (ranging from 29 μW to 100 mW electrical output power), which is limited by the allowable ultrasound intensity in *in vivo* applications, in combination with a small receiver size. This level is adequate for the power supply of, for instance, a simple sensor and its supporting signal processing.

Through-wall CET for metal enclosures

There are situations in which one would like to transfer energy wirelessly through a metal wall. Examples that come to mind are sensors in nuclear waste containers, gas cylinders, vacuum chambers, pipelines, et cetera. Basically any system qualifies where direct feed through of wires would severely complicate system design, degrade the system's performance, or is plainly impossible. Any form of CET based on electromagnetic fields runs into a wall here, quite literally. The metal wall of such an enclosure has a shielding effect that limits the coupling of an electromagnetic CET system and eddy currents in the wall cause high losses. Multiple authors have therefore proposed to use acoustic energy transfer as an alternative [10,43,47,48,59,71,74,76,113,116,130,131]. It is debatable whether this category falls under the umbrella of CET, since it is not strictly a contactless method, but it is acoustic energy transfer nonetheless.

Through-wall AET achieves high output power levels and efficiencies more easily than it does with an air or tissue medium, because of the similarity in acoustic impedance between the wall and piezoceramic material (approximately 45 Mrayl for steel and 30 Mrayl for lead zirconate titanate (PZT)). A good match in impedance implies optimal power throughput.

In [71] a through-wall acoustic energy transfer system is described that delivers 50 W at 51 % efficiency. Leung *et al.* transferred 62 W at 74 % efficiency, while Bao *et al.* [10] even managed to transfer more than 1 kW at an efficiency of 84 % by using a prestressed piezo actuator.

Air

The combination of acoustic energy transfer with a gaseous medium [18,50,60,98–100] is far less popular than biomedical or through-wall acoustic energy transfer are. In [98] it was shown theoretically that AET has the potential of reaching high efficiencies in comparison with inductively coupled CET. The maximum efficiency that was measured was 17 % and the transferred power was very low (4 µW). It should be noted that the authors indicated that the measurements were performed with a non-optimised system and are meant to be nothing more than indicative.

2.3 Challenges

As mentioned, very few publications were available on acoustic energy transfer at the moment that the research was initiated. The lack of preceding research puts it

in an unique position, making it true pioneering work. Unfortunately, it makes it a bit more difficult to give an overview of challenges than it is in well-established research fields.

Of the publications on AET that were available at the start of the research, only a handful takes an analytical approach, or even attempts to construct a model of acoustic energy transfer at all. None of these were meant for air-based acoustic energy transfer. Modelling is therefore one of the main challenges. Accurate models of the energy transfer in an acoustic energy transfer system will give fundamental insight into all effects that dominate AET behaviour. Models allow the right design choices to be made to optimise the energy transfer and efficiency. Finite element modelling could prove a useful tool in giving a comprehensive overview of the effects at play. Various existing models can possibly be combined to come up with a more comprehensive description of AET.

Overall, the thus far obtained output power levels in acoustic energy transfer are low. In air based systems only microwatt levels were reached. While this can be enough to power a very simple sensor, higher levels are desirable if acoustic energy transfer is to become a serious competitor for inductively coupled CET. Transducer design is therefore deemed a subject that deserves much attention as well. High power transducers have already been developed by Bao *et al.*, amongst others, for through-wall AET, while biomedical AET does not require high power levels due to health regulations. Acoustic energy transfer through air, however, asks for a transducer design that is able to boost the received power to at least the level of multiple Watts.

This thesis is aimed at creating understanding of the workings of acoustic energy transfer in air. It starts from basic sound wave theory and simple initial experiments, and works its way forward from there. Topics that are covered are a theoretical limit to the energy transfer efficiency, determination of losses, modelling of effects that are encountered during measurements, and design and implementation of impedance adaptation measures for transducers.

2.4   Research goals and outline of the thesis

2.4.1   Research goals

Inductively coupled systems are able to transfer energy very efficiently over short distances, but as soon as the distance becomes of the order of the size of the coils, the efficiency plummets. The obvious question to ask is whether acoustic energy

transfer can outperform these systems in such a case. The research therefore is aimed at investigating the feasibility of acoustic energy transfer through air, and finding out how it stacks up against contactless energy transfer through inductively coupled coils. To this end it is necessary to set up (multiphysical) models of the energy transfer by sound waves. Measurements on experimental setups are required, so that the models can be validated.

If acoustic energy transfer is found to be a viable method for the transfer of energy, there are several secondary questions to be answered:

- What are characteristic properties of an acoustic energy transfer system, and how can these be modelled?

- What is the limit to the power that can be transferred with a particular system, and what is the maximum efficiency that can be attained?

- What are the limiting factors in that case?

- How can the energy transfer and efficiency be increased?

It is important that the outcomes of the research have practical value, which is achieved by choosing a realistic set of requirements. The coils used in the inductive CET system of Kurs *et al.*, for example, are very large at a diameter of 60 cm. Their application will therefore be incredibly limited. Because the purpose of contactless energy transfer is to power mobile devices, a transmitter and receiver size should be chosen that reflect this mobility. The transmitter and receiver are therefore restricted to a maximum cross-sectional diameter of 20 cm in this research. Since acoustic energy transfer is expected to perform much better than inductively coupled systems at distances that are large in comparison to the transmitter and receiver dimensions, the goal is set to transfer energy efficiently over a distance of 1 m. This is a distance that allows a considerable freedom in device mobility, if it is powered contactlessly, and will certainly be of interest for many applications.

The power transfer efficiency of an inductively coupled CET system of the same dimensions will be taken as a benchmark. According to [127] such a system is able to reach approximately 2 % efficiency, although only in very favourable conditions, i.e. a coil quality factor of 1000 and neglecting the losses in the accompanying power electronics. Furthermore, the high frequencies involved introduce many difficulties in the design of an efficient inverter [122].

2.4.2 Outline of the thesis

The outline of this thesis is as follows. Chapter 3 starts with a short introduction to acoustics for the reader that is not yet familiar with this fascinating domain of

physics. The research, and especially the models, described in this thesis lean heavily on the theory of acoustic wave propagation, making it imperative to have a grasp of basic acoustic concepts. The relations and equations, as well as simple wave types, are discussed briefly. The chapter also introduces the concept of equivalent electrical networks.

The first theory of acoustic energy transfer in air is subsequently discussed in chapter 4. A theoretical limit to the energy transfer efficiency of an AET system is derived, and used to calculate the maximum attainable efficiency. Optimal electrical loading conditions for the receiving transducer are derived. First experiments are discussed and compared to the theoretical limit. To this end transducer losses are determined from vacuum impedance measurements.

The modelling of reflections in acoustic energy transfer systems is successively treated in chapter 5. A transmission line model that models the energy transfer by means of plane waves is introduced. Power and efficiency equations are derived and compared to measurements. Finite element analysis is used to construct a second model, which gives more insight into the pressure distribution at various transmitter-receiver distances. Sensitivity analysis is used to identify the most important model parameters.

The next two chapters are dedicated to impedance adaptation measures. Chapter 6 deals with the use of horns in acoustic energy transfer, for adjustment of the impedance of both the transmitter and the receiver. Stepped-exponential horns are designed and optimised by means of finite element analysis. The second part of the chapter is dedicated to analysis of parameter sensitivity of the horn drivers.

Chapter 7 deals with radiating surface enlargement as a means of impedance adaptation for bolt-clamped Langevin transducers. Measurements of the power transfer and the energy transfer efficiency are discussed. The chapter further delineates several peculiarities of the setup that were encountered during the measurements.

Finally, chapter 8 presents the main conclusions and the contributions of the research that is presented in this thesis. Lastly, it covers a number of recommendations for future research on acoustic energy transfer in air.

CHAPTER 3

A short introduction to acoustics

ACOUSTICS is the name given to the field of science that deals with the origin and propagation of sound waves. A short introduction into this intriguing field is given in this chapter for readers that may not be entirely familiar with it. It introduces the basic concepts and equations relating sound pressure and particle velocity. However, this chapter is by no means intended to give a complete overview of the entire theory. Readers are kindly directed to text books on acoustics such as [21, 34, 58, 69, 85, 120] for more information on the subject. This chapter is largely based on these books. The reader will hopefully forgive not citing these works continuously throughout the chapter.

3.1 Sound waves

What we normally call sound is the reception by the ear of variations in the air pressure. The variation of pressure, particle velocity or medium density would be a more accurate description of what sound actually is. This variation is produced through vibration of particles of the medium in whichever way. Usually a sound wave originates from a vibrating source, for instance a loudspeaker, a guitar string, or the undesired vibration of machinery.

Probably the most important intrinsic property of sound is its capability to propagate through media, whether they be of gaseous, fluid or solid nature. Sound propagates in either longitudinal or transverse waves. While both types of waves can propagate

Figure 3.1 A longitudinal wave consists of successive areas of rarefaction and compression.

through solid materials, sound waves in air are purely of the longitudinal type. Such a wave is depicted in figure 3.1. It is caused by application of a force to air particles, for example by a loudspeaker, a musical instrument, or any other source of mechanical vibrations. The particles in the direct vicinity of this sound source start to move in the direction of the force that is exerted on them, causing an accumulation of particles at a point farther ahead. If we assume a vibrating source, the force changes direction at some point in time, pulling particles in the opposite direction, leaving an area in which there are less particles. The various shades of grey in figure 3.1 indicate the density of the air. These local changes in density of the air correspond to equivalent local changes in pressure and thus particle velocity, which is what a sound wave is.

3.2 Particles, pressure and sound velocity

A *fluid particle* is a volume element that is much larger than a single molecule of the medium in which the sound wave propagates, but still is small enough to be able to consider all acoustic variables constant throughout it [58]. Particles, rather than molecules, are considered in acoustics since molecules of a fluid or gas are always in motion, even when there is no acoustic wave present. When we consider a particle, on the other hand, we have a small volume in which—on average—the influx and efflux of molecules is equal, meaning that the macroscopic properties of a particle remain unchanged. Therefore, a particle, contrarily to a molecule, can have a fixed equilibrium position, and hence is a much better element to study in the field of acoustics.

We can now define the particle displacement from this equilibrium position as

$$\vec{\xi} = \xi_x \hat{x} + \xi_y \hat{y} + \xi_z \hat{z}, \tag{3.1}$$

and consequently a particle velocity

$$\vec{u} = \frac{\mathrm{d}}{\mathrm{d}t}\vec{\xi} = u_x\hat{x} + u_y\hat{y} + u_z\hat{z}. \tag{3.2}$$

The elements u_x, u_y and u_z are the particle velocities, and $\hat{x}$, $\hat{y}$ and $\hat{z}$ are the unit vectors, in the x, y and z direction respectively.

3.2.1 The equation of state

Compressions and rarefactions normally follow each other so rapidly in sound waves that there is virtually no heat exchange between adjacent sound particles. Acoustic processes are therefore approximately adiabatic [58]. A perfect gas under an adiabatic process behaves according to

$$\frac{p_t}{p_0} = \left(\frac{\rho_t}{\rho_0}\right)^{\gamma}, \tag{3.3}$$

in which p_t and ρ_t are the pressure and the density of the gas respectively, and p_0 and ρ_0 are the pressure and density of the gas in equilibrium. The constant γ is the ratio of specific heats. This relation is slightly more complicated for a non-perfect gas, requiring the relation between pressure and density variations to be determined experimentally. Such a relationship can subsequently be expanded in a Taylor approximation, as in

$$p_t = p_0 + \left.\frac{\partial p_t}{\partial \rho_t}\right|_{\rho_0}(\rho_t - \rho_0) + \frac{1}{2}\left.\frac{\partial^2 p_t}{\partial \rho_t^2}\right|_{\rho_0}(\rho_t - \rho_0)^2 + \dots \tag{3.4}$$

Only the first order terms have to be retained if the variation of ρ is small. Let us now introduce the variation of the pressure $p = p_t - p_0$ and the density $\rho = \rho_t - \rho_0$. This allows us to derive the *equation of state* from equation (3.4), obtaining

$$\begin{aligned} p &= \mathcal{B}\frac{\rho}{\rho_0} \\ &= c^2\rho, \end{aligned} \tag{3.5}$$

where the adiabatic bulk modulus of the medium

$$\mathcal{B} = \rho_0\left.\frac{\partial p_t}{\partial \rho_t}\right|_{\rho_0} \tag{3.6}$$

and a constant $c^2 = \mathcal{B}/\rho_0$ are introduced. In case of an ideal gas these would be

$$\mathcal{B} = p_0\gamma \tag{3.7a}$$

$$c^2 = \frac{p_0}{\rho_0}\gamma. \tag{3.7b}$$

3.2.2   The continuity equation

Let us now consider a small rectangular cuboidal element that has a volume $\Delta V = \Delta x \Delta y \Delta z$, such as in figure 3.2, through which particles flow at a velocity $\vec{u} = u_x \hat{x} + u_y \hat{y} + u_z \hat{z}$. Defining the density at any point as $\rho_t(x, y, z)$, there is a net influx of mass into the element in the x-direction equal to

$$(\rho_t u_x)(x', t) \, \Delta y \Delta z - (\rho_t u_x)(x' + \Delta x, t) \, \Delta y \Delta z, \tag{3.8}$$

where the positive term is the influx at the face at $x = x'$, and the second (negative) term is the efflux at $x = x' + \Delta x$. Writing down similar equations for the y and z-directions, we obtain a total net mass influx. Because of the conservation of matter, this influx has to equal the rate $\frac{\partial}{\partial t}(\rho_t \Delta V)$ at which the mass of the element increases. Since the volume of the element ΔV is time invariant, the equation can be written as

$$\begin{aligned}
\frac{\partial \rho_t}{\partial t} \Delta x \Delta y \Delta z = & \left[(\rho_t u_x)(x', t) - (\rho_t u_x)(x' + \Delta x, t) \right] \Delta y \Delta z + \\
& \left[(\rho_t u_y)(y', t) - (\rho_t u_y)(y' + \Delta y, t) \right] \Delta x \Delta z + \\
& \left[(\rho_t u_z)(z', t) - (\rho_t u_z)(z' + \Delta z, t) \right] \Delta x \Delta y.
\end{aligned} \tag{3.9}$$

The continuity equation is now obtained by dividing both the left and right hand side by ΔV, and considering the limit $\Delta x \to 0$, $\Delta y \to 0$, $\Delta z \to 0$. Altogether this yields the so-called exact continuity equation

$$\frac{\partial \rho_t}{\partial t} = - \left(\frac{\partial (\rho_t u_x)}{\partial x} + \frac{\partial (\rho_t u_y)}{\partial y} + \frac{\partial (\rho_t u_z)}{\partial z} \right), \tag{3.10}$$

which can be conveniently rewritten as

$$\frac{\partial \rho_t}{\partial t} + \nabla \cdot (\rho_t \vec{u}) = 0. \tag{3.11}$$

Now the total density of the medium $\rho_t = \rho_0 + \rho$ can be divided into an equilibrium density ρ_0 and a change in density due to the acoustic field ρ. By means of this substitution and the identity $\nabla \cdot \left(\varphi \vec{F} \right) = (\nabla \varphi) \cdot \vec{F} + \varphi \nabla \cdot \vec{F}$, equation (3.11) can be rewritten as

$$\frac{\partial}{\partial t}(\rho_0 + \rho) + \nabla(\rho_0 + \rho) \cdot \vec{u} + (\rho_0 + \rho) \nabla \cdot \vec{u} = 0. \tag{3.12}$$

In acoustics it is mostly a fair assumption that the major variation of the density of the medium occurs due to the acoustic field, and that the medium is approximately homogeneous in equilibrium. This means that its equilibrium density ρ_0 is only a
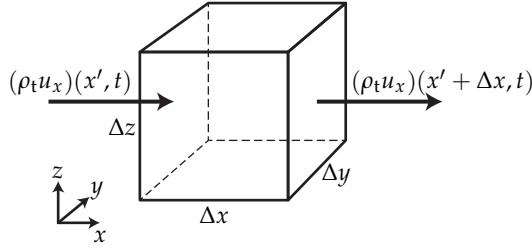
Figure 3.2   A rectangular cuboidal element with sides of length Δx, Δy and Δz through which there is a mass flow $(\rho \vec{u})$ can be used to derive the continuity equation.

weak function of time and space, or $\frac{\partial \rho_0}{\partial t} \ll \frac{\partial \rho}{\partial t}$ and $\nabla \rho_0 \ll \nabla \rho$, which can be used to simplify the equation even further, yielding

$$\frac{\partial \rho}{\partial t} + \nabla \rho \cdot \vec{u} + (\rho_0 + \rho) \, \nabla \cdot \vec{u} = 0 \,. \tag{3.13}$$

Lastly, we will neglect the cross term $\nabla \rho \cdot \vec{u}$, and assume that the density variation due to the acoustic field is small in comparison to the equilibrium density, $\rho \ll \rho_0$, to arrive at

$$\frac{\partial \rho}{\partial t} + \rho_0 \nabla \cdot \vec{u} = 0 \,. \tag{3.14}$$

Equation (3.14) is commonly referred to as the linearised continuity equation.

3.2.3   Euler's equation

The linearised continuity equation that was derived in the previous section is in itself not enough to describe acoustic phenomena, since it still contains two acoustic variables; the density ρ and the particle velocity $\vec{u}$. Another equation is to be derived to be able to solve for both variables. To this end, let us examine again a fluid element of dimensions $(\Delta x, \Delta y, \Delta z)$, only now one that moves with the fluid. We will consider the force balance on this element.

The surrounding fluid exerts a force $p_t(x', t) \, \Delta y \Delta z \, \hat{x}$ on the face at $x = x'$ and a force $-p_t(x' + \Delta x, t) \, \Delta y \Delta z \, \hat{x}$ on the face at $x = x' + \Delta x$. A similar expression holds for the forces in the y-direction, but in the z-direction we also have to consider the force due to the gravitational acceleration $\rho_t \vec{g} \Delta V$, with $\Delta V = \Delta x \Delta y \Delta z$. The total force exerted

on the volume element in all directions is therefore

$$
\vec{F}(x,y,z,t) = \left(\frac{p_t(x',t) - p_t(x' + \Delta x, t)}{\Delta x} \, \hat{x} + \right.
$$
$$
\frac{p_t(y',t) - p_t(y' + \Delta y, t)}{\Delta y} \, \hat{y} +
$$
$$
\left. \frac{p_t(z',t) - p_t(z' + \Delta z, t)}{\Delta z} \, \hat{z} + \rho_t \vec{g} \right) \Delta V \,.
\tag{3.15}
$$

This force causes an acceleration of the fluid element equal to $\vec{a} = \mathrm{d}\vec{u}/\mathrm{d}t$, which can be expanded through application of the chain rule

$$
\vec{a} = \frac{\partial \vec{u}}{\partial t} + u_x \frac{\partial \vec{u}}{\partial x} + u_y \frac{\partial \vec{u}}{\partial y} + u_z \frac{\partial \vec{u}}{\partial z}
$$
$$
= \frac{\partial \vec{u}}{\partial t} + (\vec{u} \cdot \nabla) \, u \,.
\tag{3.16}
$$

Equations (3.15) and (3.16) can be combined by means of Newton's second law $\vec{F} = \rho_t \Delta V \vec{a}$. Moreover looking at the limit $\Delta x \to 0, \Delta y \to 0, \Delta z \to 0$, one obtains

$$
-\nabla p_t + \rho_t \vec{g} = \rho_t \left(\frac{\partial \vec{u}}{\partial t} + (\vec{u} \cdot \nabla) \, \vec{u} \right) \,.
\tag{3.17}
$$

In equilibrium we have that $-\nabla p_0 + \vec{g}\rho_0 = 0$, which means that $\nabla p_t = \nabla p + \vec{g}\rho_0$, and therefore

$$
-\nabla p + \rho \vec{g} = (\rho_0 + \rho) \left(\frac{\partial \vec{u}}{\partial t} + (\vec{u} \cdot \nabla) \, \vec{u} \right) \,.
\tag{3.18}
$$

Let us now assume that $|\rho\vec{g}| \ll |\nabla p|$, $|\rho| \ll \rho_0$ and $|(\vec{u} \cdot \nabla) \, \vec{u}| \ll \left| \frac{\partial \vec{u}}{\partial t} \right|$. This yields the linear Euler's equation:

$$
\nabla p + \rho_0 \frac{\partial \vec{u}}{\partial t} = 0 \,.
\tag{3.19}
$$

3.2.4 The wave equation

The linearised continuity equation and the linear form of Euler's equation can be combined to arrive at a single equation describing sound waves of small amplitudes. Taking the time derivative of (3.14) and the divergence of (3.19) results in

the equations

$$\frac{\partial^2 \rho}{\partial t^2} + \nabla \cdot \left(\rho_0 \frac{\partial \vec{u}}{\partial t} \right) = 0 \tag{3.20a}$$

$$\nabla^2 p + \nabla \cdot \left(\rho_0 \frac{\partial \vec{u}}{\partial t} \right) = 0 \tag{3.20b}$$

in which $\nabla^2 = \nabla \cdot \nabla$ is the Laplacian. Combination of both equations yields

$$\nabla^2 p - \frac{\partial^2 \rho}{\partial t^2} = 0 \, , \tag{3.21}$$

which can be simplified even further making use of the equation of state (3.5) to arrive at the linearised lossless wave equation for propagation in fluids:

$$\nabla^2 p - \frac{1}{c^2} \frac{\partial^2 p}{\partial t^2} = 0 \, , \tag{3.22}$$

Assuming that all quantities vary at a single radial frequency ω, and thus $\overline{p} = \overline{A} e^{j\omega t}$, (3.22) can be written as the Helmholtz equation

$$\nabla^2 \overline{p} + k^2 \overline{p} = 0 \, , \tag{3.23}$$

where $k = \omega/c$ is the angular wave number.

3.3   Simple types of sound waves

In this section, two simple types of sound waves are considered; the plane wave and the spherical sound wave. Their simplicity is due to their one-dimensional nature in their respective coordinate systems (Cartesian or spherical).

3.3.1   Plane waves

Plane waves, such as shown in figure 3.1, are sound waves of which the pressure and particle velocity only depend on a single coordinate in a Cartesian coordinate system. Let us choose the z-axis for this purpose. This reduces equation (3.22) to a somewhat simpler form:

$$\frac{\partial^2 p}{\partial z^2} - \frac{1}{c^2} \frac{\partial^2 p}{\partial t^2} = 0 \, . \tag{3.24}$$

It can be shown (see for example [69]) that solutions of this equation are of the form $p(z, t) = f(z - ct)$ and $p(z, t) = g(z + ct)$. These are waves that propagate in unaltered shape and amplitude in the positive and negative z-direction respectively, with a velocity c. Thus the constant c that was introduced in equation (3.5) turns out to be the sound velocity. The particle velocity in the wave can be found by means of equation (3.19), which can be written for a plane wave that propagates in the z-direction as

$$\frac{\partial p}{\partial z} + \rho_0 \frac{\partial u_z}{\partial t} = 0. \tag{3.25}$$

This equation can be rewritten making use of the substitution $s = z - ct$.

$$\frac{\partial p}{\partial s} \frac{\partial s}{\partial z} + \rho_0 \frac{\partial u_z}{\partial s} \frac{\partial s}{\partial t} = 0$$
$$\frac{\partial p}{\partial s} - \rho_0 c \frac{\partial u_z}{\partial s} = 0 \tag{3.26}$$

Integration of the above equation with regard to s yields the relationship between the excess pressure and the particle velocity; $u_z = \frac{1}{\rho_0 c} p$. Likewise the substitution $s = z + ct$ results in $u_z = -\frac{1}{\rho_0 c} p$, which is consistent with the definition of a backwards travelling wave. The quantity

$$Z_0^a = \frac{p}{u_z} \tag{3.27}$$

is the specific, or characteristic acoustic impedance of the medium, which, for a plane wave, is equal to $Z_0^a = \rho_0 c$.

3.3.2 Spherical waves

In the case of a spherical wave the only variation occurs as a function of the radial distance from the sound source r and time t. The pressure and particle velocities do not vary in the θ and φ directions. Analogously to the previous section, the wave equation (3.22) can be rewritten for this specific case making use of the identities $x = r \sin \theta \cos \varphi$, $y = r \sin \theta \sin \varphi$ and $z = r \cos \theta$, obtaining

$$\frac{\partial^2 p}{\partial r^2} + \frac{2}{r} \frac{\partial p}{\partial r} - \frac{1}{c^2} \frac{\partial^2 p}{\partial t^2} = 0, \tag{3.28}$$

Substitution of $p(r, t) = \frac{1}{r} f(r, t)$ results in

$$\frac{\partial^2 f}{\partial r^2} - \frac{1}{c^2} \frac{\partial^2 f}{\partial t^2} = 0 \tag{3.29}$$

which is again in the same form as the one dimensional wave equation (3.24). The solution of the differential equation is therefore found in the same manner. We obtain for the pressure distribution $p(r,t) = \frac{1}{r}f(r - ct)$, which corresponds to a radially expanding wave. The solution $p(r,t) = \frac{1}{r}g(r + ct)$ exists as well of course, but describes a radially contracting wave (a wave propagating radially towards $r = 0$), which is less interesting to consider.

Making use again of (3.19) and (B.4) in appendix B (page 174), we have that

$$\frac{\partial p}{\partial r} + \rho_0 \frac{\partial u_r}{\partial t} = 0 \,. \tag{3.30}$$

Let us now assume that the pressure varies sinusoidally. For matters of simplicity, we will write it in complex notation as

$$\bar{p}(r,t) = \frac{1}{r}\,\overline{A}\,e^{j(\omega t - kr)} \,, \tag{3.31}$$

with the angular wave number $k = \omega/c$. This reduces equation (3.30) to

$$\bar{u}_r = \frac{1}{\rho_0 c}\left(1 + \frac{1}{jkr}\right)\bar{p}(r,t) \,. \tag{3.32}$$

The specific impedance for a spherically expanding wave is found from the previous equation:

$$\begin{aligned}
\overline{Z}_0^{\mathrm{a}} &= \rho_0 c \frac{1}{1 + \frac{1}{jkr}} \\
&= \frac{\rho_0 c}{1 + k^2 r^2}\left(k^2 r^2 + jkr\right) \,.
\end{aligned} \tag{3.33}$$

Contrarily to the plane wave, in which the pressure and the particle velocity are exactly in phase, the phase difference between both variables varies with the distance from the origin in a spherical wave. The factor kr can be written as $kr = 2\pi r/\lambda$, making the specific impedance depend on the ratio between the distance from the origin and the wavelength. The pressure and particle velocity are exactly out of phase for $r/\lambda = 0$, while for $r/\lambda \to \infty$ they are in phase, and the specific impedance seen by the wave is again the same as in the plane wave case:

$$Z_0^{\mathrm{a}}\Big|_{r\to\infty} = \rho_0 c \,. \tag{3.34}$$

The point source

If a spherical source pulsates with a velocity $U_0 e^{j\omega t}$ and has a radius a, we can find from 3.33 that the pressure at the surface of the source is

$$\overline{p}(a,t) = \overline{u}(a,t)\,\overline{Z}_0^a(a) \,,$$
$$= \frac{1}{1 + \frac{1}{jka}}\rho_0 c U_0 e^{j\omega t} \,, \tag{3.35}$$

Combination of the latter with equation (3.31) yields

$$\overline{p}(r,t) = \rho_0 c U_0 \frac{jka}{1 + jka}\frac{a}{r}e^{j(\omega t + k(a-r))} \,, \tag{3.36}$$

which in case of a long wavelength in comparison to the source radius reduces to

$$\overline{p}(r,t) = j\rho_0 c U_0 \frac{ka^2}{r}e^{j(\omega t - kr)} \,, \quad ka \ll 1 \,. \tag{3.37}$$

The *volume velocity Q* that is produced by our spherical source is equal to its velocity multiplied by its surface area. Consequently the volume velocity amplitude is

$$Q_0 = 4\pi a^2 U_0 \,. \tag{3.38}$$

which allows the expression for the sound pressure to be simplified to

$$\overline{p}(r,t) = \frac{j\omega \rho_0 Q_0}{4\pi r}e^{j(\omega t - kr)} \,. \tag{3.39}$$

Combination with (3.32) finally yields an expression of the particle velocity that is produced by this source:

$$\vec{\overline{u}}(r,t) = \frac{Q_0}{4\pi r^2}\,(1 + jkr)\,e^{j(\omega t - kr)}\hat{r} \,. \tag{3.40}$$

As mentioned, these expressions are only valid for long wavelengths in comparison to the radius of the spherical source. In the case of a point source, having an infinitesimally small radius, however, these equations are exact, as long as the frequency, and therefore k, is finite.

3.4   Attenuation of sound

Until now the influence of attenuation of sound waves was neglected in the discussion of wave propagation. While in many cases this is a fair assumption, the

theory put forward here will be used to discuss energy transfer by means of sound waves. This means that it is imperative to, at the very least, consider attenuation, and to investigate whether or not it can be neglected. This section slightly extends the theory described above to allow it to describe the effect that absorption has on the sound wave.

It would go too far for this short introduction to acoustics to discuss the theory of attenuation in gases and fluids and to derive sound wave equations that reflect these effects. Instead the result will be merely given here. More details can be found in standard works on acoustics. For example [58] contains an excellent analysis of absorption and attenuation. As Kinsler *et al.* describe, there are multiple effects at play that result in attenuation of a sound wave. Generally they all lead to a lossy Helmholtz equation

$$\nabla^2 \overline{p} + \overline{k}^2 \, \overline{p} = 0 \,. \tag{3.41}$$

This equation is very similar to the Helmholtz equation (3.23) that was derived earlier. The only difference is the substitution of a complex valued angular wave number

$$\overline{k} = k - j\alpha \,. \tag{3.42}$$

Here k is still defined as the ratio of the angular frequency to the sound velocity, i.e. $k = \omega/c$. Attenuation of sound waves is accounted for by introduction of the absorption coefficient α of the medium, which is a function, not only of the parameters of the medium, such as its chemical composition, temperature and pressure, but also of the frequency of the sound propagating through it.

3.5 Power and sound intensity

As the particles in a sound wave have a certain mass, their vibration implies that they possess a certain amount of kinetic energy. Likewise, the pressure variations in the gas require the exchange of potential energy within the sound wave. The presence of these forms of energy in a sound wave is of course the very reason that sound can be used to transfer energy.

3.5.1 Sound intensity

The energy that is transferred by a sound wave through a certain area perpendicular to the direction of propagation of the wave, is equal to the work performed by the

particles adjacent to this area [35]. The rate of work that is done is equal to the product of the force $\vec{F}$ that is exerted on and the velocity $\vec{u}$ of the particles. The rate of work per unit area is then given by

$$\frac{\mathrm{d}}{\mathrm{d}S}\frac{\mathrm{d}W}{\mathrm{d}t} = pu_n \tag{3.43}$$

in which $\mathrm{d}S$ is an infinitesimally small area and u_n the component of the particle velocity normal to the surface. Generalising this concept we can define a vector quantity

$$\vec{I}(t) = p(t)\,\vec{u}(t)\,, \tag{3.44}$$

which is the instantaneous sound intensity. It is in essence the energy flux density of the sound wave, i.e. the amount of energy that passes per unit time through a unit area.

In a time-stationary acoustic field, the instantaneous sound intensity can be split up into an active and a reactive component [35]. The active sound intensity $\vec{I}_a$ is the time average of the instantaneous sound intensity

$$\vec{I}_a = \frac{1}{T}\int_{t_0}^{t_0+T} p(t)\,\vec{u}(t)\,\mathrm{d}t\,, \tag{3.45}$$

and as such represents the net transport of energy in the direction of $\vec{I}_a$. The integration length T in this equation is chosen so that averaging takes place over an integer number of periods of the sound wave. Note that although the active sound intensity no longer contains a time dependency, it is a vector which still depends on the spatial position in the sound field. The reactive part of the sound intensity represents the locally oscillating exchange of energy in the sound field, without actual transport or dissipation.

The term 'sound intensity' is often interpreted as the average flow of energy in the direction of propagation $\|\vec{I}_a\|$, which is of course only meaningful when the sound wave has a distinct direction of propagation, such as a plane wave. If the vector $\vec{I}_a$ is a function of spatial coordinates as well one can still talk about the the magnitude of the sound intensity $I_a = \|\vec{I}_a\|$, but this has a different meaning in most cases, as it is the active sound intensity in the *local* direction of propagation (which is $\vec{u}/\|\vec{u}\|$). Whenever the scalar I_a is used in this thesis, it will have the latter meaning to avoid confusion. Whenever one can speak of one single direction of propagation of the sound wave, I_a will be the active sound intensity of the wave. In all other cases the vector intensity $\vec{I}$ will be used.

In acoustics mostly periodic signals with a zero average are considered, which renders the concept of intensity somewhat easier. In this case both the pressure and

particle velocity can be written as a linear combination of sinusoids at frequencies that are an integer multiple of a fundamental frequency ω. The pressure field can then be written as

$$p(\vec{r}, t) = \sum_{m=1}^{\infty} P_m(\vec{r}) \cos\left(m\omega t + \varphi_{\text{p},m}\right) . \tag{3.46}$$

An analogous expression can be found for the particle velocity

$$\vec{u}(\vec{r}, t) = \sum_{n=1}^{\infty} U_n(\vec{r}) \cos(n\omega t + \varphi_{\text{u},n}) \, \hat{u} . \tag{3.47}$$

The instantaneous sound intensity is subsequently found by combining the previous two equations and (3.44), yielding

$$\begin{aligned}
\vec{I}(\vec{r}, t) &= \sum_{m=1}^{\infty} \left[P_m(\vec{r}) \cos\left(m\omega t + \varphi_{\text{p},m}\right) \right] \sum_{n=1}^{\infty} \left[\vec{U}_n(\vec{r}) \cos(n\omega t + \varphi_{\text{u},n}) \right] \\
&= \sum_{m=1}^{\infty} \sum_{n=1}^{\infty} \vec{I}_{m,n}(\vec{r}, t)
\end{aligned} \tag{3.48}$$

The product $\vec{I}_{m,n}$ of the m-th term of the pressure and the n-th term of the particle velocity is

$$\begin{aligned}
\vec{I}_{m,n}(\vec{r}, t) &= P_m(\vec{r}) \cos\left(m\omega t + \varphi_{\text{p},m}\right) \vec{U}_n(\vec{r}) \cos(n\omega t + \varphi_{\text{u},n}) \\
&= \tfrac{1}{2} P_m(\vec{r}) \vec{U}_n(\vec{r}) \Big[\cos\left((m+n)\omega t + \left(\varphi_{\text{p},m} + \varphi_{\text{u},n}\right)\right) + \\
&\qquad \cos\left((m-n)\omega t + \left(\varphi_{\text{p},m} - \varphi_{\text{u},n}\right)\right) \Big]
\end{aligned} \tag{3.49}$$

It is clear from equations (3.45), (3.48) and (3.49) that the only components that contribute to the active sound intensity, and hence to the net transport of energy, are those components that are of equal frequency ($m = n$) and have a phase difference unequal to $\frac{1}{2}\pi$ (i.e. $\varphi_{\text{p},m} - \varphi_{\text{u},n} \neq \frac{1}{2}\pi \pmod{\pi}$)

To simplify matters even further, let us suppose that we have a pressure field that varies purely sinusoidally, i.e. $p(\vec{r}, t) = P(\vec{r}) \cos\left(\omega t + \varphi_{\text{p}}\right)$, and a particle velocity $\vec{u}(\vec{r}, t) = \vec{U}(\vec{r}) \cos(\omega t + \varphi_{\text{u}})$. There are no higher harmonics present, contrarily to the previous discussion. From the results above we have that

$$\begin{aligned}
\vec{I}_{\text{a}}(\vec{r}, t_0) &= \frac{P(\vec{r}) \, \vec{U}(\vec{r})}{2T} \int_{t_0}^{t_0 + \frac{2\pi}{\omega}} \left[\cos\left(2\omega t + \left(\varphi_{\text{p}} + \varphi_{\text{u}}\right)\right) + \cos\left(\varphi_{\text{p}} - \varphi_{\text{u}}\right) \right] \mathrm{d}t \\
&= \tfrac{1}{2} P(\vec{r}) \, \vec{U}(\vec{r}) \cos\left(\varphi_{\text{p}} - \varphi_{\text{u}}\right) .
\end{aligned} \tag{3.50}$$

When the excess sound pressure and the particle velocity are written in complex notation $\bar{p}(\vec{r}, t) = P(\vec{r})\, e^{j(\omega t + \varphi_\text{P})}$ and $\vec{\bar{u}}(\vec{r}, t) = \vec{U}(\vec{r})\, e^{j(\omega t + \varphi_\text{u})}$, one can show that the active sound intensity is

$$\vec{I}_\text{a}(\vec{r}) = \tfrac{1}{2}\,\text{Re}\left(\bar{p}(\vec{r}, t)\,\vec{\bar{u}}^*(\vec{r}, t)\right) . \tag{3.51}$$

3.6   Equivalent electrical networks

Any system of linear time-invariant differential equations can be represented by an equivalent electrical network. Such networks can prove enormously insightful, especially for electrical engineers who are used to working with such diagrams. The purpose of an electrical network is to capture the (most important) behaviour of a system in a diagram. The use of these circuits, however, is not only limited to electrical problems. Any problem that can be described by (linear) differential equations can be captured into such an equivalent network. Ideal capacitors and inductors, having the voltage-current relationships $v = L\frac{\mathrm{d}i}{\mathrm{d}t}$ and $i = C\frac{\mathrm{d}v}{\mathrm{d}t}$ respectively, are then used to represent differentiation and integration.

The cornerstone of electrical networks is the concept of impedance, introduced by Oliver Heaviside, which is defined as the ratio of the voltage across an element to the current through it. As already discussed in section 1.2, this thesis uses

$$\overline{Z}^\text{a} = \frac{\bar{p}}{\bar{u}} \tag{3.52}$$

as definition for the acoustic impedance. The superscript a is used to indicate an acoustic impedance. From this definition we find that pressure is equivalent to a voltage and particle velocity to a current. Furthermore, the relationship $\bar{p} = \overline{Z}^\text{a}\,\bar{u} = j\omega m\,\bar{u}$ shows that an inductance is equivalent to an inertance per unit area m on which the pressure p acts. A mechanical equivalent would be a mass per unit area. Equivalently, an acoustic compliance per unit area n, which behaves according to $n\frac{\mathrm{d}p}{\mathrm{d}t} = u$, translates to capacitance in the electrical case. These relationships are summarised in table 3.1.

In principle, the use of equivalent circuits is restricted to one-dimensional acoustic problems, since the current in such a diagram is a scalar quantity. As such, it cannot be used to describe a general particle velocity, which is a vector. Therefore, the direction of $\vec{u}$ should be implicitly defined, as is the case in a one-dimensional wave, such as the plane wave or the spherical wave that were discussed earlier in sections 3.3.1 and 3.3.2.

Table 3.1   Conversion from acoustic to electrical variables and parameters.

Acoustic variable		Electrical equivalent	
Pressure	p (Pa)	Voltage	v (V)
Particle velocity	u (m s^{-1})	Current	i (A)
Damping per unit area	b (N s m^{-3})	Resistance	R (Ω)
Mass per unit area	m (kg m^{-2})	Inductance	L (H)
Compliance per unit area	n (m^3 N^{-1})	Capacitance	C (F)

The use of equivalent circuits is not limited to so-called lumped element models in which the acoustic problem can be wholly represented—or rather: approximated—by means of a small number of electrical circuit components, say a single series RLC combination. Equivalent circuits can also be used in systems where one can speak of a distributed impedance, such as is the case with transmission line circuits. A sound wave propagating in a pipe is no different from an electromagnetic wave propagating along a length of conductor or a waveguide. Therefore, transmission lines are another commonly encountered form of electrical equivalents for acoustic problems.

The advantage of using equivalent circuits is that they can describe the behaviour of both the electrical and mechanical domains at the same time, through coupling elements such as transformers and gyrators [101] that link both domains. Examples will be encountered in section 4.2.

4

First steps in acoustic energy transfer

T HERE are two main performance indices for any system that is used to transfer energy, independently of whether or not it achieves it contactlessly. These are the energy transfer efficiency on one hand, and the power transfer capabilities on the other. These two factors determine the physical limitations of such a system. One expects a part of a system that transfers energy to do so without impeding the energy flow, and thus without posing any restriction on the power flow through it, within the limits in which the system is to be used of course. Efficiency is always a key aspect, as it determines how economically sound an energy transfer system is, and how much heating is to be expected. It is often the most interesting aspect on the basis of which to compare energy transfer systems.

Of course there are other characteristics of contactless energy transfer systems that can be of importance when trying to determine the best candidate in any situation, but these can be rather application dependent. One can think of issues such as the strength or presence of electromagnetic fields, for example with regard to safety, or whether there are obstacles in the line of sight between the transmitter and the receiver, the medium through which the energy is to be transmitted (especially metallic barriers can pose great difficulties for methods that rely on electromagnetic fields) or limitations on system dimensions, just to name a few.

The purpose of this chapter is to take a first look at the energy transfer that can be attained by means of contactless energy transfer through air. Therefore we will

---

This chapter is based on [98] and [100].

have to look at the specific loss mechanisms that occur in such an application. When talking specifically about acoustic energy transfer systems, the energy transfer efficiency is limited chiefly by four effects:

- the attenuation of sound waves in the medium;

- the spreading of the sound waves;

- the transduction efficiency;

- losses in electrical circuitry.

Modelling these effects is necessary to be able to judge the attainable efficiency.

Attenuation   Attenuation of sound waves in a medium occurs through a number of different principles, which vary according to the type of medium and can include viscous or frictional losses, heat conduction, molecular thermal relaxation, structural relaxation, chemical relaxation, losses at boundaries, crystal lattice defects, scattering in polycrystalline materials, and so forth [58, 69].

Spreading   Parts of the sound wave that do not reach the receiver surface will propagate into infinity and will be absorbed at some point. As such they do not contribute to the output power at the receiving end. Therefore these can be considered as losses, which can be grouped under *spreading losses*. Spreading of sound waves can occur naturally because of the radiation pattern of the source. In practice virtually no sound source radiates a collimated beam, but will always create a divergent radiation pattern. Spreading can also occur because of a change in the direction of propagation of the sound wave, because of either refraction or diffraction [85]. Refraction is the bending of sound waves due to a change in the medium. One can think of a change in sound velocity due to local temperature variation of the medium, for example. Diffraction is the bending of sound waves around objects.

Transduction   The transduction efficiency takes into account the losses that occur in the transducer which converts the electrical energy into mechanical vibrations at the transmitting side and vice versa at the receiving end. Any losses in this process, whether they be of electrical or mechanical origin, will decrease the amount of energy that is transferred to an application that is to be powered.

Circuitry   In order to work, an acoustic energy transfer system requires electrical circuitry at the transmitting and receiving ends, which inherently introduce losses. These losses fall outside the scope of this thesis, as they are a field of research in themselves, depending on the circuit topologies that are chosen.
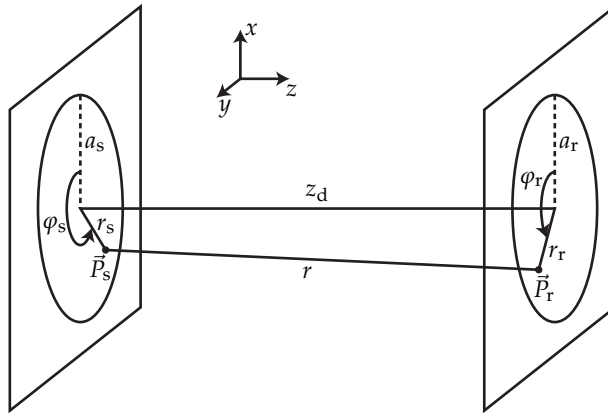
Figure 4.1 A simple acoustic energy transfer system consists of a coaxially placed circular transmitter and receiver. The squares represent the planes in which the transmitter and receiver are placed, which are assumed to be parallel to each other. The transmitting transducer is assumed to be placed in an infinite baffle.

4.1 Diffraction and attenuation

Having drawn up a list of all possible loss mechanisms in an AET system, we can make a start with the creation of a model, with the goal of arriving at an efficiency limit for a simple acoustic energy transfer system. The system that we will be looking at is, at first, a simple transmitter and receiver of circular shape placed coaxially at a distance z_d from each other. This acoustic energy transfer system is depicted schematically in figure 4.1.

4.1.1 Diffraction

Let us first examine the effect of diffraction in the model. Diffraction occurs in our simple system of figure 4.1 due to the limited size of the transmitter and receiver. The edge of the transmitter will always create a sound field that radiates over a large angular range. However, the larger the transmitter size is in comparison to the wavelength, the less pronounced the effect of its edge will be, and therefore, the less divergent its sound beam will be. If a sound beam diverges to some extent, a finite receiver size implies that not all energy that was transmitted as a sound wave is collected by the receiver. As a result, diffraction losses are influenced by the system dimensions.

Some further assumptions about the system will have to be made, if we are to be able to calculate the influence of the spreading for the simple AET system described above. Here we will make the assumption that the front face of the transmitting transducer vibrates as a whole, without flexing or bending at any point. This type of source can be modelled as a classical source: what is known in literature as a *vibrating piston source* [21, 58, 69, 85, 120]. This is essentially a circular disk of radius a_s which is mounted in an infinite baffle, of which the surface uniformly performs sinusoidal vibrations with a velocity amplitude U_0 and angular frequency ω.

Pressure and particle velocity

It is possible to calculate the pressure and particle velocity that are generated by such a piston by considering its surface to be made up of an infinite number of individual baffled point sources. The superposition of the pressure field of each individual point source results in the total pressure field of the piston source, which is achieved by integration over the piston surface. This method is commonly referred to as a Rayleigh integral, and is a special case of the more general Kirchhoff diffraction formula [69, 82].

The piston vibrates with a velocity $\overline{u} = U_0 e^{j\omega t}$, which means that every point of the piston moves at this same velocity. Every infinitesimally small section of the piston surface of area dS therefore produces a volume velocity $d\overline{Q} = \overline{u}dS$. Consequently, the volume velocity amplitude is $dQ_0 = U_0 dS$. The pressure that is generated by such a single point source at a distance r is found with help from equation (3.39) to be

$$d\overline{p}_\mathrm{P} = \frac{j\omega\rho_0 U_0}{2\pi r} e^{j(\omega t - \overline{k}r)} dS .$$

(4.1)

The corresponding particle velocity that is produced by this point source is analogously found from (3.40) to be

$$d\vec{\overline{u}}_\mathrm{P} = \frac{U_0}{2\pi r^2} \left(1 + j\overline{k}r\right) e^{j(\omega t - \overline{k}r)} \hat{r}_\mathrm{P} dS .$$

(4.2)

These equations contain a complex angular wave number $\overline{k} = k - j\alpha$ to account for the absorption by the medium by means of an absorption coefficient, as explained in section 3.4. The distance r between each source point $\vec{P}_s = r_s\hat{r} + \varphi_s\hat{\varphi}$ and receiver point $\vec{P}_r = r_r\hat{r} + \varphi_r\hat{\varphi} + z_d\hat{z}$ is given by

$$r = \left\|\vec{P}_s - \vec{P}_r\right\|$$
$$= \sqrt{r_s^2 + r_r^2 + z_d^2 - 2r_s r_r \cos(\varphi_s - \varphi_r)} .$$

(4.3)

The unit vector $\hat{r}_{\mathrm{p}}$ points in the radial direction away from the source point. The direction of $\mathrm{d}\vec{u}_{\mathrm{p}}$ at the receiver point $\vec{P}_{\mathrm{r}}$ is therefore the direction of the line $\vec{P}_{\mathrm{s}}\vec{P}_{\mathrm{r}}$. This unit vector can be written in terms of the unit vectors in the Cartesian coordinate system in figure 4.1, as

$$\hat{r}_{\mathrm{p}} = \frac{1}{r}\left((r_{\mathrm{r}}\cos\varphi_{\mathrm{r}} - r_{\mathrm{s}}\cos\varphi_{\mathrm{s}})\,\hat{x} + (r_{\mathrm{r}}\sin\varphi_{\mathrm{r}} - r_{\mathrm{s}}\sin\varphi_{\mathrm{s}})\,\hat{y} + z_{\mathrm{d}}\hat{z}\right) \qquad (4.4)$$

Without loss of generality, the case $\varphi_{\mathrm{r}} = 0$ can be considered, since the problem is symmetric around the z-axis. The total sound pressure and particle velocity at any point in the field can then be found by integration over the surface of the transmitter. Denoting the area of the transmitter by A_{s}, the pressure is found from (4.1) to be

$$\overline{p}(r_{\mathrm{r}}, z_{\mathrm{d}}, t) = \iint_{A_{\mathrm{s}}} \mathrm{d}\overline{p}_{\mathrm{p}}$$
$$= \frac{j\omega\rho_0 U_0}{2\pi}e^{j\omega t}\int_0^{a_{\mathrm{s}}}\int_0^{2\pi}\frac{e^{-j\bar{k}r}}{r}r_{\mathrm{s}}\mathrm{d}\varphi_{\mathrm{s}}\mathrm{d}r_{\mathrm{s}}\,. \qquad (4.5)$$

The particle velocity is found in exactly the same manner by integration of $\mathrm{d}\vec{u}_{\mathrm{p}}$ from (4.2). It is equal to

$$\vec{u}(r_{\mathrm{r}}, z_{\mathrm{d}}, t) = \iint_{A_{\mathrm{s}}} \mathrm{d}\vec{u}_{\mathrm{p}}$$
$$= \frac{U_0}{2\pi}e^{j\omega t}\int_0^{a_{\mathrm{s}}}\int_0^{2\pi}\frac{e^{-j\bar{k}r}}{r^2}\left(1 + j\bar{k}r\right) \times \qquad (4.6)$$
$$\frac{1}{r}\left((r_{\mathrm{r}} - r_{\mathrm{s}}\cos\varphi_{\mathrm{s}})\,\hat{x} - r_{\mathrm{s}}\sin\varphi_{\mathrm{s}}\hat{y} + z_{\mathrm{d}}\hat{z}\right)r_{\mathrm{s}}\mathrm{d}\varphi_{\mathrm{s}}\mathrm{d}r_{\mathrm{s}}\,.$$

Here a_{s} is the radius of the transmitter, and z_{d} is the distance between the transmitter and the receiver.

Careful examination of the system reveals that for $\varphi_{\mathrm{r}} = 0$ there is no net contribution of the y-component of the integrand in the calculation of the particle velocity in equation (4.6) due to rotational symmetry. Therefore the y-component of $\vec{u}$ is equal to zero. The calculated x-component of the particle velocity is equal to the r-component in the cylindrical coordinate system. Moreover, the inner integral in both (4.5) and (4.6) can be rewritten employing the system's symmetry, since in both integrals the contributions of the intervals $[0; \pi]$ and $[\pi; 2\pi]$ are equal. Hence the equations for

the pressure and particle velocity produced by the vibrating piston reduce to

$$
\begin{cases}
\overline{p}(r_r, z_d, t) = j\omega\rho_0 \dfrac{U_0}{\pi} e^{j\omega t} \displaystyle\int_0^{a_s}\int_0^{\pi} \dfrac{e^{-j\overline{k}r}}{r} r_s \mathrm{d}\varphi_s \mathrm{d}r_s \\[4mm]
\vec{\overline{u}}(r_r, z_d, t) = \dfrac{U_0}{\pi} e^{j\omega t} \displaystyle\int_0^{a_s}\int_0^{\pi} \dfrac{e^{-j\overline{k}r}}{r^2} \left(1 + j\overline{k}r\right) \times \\[4mm]
\qquad\qquad\qquad \dfrac{1}{r}\left((r_r - r_s\cos\varphi_s)\,\hat{r} + z_d\hat{z}\right) r_s \mathrm{d}\varphi_s \mathrm{d}r_s\,.
\end{cases}
\tag{4.7}
$$

From pressure to power

As was explained in section 3.5.1, the energy flux density of a (sound) pressure wave is characterised by the associated sound intensity. The sound intensity vector at any point in space in a homogenous gaseous medium can be calculated from the expressions for the pressure and particle velocity in (4.7) using (3.51):

$$
\begin{aligned}
\vec{I_a}(r_r, z_d) &= \tfrac{1}{2}\,\mathrm{Re}\left(\overline{p}\,\vec{\overline{u}}^{*}\right) \\
&= I_{a,r}\hat{r} + I_{a,z}\hat{z},
\end{aligned}
\tag{4.8}
$$

The total intensity at any point is then found from the euclidian norm of the intensity vector:

$$
\begin{aligned}
I_a(r_r, z_d) &= \left\|\vec{I_a}\right\| \\
&= \sqrt{I_{a,r}^2 + I_{a,z}^2}\,.
\end{aligned}
\tag{4.9}
$$

Numeric integration, e.g. by means of the MATLAB integral2 function, allows the calculation of the diffraction pattern of the circular piston source. An example of such a pattern is shown in figure 4.2 as a function of z and r. Attenuation was omitted in this simulation, i.e. $\overline{k} = k$.

As is immediately clear from the radiation pattern, the diffraction that occurs at the edge of the piston itself prevents a truly perfect focus. A piston source does not produce a plane wave, but it rather creates a main on-axis lobe and many so-called side lobes. Both the main and the side lobes diverge, and therefore a receiver of finite dimensions will never be able to collect all radiated energy.

Figure 4.2 shows a clear focal point to the radiation pattern of the source where the sound intensity is the greatest, around $z_d = 400\,\text{mm}$. This focal point can be employed for AET, although placement of the receiver at this location does not
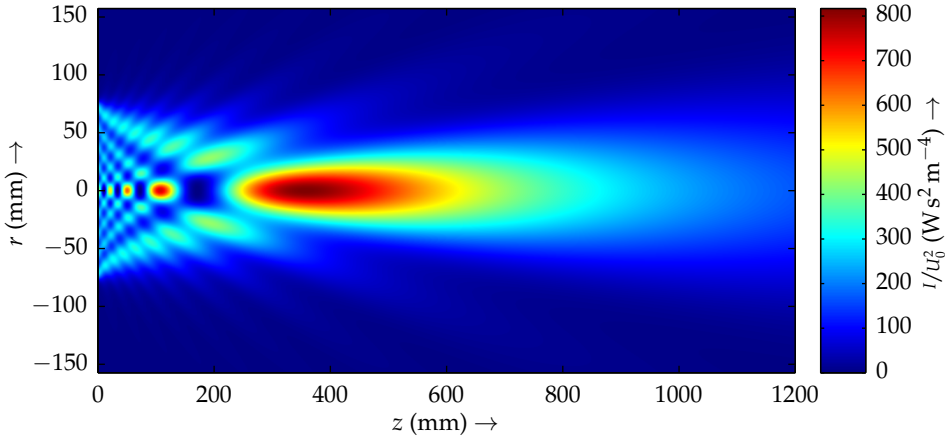
Figure 4.2   The sound intensity pattern of a vibrating piston shows the diffraction of the sound field by the aperture. The sound intensity is normalised to the piston velocity squared to render it independent of the input power. For the simulation $a_s = 7.83$ cm, and $f = 20$ kHz were used.

necessarily result in the highest possible output power. Since the sound intensity is an energy flux density, its integral over the receiver surface yields the energy flow through that surface. Therefore the shape and size of that receiving surface determine where the maximum power can be harvested from the sound wave.

In the system in figure 4.1 the total received power is

$$\Pi_r = 2\pi \int_0^{a_r} I_a(r_r, z_d)\, r_r \mathrm{d}r_r \, . \tag{4.10}$$

One could argue that it is not entirely correct to consider the total sound intensity I_a, as it also contains a contribution of the r-component, and that one should only look at the component $I_{a,z}$ normal to the receiver surface in figure 4.1. Since a limit to the energy transfer efficiency is considered in this chapter, we will, however, opt to use the total intensity, as an intelligent receiver design could possibly also make use of the r-component that is present in the sound wave.

Energy transfer efficiency

So far only pressures, particle velocities and the available power at the site of the receiver have been discussed. If we go one step further, we can examine the energy
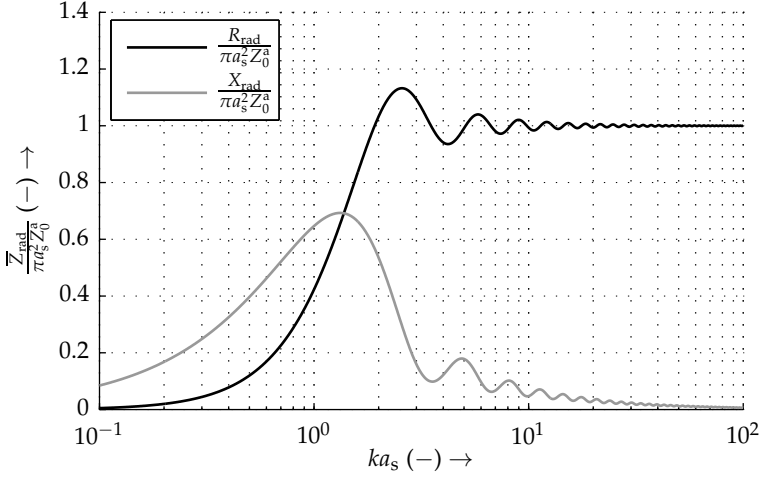
Figure 4.3 The normalised radiation impedance of a circular piston source converges to $\overline{Z}_{rad}/\pi a_s^2 Z_0^a = 1 + j0$ for high values of ka_s.

transfer efficiency due to diffraction η_{dif}, which can be defined as the ratio of the received power to the total radiated power

$$\eta_{dif} = \frac{\Pi_r}{\Pi_{rad}} \; . \tag{4.11}$$

Without going into detail, the radiation impedance, i.e. the ratio of force over velocity, that the piston works against is given by (see for example [58, 69])

$$\begin{aligned}
\overline{Z}_{rad} &= R_{rad} + jX_{rad} \\
&= \rho_0 c \pi a_s^2 \left(1 - 2\frac{J_1(2ka_s)}{2ka_s} + j2\frac{\mathbf{H}_1(2ka_s)}{2ka_s} \right) ,
\end{aligned} \tag{4.12}$$

with $J_1(x)$ the first-order Bessel function of the first kind and $\mathbf{H}_1(x)$ the first order Struve function [3, 5]. For completeness, the radiation impedance is plotted in figure 4.3 as a function of ka_s.

The power that is radiated by the source is then found from

$$\begin{aligned}
\Pi_{rad} &= \tfrac{1}{2}U_0^2 R_{rad} \\
&= \tfrac{1}{2}U_0^2 \rho_0 c \pi a_s^2 \left(1 - 2\frac{J_1(2ka_s)}{2ka_s} \right) ,
\end{aligned} \tag{4.13}$$

Combining equations (4.10), (4.11) and (4.13), the diffraction dependent ratio of

received to transmitted power is then found to be

$$\eta_{\text{dif}} = \frac{4}{U_0^2 \rho_0 c a_{\text{s}}^2 \left(1 - 2\frac{\text{J}_1(2ka_{\text{s}})}{2ka_{\text{s}}}\right)} \int\limits_0^{a_{\text{r}}} I_{\text{a}}(r_{\text{r}}, z_{\text{d}}) \, r_{\text{r}} \mathrm{d}r_{\text{r}} , \qquad (4.14)$$

which, when considering (4.7) and (4.9), is independent of U_0, and thus of the input power.

It is possible to find an analytical expression for (4.14) by making use of far field approximations (see for example [58, 69]), namely $r_{\text{r}} \ll r$. Unfortunately, these approximations cannot be guaranteed to be valid in the region of interest. The far field approximation, as the name implies, neglects the near field that is seen to exist close to the source in figure 4.2. For our efficiency limit it might be beneficial to work in this region, and as such it should be included in the analysis. Therefore (4.14) is to be calculated numerically.

The energy transfer efficiency due to diffraction is shown in figure 4.4 as a function of the frequency of vibration of the piston. The efficiency is depicted for a transmitter and receiver radius $a = a_{\text{s}} = a_{\text{r}}$ of 2, 5 and 10 cm, and a distance between the two of $z_{\text{d}} = 1$ m. From the graphs it is immediately clear that, in order to keep the diffraction losses low, a frequency should be used that is as high as possible. This is easily explained qualitatively. As the ratio between the transmitter radius and the wavelength grows, as it does for an increasing frequency, the transmitter transforms from a point source to a very large plate, in comparison to the wavelength. So while the piston source emits sound waves almost omnidirectionally at low frequencies, it creates virtually plane waves at extremely high frequencies. Therefore high frequencies imply a collimated beam between the transmitter and the receiver. This effect is also very apparent from the difference in the efficiency for an increase in the transducer dimensions, effectively increasing the ratio between transmitter size and wavelength for an equal frequency. Therefore a larger transmitter is more efficient at lower frequencies. Increasing the size of the receiver has the same effect, since it allows a larger part of the radiated energy to be captured, as a result of a larger receiver.

The diffraction losses that are calculated in this section are of course only valid in the case of a transmitter that behaves as a circular piston, and a circular receiver that absorbs all the energy of the sound wave that impinges upon it. This is not a situation that is likely to occur in an actual system, but it will serve to obtain insight in how such a system will perform. Still, there are some improvements possible over this system that would allow less diffraction losses. One could, for example, apply focusing (see [77, 79] for instance), or use low-diffraction beam patterns [30, 31, 90, 102].
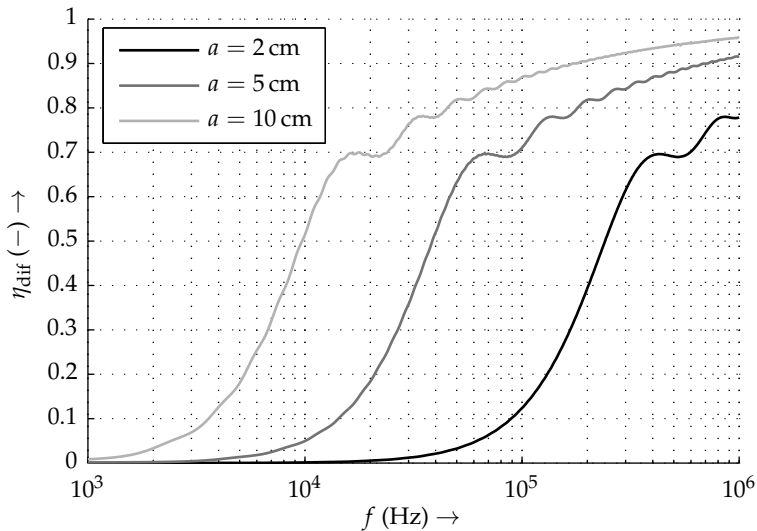
Figure 4.4 The energy transfer efficiency η_{dif} solely due to diffraction losses shows an increases with the frequency of vibration of the piston source. The efficiency is plotted for a number of transmitter and receiver radii $a = a_{\text{s}} = a_{\text{r}} \in \{2, 5, 10\}$ cm and a distance $z_{\text{d}} = 1$ m between the two.

4.1.2 Attenuation

A great advantage of a contactless energy transfer system that is based on inductive energy transfer is that attenuation and absorption in the medium barely have any influence on the energy transfer efficiency. This is, of course, only true when no conductive materials other than the inductors themselves are present in the vicinity of the two coils. Induced eddy currents in any material will lead to dissipation, and thus losses.

Acoustic waves suffer much more from absorption and attenuation by the medium in which they propagate, unfortunately. Section 3.4 already briefly touched on the subject of the modelling aspect of attenuation and absorption in fluids and gases. It explains that it is possible to introduce an absorption constant α with which the angular wave number can be extended to account for losses.

The question is now how to choose a good value for the absorption constant. This is a whole field of research in itself, and the easiest method is therefore to consult literature on the subject. This thesis only covers the use of sound waves for the wireless transfer of energy through air, for which some data are available on sound attenuation, although figures differ from publication to publication. The data in [12, 13, 33], however, are consistent with both an ANSI and an ISO norm (see the

references in [13]), and are cited in many works on acoustics (e.g. [58,69]). Therefore these seem to be a good reference and will be used in the remainder of this thesis.

The formulas in [13] describe the dependency of the attenuation coefficient α in (3.42) as a function of the air temperature, its relative humidity, the atmospheric pressure and the sound wave frequency. The value of this attenuation constant stems from an analytical model of energy transfer mechanisms in an air mixture consisting of nitrogen, oxygen, water vapor and carbon dioxide, and agrees well with experimentally determined values.

Since the attenuation constant is part of the angular wave number $\bar{k}$, it is not directly clear from (4.7) how it affects the efficiency of our acoustic energy transfer system. The exact relationship between the efficiency and the attenuation constant can only be found through integration. It is, however, possible to obtain a reasonable estimate of the influence of the attenuation constant by assuming that there is a single travelling wave between the transmitter and the receiver, which is not too bold an assumption as long as the distance z_d is large in comparison to the receiver radius a_r.

The damped travelling wave solution [58] is then

$$\bar{p}(z,t) = P_0 e^{-\alpha z} e^{j(\omega t - kz)} \tag{4.15}$$

of which the sound intensity is, from (3.27) and (3.44),

$$
\begin{aligned}
I_a(z) &= \frac{1}{2\rho_0 c} \left(P_0 e^{-\alpha z} \right)^2 \\
&= I_a(0)\, e^{-2\alpha z} .
\end{aligned}
\tag{4.16}
$$

A good first order approximation of the energy transfer ratio due to attenuation is obtained by division of the sound intensity at $z = z_d$ by that at the transmitting surface $I(0)$, resulting in

$$\eta_{\text{att}} = e^{-2\alpha z_d} . \tag{4.17}$$

This energy transfer efficiency, as it has been calculated above, is by definition independent of the transmitter and receiver dimensions, since we assumed a simple travelling wave. It only depends on the distance between the source and the receiving element. The graph in figure 4.5 shows η_{att} for a distance of $z = z_d$. From it we see that an increase in sound frequency leads to higher attenuation losses. The attenuation constant that was used to calculate the graph was derived for a relative humidity of the air of 45 %, an atmospheric pressure of 1 atm and a temperature of 20 °C.
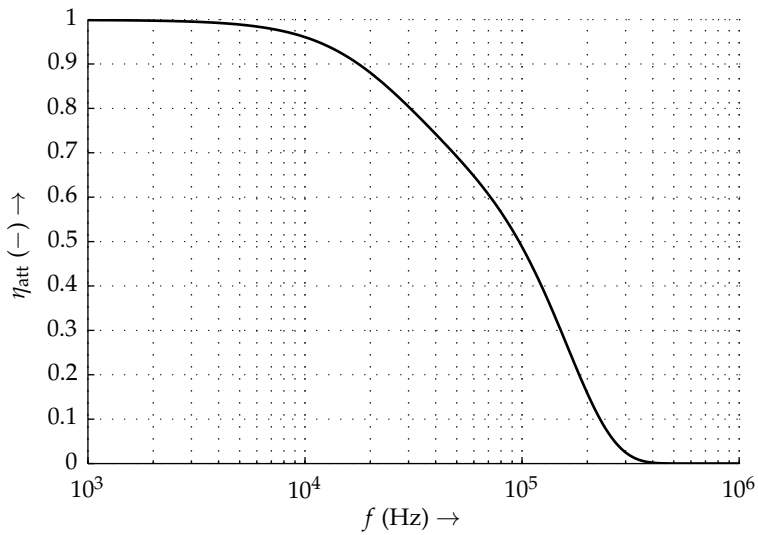
Figure 4.5 The influence on the energy transfer efficiency of the attenuation by the air η_{att} of a travelling wave is defined as the sound intensity at a distance $z = z_d$ along the propagation direction of the wave divided by the intensity at $z = 0\,\text{m}$. The efficiency due to attenuation is plotted here for a distance $z_d = 1\,\text{m}$, a relative humidity of the air of 45 %, an atmospheric pressure of 1 atm and a temperature of 20 °C

4.1.3 Combined energy transfer efficiency

From figures 4.4 and 4.5 one can see that the energy transfer efficiency due to diffraction increases with an increase in frequency, while the converse is true for the energy transfer efficiency due to attenuation by the medium. This implies that there is an optimum driving frequency for a given set of system dimensions (i.e. the transmitter and receiver radii a_s and a_r and the distance z_d that is to be crossed), where the *total* energy transfer efficiency is optimal.

In the previous, the efficiency as a result of diffraction and attenuation were investigated as separate effects. While this is a good approximation to get a feeling for the effect that attenuation has, it is in practice necessary to consider both effects simultaneously. For this reason from here on the total energy transfer efficiency will be considered, not as the product $\eta_{dif}\eta_{att}$, but rather through proper calculation of the pressure and particle velocity in (4.7) by means of a complex angular wave number $\bar{k}$.

The total energy transfer efficiency η_t is depicted in figure 4.6 for transmitter and receiver radii $a = a_s = a_r$ of 2, 5 and 10 cm. These graphs clearly show that, indeed, maxima in the energy transfer efficiency occur as a direct result of the combined effects of diffraction and attenuation. For the the chosen transmitter and receiver radii, the optimal efficiency is 64 %.

In general, an increase of the transmitter and receiver radii leads to less diffraction losses. Consequently, the efficiency is only limited by constraints regarding the transmitter and receiver dimensions (and a maximum efficiency of 100 % of course). These constraints can either be posed by the application itself, or by the manufacturing process, because of impracticality or just plain impossibility.

The remaining free parameter in the system is the distance z_d from the transmitter to the receiver. Figure 4.7 shows the decay of the energy transfer efficiency that accompanies an increase in distance between the sending and the receiving elements. Do note that the efficiency does not per se decrease monotonically. In the near field it can have numerous local maxima.

The on-axis pressure in the far field ($z > \frac{\pi a_s^2}{\lambda}$, valid for large values of ka_s) of a circular piston source is given by (see for example [69])

$$\bar{p}(z) \approx \frac{j\rho_0 \omega U_0 a_s^2}{2z} e^{j(\omega t - \bar{k}z)} \, . \tag{4.18}$$

The pressure is thus proportional to $\frac{1}{z}e^{-\alpha z}$. If the frequency, and therefore the attenuation coefficient α, is sufficiently low [13], the pressure decreases to a good approximation with $\frac{1}{z}$, implying that the on-axis intensity (and therefore the power
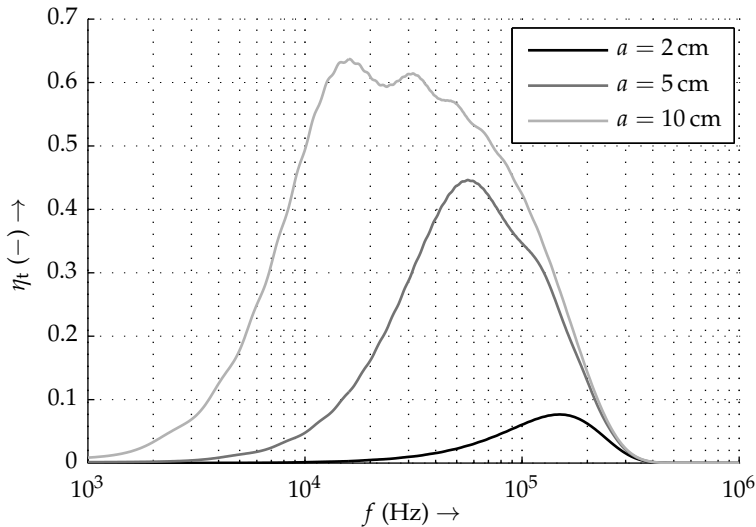
Figure 4.6 The combined energy transfer efficiency due to diffraction and attenu-ation by the air η_t at a distance $z_d = 1\,\text{m}$ has a distinct maximum. It is plotted here for equal transmitter and receiver radii a of 2, 5 and 10 cm.

and efficiency) is proportional to $\frac{1}{z^2}$. Due to the spherical wave expansion in the far field, the on-axis intensity in the far field is then

$$
\begin{aligned}
I &\approx \tfrac{1}{2} \frac{|\bar{p}|^2}{Z_0^a} \\
&\approx \frac{\rho_0 \omega^2 U_0^2 a_s^4}{8c} \frac{e^{-2\alpha z}}{z^2} \,.
\end{aligned}
\tag{4.19}
$$

With the assumption that the intensity is constant over the surface of the receiver, and thus that the received power Π_r is merely the product of the receiving surface area and the intensity, the received power becomes

$$
\Pi_r = \frac{\pi \rho_0 \omega^2 U_0^2 a_s^4 a_r^2}{8c} \frac{e^{-2\alpha z}}{z^2} \,.
\tag{4.20}
$$

The total radiated power Π_{rad} is obtained from equation (4.13), with which the approximate total efficiency is

$$
\begin{aligned}
\tilde{\eta}_{t,\alpha} &= \frac{\Pi_r}{\Pi_{\text{rad}}} \\
&= \tilde{\eta}_t e^{-2\alpha z} \,.
\end{aligned}
\tag{4.21}
$$
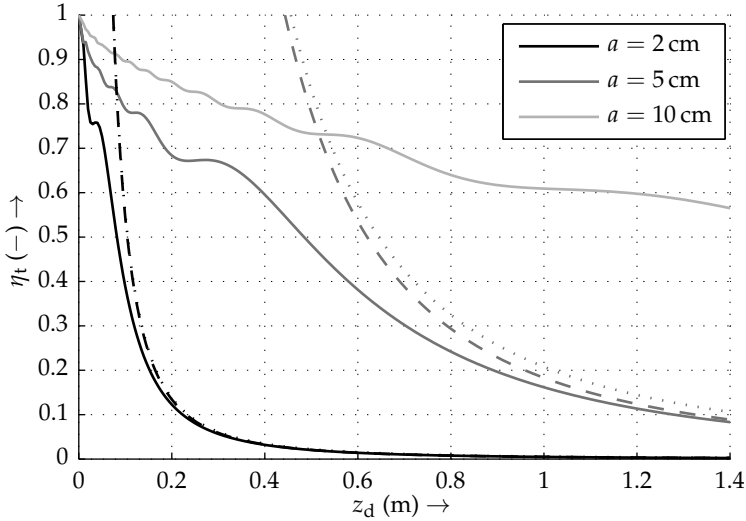
Figure 4.7   The energy transfer efficiency η_t decays as a function of z_d. It is shown here for a frequency $f = 20\,\text{kHz}$ and equal transmitter and receiver radii a of 2, 5 and 10 cm. The dashed lines represent the far field approximated efficiency with attenuation $\tilde{\eta}_{t,\alpha}$, while the dotted lines give the approximate efficiency without attenuation $\tilde{\eta}_t$.

The approximate efficiency without attenuation is given by

$$\tilde{\eta}_t = \frac{k^2 a_s^2 a_r^2}{4z^2 \left(1 - \frac{2J_1(2ka_s)}{2ka_s}\right)} \; . \tag{4.22}$$

Figure 4.7 reveals that indeed the efficiency is to a good approximation proportional to $\frac{1}{z^2}$ in the far field.

4.1.4   Optimisation

Although the previous sections already demonstrated that the transmitter and receiver radii a_s and a_r, and the sound frequency f have a pronounced effect on the achievable efficiency, it would be interesting to see what the maximum efficiency can be for an AET system, given the constraints introduced in section 2.4.1. Let us assume that a distance of $z_d = 1\,\text{m}$ is to be crossed, and that both radii are allowed to assume a value between 0 and 10.0 cm. The frequency is left unconstrained. Logically, the optimal value of a_r is the maximum of 10 cm, since this allows the most energy to be

captured, and hence the diffraction losses to be lowest, assuming, of course, that an increase in receiver size does not contribute to an increase in its losses.

The optimal values of the remaining two parameters can be found by minimising the power loss ratio:

$$\underset{a_s \in \mathcal{U}, f \in \mathbb{R}^+}{\arg\min} \ (1 - \eta_t) \,, \qquad \mathcal{U} := (0; 10] \,\text{cm} \,. \tag{4.23}$$

Doing so for a distance $z_d = 1\,\text{m}$, for example by means of the MATLAB fminsearch optimisation routine, yields the values $a_s = 7.83\,\text{cm}$ and $f = 20.53\,\text{kHz}$. The corresponding maximum efficiency at $1\,\text{m}$ distance is $65.0\,\%$. Recollecting the $64\,\%$ that the model predicts in the case of $a_s = a_r = 10\,\text{cm}$, the gain in efficiency through optimisation is only marginal.

Construction of solid piezo transducers with these desired radii of $7.83\,\text{cm}$ and $10\,\text{cm}$ is quite impractical. It is difficult to design transducers of these sizes that are sufficiently rigid at the desired frequency of $20\,\text{kHz}$ or higher. One possible solution is the construction of a transducer array, in which a large number of small transducers approximate the desired active surface. The advantage of using a transducer array over a single element is that it can be used for beam steering. This principle is commonly used in medical ultrasonography (it is also used in phased array radar applications). Beam steering can be used in AET applications to overcome low output power due to misalignment of the transmitter and receiver. This is necessary when the location of the transmitter and the receiver is not fixed, or otherwise a priori unknown.

4.2 Transducer efficiency

The last important loss component in an AET system is that which occurs in the transmitter and the receiver. These transducers *can* be quite efficient. According to e.g. [66], no more than $10\,\%$ losses should be expected when using bending mode piezoelectric transducers that are mounted on the first nodal circle. This construction has the advantage of having a high mechanical quality factor of the mounting. Still, often a considerable part of the energy that is lost in AET is due to the losses in the transmitting and receiving transducers. A good model of the transducer is therefore of the essence to be able to estimate the total losses in an AET system.

Equivalent electrical networks, such as introduced in section 3.6, are a convenient method of describing the behaviour of a transducer (see [17, 65, 75, 87, 101, 117, 123, 124]) and can therefore be used to assess the losses that occur in the energy

conversion process between the electrical and mechanical domains. Although the circuit can only describe a one-dimensional model, as was explained earlier, equivalent circuits can still be of value for determining the losses in actuators. They will allow us to express the efficiency of a transducer in terms of its quality factors and resonance frequency.

Piezoelectric transducers

Piezoelectric crystals exhibit a net polarisation, which is caused by an atomic lattice that does not have a centre of symmetry [49, 103]. Such atomic lattices can be found for example in naturally occurring crystals such as quartz and tourmaline. The polarisation of the material means that it can be deformed by application of an electric field, or inversely, that an electric field is created by deforming the crystal. The result is a linear interaction between its electrical and mechanical parameters [49, 57, 103].

A piezoelectric actuator generally vibrates in multiple directions. These vibrations require a six-dimensional description; its strain has three normal components (S_{xx}, S_{yy} and S_{zz}) and three shear components (S_{xy}, S_{xz} and S_{yz}). Likewise the stress in a piezoelectric material has the components T_{xx}, T_{yy}, T_{zz}, T_{xy}, T_{xz} and T_{yz} [49, 63]. Piezoelectric crystals are usually analysed in terms of tensors, which allow for the description of behaviour with multiple degrees of freedom that is required.

The dynamical behaviour of a piezoelectric transducer can be captured in a limited frequency range in an electrical equivalent network as depicted in figure 4.8. It models the air load on the diaphragm by a dissipative component R_a and a reactive component X_a. The mechanical part of the transducer is modelled by a resistive, a mass, and a compliance component (R_m, L_m and C_m respectively). The mechanical domain is coupled to an electrical section through a transformer. The electrical domain contains a capacitor C_e to account for the capacitive behaviour of a piezoelectric element, and a resistance R_e that models the ceramic's dielectric losses.

Contrarily to the tensor description, we have only a one-dimensional model in this case, as it describes the transducer's velocity as a scalar quantity u. Although the material of the transducer typically vibrates in all six directions, the vibration in one single direction is often dominant, which justifies the description of the transducer's behaviour by means of a one-dimensional model.

The transformer with transfer ratio φ in figure 4.8 originates from the behaviour of a piezoelectric crystal. The change in electric displacement field due to a strain S is $D_S = eS$, and the developed stress due to an electric field E is $T_E = eE$ [49, 57]. The parameter e is the piezoelectric stress constant. Inclusion of the dielectric properties of the material and the compliance of the material results in the constitutive
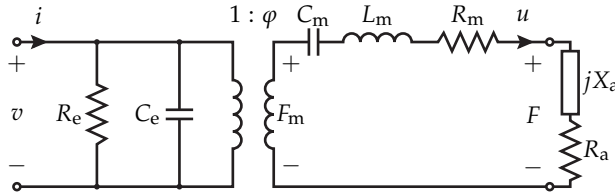
Figure 4.8 The behaviour of a piezoelectric transducer around its resonance frequency can be captured in an equivalent electrical circuit.

piezoelectric relations

$$D = eS + \varepsilon^S E \tag{4.24a}$$

$$T = c^E S - eE. \tag{4.24b}$$

Here ε^S is the material's permittivity for constant strain, and c^E is the elastic constant for constant electric field. Considering a section of the material of length l and area A, the current due to a strain S is given by $i_S = A\frac{\mathrm{d}D_S}{\mathrm{d}t} = \frac{eA}{l}u$, and the force due to an applied electric field is $F_E = T_E A = \frac{eA}{l}v$. Hence the relationship between the mechanical and electrical domain is described by a transformer with a transfer ratio $\varphi = \frac{eA}{l}$ for a simple 33-mode actuator in which the strain is uniform throughout the material. The coupling between both domains can even by described by means of a transformer in cases where this last requirement does not hold, as explained in e.g. [65, 94].

Lorentz force transducers

The most common loudspeakers that are in use today for sound reproduction are of the voice coil type. These are in fact Lorentz force actuators. Ribbon loudspeakers fall into this category as well, as their principle of operation is exactly the same; they consist of a conductive material that is suspended in a magnetic field. The material experiences a force when a current is passed through it. In the case of a voice coil loudspeaker the conductive material is a copper coil, which is mechanically connected to a cone, while the material in a ribbon speaker is a thin foil that serves directly as the radiating surface. For more information, see [15, 20, 87, 101] for example.

Just as is the case for piezoelectric transducers, the behaviour of a Lorentz force actuator is easily captured in an equivalent circuit diagram, which is shown in figure 4.9. Not very surprisingly, its circuit diagram is remarkably similar to figure 4.8.

Let us assume that we have a voice coil actuator with a coil conductor length l suspended in a homogeneous magnetic field of flux density B, moving at a velocity
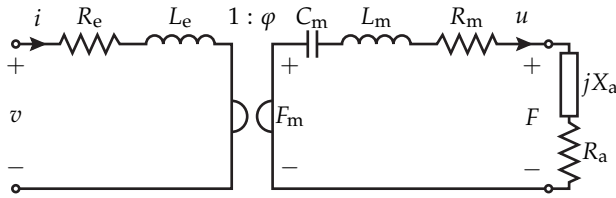
Figure 4.9 The equivalent electrical circuit of a voice coil loudspeaker or transducer is largely similar to that of a piezoelectric transducer.

u. The diaphragm that is attached to the coil experiences a counteracting force F from the air that it puts into motion. The Lorentz force that acts on the coil due to the current i that it carries is $F_m = Bli$, while the movement of the voice coil induces an electromotive force $v_{EMF} = Blu$. This behaviour can be represented in the circuit diagram by a gyrator (see for example [101, 121]) with a transfer ratio $\varphi = Bl$. The mechanical branch of the circuit diagram is exactly equal to that of the piezoelectric transducer; the mass of the moving part is accounted for by an inductance L_m, the compliance of the system by C_m and the losses by R_m. Contrarily to the piezoelectric case, the Lorentz force actuator mainly consists of a moving coil which has an inductance L_e and a wire resistance R_e.

Careful examination reveals that the equivalent circuit of the Lorentz force transducer in figure 4.9 is actually the dual network of that of the piezoelectric transducer in figure 4.8[1].It is therefore only necessary to investigate the efficiency of either of the transducers.

Efficiency

Let us take a closer look at the efficiency of the piezoelectric transducer, departing from the equivalent circuit in figure 4.8. It can be simplified to the circuit diagram of figure 4.10. The impedances $\overline{Z}_1$, $\overline{Z}_2$ and $\overline{Z}_3$ of the three circuit elements can be easily derived from figure 4.8 and are found to be

$$\overline{Z}_1 = \frac{1}{1 + \omega^2 R_e^2 C_e^2} \left(R_e - j\omega R_e^2 C_e \right) \tag{4.25a}$$

$$\overline{Z}_2 = \frac{1}{\varphi^2} \left(R_m + j \left(\omega L_m - \frac{1}{\omega C_m} \right) \right) \tag{4.25b}$$

$$\overline{Z}_3 = \frac{1}{\varphi^2} \left(R_a + j X_a \right) . \tag{4.25c}$$

---

[1]The gyrator converts voltages to currents and viceversa, and thus the impedance observed at the primary side is the reciprocal of the secondary side impedance.
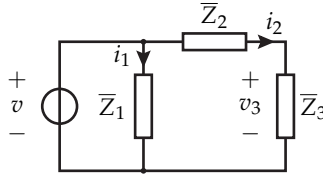
Figure 4.10   A simplified equivalent electrical circuit of a piezoelectric transducer driven by a voltage source.

The power dissipated in every impedance is then

$$\Pi_n = \tfrac{1}{2} \operatorname{Re}(\overline{v}_n \, \overline{i}_n^*), \qquad \forall n \in \{1, 2, 3\}, \tag{4.26}$$

with $\overline{v}_n$ the voltage across impedance $\overline{Z}_n$ and $\overline{i}_n$ the current through it. From this network we have for the power Π_1, Π_2 and Π_3, and the efficiency η_{tr}

$$\Pi_1 = \frac{\operatorname{Re}\left(\overline{Z}_1\right)}{2 \left|\overline{Z}_1\right|^2} \, |\overline{v}|^2 \tag{4.27a}$$

$$\Pi_2 = \frac{\operatorname{Re}\left(\overline{Z}_2\right)}{2 \left|\overline{Z}_2 + \overline{Z}_3\right|^2} \, |\overline{v}|^2 \tag{4.27b}$$

$$\Pi_3 = \frac{\operatorname{Re}\left(\overline{Z}_3\right)}{2 \left|\overline{Z}_2 + \overline{Z}_3\right|^2} \, |\overline{v}|^2 \tag{4.27c}$$

$$\eta_{\mathrm{tr}} = \Pi_3 \left(\sum_{n=1}^{3} \Pi_n \right)^{-1}, \tag{4.27d}$$

which, after some algebraic manipulation, brings us to

$$\eta_{\mathrm{tr}} = \frac{\varphi^2 R_{\mathrm{a}} R_{\mathrm{e}}}{\left(R_{\mathrm{m}} + R_{\mathrm{a}}\right)^2 + \left(\omega L_{\mathrm{m}} - \frac{1}{\omega C_{\mathrm{m}}} + X_{\mathrm{a}}\right)^2 + \varphi^2 R_{\mathrm{e}} \left(R_{\mathrm{m}} + R_{\mathrm{a}}\right)}. \tag{4.28}$$

The equivalent circuit diagram of the Lorentz force actuator is, as mentioned earlier, the dual circuit of that of the piezoelectric actuator. It is therefore not very astonishing that the expression for the efficiency in [87] is very similar to that derived above. In fact, upon closer examination it is exactly equivalent when accounting for the substitution of impedances by admittances through the use of the dual circuit.

If we now assume that the reactive part of the air loading on the transducer is dominantly mass-like, i.e. $X_{\mathrm{a}} = \omega L_{\mathrm{a}}$, the total impedance of the mechanical branch becomes

$$Z_{\mathrm{m}} = R_{\mathrm{t}} + j \left(\omega L_{\mathrm{t}} - \frac{1}{\omega C_{\mathrm{m}}} \right). \tag{4.29}$$

in which the equivalent total mechanical resistance is given by $R_t = R_m + R_a$ and the equivalent total mass is $L_t = L_m + L_a$.

The output of the piezoelectric transducer will be highest at the mechanical resonance frequency ω_0, which follows from the condition $\frac{d}{d\omega}|Z_m| = 0$ and gives

$$\omega_0^2 = \frac{1}{L_t C_m} \, . \tag{4.30}$$

The expression for the efficiency in (4.28) is quite obscure, and it does not serve much purpose in gaining insight into the behaviour of a transducer. This can be somewhat improved by rewriting it in terms of the resonance frequency, given above, and its quality factors. Let us introduce firstly a mechanical quality factor Q_m, which relates the mechanically dissipated energy to the stored mechanical energy. The latter is stored in the resonant circuit formed by L_t and C_m;

$$E_{\text{stored,m}}(t) = \tfrac{1}{2} L_t u^2(t) + \tfrac{1}{2} C_m F_C^2(t) \, . \tag{4.31}$$

The force F_C is the 'voltage' across the capacitance C_m, or, equivalently, the net force acting on the lumped element compliance of the transducer. At the resonance frequency the stored energy is constant and equal to

$$E_{\text{stored,m}} = \tfrac{1}{2} L_t U^2 \, , \tag{4.32}$$

with U the amplitude of the transducer's velocity. The power that is dissipated in the mechanical resistance R_t is given by $P_{\text{diss,m}} = \tfrac{1}{2} R_t U^2$, and thus the energy that is dissipated in a single cycle is

$$E_{\text{diss,m}} = \frac{2\pi}{\omega} P_{\text{diss,m}} \, . \tag{4.33}$$

This yields a mechanical quality factor

$$Q_m = 2\pi \frac{E_{\text{stored,m}}}{E_{\text{diss,m}}} = \frac{1}{R_t} \sqrt{\frac{L_t}{C_m}} \, . \tag{4.34}$$

The mechanical losses in the resistances R_m and R_a are not the only losses in the transducer. The losses in the electrical resistance R_e should be considered as well. Doing so leads to the definition of an electrical quality factor Q_e, in analogous fashion to [117]. The power dissipated in the resistance is equal to $P_{\text{diss,e}} = \tfrac{1}{2} R_t^2 / \varphi^2 R_e U^2$, which renders the electrical quality factor

$$Q_e = 2\pi \frac{E_{\text{stored,m}}}{E_{\text{diss,e}}} = \frac{\varphi^2 R_e}{R_t^2} \sqrt{\frac{L_t}{C_m}} \, . \tag{4.35}$$

These definitions allow the efficiency of the piezoelectric transducer in equation (4.28) to be written in a somewhat simpler form as

$$\eta_{tr} = \frac{\frac{Q_e}{Q_m}}{1 + \frac{Q_e}{Q_m} + \left(\frac{\omega}{\omega_0} - \frac{\omega_0}{\omega}\right)^2 Q_m^2} \frac{R_a}{R_a + R_m} \tag{4.36}$$

This equation is, after minor rearrangement of terms, equal to that of a voice coil loudspeaker [2], which is expected, given the duality of the equivalent circuits of both transducer types. Note that all parameters in (4.36) can be derived from the electrical impedance seen at the electrical port of the transducer. From electrical impedance measurements one cannot separate R_a from R_m and X_a from $(\omega L_m - 1/\omega C_m)$. However, it is possible to measure these components indirectly, by measuring the impedance under two loading conditions; operating in air, and in vacuum (which effectively shorts the air load $R_a + jX_a$), or using another *a priori* know acoustic load.

Unlike traditional loudspeakers, the electrical losses can often be neglected in piezoelectric transducers. A traditional voicecoil loudspeaker suffers from the resistive loss in its copper coil. This coil is traditionally designed to be extremely lightweight since it should not add significant mass to that of the cone and the air it displaces [20]. The resulting voice coil design is therefore a tradeoff between losses and added mass. This is not to say that Lorentz force actuators with low electrical losses cannot be constructed. The electrical losses in a piezoelectric transducer, on the other hand, are mostly of dielectric nature. These are normally insignificant for piezoelectric materials. Discarding the electrical losses changes the expression for the efficiency of the transducer (4.36) to the somewhat unsurprising result

$$\lim_{Q_e \to \infty} \eta_{tr} = \frac{R_a}{R_a + R_m}, \tag{4.37}$$

which is again equivalent to the approximation in [2] for a large value of Bl.

Operation as a receiver

The equivalent circuits of the piezoelectric and Lorentz force actuator are in principle reversible; decoupling the air load R_a and X_a and applying a force or velocity will produce a corresponding voltage v at the electrical port. Connection of an electrical load between the terminals will then also allow a current i to flow.

The efficiency of a receiver is easily calculated in much the same manner as it was derived for the transmitter. Its equivalent circuit diagram can be simplified to that depicted in figure 4.11, where the impedance of the mechanical branch is
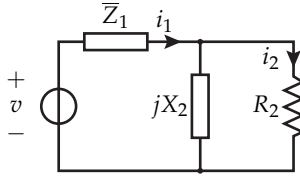
Figure 4.11   A simplified equivalent electrical circuit of a piezoelectric transducer operating as a receiving element.

$\overline{Z}_1 = R_m + j\left(\omega L_m - 1/\omega C_m\right)$, the electrical reactance is $X_2 = 1/\omega C_e$ and the electrical resistance is $1/\left(\varphi^2 R_2\right) = 1/R_e + 1/R_L$. The resistance R_L is the load resistance that is connected to the electrical terminals. It is easy enough to show that the efficiency of the transducer in this case is

$$\eta_{tr} = \frac{R_2}{R_m + R_2 + \frac{R_m R_2^2}{X_2^2}}. \tag{4.38}$$

Interestingly enough, the efficiency of the receiving transducer does not depend on the mass nor on the compliance of the transducer. Please note that they do influence the output power, since the current i_1 depends on the total value of $Z_1 + (R_2 \parallel jX_2)$, which is at a maximum at the resonance frequency $\omega_0 = \frac{1}{\sqrt{L_m C_m}}$. This resonance frequency can be different from that of the transmitting transducer, where the radiation reactance X_a also plays a role in the resonance frequency (cf. equation (4.30)). A different resonance frequency can be problematic if both transducers have a very high quality factor, which would lead to a low energy transfer in the case of a frequency mismatch. This tends to be less of a problem for larger transducers, as can be gathered from figure 4.3, since X_a approaches 0 for large values of ka_s, which is ratio of the transducer circumference to the wavelength. In other situations one should take care through proper design of the transducers that the resonance frequency of the transmitter and the receiver match.

The only frequency dependent component in (4.38) is introduced by the electrical reactance X_2, and thus the electrical capacitance C_e of the piezo element. The efficiency of the receiver will be optimal if we can make X_2 approach an infinite value. In that case the efficiency of the transducer becomes

$$\lim_{X_2 \to \infty} \eta_{tr} = \frac{R_2}{R_m + R_2}. \tag{4.39}$$

Or, when neglecting the dielectric losses, the expression reduces even further to

$$\lim_{\substack{X_2 \to \infty \\ R_e \to \infty}} \eta_{tr} = \frac{\varphi^2 R_L}{R_m + \varphi^2 R_L}. \tag{4.40}$$
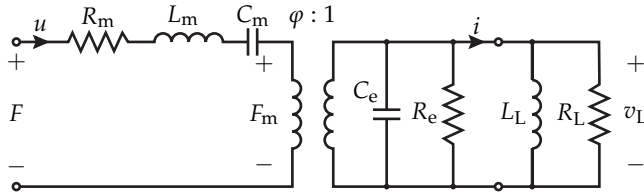
Figure 4.12 The parasitic electrical capacitance of a piezoelectric transducer can be compensated for by addition of an external inductor L_L.

Compensation inductance

The reactance X_2 should approach an infinite value to obtain an optimal efficiency. This can be achieved by changing it from the single parasitic capacitance C_e to a parallel combination of the capacitance and an externally connected inductance L_L in parallel to the load resistance, such as depicted in figure 4.12. The reactance of the parallel combination of C_e and L_L indeed approaches infinity at a resonance frequency $\omega_{0,e} = 1/\sqrt{L_L C_e}$. While this improves the efficiency, it is mostly interesting for the increase in output power that can be attained.

Starting from the circuit diagram in figure 4.11, the received output power is

$$\Pi_r = \frac{1}{2R_2} \left| \frac{\overline{Z}_2}{\overline{Z}_1 + \overline{Z}_2} \right|^2 |v|^2, \quad \text{with} \quad \overline{Z}_2 = \frac{jR_2 X_2}{R_2 + jX_2}$$

$$= \frac{1}{2} \frac{R_2 X_2^2}{(R_1 R_2 - X_1 X_2)^2 + (R_1 X_2 + R_2 (X_1 + X_2))^2} |v|^2 .$$

(4.41)

From the received power it is possible to obtain a value for the optimal load resistance R_2, by setting $\frac{d}{dR_2} \Pi_r$ equal to 0. In the following it will be assumed that the force F that drives the transducer (represented by a voltage v in figure 4.11) is independent of the value of R_2. This is a reasonable assumption for a heavy and stiff transducer, in which the values of R_m, L_m and $1/C_m$ are large. A bit of mathematics leads us to the optimal value of R_2:

$$R_2^2 = \frac{R_1^2 + X_1^2}{R_1^2 + (X_1 + X_2)^2} X_2^2,$$

(4.42)

or, when converted to the parameters of figure 4.12:

$$(R_e \| R_L)^2 = \frac{R_m^2 + \left(\omega L_m - \frac{1}{\omega C_m}\right)^2}{R_m^2 + \left(\omega L_m - \frac{1}{\omega C_m} - \frac{\varphi^2}{\omega C_e}\right)^2} \frac{1}{\omega^2 C_e^2} .$$

(4.43)

In practice one will want to work at the resonance frequency of the system, reducing the influence of the reactive system components and maximising the excursion of the transducers. Following this assumptions allows for the mechanical reactance X_1 to be set to 0. Therefore, the optimal value of R_2 becomes

$$R_2^2 = \frac{R_1^2 X_2^2}{R_1^2 + X_2^2}.$$ (4.44)

This renders the output power equal to

$$\Pi_r = \frac{1}{4R_1} \frac{1}{1 + \sqrt{1 + R_1^2/X_2^2}} |v|^2,$$ (4.45)

which, in terms of the parameters of the equivalent circuit diagram in figure 4.12 is

$$\Pi_r = \frac{1}{4R_m} \frac{1}{1 + \sqrt{1 + \frac{R_m^2 C_e^2}{\varphi^2 L_m C_m}}} |F|^2,$$ (4.46)

If the resistance R_1 is large in comparison to X_2, or $R_1/X_2 \gg 1$, the output power approaches

$$\Pi_r \approx \frac{1}{4R_1} \frac{X_2}{R_1} |v|^2 \approx 0\,\mathrm{W}.$$ (4.47)

On the other hand, compensating the electrical capacitance C_e by means of an inductance ($X_2 \to \infty$), the output power (4.45) logically is

$$\lim_{X_2 \to \infty} \Pi_r = \frac{1}{8R_1} |v|^2 = \frac{1}{8R_m} |F|^2.$$ (4.48)

This shows that proper compensation of the electrical capacitance of a piezoelectric transducer acting as a receiver in an AET system can result in much higher output power. However, it also shows that compensation will not improve the performance in systems where the mechanical damping in the transducer is low in comparison to the reactance presented by the parasitic capacitance:

$$\frac{R_1}{X_2} \ll 1.$$ (4.49)

The load resistance was chosen in this section such that the maximum output power is obtained. This is not always the best choice, since it inevitably means that 50 % of the received power is lost in the damping of the transducer. If the losses are sufficiently low, or the available power is greater, one could opt to choose a higher load resistance, such that the efficiency is higher, but at the cost of a reduced received output power.
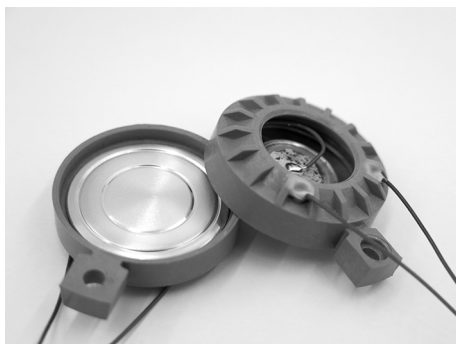
Figure 4.13 PX051 piezoelectric transducers fabricated by EMCT SA are used for the first experiments.

4.3   Experimental verification of the model

Validation of the model described in section 4.1 does not necessarily have to occur using the optimal transmitter and receiver dimensions that were found in section 4.1.4. Rather than using such large transducers, single transducers of a smaller size can be used, thereby significantly reducing the complexity of the construction of a test setup. PX051 piezo transducers produced by EMCT SA, Switzerland [32] were selected to serve both as transmitter and receiver. These are small unimorph piezo-electric bender elements, attached to a 1.2 cm radius, thin, aluminium diaphragm, as can be seen in the photograph of figure 4.13. The transfer of energy between two of these transducers is examined as a function of the distance between them for these first indicative measurements.

4.3.1   Parameter identification

It is necessary to estimate the losses of the transmitter and the receiver to be able to make a fair comparison between the theoretical limit and the measurement results. Section 4.2 describes a method of estimating these losses from the parameters of the equivalent circuit diagram of the transducer. This circuit diagram is valid for bender transducers, according to [24], and hence can be used. As mentioned, all parameters in equation (4.36) can be found from electrical impedance measurements. Two separate measurements are necessary, since the mechanical branch is a series connection of the transducer parameters $R_m + j\left(\omega L_m - 1/\omega C_m\right)$ and the radiation impedance $R_a + jX_a$, implying that they are indistinguishable when observed from the electrical port. Their values can, however, be found through two separate measurements. The radiation impedance depends on the medium in which the

Figure 4.14 *In vacuo* impedance measurements were conducted using a small vacuum chamber. This allowed the simultaneous measurement of six transducers.

transducer operates. The transducer will experience no opposing force from the medium if it is placed in a vacuum, and therefore the radiation impedance will be equal to zero. Equivalently, the force F at the mechanical terminals in figure 4.9 will be zero. The radiation impedance will hence effectively be short circuited, and impedance measurements will yield only the transducer parameters. The radiation impedance can subsequently be found from the difference between the measurements in air and the *in vacuo* measurements. Do note that this is the sum of the radiation impedance at the front and the back of the transducers. The resistive part of the back impedance also acts as a loss term during normal operation.

An Agilent 4294A precision impedance analyser was used to measure the transducers' impedance as a function of frequency. A small vacuum chamber (a photograph of which can be seen in figure 4.14) facilitated the *in vacuo* measurements. Twelve transducers were measured to be able to judge the component variation. These transducers were cherry-picked to have a resonance frequency in the vicinity of 17 kHz, as the main resonance frequency was found to vary to a large extent from one transducer to another.

The model of figure 4.15 was fitted to the electrical impedance, which was measured in the range of 14 to 22 kHz. The transducer impedance contains multiple resonances, besides the main resonance (which produces the largest acoustic output). These are accounted for through the parallel mechanical branches in figure 4.15. They are fitted together with the main branch consisting of L'_m, C'_m and R'_m to improve the estimate of the parameters of interest. Figure 4.16 shows an example of the fitted impedance curve of a PX051 transducer. The maximum error of the fitted impedance
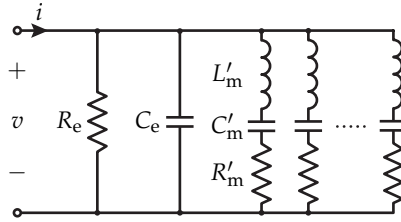
Figure 4.15 The equivalent transducer circuit used for parameter fitting contains multiple RLC branches to be able to describe multiple resonances.

magnitude is 4 % for the air measurements and 5 % for the vacuum measurements. The error in the phase is at maximum 3°. The phase error shows an offset, which likely appears due to a small parasitic resistance in the measurements.

Table 4.1 lists the resulting parameters and the difference between the measurements in air and in vacuum for all twelve transducers. The values of R_e are sufficiently high for these transducers to justify the use of equation (4.37) to calculate the efficiency of the transmitting transducer. Therefore the main parameters of interest are the values of R'_m in air and in vacuum. The average efficiency according to (4.37) is $\eta_{\text{transm}} = 0.48$ for this set of transducers. Hence these transducers are not very efficient. In practice the efficiency will be even lower due to radiation from the back of the transducer.

Table 4.1 indicates that, indeed, there is a large component variation between transducers, even among a set that was selected on the basis of a comparable resonance frequency. Furthermore, X_a is small, which would normally be beneficial, reducing the difference in resonance frequency between the transmitter and the receiver. This is relatively unimportant for these transducers since the resonance frequency varies wildly already. Lastly, the value of R_e is much larger in vacuum than it is in air for most transducers. Possibly an (albeit negligibly small) part of the radiation losses of the transducer are accounted for by R_e in the model.

The parameters of the transducers are also depicted by means of bar graphs in figure 4.17. These graphs show the large variation that occurs in L'_m, C'_m and R'_m (figures 4.17a, 4.17b and 4.17c respectively). The graphs of L'_m and C'_m seem to be inversely related, which is logical, since the transducers were selected based on their similar resonance frequency. This is confirmed by figure 4.17e (from (4.30)). There also appears to be a correlation between L'_m and R'_m. Figure 4.17f reveals that this correlation leads to a mechanical quality factor Q_m that varies much less between transducers than their equivalent circuit parameters do. A similar quality factor Q_m, however, does not necessarily lead to an equal power output or transducer efficiency, as is also indicated by equation (4.36).

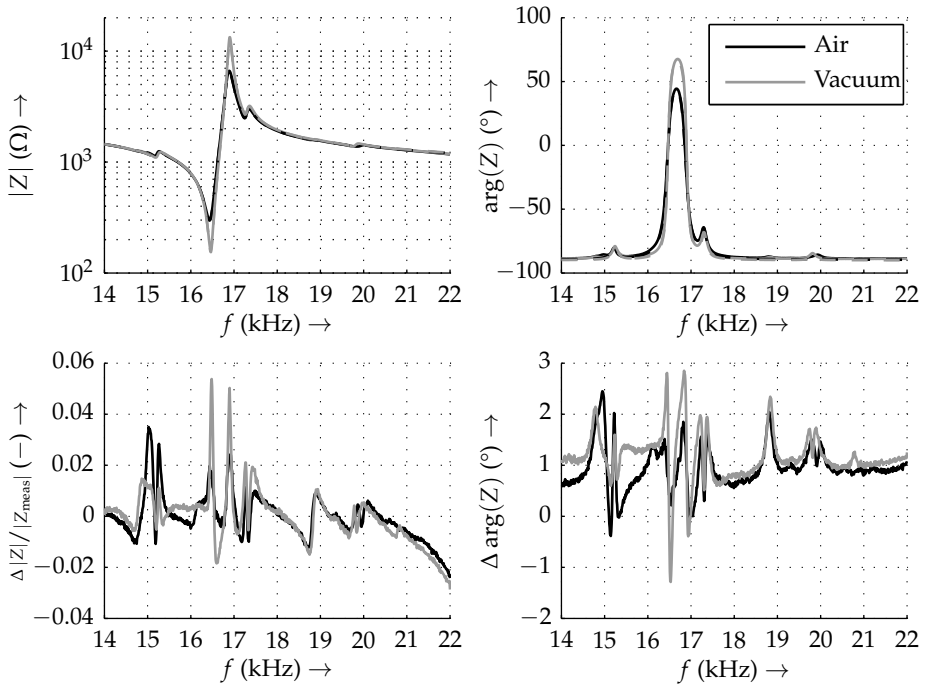**Figure 4.16**   The top graphs show the magnitude and phase of the electrical impedance of transducer 2 (cf. table 4.1). The measured (solid line) and fitted impedance (dashed line) are virtually indistinguishable. The magnitude error and the phase error are given for reference, where $\Delta |Z| = |Z_{\text{meas}}| - |Z_{\text{mod}}|$ and $\Delta \arg(Z) = \arg(Z_{\text{meas}}) - \arg(Z_{\text{mod}})$.

Table 4.1 The equivalent circuit parameters of 12 transducers were obtained from impedance measurements in air and vacuum.

| Transducer		L'_m (mH)	C'_m (pF)	R'_m (Ω)	C_e (nF)	R_e (Ω)
1	Air	297.4	306.7	363.0	6.250	$9.959 \cdot 10^4$
	Vacuum	289.3	313.5	182.6	6.218	$9.775 \cdot 10^{15}$
	Difference	8.2	-6.8	180.3	0.033	$-9.775 \cdot 10^{15}$
2	Air	272.8	343.1	309.6	6.492	$2.258 \cdot 10^5$
	Vacuum	267.2	349.6	155.7	6.453	$3.809 \cdot 10^{16}$
	Difference	5.6	-6.5	153.9	0.038	$-3.809 \cdot 10^{16}$
3	Air	244.6	376.1	285.7	6.448	$1.947 \cdot 10^5$
	Vacuum	241.0	381.2	133.3	6.411	$8.277 \cdot 10^{14}$
	Difference	3.6	-5.1	152.4	0.037	$-8.277 \cdot 10^{14}$
4	Air	222.8	402.1	256.5	6.713	$1.973 \cdot 10^5$
	Vacuum	217.9	409.0	126.2	6.658	$3.602 \cdot 10^{16}$
	Difference	4.9	-6.9	130.3	0.055	$-3.602 \cdot 10^{16}$
5	Air	286.2	296.5	360.7	6.176	$1.566 \cdot 10^5$
	Vacuum	293.7	287.0	198.9	6.143	$2.765 \cdot 10^{15}$
	Difference	-7.6	9.6	161.9	0.033	$-2.765 \cdot 10^{15}$
6	Air	263.0	347.4	291.2	6.394	$1.804 \cdot 10^5$
	Vacuum	255.5	356.0	151.1	6.378	$2.189 \cdot 10^{15}$
	Difference	7.6	-8.6	140.1	0.016	$-2.189 \cdot 10^{15}$
7	Air	261.1	323.1	306.8	6.378	$9.997 \cdot 10^4$
	Vacuum	244.9	342.6	170.8	6.305	$2.687 \cdot 10^5$
	Difference	16.2	-19.5	136.0	0.073	$-1.687 \cdot 10^5$
8	Air	310.4	297.6	379.6	5.924	$2.447 \cdot 10^5$
	Vacuum	303.7	302.5	179.5	5.878	$8.195 \cdot 10^5$
	Difference	6.7	-4.9	200.1	0.046	$-5.748 \cdot 10^5$
9	Air	257.1	361.8	300.3	6.594	$1.537 \cdot 10^5$
	Vacuum	255.8	362.0	162.5	6.576	$2.402 \cdot 10^5$
	Difference	1.3	-0.2	137.8	0.018	$-8.654 \cdot 10^4$
10	Air	388.8	238.6	390.0	6.472	$6.241 \cdot 10^4$
	Vacuum	367.2	251.7	264.1	6.484	$6.244 \cdot 10^{16}$
	Difference	21.7	-13.1	126.0	-0.012	$-6.244 \cdot 10^{16}$
11	Air	282.2	340.1	326.5	6.762	$2.686 \cdot 10^5$
	Vacuum	279.1	343.6	167.4	6.850	$6.340 \cdot 10^{15}$
	Difference	3.0	-3.6	159.1	-0.088	$-6.340 \cdot 10^{15}$
12	Air	277.3	331.3	331.1	5.991	$1.543 \cdot 10^5$
	Vacuum	270.1	338.3	153.6	5.995	$1.378 \cdot 10^{17}$
	Difference	7.3	-7.0	177.5	-0.003	$-1.378 \cdot 10^{17}$
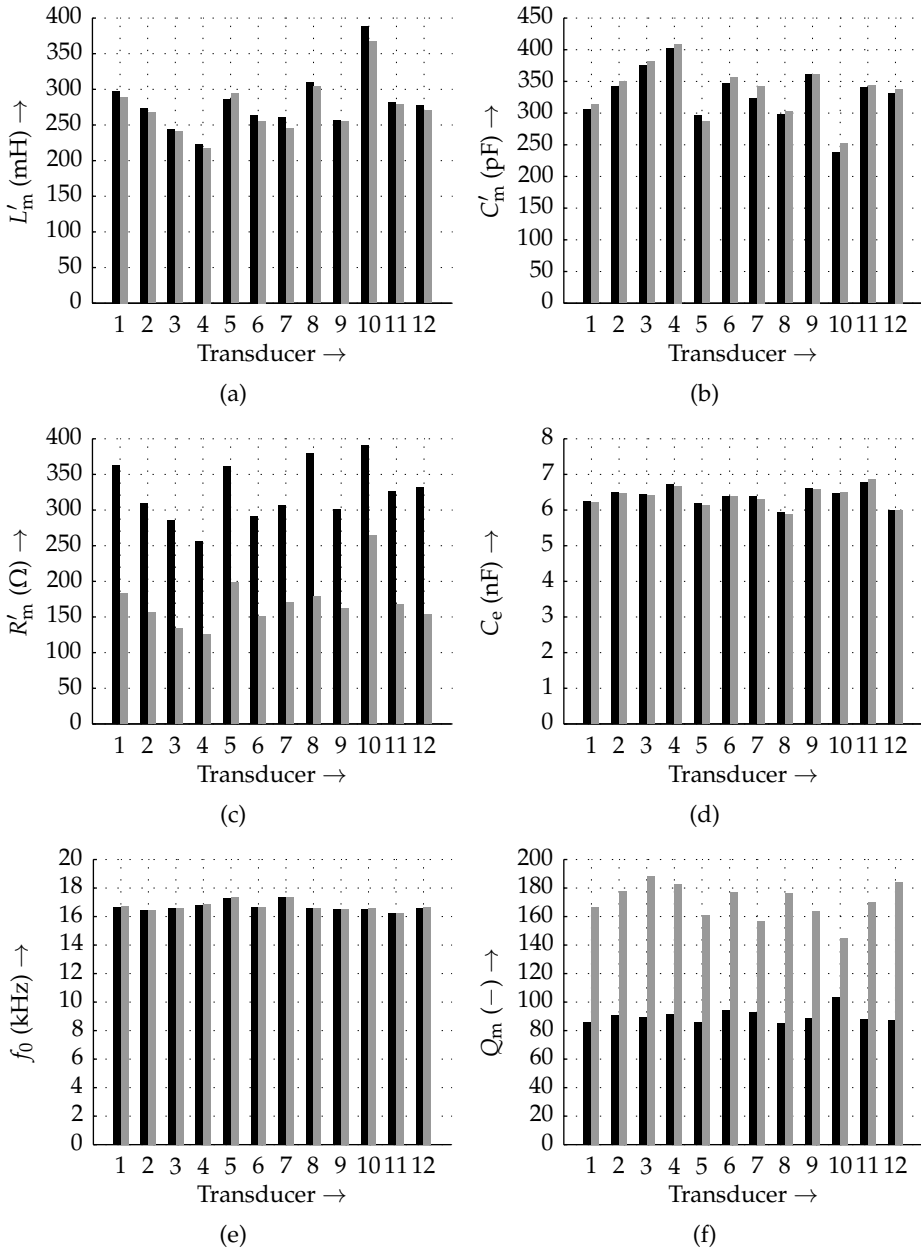
Figure 4.17 Bar plots of the transducer parameters clearly show the parameter variation, even though the transducers were cherry-picked. The black bars represent the impedance measurements in air, and the grey graphs those in vacuum.

4.3.2 Setup

One of the assumptions made during the derivation of the model is the coaxial place-ment of the transducers, just as in the system of figure 4.1. Consequently, an accurate alignment of the transmitting and receiving transducers is required. Furthermore, the distance between the two is to be accurately measured and precisely controlled for these measurements. This is achieved through the use of a milling machine as a means for distance variation between, and alignment of the transducers. A photograph of the setup can be seen in figure 4.18. The machine is fitted with a linear encoder system that has an accuracy of 10 µm, which should be adequate, given that the resonance frequency at which the transducers are used is approximately 17 kHz, implying a wavelength $\lambda = 20$ mm. The resolution of the positioning system is therefore orders of magnitude smaller than the wavelength.

Care should be taken when doing such measurements that the vibrations of the transmitter only couple with the receiver via the medium (the air in this case) and not via the platform on which they are mounted. The coupling via the milling machine is nil in this case. Therefore all received power can be considered to have been transferred through the air.

Due to their physical construction the PX051 transducers are not suited for high power levels. This shows in low voltages and particularly low current amplitudes (i.e. tenths of milliamperes). Amplification is therefore necessary to properly measure the currents. Care should be taken that the amplifier does not introduce an error in the power measurements. An amplifier always inserts a certain phase shift between its input and output signal. Since we are concerned with power measurements, the phase relation between the transducer's voltage and current is of importance and should be maintained. This is achieved in this setup by using an identical amplifier circuit for the measurement of the transducers' voltages and their currents. The output of the amplifiers is measured with a LeCroy WaveRunner 44Xi oscilloscope, which calculates the power as the cyclic average of the product of the voltage and current.

The transducers were used at their mechanical resonance frequency ω_0. Since the reactive component X_a of the radiation impedance is negligible, the resonance frequencies of the transmitter and the receiver are approximately equal.

The load resistance R_L was varied to obtain maximum power transfer, which resulted in an optimal value of $R_L = 1990.3\,\Omega$. A compensation inductance was used, as described in section 4.2 to maximise the power output at the receiving side. From measurements with an Agilent 4294A impedance analyser the resonance frequency of a freely radiating PX051 transducer is measured to be $f_0 = \frac{\omega_0}{2\pi} = 17.0$ kHz. The measurements of energy transfer efficiency versus distance were therefore conducted
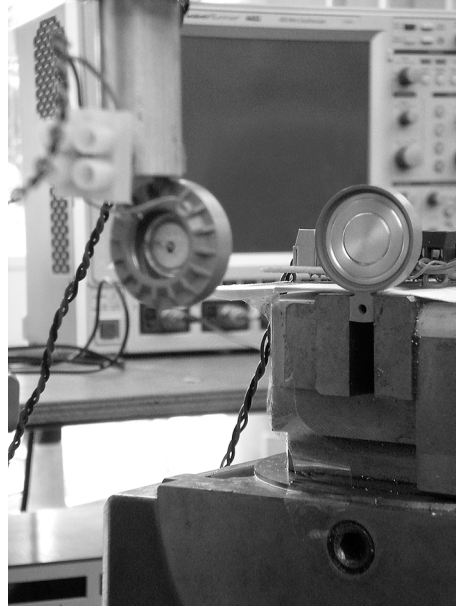
Figure 4.18   Two PX051 transducers are mounted on a milling machine to facilitate accurate alignment and distance variation.

at this frequency. The electric capacitance of the piezo transducer was measured to be approximately $C_e = 6.0\,\text{nF}$. Therefore an inductor of $L_L = 15\,\text{mH}$ was used to make the resonance frequency of the L_L-C_e combination equal to the mechanical resonance frequency ω_0.

The input power was delivered by an arbitrary waveform generator. No output rectifier was used at the receiving side for the sake of simplicity, since our interest lies primarily with the energy transfer by means of sound waves and not as much with the influence of the electrical circuitry.

4.3.3   Measurement results

Figure 4.19a shows the measured efficiency of the energy transfer between an identical transmitting and receiving piezo element. The efficiency is measured as the ratio of average electrical output power of the receiving transducer to the average electrical input power of the transmitting transducer. The graph also includes the theoretical limit for this setup, which was derived in section 4.1. The theoretical limit includes a transmitter efficiency $\eta_\text{transm} = 0.48$ as determined in section 4.3.1 and a receiver efficiency $\eta_\text{rec} = 0.50$, assuming a perfectly matched load resistance

R_L. The measured input power Π_{in} and output power Π_{out} are plotted as a function of the distance z_d in figure 4.19b. Separate points are indicated in both graphs where the energy transfer was measured at higher power levels. These measurements were limited by the breakdown voltage of the transmitting piezo element. The input power, output power and efficiency that were measured during this maximum-power measurement are

$$\Pi_{in, \text{ Max power}} = 184.9 \, \text{mW}$$
$$\Pi_{out, \text{ Max power}} = 40.0 \, \text{mW}$$
$$\eta = 21.6 \, \%.$$

The higher efficiency obtained at maximum power is most likely due to the use of a different set of piezo elements with slightly different parameters, as the transducers suffer heavily from component variation (see also table 4.1). Possibly there was less discrepancy in the resonance frequencies of the transducers for this set, or internal losses were lower for one or both transducer(s).

There are some notable differences between the measured efficiency and the theoretical limit in figure 4.19a. First and foremost, the efficiency shows a very peaky behaviour, revealing many local maxima and minima as a function of distance. These are a direct result of reflections that occur at the surfaces of both the receiving and the transmitting transducers. A wave that arrives at the face of the transducer bounces into it if the transducer is not moving at the same velocity as the particles in the wave. This causes the wave to reflect, travelling back to the transmitter, from which it will reflect again, et cetera. This leads to (partial) standing waves, or spatial resonances. Whenever the distance z_d is a multiple of the half wavelength $\frac{1}{2}\lambda$, the total phase shift that a sound wave undergoes on a round trip from transmitter to receiver and back to transmitter is 360 degrees, and thus a resonance occurs. This is the same effect on the basis of which lasers work, and which occurs in incorrectly terminated transmission lines. Obviously, reflections are not considered in the model derived in section 4.1, since the assumption was made that the receiver extracts all the available energy from the incoming sound wave, prohibiting the existence of a reflected wave. Reflections will be discussed in more detail in chapter 5.

Another difference from the theoretical model is found in the level of the measured efficiency, which decreases decidedly faster than the model predicts. The level of the first peak is well approximated by the model, especially for the high power measurement ($\eta = 0.2163$ from the measurement versus $\eta = 0.2171$ predicted by the model). Consequent peaks are much lower than the modelled efficiency. This can be attributed to the fact that the pressure and particle velocity change significantly due to the reflections with respect to that predicted by the simple model describing the radiation pattern of a circular piston. Moreover, the PX051 transducers have an open back, as can be seen in figure 4.13), implying that part of the acoustic energy
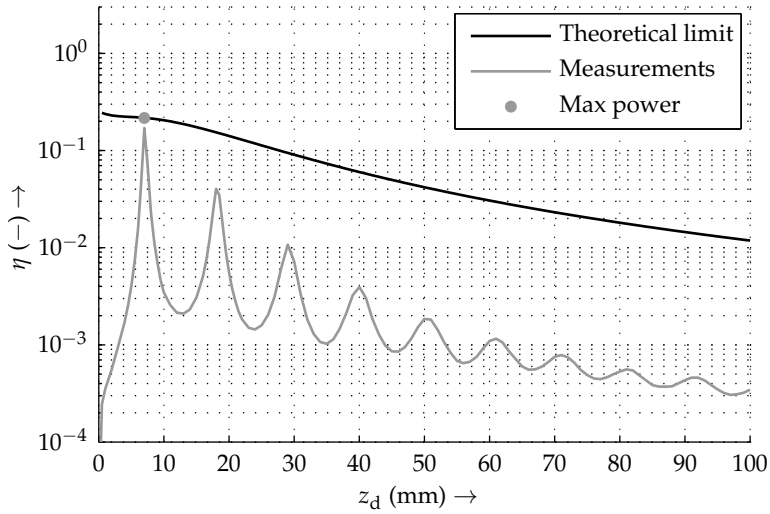
(a)
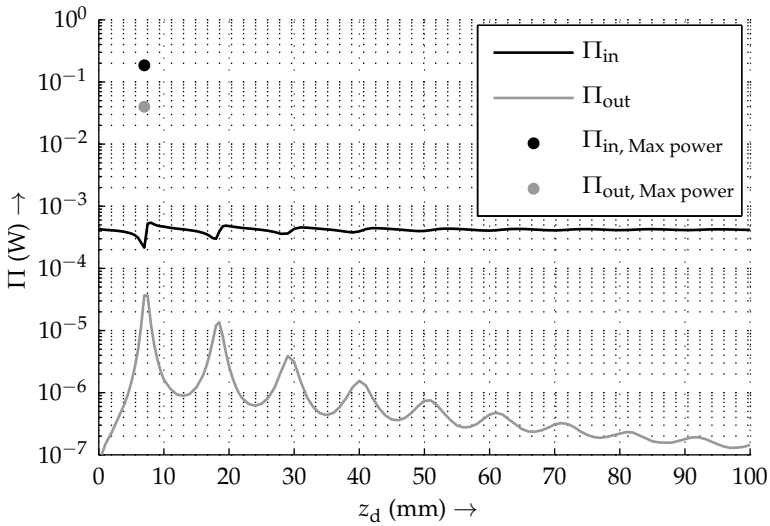
(b)

Figure 4.19 The source-to-load energy transfer efficiency η of two EMCT PX051 piezo transducers was measured as a function of the distance z_d between them (a). The theoretical limit for this setup is shown for reference. The corresponding measured electrical input and output power are shown in (b). The radius of the transducers is 1.2 cm.

is radiated from the back of the transmitter and does not contribute to the energy transfer.

Finally, the optimal value of the load resistance $R_L = 1990.3\,\Omega$ was found as the load resistance that yields the highest output power at the first spatial resonance peak. From (4.44), the assumption that R_e is sufficiently high, and a compensated capacitance C_e, one expects that $R_L = R_m/\varphi^2 = R'_m$. Strangely enough, comparison with table 4.1 tells us differently. From it one would expect the value of the load resistance to lie between $125\,\Omega$ and $390\,\Omega$ [2]. The most likely explanation for this inconsistency would be an inadequate model on the basis of which the optimal load resistance was derived.

Another possible explanation for the observed difference between the optimal load resistance and the internal resistance of the transducer is an excessively large value of R'_m, either through component variations or because of a faulty transducer, although this seems unlikely judging from the variation encountered in table 4.1. The maximum value of R'_m that was measured was $200.1\,\Omega$.

A last possibility to explain the difference is a measurement error in determining the optimal load resistance, which yielded an incorrect value of R_L. Since these measurements are quite demanding to perform there is always a possibility that errors are made. Some indication in this direction can be found in the results of a separate set of energy transfer measurements with a different set of transducers, where an optimal load of $R_L = 420\,\Omega$ was found. These measurements were performed without compensation inductance. A corresponding value of R'_m is found from (4.44) as

$$R'_m = \sqrt{\frac{R_L^2}{1 - \omega^2 R_L^2 C_e^2}} = 436.1\,\Omega, \tag{4.50}$$

with $\omega = 2\pi \cdot 17.0\,\text{kHz}$, $R_L = 420\,\Omega$ and $C_e = 6.0\,\text{nF}$. Although this value is much lower than that found in the experiments described above, still it is not low enough to fall into the range indicated by table 4.1. It is possible that the difference in optimal load resistance is attributable to the distance between the transmitter and the receiver at which the maximum output power was sought. The load resistance for the first set of measurements was determined at the first output power peak, while the second was optimised at $z_d = 10\,\text{cm}$. Still, the second value is too large to be able to attribute the high values of R_L to a measurement error.

---

[2] A transducer loss resistance $R'_m = 390\,\Omega$ implies that all power is radiated from the back of the transducer, when operating under free radiating conditions, which is certainly not the case. In practice its value will be lower.

4.4   Conclusions and discussion

The theoretical limit to the energy transfer efficiency of an AET system is derived in this chapter based on an identification of the losses that occur in such a system. The model that it is derived from includes diffraction, attenuation and transducer losses. Optimal electrical loading conditions were derived based on this model.

Acoustic energy transfer achieves a maximum efficiency of 65 % over a distance of 1 m, when the radii of the transmitter and receiver are restricted to 10 cm. This theoretical limit is based on diffraction and attenuation losses only. For the inclusion of transducer losses, one can look at examples of high efficiency transducers such as found in literature; for example Gallego-Juarez *et al.* [38], who reported an 82 % efficient high power transducer, or Kritz [66], who published a paper on a 93 % efficient ultrasound transducer. Assuming that the transmitter operates at the latter efficiency and the receiver is (according to (4.39) and (4.44)) 50 % efficient, the resulting total efficiency limit is 30 %. If the electrical loading of the receiving transducer is optimised for maximum efficiency, rather than maximum output power, even higher efficiencies up to 60 % can be attained.

According to Waffenschmidt & Staring [127], an inductively coupled CET system with the same transmitter and receiver dimensions would have an efficiency of approximately 2 %, assuming coil quality factors of 1000. Mur-Miranda *et al.* [84] use a different approach to the maximum energy transfer of an inductive CET system and arrive at approximately 6 % efficiency for the same dimensions and quality factors. Hence AET has the potential to perform *at least* 5 to 10 times better in terms of efficiency. This advantage of AET over inductive CET grows very rapidly with the distance that is to be crossed, since the efficiency of AET is approximately inversely proportional to z_d^2 (cf. equation (4.21)), while that of inductive CET is inversely proportional to z_d^6 [84].

The model on which the theoretical limit is based was validated through experiments in which the energy transfer between two piezoelectric unimorph bender elements was measured. These first indicative measurements show that energy transfer by means of sound waves is feasible. The maximum output power that was reached (40 mW) is a bit too low to be useful for many applications. This can be attributed to the low power handling capabilities of the transducers that were used for the experiments. There are, however, applications in which power transfer of this order of magnitude is quite adequate. Examples that come to mind are powering remote sensor applications, MEMS (microelectromechanical systems) and charging biomedical implants

The measured efficiency and power show a clear influence of reflections of the sound waves from the faces of the transducers. Both quantities show distinct peaks as a

function of the distance between the transmitter and the receiver, corresponding to half-wavelength intervals. These spatial resonances (figure 4.19) can be minimised by appropriate termination of the acoustic path. Just like a transmission line, the acoustic impedance of the receiver should be matched to the characteristic impedance Z_0^a of the air. Chapter 5 discusses reflections in more detail. Acoustic impedance transformers, such as diaphragms [15, 20], horns [20, 44, 69, 105, 106, 128], and $\frac{1}{4}\lambda$-matching layers [17, 41, 64], can be used for this purpose. Diaphragms and horns are used most widely in combination with air transducers. Both are extensively used for audio reproduction among other purposes. Chapters 6 and 7 examine their application to acoustic energy transfer.

The measured efficiency corresponds very well to the theoretical limit model at the first spatial resonance peak. The decline in efficiency with the distance between both transducers proved to be greater in reality than predicted by the model. This is most likely due to the pressure and particle velocity distribution being altered drastically by the reflections.

Both the calculated efficiency limit and the measured maximum efficiency show good agreement with those attained by Ozeri *et al.* [88, 90], who reported respectively 27 % and 39.1 % over short distances through a very lossy medium. The measured efficiency, peaking at 21.6 %, is a bit lower. This however, is a quite good result, considering that open back transducers are used and the transducers have not been optimised for this purpose

It is clear from the difference between the value of the optimal electric load R_L and the value of the mechanical transducer resistance R_m', that the models of the transducers are not entirely correct. The optimal load resistance was derived under the assumption that it does not have any influence on the pressure acting on the receiving transducer. This assumption is in practice not valid. The transducer presents an equivalent acoustic impedance to the incoming sound wave. This impedance, which depends on the value of the load resistance, determines the occurrence of reflections and their intensity (see the experimental results in [89]). Therefore it also influences the pressure at the face of the receiver. Hence the assumption that p at the face of the receiver is independent of R_L is most likely inaccurate.

Assuming that the transmitter and the transmission path up to the receiver can be modelled by a Thévenin equivalent voltage source F_{Th} and series impedance $\overline{Z}_{Th}^a = R_{Th} + jX_{Th}$, the optimal load resistance for a compensated capacitance C_e becomes $R_2 = R_1 + R_{Th}$. From there one can deduce that the Thévenin equivalent resistance (referred to the electrical domain) $R_{Th}' = \frac{1}{\varphi^2}R_{Th}$ lies somewhere between 640 Ω and 1.9 kΩ.

Another problem with the models is that they describe lumped element behaviour,

which is not an accurate description of the real behaviour of the transducers. While it is accurate enough to model the transducer from an electrical viewpoint (i.e. its impedance), the mechanical behaviour can be entirely different. Whenever the transducer is large in comparison to the wavelength of the material, one should resort to wave equations to describe the pressure and displacement. Models that are often used are, according to [57], the Mason, the Redwood [94] and the KLM model [65]. The latter two use transmission lines to describe the waves that travel through the transducer's material. Unfortunately, these models are one-dimensional as well, and are therefore not suited for transducers that vibrate in multiple dimensions. Such a model could very well describe the vibration of the bender elements that were used for the experiments in this chapter, but this model does then not simply have a mechanical port to which the air load can be connected, since the vibration of the entire surface of the transducer couples transversely to the medium. The opposing force presented by the medium that the transducers experience therefore becomes a distributed mass-resistance element in the transmission line.

One can conclude from the measurements that the main challenges for AET lie with the design of transducers that can handle large amounts of power at sufficiently high efficiency. Additionally, impedance matching at the side of the receiver is required to overcome reflections, and thus the spatial resonances that restrict a free placement of the receiver.

5

Reflections

O NE IMPORTANT ASPECT of acoustic energy transfer systems has not been modelled up to now; the model that was presented in the chapter 4 assumed that all energy that arrives at the receiving transducer is absorbed, while in reality—as indicated by the measurements of figure 4.19—a sound wave that impinges upon the surface of the receiver will partly reflect. These reflections of the sound waves from the surfaces of both the transmitter and the receiver drastically alter the behaviour of an acoustic energy transfer system from that predicted by the previously introduced idealised model. The reflections cause the energy transfer efficiency as well as the input and output power to have very sharp peaks at half-wavelength intervals. This is a very important practical aspect of AET, as the peaks imply fixed locations of high power transfer, and others where it is nil. A receiver can therefore only be placed at fixed distances from the transmitter, which restricts the usefulness of such a system.

If one is to overcome this problem, it is first to be properly understood. This is accomplished through modelling of the reflections and their influence on the energy transfer. Once a model of the reflections is obtained, attention can be turned towards mitigation of the problem.

Sound wave propagation in a medium is equivalent to an electromagnetic wave travelling in a transmission line. Reflections occur in such a waveguide whenever there is an impedance mismatch in it, or at its extremities [92]. The same applies for

This chapter is based on [99].

sound wave propagation. The impedance of the transducer (the opposing pressure it produces when it moves at a unit velocity) should match with that of the medium it operates in. In case of inequality of these ratios of pressure to velocity, the medium's particles will collide with the transducer surface, and reflections arise.

A sound wave emanating from the transmitter reflects at the receiver's surface, thereupon reverses direction and returns to the transmitter, where it reflects again. This process repeats itself until all energy is dissipated. Whenever the phase relation between the transmitted and the reflected wave is an exact multiple of 360° upon return of the latter to its source, a resonance condition occurs where so-called constructive interference takes place. The reflected wave will leave the surface of the transmitter exactly in phase with the wave it newly generates. The result is a standing wave where the pressure amplitude of the original wave is greatly amplified through reflection upon reflection, much like the working principle of a laser [56]. The phase relationship between the two waves is determined by the distance between the transmitter and the receiver and the sound velocity in the medium. Equally, an out-of-phase relationship between the reflected wave and the one originating from the transmitter yields destructive interference, effectively cancelling the original incident wave.

This chapter presents two models of reflections; one model based on transmission line theory, and the other a finite element (FE) model.

5.1 Transmission line models

The first models that spring to mind when discussing reflections are, at least for electrical engineers, transmission line models, although they are found in acoustics as well (think of transmission line loudspeakers for example [15]). These models are used to describe the propagation of electromagnetic waves inside transmission lines that are long in comparison to the wavelength. Notable examples are telegraph lines, long power lines and high frequency traces on printed circuit boards.

Transmission line models are one-dimensional models that in essence describe plane waves propagating along the length of, for example, a conductor (see for instance [92]). In the case of a true transmission line these waves are normally confined to a waveguide, but this is by no means a requirement imposed by the model. The description works just as well for a plane wave. The sound waves in a typical AET system are no plane waves, and therefore a transmission line model will never be able to give an exact representation of the reflections. Nevertheless, the model is a good starting point for their description.

5.1.1   Pressure and impedance

Recalling section 3.3.1, the generalised solution to the differential equation governing a plane pressure wave (3.24) is $p(z,t) = f(z-ct) + g(z+ct)$. The acoustic energy transfer system that is being discussed was said to work at a single frequency. Therefore the solution also assumes a single frequency, which is in complex notation

$$\overline{p}(z,t) = \overline{P}^+ e^{j\left(\omega t - \overline{k}z\right)} + \overline{P}^- e^{j\left(\omega t + \overline{k}z\right)} . \tag{5.1}$$

These are two sinusoidal pressure waves, the first having an amplitude P^+ travelling in the positive z-direction and the second a wave of amplitude P^- travelling in opposite direction. Again, the complex angular wave number $\overline{k} = k - j\alpha$ accounts for attenuation in the transmission line through an attenuation constant α, as was introduced in section 3.4.

The corresponding particle velocity is then found through application of (3.27):

$$\overline{u}(z,t) = \frac{\overline{P}^+}{Z_0^a} e^{j\left(\omega t - \overline{k}z\right)} - \frac{\overline{P}^-}{Z_0^a} e^{j\left(\omega t + \overline{k}z\right)}, \tag{5.2}$$

where the subtraction accounts for the negative direction of propagation, and hence the associated negative particle velocity, of the backwards travelling wave. Let us now assume that this backwards travelling wave originated through reflection of the forward travelling wave. A reflection coefficient $\mathcal{R}$ can then be introduced that relates the complex amplitude of the positive and negative (reflected) wave at the site of the receiver $z = z_d$:[1]

$$\mathcal{R} = \frac{\overline{P}^- e^{j\overline{k}z_d}}{\overline{P}^+ e^{-j\overline{k}z_d}} = \frac{\overline{P}^-}{\overline{P}^+} e^{j2\overline{k}z_d} . \tag{5.3}$$

Dropping the superscript of the pressure amplitude, the pressure and particle velocity are now given by

$$\overline{p}(z,t) = \overline{P}e^{j\omega t} \left(e^{-j\overline{k}z} + \mathcal{R}e^{-j\overline{k}(2z_d - z)} \right) \tag{5.4a}$$

$$\overline{u}(z,t) = \frac{\overline{P}}{Z_0^a} e^{j\omega t} \left(e^{-j\overline{k}z} - \mathcal{R}e^{-j\overline{k}(2z_d - z)} \right) . \tag{5.4b}$$

---

[1] Generally, a coordinate transformation is applied in transmission line theory that renders the distance between a point on the transmission line and the reflecting interface positive and places the the load at $z = 0$. In this derivation it is chosen not to do so, to be able to maintain the same coordinate system as defined earlier, i.e. a source at $z = 0$ and a (reflecting) receiver at $z = z_d$. Both approaches are equivalent in terms of results.

Now that we have an expression for the pressure (5.4a) and the particle velocity (5.4b), it is possible to define the acoustic impedance at any point along the wave's path. It is equal to the ratio of pressure over particle velocity, which is

$$\overline{Z}^a(z) = Z_0^a \frac{e^{-j\bar{k}z} + \mathcal{R}e^{-j\bar{k}(2z_d-z)}}{e^{-j\bar{k}z} - \mathcal{R}e^{-j\bar{k}(2z_d-z)}} \,. \tag{5.5}$$

Suppose that at $z = z_d$ the transmission line is terminated by a load impedance $\overline{Z}_L^a = R_L + jX_L$. It imposes a boundary condition $\overline{Z}^a(z_d) = \overline{Z}_L^a$, which allows us to derive the value of the reflection coefficient $\mathcal{R}$ using (5.5). It yields the well-known relation

$$\mathcal{R} = \frac{\overline{Z}_L^a - Z_0^a}{\overline{Z}_L^a + Z_0^a} \,. \tag{5.6}$$

Note that it is assumed here that the characteristic impedance of the medium is a real quantity, i.e. $Z_0^a \in \mathbb{R}$. This is a fair assumption when dealing with plane waves (cf. section 3.3.1), although it may not necessarily be the most realistic choice, as it can be different for other types of sound waves. However, for matters of simplicity, it will be assumed in the following that it is a real valued constant.

From equation (5.5) we can also find the acoustic impedance that opposes the vibration of the transmitter, which is equal to

$$\overline{Z}^a(0) = Z_0^a \frac{1 + \mathcal{R}e^{-j2\bar{k}z_d}}{1 - \mathcal{R}e^{-j2\bar{k}z_d}} \,. \tag{5.7}$$

Lastly, the pressure amplitude $\overline{P}$ of the travelling wave follows from a boundary condition at $z = 0$. Assuming that at the beginning of the transmission line the pressure is defined by a pressure source $\overline{p}(0,t) = P_0 e^{j\omega t}$, the pressure amplitude is found from equation (5.4a) to be equal to

$$\overline{P} = \frac{P_0}{1 + \mathcal{R}e^{-j2kz_d}} \,. \tag{5.8}$$

5.1.2 Power and efficiency

The input power and output power of the transmission line are given by

$$\Pi_{in}^a = \tfrac{1}{2}A_s \left| \frac{\overline{p}(0)}{\overline{Z}^a(0)} \right|^2 \mathrm{Re}\left(\overline{Z}^a(0)\right) \tag{5.9a}$$

$$\Pi_{out}^a = \tfrac{1}{2}A_r \left| \frac{\overline{p}(z_d)}{\overline{Z}_L^a} \right|^2 \mathrm{Re}\left(\overline{Z}_L^a\right) , \tag{5.9b}$$

with $A_s = \pi a_s^2$ and $A_r = \pi a_r^2$ the surface areas of the transmitter and the receiver respectively. Equations 5.9 can be rewritten by combining (5.4a), (5.6), (5.7) and (5.8). With help of some algebra and a touch of wizardry, one now finds that the power delivered by the source at $z = 0$ is equal to

$$\Pi_{in}^a = \frac{Z_1^{a2} \sinh(2\alpha z_d) + Z_3^{a2} \cosh(2\alpha z_d)}{Z_1^{a2} \cosh(2\alpha z_d) + Z_3^{a2} \sinh(2\alpha z_d) + Z_2^{a2} \cos(2kz_d) + Z_4^{a2} \sin(2kz_d)} \frac{A_s P_0^2}{2Z_0^a},$$
(5.10)

and the output power at $z = z_d$ is

$$\Pi_{out}^a = \frac{R_L}{Z_1^{a2} \cosh(2\alpha z_d) + Z_3^{a2} \sinh(2\alpha z_d) + Z_2^{a2} \cos(2kz_d) + Z_4^{a2} \sin(2kz_d)} A_r P_0^2,$$
(5.11)

with

$$Z_1^{a2} = R_L^2 + X_L^2 + Z_0^{a2} \tag{5.12a}$$
$$Z_2^{a2} = R_L^2 + X_L^2 - Z_0^{a2} \tag{5.12b}$$
$$Z_3^{a2} = 2R_L Z_0^a \tag{5.12c}$$
$$Z_4^{a2} = 2X_L Z_0^a, \tag{5.12d}$$

The efficiency of the energy transfer through the transmission line consequently is

$$\begin{aligned} \eta &= \frac{\Pi_{out}^a}{\Pi_{in}^a} \\ &= \frac{A_r}{A_s} \frac{Z_3^{a2}}{Z_1^{a2} \sinh(2\alpha z_d) + Z_3^{a2} \cosh(2\alpha z_d)}. \end{aligned}$$
(5.13)

5.1.3 Location of peaks

Assuming that $[Z_1^{a2} \cosh(2\alpha z_d) + Z_3^{a2} \sinh(2\alpha z_d)]$ varies slowly with respect to z_d in comparison to $[Z_2^{a2} \cos(2kz_d) + Z_4^{a2} \sin(2kz_d)]$, we have from (5.11) and $\frac{d\Pi_{out}}{dz_d} = 0$ that there are peaks and troughs in the output power whenever

$$\tan(2kz_d) = -\frac{2X_L Z_0^a}{R_L^2 + X_L^2 - Z_0^{a2}}, \tag{5.14}$$

which implies that the peak-pattern can have an offset for $X_L \neq 0$. Notice that because of the π-periodicity of the tangent function, peaks indeed occur at half wavelength intervals. Equation (5.14) also shows that the larger $|\overline{Z}_L^a|^2 = R_L^2 + X_L^2$ is, the smaller this offset will be.

5.1.4 Attenuation coefficient

The attenuation coefficient α normally only represents the absorption by the medium. However, the attenuation coefficient in (5.10), (5.11) and (5.13) is used to account for all losses in the wave propagation. As was discussed in section 4.1.1, a typical acoustic energy transfer system not only suffers from absorption, but also experiences a decreased efficiency through beam spreading losses. Both effect must be included in the absorption coefficient for the transmission line model to represent the behaviour of the actual system. The idea of inclusion of these losses in a transmission line model was proposed in [52]. The authors used an electrical circuit representation of the transmission line, were the conductance per unit length was used to model the spreading losses and the resistance part represented the absorption losses.

In the case of a simple transmission line, the attenuation coefficient in equations (5.10), (5.11) and (5.13) normally assumes a constant value. In the system that is being considered, however, a single value for α will almost certainly not lead to the desired results. Since the spreading losses depend on the distance from the transmitter, the attenuation constant will be a function of distance as well. In the transmission line model $e^{-\alpha z}$ is the factor that relates the pressure amplitude at a distance $z = z'$ to that at $z = 0$. In practice one cannot speak of a single pressure amplitude $|\overline{p}(z)|$, since the transmitter does not produce plane waves (see figure 4.2). Hence average pressure amplitudes will be used as an approximation. The averages are taken over the faces of the receiving and transmitting transducers respectively. We know from the model derived in chapter 4 what the absorption and spreading losses are. Using these it is possible to derive a 'lumped element' value of α. This gives an absorption coefficient

$$
\begin{aligned}
\alpha &= -\frac{1}{z'} \ln \left| \frac{\overline{p}_{\text{avg}}(z')}{\overline{p}_{\text{avg}}(0)} \right| \\
&= -\frac{1}{z'} \ln \left| \frac{a_{\text{s}}^2 \int_0^{a_{\text{r}}} \overline{p}(r_{\text{r}}, z', t)\, r_{\text{r}} \mathrm{d}r_{\text{r}}}{a_{\text{r}}^2 \int_0^{a_{\text{s}}} \overline{p}(r_{\text{s}}, 0, t)\, r_{\text{s}} \mathrm{d}r_{\text{s}}} \right|.
\end{aligned} \tag{5.15}
$$

The pressure $\overline{p}(r_{\text{r}}, z', t)$ at $z = z'$ is found from equation (4.7), but the pressure at $z = 0$ is unfortunately not so easily calculated, since its computation involves a singular integral when using (4.7). This singularity is, however, easily circumvented by changing the coordinate system [58].

Suppose that we have a source point $\vec{P}_{\text{s}}$ and a receiving point $\vec{P}_{\text{r}} = r_{\text{s}}\hat{r} + 0\hat{\varphi}$. The distance between the two is $r = \|\vec{P}_{\text{s}} - \vec{P}_{\text{r}}\|$. Choosing the point $\vec{P}_{\text{r}}$ as the centre of the
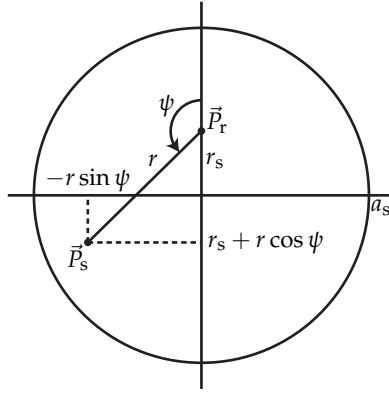
Figure 5.1 A change of coordinate system removes the singularity from the integral that yields $\overline{p}(r_s, 0, t)$.

cylindrical coordinate system for integration (see figure 5.1) we have

$$\overline{p}(r_s, 0, t) = \frac{j\omega\rho_0 U_0}{\pi} e^{j\omega t} \int_0^{\pi} \int_0^{r_{max}} \frac{e^{-j\overline{k}r}}{r} r \, dr \, d\psi \, , \tag{5.16}$$

where the integration limit of the inner integral follows from figure 5.1:

$$a_s^2 = r_{max}^2 \sin^2 \psi + (r_s + r_{max} \cos \psi)^2$$

$$r_{max} = \sqrt{a_s^2 - r_s^2 \sin^2 \psi} - r_s \cos \psi \, . \tag{5.17}$$

This allows the pressure at the face of the transmitter to be expressed as a single integral:

$$\overline{p}(r_s, 0, t) = \frac{j\omega\rho_0 U_0}{\pi\overline{k}} e^{j\omega t} \left(\pi - \int_0^{\pi} e^{-j\overline{k}r_{max}} d\psi \right) \, . \tag{5.18}$$

The PX051 transducers that were used earlier in section 4.3 are taken as a test case for the description of reflections in an AET system. Therefore α is calculated from (5.15) using transmitter and receiver radii $a_s = a_r = 1.2$ cm and a frequency $f = 17.0$ kHz. The result is shown in figure 5.2. It is clear that, indeed, α is a function of the distance z' from the transmitter. The relatively high values of α for small z' may be caused by numerical errors, either due to the division by z' in (5.15) or because of the integral in the calculation of $\overline{p}(r_r, z', t)$ being close to singular for small z'. The ability of α to represent actual system behaviour for small z' is likely to be low anyway, since it involves calculation of the average pressure in the near field—a near field that only
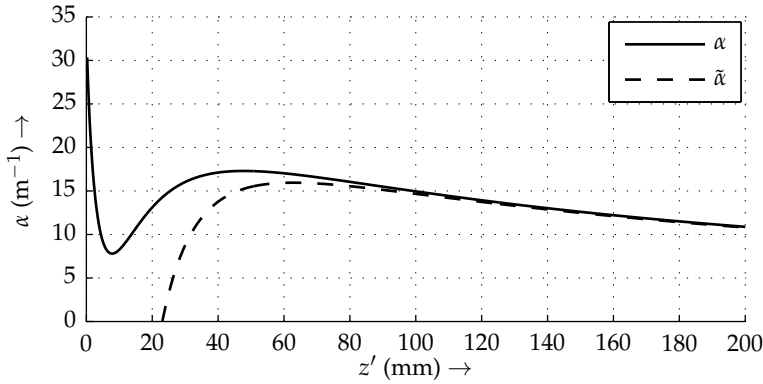
Figure 5.2 The lumped element attenuation constant α for a transmission line model of a rigid circular piston radiator varies as a function of the distance z' between the transmitter and the point of observation. A far field approximation $\tilde{\alpha}$ shows good resemblance for large values of z'.

exist under free radiating conditions. The behaviour will likely be very different from free radiation when the receiver is placed in close proximity to the transmitter.

Figure 5.2 also contains an approximation for α from equation (5.15), where the source pressure is derived from

$$\overline{p}_{\text{avg}}(0) = \frac{\overline{Z}_{\text{rad}}}{\pi a_{\text{s}}^2} U_0 e^{j\omega t} . \tag{5.19}$$

The average pressure $\overline{p}_{\text{avg}}(z')$ at $z = z'$ is assumed to be equal to the far-field on-axis pressure from equation (4.18). The far-field approximation of the attenuation constant is then

$$\tilde{\alpha} = -\frac{1}{z'} \ln\left(\frac{\rho_0 \omega \pi a_{\text{s}}^4}{2z' \left| \overline{Z}_{\text{rad}} \right|} \right) , \tag{5.20}$$

which, according to figure 5.2, is a good approximation for α in the far field of the radiator. Therefore, the numerical integration in (5.15) is not strictly necessary if only values of z_{d} are considered that are large in comparison to the transmitter size.

5.1.5 Simulation results

Figure 5.3 shows simulation results of the energy transfer in the transmission line approximation of the AET system. The load $\overline{Z}_{\text{L}}^{\text{a}}$ was chosen to be real, and the radii of the transmitter and the receiver are equal ($a_{\text{s}} = a_{\text{r}} = 1.2\,\text{cm}$). The graphs show that

for $\overline{Z}_L^a = Z_0^a$ (black line) there indeed are no reflections; the input power does not vary as a function of the distance between the transmitter and the receiver, and the output power only decreases with distance due to the losses in the system. The more the load impedance deviates from this optimal termination, the more reflections emerge, and the more pronounced the peaks become. The losses naturally increase as well as a result of the greater impedance mismatch, which is apparent from the efficiency η in figure 5.3.

Figure 5.4 shows similar results for the same system, but now for various complex load impedances. Again, the input power and output power contain peaks at half-wavelength intervals when $\overline{Z}^a \neq Z_0^a$. Note that reflections are even present when the absolute value of the load impedance is equal to Z_0^a, but it has a small complex phase angle. The efficiency is barely influenced by the reactance of the load.

Although there is still a separation of one half wavelength visible between consecutive peaks, the peaks for low values of $|\overline{Z}_L^a|$ are slightly offset in z_d (this is clearly visible in figure 5.5, which shows a detail of the input power). The difference between graphs for real and complex load impedance decreases rapidly for an increase in $|\overline{Z}_L^a|$. This is in line with (5.14). For $|\overline{Z}_L^a| \geq 20Z_0^a$ the graphs are virtually indistinguishable.

Comparing these results with the measurements in figure 4.19, one notices immediately that, although the shape of the output power is fairly similar, the shape of the input power, on the other hand, is very different. Accordingly, sharp peaks appear in the measured efficiency, while the simulated efficiency curve is fairly smooth.

The simulated efficiency contains minima and maxima when $\frac{d\eta}{dz_d} = 0$, or

$$\left. \frac{d\alpha}{dz'} \right|_{z_d} = -\frac{\alpha(z_d)}{z_d} . \tag{5.21}$$

The absorption coefficient should satisfy this criterion at quarter-wavelength intervals to accommodate both maxima and minima in the energy transfer efficiency. Clearly from figure 5.2 it does not.

Note that in both figure 5.3 and 5.4 the resonance peaks (for high load impedance) occur at half wavelength intervals, starting from $z_d = \frac{1}{4}\lambda$. This is due to the choice of a pressure source at $z = 0$. The peaks would occur at $z_d = \frac{1}{2}n\lambda$ $\forall n \in \mathbb{Z}^{\geq 0}$ should a velocity source have been chosen. This is entirely determined by the impedance of the transmission line at $z' = 0$, since a pressure source delivers maximum power to a low impedance, while a velocity source delivers its maximum power when the impedance of the transmission line is high.
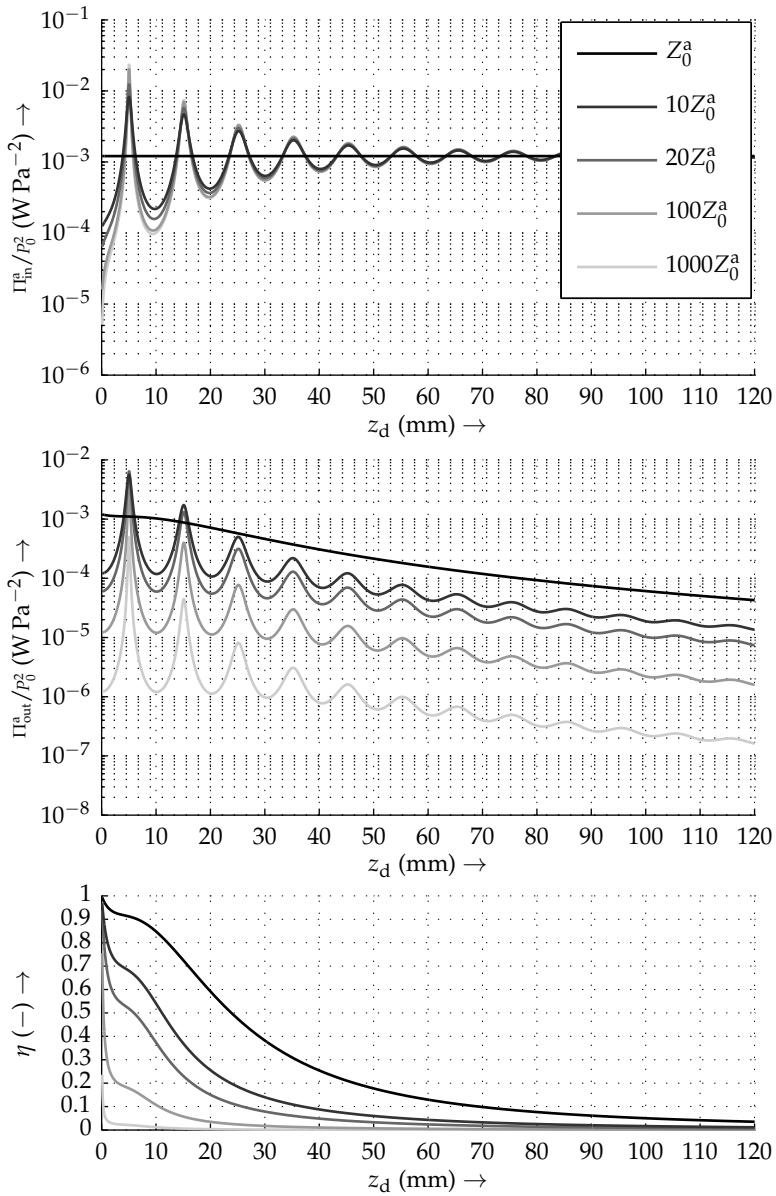
Figure 5.3 Simulation results of the transmission line representation for various values of $\overline{Z}_{\mathrm{L}}^{\mathrm{a}}$ show reflections for $\overline{Z}_{\mathrm{L}}^{\mathrm{a}} \neq Z_0^{\mathrm{a}}$. The simulation results were obtained for $a_{\mathrm{s}} = a_{\mathrm{r}} = 1.2\,\mathrm{cm}$ and $f = 17\,\mathrm{kHz}$. The input power Π_{in} and output power Π_{out} are normalised to the squared pressure amplitude at $z = 0$.
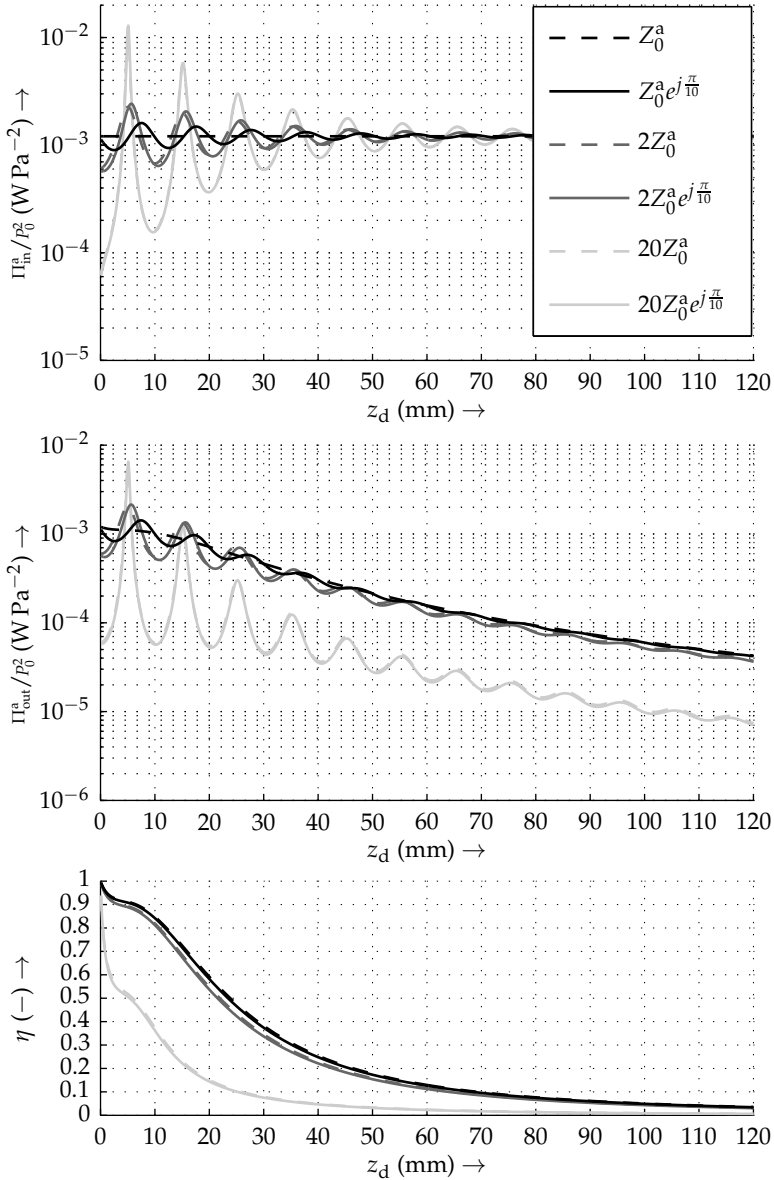
Figure 5.4   Complex load impedances can add an offset to the location of reflection peaks in the transmission line model, when the load impedance magnitude is close to the medium's characteristic impedance.
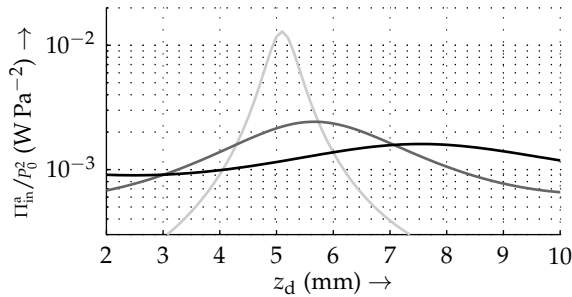
Figure 5.5   Close up of the input power of the transmission line for various complex load impedances. The offset in the location of the peaks is clearly visible. The colours represent the same load impedances as in figure 5.4: $Z_0^a e^{j\frac{\pi}{10}}$ (black), $2Z_0^a e^{j\frac{\pi}{10}}$ (dark grey) and $20Z_0^a e^{j\frac{\pi}{10}}$ (light grey).

5.1.6   Parameter fitting

The purpose of the transmission line model is to describe the effect that reflections have on the behaviour of a real acoustic energy transfer system. It is therefore interesting to examine the extent to which our simple one-dimensional model agrees with power measurements of such as system.

Measurements

The model is compared to measurements that were obtained using two PX051 transducers, one of which was mounted on a position controlled linear motor fitted with a linear encoder system. This allowed a positioning accuracy of 1 μm. The distance between the transducers was varied in 25 μm increments for the measurements.

The input power to the transmitter was supplied by a Kepco BOP72-6M power operational amplifier. It was measured by means of the method described in section 4.3.2; A Teledyne LeCroy HDO6034 12-bit oscilloscope measured the power as the cyclic average of the product of the input voltage and current (which was measured with a Tektronix TCP312 probe and TCPA300 amplifier). The delay between the voltage and current probes was compensated using a LeCroy DCS015 deskew calibration source.

The output power was found from the voltage across the load resistance, measured for reasons of accuracy with an Agilent 34401A multimeter. The load resistance was accurately measured for this purpose using the same multimeter and a four-wire resistance measurement. Its optimal value proved to be $R_L = 420\,\Omega$. The electrical capacitance was not compensated.
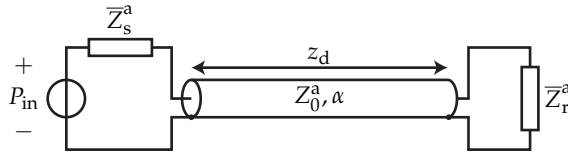
Figure 5.6 The equivalent circuit model that is used for parameter fitting represents the transmitting and receiving piezo element by complex impedances.

Parameters

The simulation results of the transmission line model cannot directly be compared to measured values of the electrical input power and output power since the model only encompasses the acoustic domain. To be able to do so, a transducer model, as introduced in section 4.2 is necessary to couple the mechanical and electrical domains.

This raises the problem that not all system parameters are known. The transformer ratio φ of the transmitting and receiving piezo transducers in figures 4.8 and 4.12 cannot be readily measured electrically. Moreover, due to the component variation described in section 4.3.1 the transducer parameters must be estimated through parameter fitting. Doing so for the complete model, consisting of the transducer models of figures 4.8 and 4.12 coupled to the transmission line model, did not yield satisfying results. A simplified (but equivalent) transducer model was therefore used for parameter fitting. The transmitter is replaced by a pressure source $P_{in}e^{j\omega t}$ and a complex series-impedance $\overline{Z}_s^a$, effectively only taking the mechanical impedance branch into account (the electrical capacitance has no influence, and the dielectric losses are neglected). The receiver is replaced by its equivalent acoustic impedance $\overline{Z}_r^a$. The corresponding circuit diagram is depicted in figure 5.6.

Because the output impedance $\overline{Z}_r^a$ is composed of the transducer parameters on one hand and the electric load on the other, the electrical output power is not equal to the received acoustic power at $z = z_d$. Part of the received energy is dissipated in the transducer. It is assumed that the electrical output power is half the received acoustic power $\Pi_{out} = \frac{1}{2}\Pi_{out}^a$ due to the optimal termination of the receiver. Moreover, since the transformer ratio φ is unknown, the source amplitude P_{in} must also be fitted.

The casing of the PX051 transducers extends about 1 mm beyond the aluminium diaphragm (see figure 4.13), which effectively lengthens the acoustic path by approximately 2 mm. Since the distance between the transducers is measured between these edges, an offset z_0 is added to the model, and is fitted to the measurements as the influence of this edge is unknown.

Results

Figure 5.7 depicts the fitted simulation results of the transmission line model. The graph shows two different fit results: one for which the transmission line length offset z_0 was kept equal to 0, and one in which all parameters were fitted. The fitted model shows a good resemblance to the measurement results, although the quality of the fit for $z_0 = 0$ is somewhat lower.

It proved necessary to adjust the angular wavenumber $k = 2\pi/\lambda$ for the distance between the peaks to match with the measurements. The effective wavelength used for fitting is 6 % larger than was expected from the driving frequency $f = 17.0\,\text{kHz}$ used for the measurements. This is possibly caused by a higher sound velocity due to different ambient conditions (e.g. temperature, relative humidity). The reader with a keen eye will observe that not all peaks of the fitted results coincide with their measured counterparts. It is very likely that changes in the ambient temperature during the measurements caused the sound velocity and thus the wavelength to change, thus altering the wavelength.

The fitted system parameters are given in table 5.1. Since the fit yielded a negative distance offset z_0, the corresponding graphs of power and efficiency in figure 5.7 start at $z_\text{d} = -z_0$, ignoring negative distances between the transmitter and the receiver.

From table 5.1 it is clear that in both cases the obtained parameter values are not realistic. The imaginary parts of $\overline{Z}_\text{s}^\text{a}$ and $\overline{Z}_\text{r}^\text{a}$ are sizable. This is unexpected, given that the transducers should be operating at, or very near to their mechanical resonance frequencies, corresponding to a (near) zero series reactance. The fact that $\overline{Z}_\text{r}^\text{a}$ is about two orders of magnitude smaller than $\overline{Z}_\text{s}^\text{a}$ is also striking, as one would expect it to be comparable, albeit slightly larger due to the presence of a load impedance. Moreover, the value of z_0 that was found for the second fit is far off from the 2 mm that were expected due to the transducer construction. Instead, a large negative value was found, which is completely non-physical, as it decreases the distance between both transducers. The source amplitude P_in is a bit high, amounting to a sound pressure level at $z = 0$ of approximately 138 dB.

It is expected that the behaviour of the model is not very accurate for small values of z_d, due to the free field conditions under which α was derived. For small values of z_d, the virtual location of the receiver is in the near field, which changes considerably when a reflecting transducer is present. In addition, the second set of parameters was fitted to the measurement data from $z_\text{d} = 40\,\text{mm}$ to 150 mm. The fact that the rest of the simulated power and efficiency match so well with the measurements indicates that the transmission line model does have predictive value, even though the parameters that are found through fitting seem to be not in line with expectations.
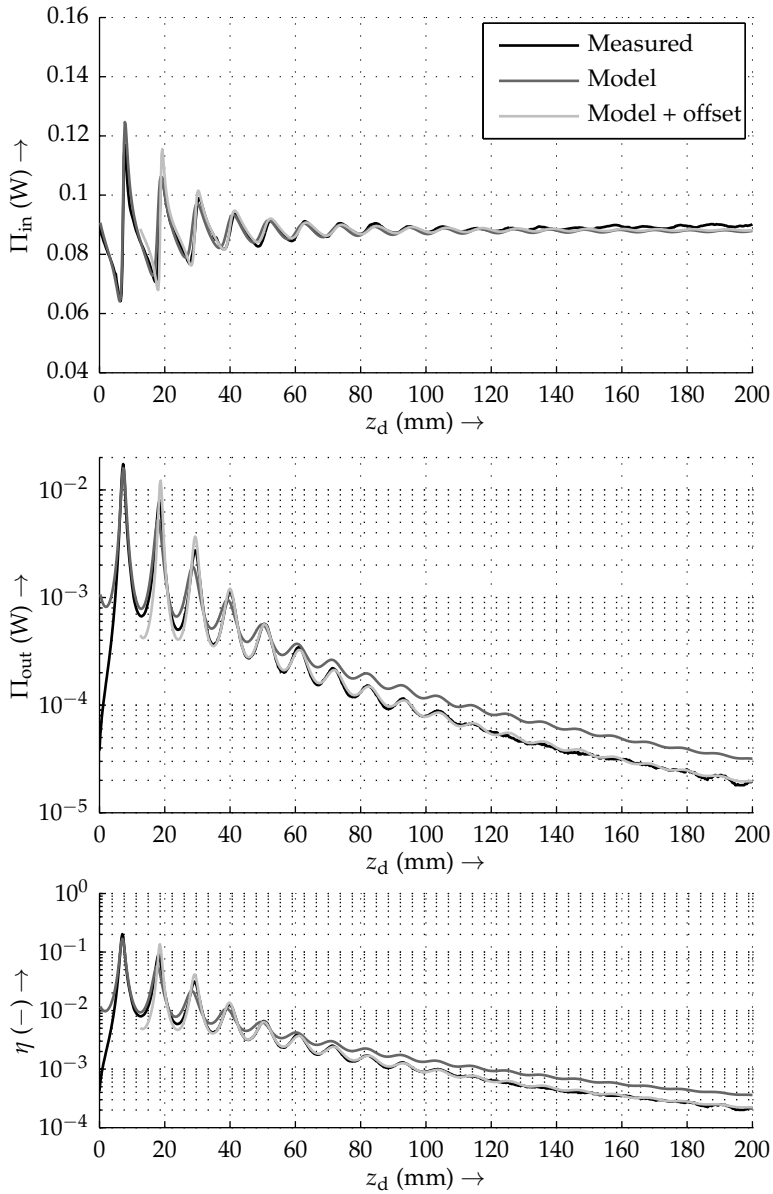
Figure 5.7   The fitted transmission line model shows a good resemblance to the measured energy transfer as a function of the distance z_d between the transmitter and the receiver. The second set of fit results accounts for a possible offset in the transmission line length.

Table 5.1 Fitted parameter values of the transmission line model, both with and without position offset.

Parameter	$z_0 = 0$	$z_0 \neq 0$	Unit
P_{in}	1.68	1.978	kPa
$\overline{Z}_{\text{s}}^{\text{a}}$	$2.39 + j3.53$	$3.92 + 4.97$	$\text{kN}\,\text{s}\,\text{m}^{-3}$
$\overline{Z}_{\text{r}}^{\text{a}}$	$62.12 - j220.66$	$41.02 - j102.77$	$\text{N}\,\text{s}\,\text{m}^{-3}$
z_0	0	-12.32	mm

The accuracy of the measurements is high enough for the parameters to be fitted. The maximum measurement error in the output power measurement at its lowest measured value of $\Pi_{\text{out}} = 19.5\,\mu\text{W}$ is $\epsilon_{\Pi_{\text{out}}} = 29.1\,\text{nW}$, or 0.15 %. The distance was varied in 250 μm increments, in order to capture all peaks adequately. Accordingly, the total measurement comprises 801 measurement points, which is sufficient for parameter fitting.

5.2 Finite element modelling

It is nearly impossible to create an analytical model of an AET system that yields closed form solutions, without resorting to approximations and simplifications. This is mostly due to the inherent multiphysical and three-dimensional nature of such a system. Finite element (FE) analysis seems ideal in this respect, since it is capable of solving the differential equations that govern every domain of physics, coupling them through boundary conditions. Via subdivision into small elements such a method is capable of tackling multidimensional problems with considerable ease.

The AET system was modelled using a finite element method in Comsol Multiphysics in an attempt to create a comprehensive model that describes:

- the coupling between the electrical and mechanical domains through a piezo-electric material

- the structural mechanics governing the behaviour of the piezoelectric patch and the aluminium diaphragm

- the coupling of the transducer to the medium

- the wave propagation through the medium

- and lastly, and most importantly for this chapter: the occurrence of reflections at boundaries.

Figure 5.8   The geometry that is used for the finite element analysis is a slight simplification of the PX051 piezo transducer. The piezoelectric material is indicated in black, the casing of the transducer in grey and the hatched part is an aluminium diaphragm. The model is axisymmetric around the dashed line at $r = 0\,\mathrm{m}$.

The FE model mainly comprises two piezo transducers placed a distance z_d apart with aligned centres. The transducer model, the geometry of which is shown in figure 5.8, is a simplification of the EMCT SA PX051 piezo transducers that were used for earlier experiments. The values of the parameters in figure 5.8 are given in table 5.2.

The casing of a transducer, indicated in grey in figure 5.8, is assumed to be sufficiently rigid to neglect its vibrations. Therefore it is modelled as an acoustic hard wall, which is a perfectly reflecting boundary condition where the normal particle velocity vanishes. In the model, the transducers are placed in a spherical air domain surrounded by a so-called perfect matching layer, which is a coordinate transformation simulating an infinite air domain. This prevents reflections from the domain boundaries. The model does not include sound absorption in the air or mechanical losses in the transducers.

The electrical contacts of the piezoelectric material are located on its top and bottom. Logically, these are the same contacts that were used for polarisation of the material. Hence the piezoelectric material is assumed to be polarised in the z-direction. The exact type of piezoelectric ceramic that is used in the transducers is unknown. Simulations of the maximum energy transfer efficiency were performed for various PZT (lead zirconate titanate) grades. Table 5.3 lists the efficiency of the AET system at the first peak in the transfer efficiency, as well as the distance between the transducers z_d and frequency f at which this peak occurs. The table indicates that, although the

Table 5.2 Parameters of the PX051 FE model

Parameter	Value	Unit	Parameter	Value	Unit
r_d	1.10	cm	c_b	900	µm
h_d	165	µm	c_c	4.80	mm
r_p	4.95	mm	c_d	1.60	mm
h_p	200	µm	c_e	1.69	mm
r_{s1}	6.45	mm	c_f	2.20	mm
r_{s2}	9.60	mm	c_g	2.00	mm
c_a	900	µm			

efficiency can vary considerably, the distance and frequency at which the efficiency peaks do not change substantially. One cannot choose a piezoelectric material based on these figures alone. Proper characterisation of the material is required (measurement of piezoelectric constants, compliance, density, permittivity, et cetera). Since the type of piezoelectric material is unknown, PZT-5A is used in the model. Based on the value of the electrical capacitance C_e from table 4.1 and the radius r_p and thickness h_p of the piezoelectric ceramic from table 5.2, the required value of the relative permeability under constant strain in the 33-direction should be approximately

$$\varepsilon_{r,33}^{S} = \frac{h_p}{\varepsilon_0 \pi r_p^2} C_e \approx 1760. \tag{5.22}$$

PZT-5A has a relative permeability of approximately 827, which indicates that the material parameters of the actual transducer are different. This, however, only allows one to conclude that the transducers' piezoelectric material is not PZT-5A. It is not certain that the other parameters of the material deviate as well. On the same grounds, choosing a material with a higher relative permittivity does not imply that it is a better choice with respect to the other parameters.

5.2.1 Results

Since the FE model is able to model the physics describing each domain and correctly take into account the boundary conditions between them, it should in principle be able to accurately describe reflections. Where the transmission line model is only able to describe one-dimensional waves and lumped-element boundary conditions, the finite element model does not pose such restrictions.

Table 5.3 Maximum energy transfer efficiency $\eta_{\max}$ at a distance $z_{d\max}$ and a frequency $f_{\max}$ for various piezoelectric materials

Material	$\eta_{\max}$ (%)	$z_{d\max}$ (mm)	$f_{\max}$ (kHz)
PZT-2	33.4	5.71	17.67
PZT-4	57.2	5.84	17.79
PZT-4D	60.5	5.94	17.68
PZT-5A	67.1	6.37	17.12
PZT-5H	69.6	6.56	17.15
PZT-5J	69.1	6.56	17.05
PZT-7A	31.4	5.53	18.05
PZT-8	50.1	5.75	17.85

Input power, output power and efficiency

Figure 5.9 presents a comparison between measurement results and the outcome of FE simulations of the model described above. There is a reasonably good agreement between the two. The resonance peaks that are characteristic for reflections are clearly present in the input power Π_{in}, the output power Π_{out} and the efficiency η. The peaks do not exactly coincide in terms of the distance z_d, since the frequency that was used for the simulations was a bit higher than that used in the measurements. In both cases the frequency was varied to obtain the maximum output power, which yielded $f = 17.00\,\text{kHz}$ for the measurements and $f = 17.15\,\text{kHz}$ for the simulations.

The behaviour of the input power Π_{in} shows some discrepancy between measurements and simulations. Firstly, it is much higher, about a factor of two for large z_d in the simulations. Since this situation is not too different from a free field simulation, this implies that the transducer model is not correct. Most likely the difference is caused by the absence of transducer losses in the FE model. Furthermore, the variation of the input power with the distance is very different as well. Where the measured input power first drops for an increase in z_d, the simulated input power rises steadily. The measured input power then rises sharply, while the measure input power does the exact opposite. From the transmission line model it is understood that this behaviour is determined by the source impedance (compare figures 5.3 and 5.7). Possibly this is therefore also a result of the omission of transducer losses, but is can just as easily be caused by an incorrect piezo material or other parameter inaccuracies.

Both the amplitude of the peaks and the decline with z_d of the output power Π_{out} are very comparable. The level of the output power is very different, but this is likely due to the input power that is of greater magnitude than expected and the absence of losses in both the transducers and the air.
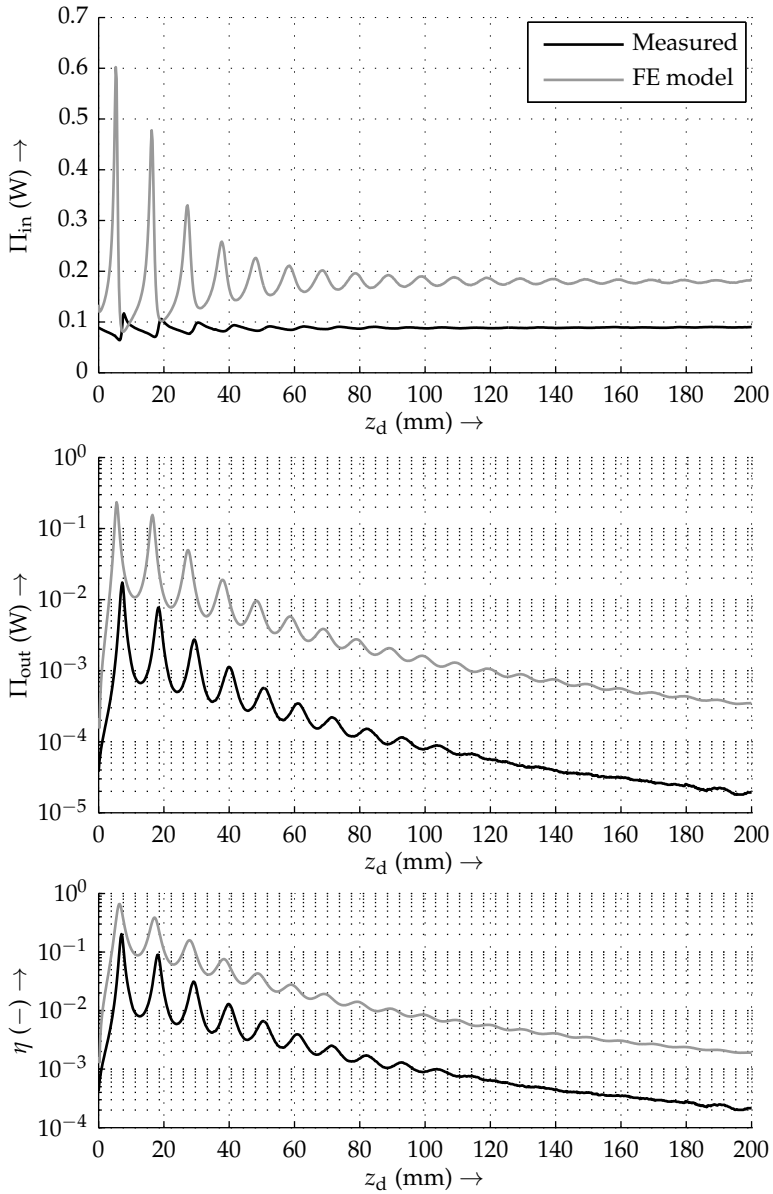
Figure 5.9 The energy transfer efficiency η was calculated by means of FE analysis as a function of the distance z_d between the transmitting and receiving piezo elements. A driving frequency of $f = 17.152\,\text{kHz}$ was used for the simulations.

Lastly the efficiency is again comparable, although the effect of the reflections is not as pronounced in the FE results as it is in the measurements. This is put down chiefly to the discrepancy in the input power, considering the similarity in Π_{out}. The efficiency is approximately a factor ten higher than expected. The absence of losses in the model naturally boosts the efficiency. Furthermore, as already indicated by table 5.3, a wrong choice of piezoelectric material can lead to a large deviation in efficiency.

Pressure amplitude

The reflections cause distinct maxima and minima in the energy transfer and its efficiency. It is interesting to examine what these maxima and minima mean in terms of the pressure amplitude in the r, z-domain. Our finite element model is a useful tool in this regard, since it calculates this pressure.

There are two ways of approaching the energy transfer; one could either opt to look at the maximum output power, or the maximum efficiency. These two cases do not necessarily coincide, and in practice occur for slightly different frequencies and distances. Both situations will be considered here.

A pattern search algorithm [46] was used for finding the maximum output power and efficiency to prevent false maximum detection due to the numerical inaccuracy of the solver. The model predicts the maximum output power to be produced at a distance $z_{\text{d}} = 5.557$ mm and a frequency $f = 17.152$ kHz. The first minimum of the output power at the same frequency was found at $z_{\text{d}} = 11.1$ mm. Analogously, the maximum efficiency was found for a distance $z_{\text{d}} = 6.373$ mm and $f = 17.123$ kHz. The first minimum of the efficiency at the same frequency occurred at $z_{\text{d}} = 12.1$ mm. The precision of z_{d} at the minima is lower due to relatively higher noise from the FE solver.

Figure 5.10 shows the FE simulation results of the pressure amplitude in these four situations. The standing waves that originate due to the reflections from both transducers are clearly visible as alternating amplitude maxima and minima in the z direction. The pressure amplitude distribution is very different when looking at the situation where we have maximum output power (figure 5.10a) or maximum efficiency (figure 5.10c). The pressure amplitude immediately in front of the diaphragm of the receiver (top transducer) is about a factor two higher than in the case of maximum efficiency, naturally leading to a higher output power. Unfortunately, figure 5.10a also shows that a large part of the power radiates away from the back of the transmitter. Figure 5.10c indeed shows a situation where the efficiency will be much higher, as the pressure amplitude is high in front of both transducers, implying that the transmitter delivers most of its energy to the medium

at the front, and the receiver absorbs much of this energy. This figure shows very well how reflections, and the standing waves that ensue, cause the impedance of the medium to increase, and the matching of the transducer with the medium to improve.

The pressure amplitude distribution in case of minimum output power (figure 5.10b) and minimum efficiency (figure 5.10d) are virtually indistinguishable. The most important observation to be made from the two figures is that the pressure amplitude at the diaphragm of the receiver is negligible, and therefore the output power is as well. The transmitter still delivers its energy to the medium, both at the front and the back of the diaphragm.

5.2.2 Parameter sensitivity

Table 5.3 already indicated that the performance of the system heavily depends on the material parameters. The maximum of the simulated efficiency of the system lies between 33 % and 70 %, depending on the choice of PZT-grade. The material not only influences the maximum output power and efficiency, but also the resonance frequency at which these occur. This change in efficiency offers great opportunities to increase the energy transfer efficiency, by choosing the right materials for the construction of the transducers.

If the simulation results can be altered to such a large extent by changing one material for another, the question arises how the results are influenced by the model's other parameters, such as the dimensions listed in table 5.2, or the material properties of the diaphragm and the piezoelectric ceramic. Quantitative information about the influence of model parameters can be obtained from a sensitivity analysis. The purpose of such an analysis is twofold; it gives information on how parameter deviation influences the outcome of the model, in other words: how accurately parameters should be known to be able to construct an accurate model, while, on the other hand, if performance improvement is the main topic of interest, it indicates which parameters will change the system's output most.

The finite element model was used to investigate the sensitivity of the system to parameter changes. The choice of output variable on the basis of which the sensitivity analysis is to be performed is an important one. The most useful choice for AET is the output power. Unfortunately it depends heavily on the exact location of the receiver and the driving frequency because of the reflections. For a fair comparison one will have to look at the change in the maximum output power $\Pi_{out,max}$ for a change in a parameter. The distance $z_{d_{max}}$ and frequency f_{max} at which the maximum output power occurs and their change are also of interest.
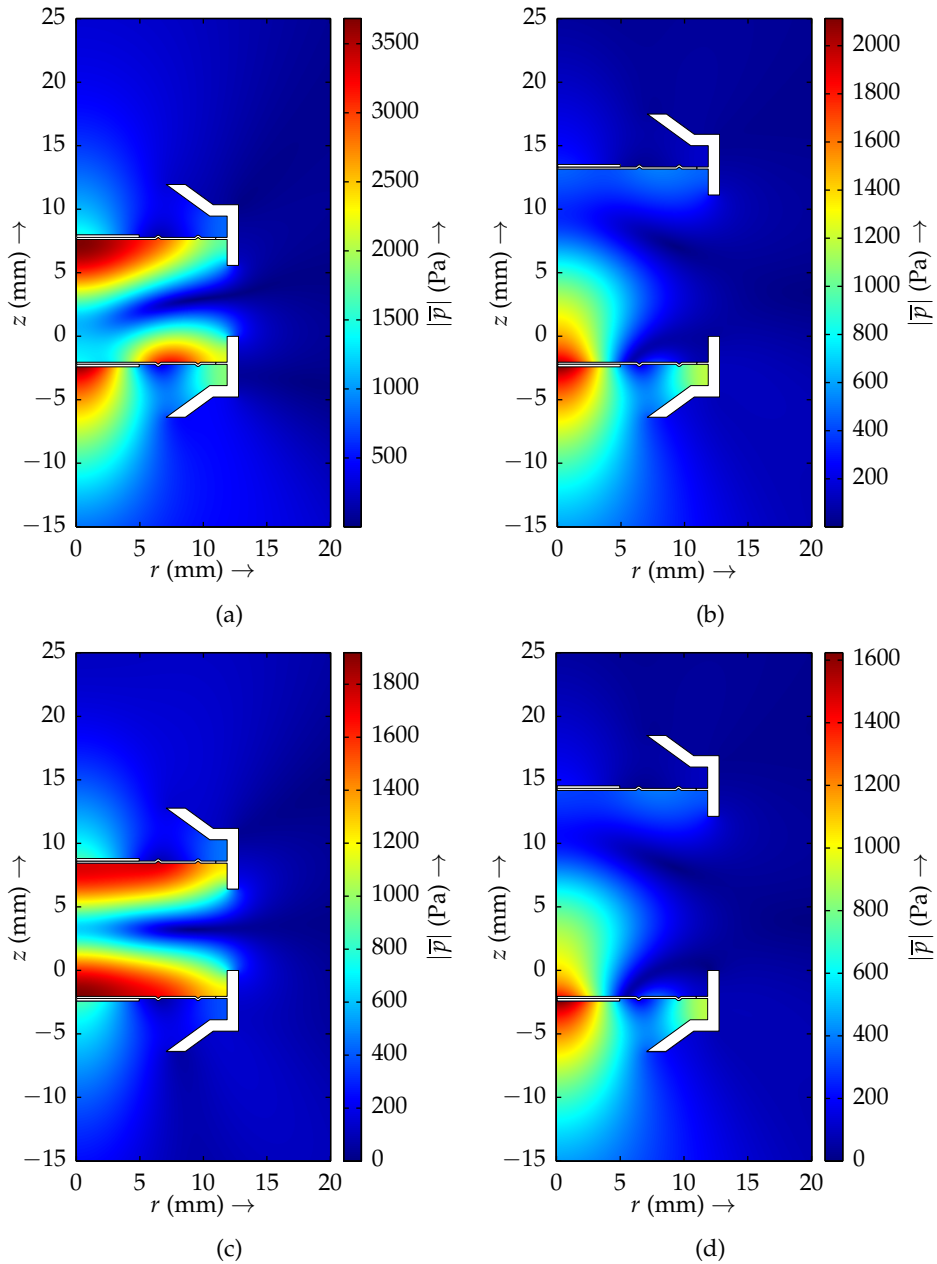
Figure 5.10   Pressure amplitude from FE simulations: maximum output power (a), minimum output power (b), maximum efficiency (c) and minimum efficiency (d).

The sensitivity analysis was carried out for all geometric parameters in table 5.2, the load resistance R_L, the piezoelectric stress constant e in the 31, 33 and 15 directions, the elasticity matrix c^E (on account of practical reasons the whole matrix is scaled as $c^E = \lambda c_0^E$, and only λ is varied), the relative permittivity $\varepsilon_{r,33}^S$ of the PZT material, its density ρ_{PZT}, the Young's modulus E_{Al} of the diaphragm, its density ρ_{Al} and the Poisson's ratio ν_{Al}.

Each parameter p was varied by a small increment σp_0 from its default value p_0, after which the new maximum output power $\Pi_{max,out}(p)$ was sought by means of a pattern search algorithm:

$$\Pi_{out,max}(p) = \max_{z_d, f} \Pi_{out} \tag{5.23a}$$

$$(z_{dmax}(p), f_{max}(p)) = \arg\max_{z_d, f} \Pi_{out} \tag{5.23b}$$

From the variation in the maximum output power one can determine the relative sensitivity of a variable y for a change in parameter p as

$$\frac{\partial y}{\partial p}\frac{p_0}{y_0}, \quad \forall y \in \{\Pi_{out,max}, z_{dmax}, f_{max}\} \tag{5.24}$$

To reduce the influence of numerical errors from the simulation, the partial derivative is calculated by means of a five-point Lagrange's formula [5]. The relative sensitivity is then

$$\frac{\partial y}{\partial p}\frac{p_0}{y_0} = \frac{y((1-2\sigma)\,p_0) - y((1+2\sigma)\,p_0)}{12\sigma y_0} - 2\frac{y((1-\sigma)\,p_0) - y((1+\sigma)\,p_0)}{3\sigma y_0} \tag{5.25}$$

This sensitivity analysis was performed for $\sigma = 1 \cdot 10^{-3}$.

The relative sensitivities of the output power to changes in the parameters are listed in table 5.4. The output power is affected most by the radius of the aluminium diaphragm r_d. Fortunately, it is easy to measure, and is therefore unlikely to introduce modelling errors. Other important parameters are the radius and thickness of the piezoelectric patch, the latter being somewhat more difficult to accurately measure. Furthermore the output power is sensitive to changes in the location r_{s1} of the first notch in the diaphragm, and a number of dimensions of the casing. Surprisingly, the material properties of the diaphragm have little influence on the output power. The material properties of the piezoelectric ceramic seem to influence it much more. Especially the elasticity of the material and the piezoelectric stress constant in the 33-direction affect the output power.

Not only the efficiency is influenced by the variation of parameters, but also the position and the frequency at which the efficiency maxima occur are subject to change. This change is reflected by $\frac{\partial z_{dmax}}{\partial p}\frac{p_0}{z_{dmax0}}$ and $\frac{\partial f_{max}}{\partial p}\frac{p_0}{f_{max0}}$. It is striking that the

Table 5.4 Relative change in the maximum energy transfer efficiency η_{max}, its location z_{dmax} and resonance frequency f_{max} for a relative change in a parameter p

p	$\dfrac{\partial \Pi_{out,max}}{\partial p}\dfrac{\Pi_{out,max0}}{p_0}$	$\dfrac{\partial z_{dmax}}{\partial p}\dfrac{p_0}{z_{dmax0}}$	$\dfrac{\partial f_{max}}{\partial p}\dfrac{p_0}{f_{max0}}$	p	$\dfrac{\partial \Pi_{out,max}}{\partial p}\dfrac{p_0}{\Pi_{out,max0}}$	$\dfrac{\partial z_{dmax}}{\partial p}\dfrac{p_0}{z_{dmax0}}$	$\dfrac{\partial f_{max}}{\partial p}\dfrac{p_0}{f_{max0}}$
r_d	-7.8	2.9	-1.9	R_L	0.5	-0.5	0.0
h_d	0.8	-1.1	0.6	e_{31}	1.2	-0.6	0.0
r_p	2.9	0.1	-0.0	e_{33}	1.9	-0.6	0.0
h_p	-4.4	5.2	0.2	e_{15}	0.4	-0.5	0.0
r_{s1}	-2.4	6.9	-0.2	c^E	-2.5	0.8	0.1
r_{s2}	-0.9	6.3	-0.0	$\varepsilon^S_{r,33}$	0.6	-0.6	-0.0
c_a	-0.3	3.0	-0.1	ρ_{PZT}	0.4	5.0	-0.2
c_b	-2.0	5.9	-0.1	E_{Al}	0.5	3.7	0.2
c_c	-3.6	6.7	-0.2	ρ_{Al}	-0.2	2.9	-0.4
c_d	-3.7	4.6	-0.1	ν_{Al}	0.1	3.4	0.0
c_e	0.3	2.7	-0.0				
c_f	0.6	3.9	-0.1				
c_g	0.3	1.6	-0.0				

frequency at which the output power is at its maximum virtually does not change. Only a change in the diaphragm radius seems to have any effect. One would expect the resonance frequency of the transducer to change when this radius increases, but then again, one would also expect it to change when altering parameters such as the thickness of the diaphragm, the compliance of the materials, their density, et cetera. The fact that a relative sensitivity is used probably obscures this change because of the high value of $f_{max,0}$.

The accuracy of the finite element simulations used to derive table 5.4 is a matter of concern. The listed sensitivities were checked by decreasing the mesh size, using larger initial step sizes in the pattern search, and using a larger value for σ. The results were all comparable, although the decimals are subject to change. There are a two main reasons for this inaccuracy: the accuracy of the solver (which also can lead to false maxima detection of the pattern search algorithm) and the remeshing that is required for every change of a geometric parameter.

5.3 Conclusions and discussion

The efficiency of an AET system is affected by reflections, causing a great dependence of the energy transfer efficiency on the distance between the transmitter and the

receiver. The peaks in the output power and efficiency, which are a consequence of the reflections, restrict the free placement of the receiver if a high energy transfer efficiency and output power are desired.

One possible approach to dealing with reflections is to design a system were they do not play a large role. An example is the system by Shahab *et al.* [109, 111], that uses a receiver that is small in comparison to the wavelength, and a spherically radiating source. The disadvantages of such a system are the low received power and the low transfer efficiency as a consequence of these design choices. It does, however, greatly simplify the modelling of the system. In contrast, in this chapter effort was made to model reflections, since they prove a key aspect of an AET system where a high directionality is used in combination with a receiver of dimensions comparable to or larger than the wavelength.

This chapter outlines two models that describe the reflections that occur in an AET system where the transducers are imperfectly matched to the medium between them. The first model, based on transmission line theory, is a completely analytical model, based on one-dimensional wave propagation, where the combined diffraction and absorption losses are accounted for by means of a lumped attenuation constant. This constant is derived from a vibrating piston model. The second model is a finite element model of the system where the electrical, mechanical and acoustical domains are described and linked to each other through appropriate boundary conditions.

The transmission line model is able to model reflections, but depends heavily on a good transducer model. It is possible to approach measured values of the input and output power to a good degree by means of this model, but the resulting transducer parameters are unrealistic. Without a properly validated transducer model, of which all the parameters are *a priori* known, it is impossible to say whether the good quality of the fitted model's simulation results is a consequence of the correctness of the transmission line model, or that all errors in the model are smoothed away by the parameter fitting and end up in the transducer model parameters. Measurements of acoustic variables (pressures and velocities) would allow a direct comparison to values from the transmission line model and can therefore be used to validate the model, in the absence of sufficient knowledge of the transducer model.

Notwithstanding this consideration, the transmission line models seems to be able to describe the reflections that occur in a typical AET system quite well. Hence, it would seem that the transmission line model is at the very least a step in the right direction.

The transmission line model predicts that, as one would expect, the resonance peaks as a function of the distance between the two transducers completely disappear when the receiving transducer presents an impedance to the medium that is exactly

equal to the medium's characteristic impedance.

Although finite element analysis seems to be able to describe reflections and the general behaviour of an acoustic energy transfer system, it is far from the holy grail in modelling. The FE model is able to model reflections, but the predicted output power is an order of magnitude too high. The variation of the input power with the distance between the two transducers is considerably different from the measurements. This suggests that the transducer is likely incorrectly modelled. This can be caused by parameter deviation, an incorrectly modelled geometry, the absence of losses, unmodelled nonlinear behaviour, or a combination of any of these.

A sensitivity analysis indicates that a change of piezoelectric material can have a great impact on the energy transfer efficiency. Other important parameters are the diaphragm radius, the piezoelectric disc dimensions and the dimensions of the plastic casing. It will therefore require much effort and proper characterisation of all system, geometry and material parameters to arrive at a model that is able to describe the quantities of interest to an adequate level of accuracy.

The transmission line model predicts that a perfect termination of the acoustic path leads to a total absence of reflections. The impedance of the receiving transducer must therefore be adapted to the medium's characteristic impedance. Impedance matching of transducers to a medium can be achieved in a number of ways. A method that is often applied for piezoelectric transducers is the use of quarter-wavelength matching layers [17, 41, 64]. As the name implies, these are layers of a thickness corresponding to a quarter of a wavelength in the material, that are bonded to the radiating face of the transducer. The material itself is chosen to have a characteristic impedance between the transducer's and medium's characteristic impedances. Often multiple consecutive layers are used for an even better adaptation [41], each one successively decreasing in characteristic impedance from that of the transducer to the loading medium. Matching layers are used less frequently in air, because of the need for very low acoustic impedance materials, which are generally extremely lossy and ill suited for use with piezo transducers due to difficulties in bonding them to the transducer surface, in tuning them to the transducer's resonance frequency and their porosity [6, 7, 132]

Acoustic horns (as applied for example in horn drivers, sirens and megaphones) [15, 20, 44, 61, 62, 128] can be used to convert the large reactive radiation impedance of a small transducer into a larger real impedance, and can convert a small transducer velocity to a larger particle velocity in the horn. Moreover, a horn gives control over the directivity of the transducer, which is another desirable feature in an AET system.

A final often applied method of impedance matching is the enlargement of the radiating surface of the transducer, commonly accomplished with membranes or diaphragms, such as the cone in a traditional voice coil loudspeaker [15, 20], or

trough the use of multiple direct radiators in parallel.

The last two methods of impedance adaptation will be examined in more detail in the next two chapters. Chapter 6 deals with the use of horns in AET systems operating in air. Chapter 7 investigates the influence of an increased radiation surface on the energy transfer.

6 Horns

REFLECTIONS are caused by an impedance mismatch at the side of the receiver, basically no differently from a poorly terminated transmission line, as was explained in the previous chapter. They are undesirable, in the sense that they introduce maxima and minima into the energy transfer and the efficiency, and thereby limit the placement of the receiver to distinct locations where the energy transfer peaks. A receiver that presents a perfect impedance match to the medium is able to absorb all the energy contained in the incident wave, without generating reflections (see figure 5.3). But it is not only an impedance mismatch at the receiving end that affects the energy transfer. The impedance mismatch that exists between the transmitting transducer and the medium limits the power that can be transferred. A perfectly matched transmitter transfers the maximum amount of energy to the medium.

Impedance adaptation for transducers in essence amounts to conversion of either the pressure or the particle velocity at the radiating face of the transducer, or both. As a result the transducer experiences a better match with its own impedance. Section 5.3 already mentioned a number of methods with which this can be accomplished. This chapter specifically addresses the use of horns for this purpose. It describes the design and optimisation of horns for AET that employ internal reflections to boost the throat impedance.

This chapter is based on [99] and [100].

6.1 Waveguides

Let us first look at what a horn actually is. In essence it is a structure that limits the spreading of a wave. It is therefore a waveguide; a structure that guides the sound wave as it propagates along a path. In its simplest form, a waveguide is a pipe of a constant cross section. This type of wave guide was already discussed in section 5.1, where it was used to model reflections analytically.

Let us apply the coordinate transformation mentioned in footnote 1 on page 75, setting $z = -l$, and terminating the waveguide with an impedance $\overline{Z}^a(0) = \overline{p}(0)/\overline{u}(0)$ at $z = 0$. A positive l corresponds to a location a distance l to the left of $z = 0$. Equations (5.1) and (5.2) can be combined to find the impedance $\overline{Z}^a(l)$ as

$$\overline{Z}^a(l) = Z_0^a \frac{\overline{Z}^a(0) + jZ_0^a \tan(kl)}{Z_0^a + j\overline{Z}^a(0) \tan(kl)}, \tag{6.1}$$

which is a well-known standard expression[1]. Losses are neglected in this case, hence k is real.

If the cross-sectional area of the waveguide changes at $z = 0$ from A_1 to A_2, such as depicted in figure 6.1, the situation becomes somewhat different. We will make the assumption here that the waves inside the waveguide are always plane waves. Imagine that we have a pressure $\overline{p}(0^-)$ and a particle velocity $\overline{u}(0^-)$ immediately left of the discontinuity and a pressure and particle velocity $\overline{p}(0^+)$ and $\overline{u}(0^+)$ to the right. The pressure should be continuous across the boundary, implying that $\overline{p}(0^-) = \overline{p}(0^+)$. Continuity relations also dictate that the mass flow (and hence the volume flow) be constant across the discontinuity, or $A_1\overline{u}(0^-) = A_2\overline{u}(0^+)$. Therefore the impedances directly left and right of the discontinuity are related by

$$\overline{Z}^a(0^-) = \frac{A_1}{A_2}\overline{Z}^a(0^+). \tag{6.2}$$

A step change in the diameter of a pipe can therefore be used to increase the impedance seen by a transducer or the medium (or decrease it when desired).

Now, let us consider the impedance a distance l away from the discontinuity. It follows from the combination of (6.1) and (6.2), and is equal to

$$\overline{Z}^a(l) = Z_0^a \frac{A_1\overline{Z}^{a^+} + jA_2Z_0^a \tan(kl)}{A_2Z_0^a + jA_1\overline{Z}^{a^+} \tan(kl)}, \tag{6.3}$$

---

[1]On a side node, equation (6.1) explains how quarter-wavelength matching layers can be used for impedance adaptation. For a length corresponding to a quarter-wavelength $kl = \frac{1}{2}\pi$, the impedance becomes $\overline{Z}^a(l) = Z_0^{a^2}/\overline{Z}^a(0)$ and can thus be tuned by a proper choice of Z_0^a. The only other length that yields a real impedance is $l = \frac{1}{2}\lambda$, resulting in the not overly useful $\overline{Z}^a(l) = \overline{Z}^a(0)$.
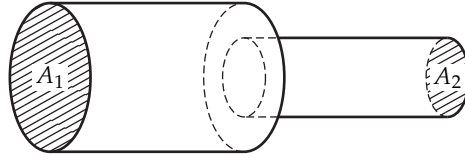
Figure 6.1   A waveguide with a change in cross-sectional area at $z = 0$.

using the shorthand notation $\overline{Z}^{a+} = \overline{Z}^a(0^+)$.

6.2   Exponential horns

If the cross-sectional area of a pipe changes continuously, instead of abruptly as in figure 6.1, and it increases monotonically, such a pipe is normally referred to as a horn [69]. Based on the force and mass balance in a horn, one can derive a differential equation that describes the pressure in it. This equation, known as Webster's horn equation [69, 128], is given by

$$\frac{\partial^2 p}{\partial z^2} + \frac{d \ln(A)}{dz} \frac{\partial p}{\partial z} = \frac{1}{c^2} \frac{\partial^2 p}{\partial t^2} \, . \tag{6.4}$$

It is derived under the assumption that the waves in the horn are (nearly) plane, which is only possible as long as the surface area A changes very slowly as a function of z.

Let us now look at a horn of which the surface area varies exponentially as

$$A(z) = A_0 e^{mz} \, , \tag{6.5}$$

with m the flare constant of the horn. The differential equation (6.4) for the pressure waves in this horn can then be written as

$$\frac{\partial^2 p}{\partial z^2} + m \frac{\partial p}{\partial z} = \frac{1}{c^2} \frac{\partial^2 p}{\partial t^2} \, . \tag{6.6}$$

Substitution of a plane wave solution $\overline{p}(z, t) = P e^{\overline{\sigma} z} e^{j \omega t}$ gives

$$\overline{\sigma}^2 + m \overline{\sigma} + k^2 = 0 \, , \tag{6.7}$$

where the angular wave number $k = \omega/c$ is again introduced. This equation has the solutions $\overline{\sigma} = -\alpha \pm j\beta$, with $\alpha = \frac{1}{2}m$ and $\beta = \sqrt{k^2 - \alpha^2}$. Note that a travelling wave solution only exists for $\beta \in \mathbb{R}$, or $\omega > \omega_c = \frac{1}{2}mc$. The horn therefore has a distinct cutoff frequency and acts as a high pass filter.

6.2.1 Infinite horns

If we make the assumption that the horn is infinitely long, there is no interface from which reflections can occur, and hence there will only be a wave travelling in the positive z-direction. This wave corresponds to the solution $\overline{\sigma} = j\beta - \alpha$, or

$$\overline{p}(z,t) = Pe^{-\frac{1}{2}mz}e^{j(\omega t - \beta z)} . \tag{6.8}$$

The factor $e^{-\frac{1}{2}mz}$ is the dilution [69] that accounts for the waves having to cover an area that increases with the spatial coordinate z.

The particle velocity $\overline{u}(z,t)$ in the horn can be obtained from the solution of the pressure (6.8) by means of equation (3.19), which can be written in this case as

$$
\begin{aligned}
\overline{u} &= -\frac{1}{j\rho_0\omega}\frac{\partial \overline{p}}{\partial z} \\
&= \frac{\overline{p}}{Z_0^a}\left(\sqrt{1-\left(\frac{\omega_c}{\omega}\right)^2}-j\frac{\omega_c}{\omega}\right) .
\end{aligned}
\tag{6.9}
$$

The ratio between the pressure and the particle velocity gives us the effective characteristic impedance that the wave experiences inside the horn. It is equal to

$$
\begin{aligned}
Z_{0,h}^a &= \frac{\overline{p}}{\overline{u}} \\
&= Z_0^a\left(\sqrt{1-\left(\frac{\omega_c}{\omega}\right)^2}+j\frac{\omega_c}{\omega}\right) .
\end{aligned}
\tag{6.10}
$$

Note that this impedance does not depend on the z-coordinate and thus is constant throughout the horn. Therefore it is effectively the impedance that a source placed at the the throat (the narrow end) of the horn will have to work against. The radiation resistance of this transducer, determining its radiated power, hence is equal to

$$
\begin{aligned}
R_{\mathrm{rad},h} &= A_0\,\mathrm{Re}\left(Z_{0,h}^a\right) \\
&= A_0 Z_0^a\sqrt{1-\left(\frac{\omega_c}{\omega}\right)^2} .
\end{aligned}
\tag{6.11}
$$

Comparing this radiation impedance to that of a circular piston, given by equation (4.12), one can see in figure 6.2 that the low frequency radiation of a plane piston is greatly improved by application of a horn. This is a great advantage for audio applications, as is the flat frequency response of the horn in comparison to the piston radiator. Unfortunately, acoustic energy transfer does not really benefit from either,
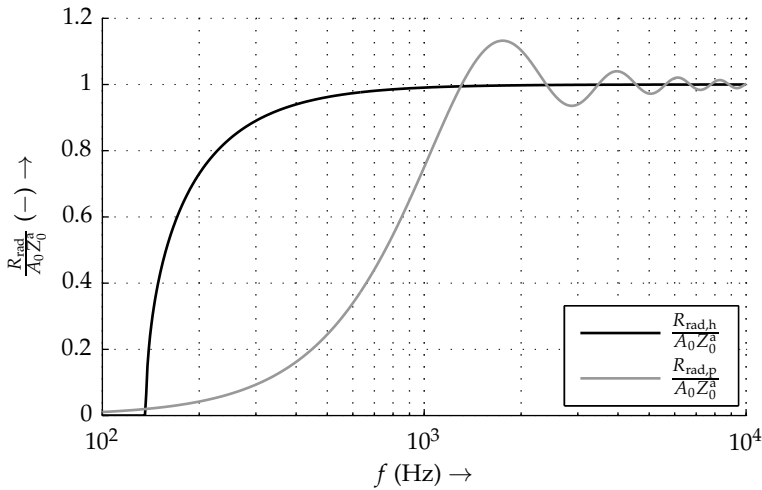
Figure 6.2 The normalised radiation impedance of a circular piston source of $r_0 = 8\,\mathrm{cm}$ radius is boosted for low frequencies by the addition of an infinite exponential horn ($m = 5\,\mathrm{m}^{-1}$).

as long as the transmitter size is not too small in comparison to the wavelength. In the high frequency region, the impedance seen by the transmitter is approximately equal to $A_0 Z_0^a$, whether a horn is used or not. The advantage of the horn lies in confining the radiated power to a restricted volume, instead of the source radiating omnidirectionally (which it does for a small transmitter size in comparison to the wavelength, and thus low frequencies). In principle an increased transducer size gives the same result as the addition of a horn. Horns are often used in loudspeaker systems, rather that large diaphragms, because the mass of a diaphragm increases faster than its area, since a certain rigidity should be maintained [34]. Therefore a small loudspeaker coupled to a horn will be more efficient than a large direct radiator. A larger radiation surface can also be obtained by using multiple direct radiators driven in parallel, but horn loudspeakers perform much better in this situation in general as well, due to difficulties in getting these loudspeakers to radiate at a uniform phase, because of spacing, complex vibration of the diaphragm, and production variation. The resulting radiation is often irregular and has an unpredictable response and directivity [15].

6.2.2 Horns of finite length

Equation (6.7) predicts a wave travelling in the positive z-direction and one going in the opposite direction. Only the former was used in the derivation of the sound field

in the infinite horn, since reflections can never occur in it. In practice, however, a horn will always have a finite length. An infinite horn can at best only be approximated. The true pressure field will therefore be a superposition of both solutions.

A complete derivation of the pressure field inside a horn of finite length will not be given in this section. Instead the resulting throat impedance will merely be given. It is equal to (see [21, 120]):

$$\overline{Z}_t^a = Z_0^a \frac{jZ_0^a \, \sin(\beta l) + \overline{Z}_m^a \, \cos(\beta l + \theta)}{j\overline{Z}_m^a \, \sin(\beta l) + Z_0^a \, \cos(\beta l - \theta)} , \tag{6.12}$$

with $\tan \theta = \alpha/\beta$. Since we are now dealing with a horn of finite length l, the throat impedance $\overline{Z}_t^a$ depends on the impedance $\overline{Z}_m^a$ at the mouth of the horn (the wide end). The form of (6.12) is reminiscent of the equation describing the impedance of a transmission line (6.1), which a horn of course is in a certain sense.

The value of the mouth impedance $\overline{Z}_m^a$ is normally approximated in literature by that of a baffled circular piston source (see equation (4.12)). This is an exact representation as long as the waves arriving at the mouth of the horn are plane waves and the horn mouth is embedded in a baffle. In practice it will therefore only be an approximation. Note that $\overline{Z}_m^a$ is an acoustic impedance, instead of a mechanical impedance. The radiation impedance from (4.12) should therefore be divided by the mouth surface area.

Figure 6.3 depicts the throat impedance from equation (6.12) for a horn mouth radius of 10 cm, 20 cm, 30 cm and that of an infinite horn. The throat radius is 8 cm in all four situations, and the horn flare constant is $m = 5 \, \text{m}^{-1}$, just as in figure 6.2. The graphs show that the longer the horn is, the more its throat impedance approaches that of an infinite exponential horn. The horn impedance now peaks at certain resonance frequencies, as a consequence of the horn's finite length. These peaks surpass the Z_0^a-level, which can at maximum be attained by means of an infinite horn, and which is approximately the maximum radiation resistance of a plane piston. A finite horn is therefore capable of boosting the impedance seen by the transducer.

The asymmetric oscillations that are visible in the throat impedance (for example around $f = 2 \, \text{kHz}$ for $r_m = 10 \, \text{cm}$) are caused by the oscillatory behaviour of the radiation impedance of a circular piston, (see figure 4.3 or 6.2). Furthermore, the first peak of the impedance is significantly higher than the others for small horn mouth sizes. This is a direct result of the low radiation impedance of the mouth for small sizes and low frequencies (cf. figure 4.3), having large reflections as a result, comparable to a large impedance mismatch in a transmission line.
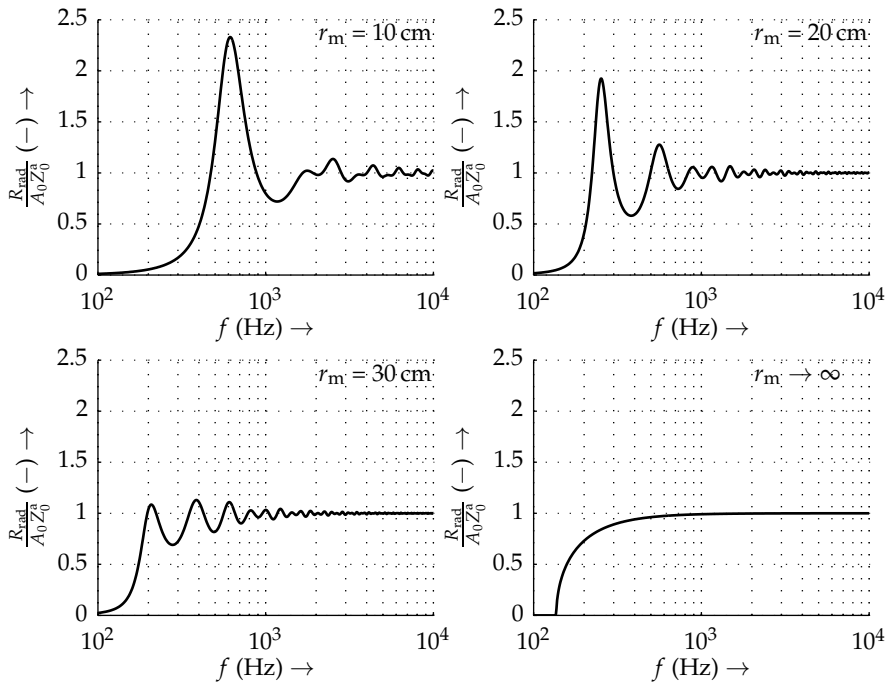
Figure 6.3 The normalised throat impedance for an exponential horn having throat radius $r_t = 8\,\text{cm}$ and flare rate $m = 5\,\text{m}^{-1}$, for a mouth radius $r_m = 10\,\text{cm}$, $20\,\text{cm}$ and $30\,\text{cm}$, and an infinite horn (from equation (6.11)).

6.3 Introductory measurements

A simple first test setup was built to investigate the effect that horns have on the energy transfer efficiency. Again, two PX051 piezo transducers were used for these experiments, one on the transmitting and one on the receiving side. Two horns, one for the transmitting and one for the receiving transducer, were constructed to test for influence on the reflection and the energy transfer efficiency as a whole. As a first attempt, a readily available shape was used as a horn. The horns are made out of PET with a thickness of 0.25 mm.

A finite element model of the AET system with horns was made for comparison. The horns are added to the FE model of the PX051 transducers, which was described in section 5.2, to obtain the model in figure 6.4. The total FE model contains two of these transducer-horn combinations placed a distance z_d apart in an air domain, surrounded by a perfect matching layer. The horns are modelled in the simulation as a rigid reflecting boundary. Their geometry is approximated by a linear segment, followed by a quadratic Bézier curve. The linear part at the throat of the horn is described by

$$r_h(z) = 13.2 \, \text{mm}, \quad 0 \, \text{mm} \le z < 9.50 \, \text{mm}, \tag{6.13}$$

while the second part is given by the rational quadratic Bézier curve:

$$\vec{B}(t) = r_h(t)\,\hat{r} + z(t)\,\hat{z} \tag{6.14}$$

$$= \frac{(1-t)^2\,\vec{P}_0 w_0 + 2t\,(1-t)\,\vec{P}_1 w_1 + t^2 \vec{P}_2 w_2}{(1-t)^2\,w_0 + 2t\,(1-t)\,w_1 + t^2 w_2}, \quad t \in [0,1], \tag{6.15}$$

with

$$P = \begin{pmatrix} \vec{P}_0 & \vec{P}_1 & \vec{P}_2 \end{pmatrix} = \begin{pmatrix} 13.2 & 23.4 & 32.3 \\ 9.50 & 26.8 & 80.0 \end{pmatrix} \text{mm}, \tag{6.16}$$

$$w = \begin{pmatrix} w_0 & w_1 & w_2 \end{pmatrix} = \begin{pmatrix} 1 & 3.62 & 1 \end{pmatrix}. \tag{6.17}$$

6.3.1 Results

The measured energy transfer efficiency of the AET system with PX051 transducers and horns is shown in figure 6.5, together with the corresponding simulation results obtained from the FE model. There are some dissimilar peaks to be found in the region $0 \, \text{mm} < z_d < 60 \, \text{mm}$. These are possibly caused by resonances in the horns, i.e. structural vibrations that are not modelled in FE analysis. All other
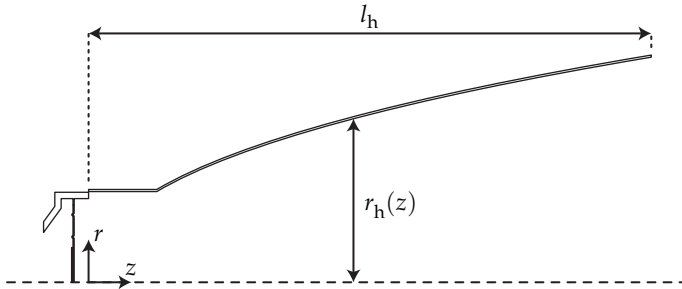
Figure 6.4 The radius $r_h(z)$ of the horns that are used in the measurements is described in the FE model by means of Bézier curves. They are modelled as ideal hard acoustic boundaries.

characteristics of the simulated and experimentally determined efficiency are very similar. The relative amplitude of the peaks in comparison to their mean is equal from approximately $z_d = 100\,mm$ onwards, just as is their shape. As one can see, the mean of the measured efficiency and the efficiency predicted by the FE model differ approximately by a factor 2.3 for distances $z_d > 100\,mm$. The peaks are also shifted to the right by 3.1 mm, which is possibly caused by a small offset in the reference position during the measurements.

Let us now turn our attention towards the differences between the efficiency with and without horns, which is of course our main interest. Both measurements are plotted in figure 6.6 to be able to compare them directly. The distance z_d is measured between the horn mouths, or between the casings of the transducers for the measurements without horns. The actual distance travelled between the transducers in the case with horns is therefore larger by $2l_h = 160\,mm$. It is, however, fair to compare the efficiency for an equal separation between the extremities of the transducers—including horns—as this is the distance one would be interested in for contactless energy transfer.

Figure 6.6 shows that horns can drastically increase the efficiency of AET, by an order of magnitude or more, although the peak efficiency is lower (5.1 % with horns, versus 27.7 % without). The milder drop-off as a function of the distance z_d is very striking, and can be explained by the larger radiating surface of the transmitter, leading to less diffraction losses, and the increased receiver area, which allows it to catch more energy (cf. figure 4.7). Adding horns to the transducers in an AET system does not reduce reflections per se, as the peaks due to reflections became larger by the addition of the horns. This is in all likelihood a consequence of a suboptimal horn design. The exact cause was not verified.

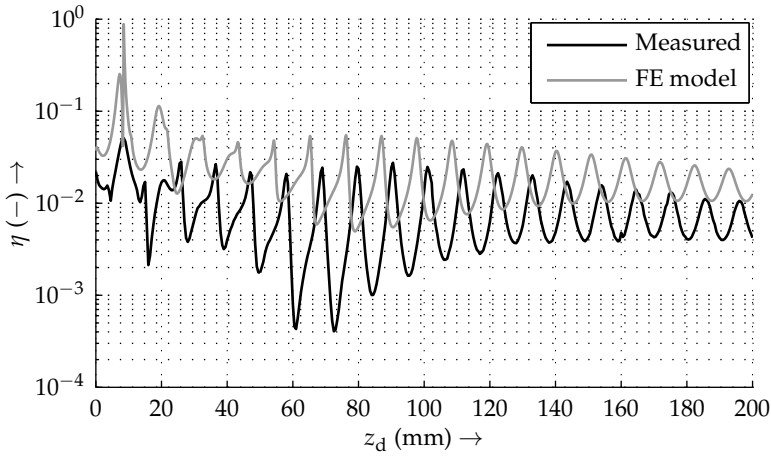All-in-all there are enough interesting features to figure 6.6 to justify more exper-

Figure 6.5 Measurements and simulations of an AET system fitted with horns differ in amplitudes and mean values of the spatial resonance peaks. Moreover, there are some resonance peaks present in the measurement results for small values of z_d that are absent in the FE simulations. For large z_d, the results agree to a larger extent.
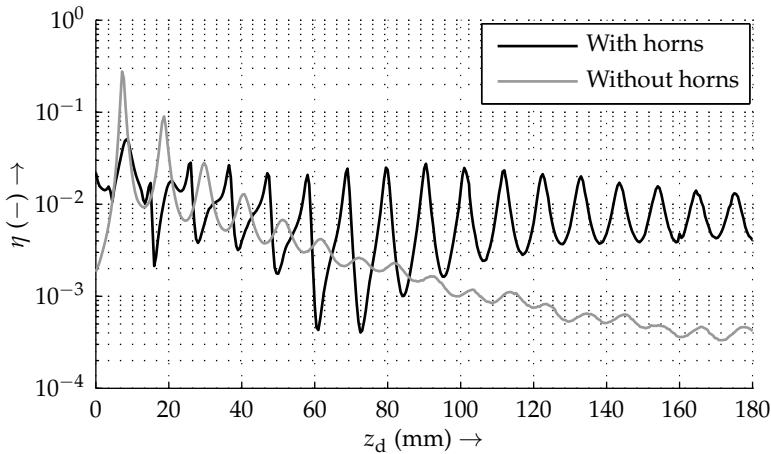

Figure 6.6 Measurements show that the addition of horns to an AET system can significantly enhance the efficiency of the energy transfer. Moreover, the decline of the efficiency is much milder when the horns are added.

iments in an attempt to boost the output power and to decrease reflections. The remainder of this chapter is dedicated to the design of specific horns for AET and their optimisation.

6.4   Stepped-exponential horns

Horn design commonly focuses on obtaining a frequency response that is as flat as possible [21, 44, 58, 69, 120], being a desirable feature in sound generation for audio purposes. However, since acoustic energy transfer normally makes use of a single frequency, or at most a very narrow frequency band, it is possible to design a horn in which its resonance characteristics are deliberately used to obtain a high output at the desired frequency. Reflections in the horn, which occur due to its finite length, can be used to tune the impedance in such a way that the horn has a large transformation ratio. This possibility was already coined much earlier, but was usually considered undesirable or unnecessary (see for example [44]). On another note, the horns for audio systems are normally designed to have a constant directivity, with low beam forming, while an AET system contrarily benefits from having a very high directivity, or otherwise put: a narrow beam width.

This section focuses on the design of horns that provide a large impedance step in an attempt to reduce reflections and to increase the transferred power. The resonance frequency of the horn is matched to that of the driving transducer to obtain the maximum output pressure. Two concepts from section 6.1 are married to this end; a stepped radius waveguide is utilised to obtain a large step in impedance, which is then coupled to an exponential horn section. A cross section of the total structure is depicted in figure 6.7. The radius of the horn is given by

$$r(z) = \begin{cases} r_1, & 0 \leq z < l_1 \\ r_2 e^{\frac{1}{2}m(z-l_1)}, & l_1 \leq z < l_2 \end{cases}. \tag{6.18}$$

The first section, consisting of a step in bore radius from r_1 to r_2, boosts the impedance, but the accompanying decrease in radiating surface means that the directivity is also reduced in comparison to that of the original transducer. As indicated previously, a horn can be used in such a case to both increase the radiation resistance and to improve the directivity. The length l_2 of the exponential section can moreover be chosen advantageously to gain an extra boost in impedance. The total impedance presented to the transducer at $z = 0$ is then equal to the combination of (6.3) and (6.12), with $\overline{Z}^{a+} = \overline{Z}_t^a$.
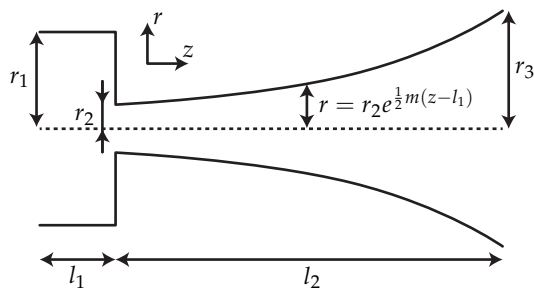
Figure 6.7 A stepped exponential horn has a constant radius at its throat, changing stepwise into a smaller radius, which flares out again exponentially.

These equations only describe the behaviour of the horns up to a certain accuracy. The derivation of the throat impedance of the finite exponential horn assumes that the horns are slender, i.e. that mouth radius r_3 is not much larger than the throat radius r_2. This is a requirement that is not mentioned properly in literature, but that is rather just lightly touched upon and subsequently ignored. Although the impedance graphs of figure 6.3 seem to converge to that of an infinite horn for an increase in mouth radius, they actually diverge again for even larger mouth radii. This stems from the assumption of plane waves that no longer holds in these cases. The derivation of both (6.3) and (6.12) made use of this assumption, which is a further cause of concern, since this requires the horn's radial dimensions to be much smaller than a wavelength. In practice this will not be the case either, which can give rise to radial modi. Lastly, one is interested in the transferred power and the efficiency at which this occurs, which the impedance does not directly give an account of. Here the directivity of the horn also comes into play, which is not described by these simple impedance equations.

Because of these reasons finite element analysis is used for design and optimisation of the horns, even though it is much more computationally intensive. The FE model consists of the geometry of the PX051 piezoelectric transducers, which was presented earlier in section 5.2, coupled to the horn structure of figure 6.7. For the sake of simplicity, an axisymmetric model is used and the horn walls are modelled as hard boundaries. The horns are assumed to be sufficiently rigid to be able to neglect their structural mechanical properties. No losses in the transducers, the horns or wave propagation were modelled in the FE model for the design and optimisation of the horns. All losses in the model solely occur due to acoustic energy that is not captured by the receiver.

To attain maximum power transfer, the dimensions of the horns are optimised using the MATLAB patternsearch minimisation algorithm and the FE model. The power

Table 6.1   Optimisation yields different dimensions for both the transmitter and receiver horns.

Parameter	Transmitter (mm)	Receiver (mm)
r_1	11.70	11.70
r_2	3.01	5.65
r_3	24.03	41.01
l_1	17.95	18.43
l_2	149.18	146.21
m	27.8	27.1

transfer has many local optima, largely due to the reflections in the horns, requiring the use of a global optimisation algorithm. Because there is no way of confirming whether a found solution is actually globally optimal, the optimisation was started from a large number of initial parameter sets to obtain a design of which optimality is sufficiently probable. The optimisation goal in this case is maximisation of the received power, dissipated in a $2\,\text{k}\Omega$ load connected to the receiving transducer. This load resistance was chosen based on the optimal value found in section 4.3.2. A driving frequency of $17\,\text{kHz}$ is used in the optimisation, which is the nominal resonance frequency of the piezo transducers that are used. The distance z_d between the mouths of the horns was set to $10\,\text{cm}$.

The horn parameters of both the transmitter and receiver are varied in the optimisation, as it is expected that this leads to a higher power output. In principle, the design of the mouth and flare of the transmitter should be aimed at arriving at an optimal directivity, to decrease the spreading losses. A large mouth, and hence a large receiving surface, is beneficial for the receiver on the other hand. The receiving horn should at the same time provide a good impedance match so that little energy is reflected. Therefore the horns are optimised simultaneously. The resulting parameters of the optimised designs are given in table 6.1.

6.4.1   Transducer losses

Initial measurements showed large differences between the measured transferred power and efficiency and the predictions from the FE model. The FE model was therefore extended with the transducer losses from section 4.3.1. As was already discussed, the internal resistance varies wildly between transducers. A resistance $R_\text{m} = 190\,\Omega$ is used in the FE model to compensate for the losses in the transducer.

The losses are added exactly as they are measured: as a lumped element resistance. This is accomplished by addition of an electrical circuit to the FE simulation, which is
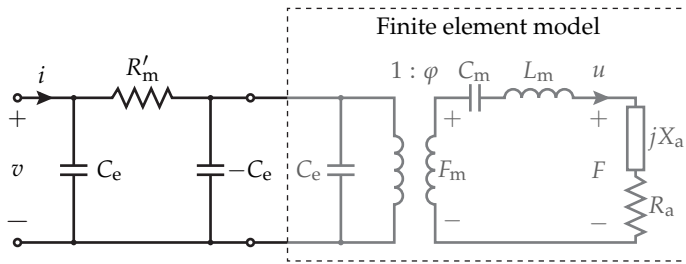
Figure 6.8   The transducer losses are incorporated into the FE model as a lumped element resistance. A negative capacitance is used to cancel the transducers parasitic capacitance. The equivalent circuit of the transducer is represented in grey since it is not the real FE transducer model, but is merely drawn for comprehensibility of the principle.

connected virtually to the terminals of the piezoelectric ceramic. First, the electrical impedance is determined from the original FE model of the PX051 transducers by means of a frequency sweep. Subsequently, it is assumed that the equivalent circuit of the PX051 model in the FE model is of the form of figure 4.8. Its circuit parameters are then determined making use of the method described in section 4.3.1. Now the transducer losses should be added as a series element in the mechanical branch of the equivalent circuit. To this end a negative capacitance $-C_e$ is placed in parallel to the transducer in simulation, which cancels the transducer's own electrical capacitance. A resistance $R'_m = 190\,\Omega$ is then connected between a capacitance C_e and the transducer terminals. The principle is shown graphically in figure 6.8.

6.4.2   Experimental results

The horn designs that were obtained from the optimisation were CNC-machined out of solid aluminium. They were fitted with the PX051 piezoelectric transducers that were also used for earlier experiments. These transducers were cherry-picked for the experiments to have a resonance frequency of 17.0 kHz, since the horns were designed to work at this frequency. The horns were successively mounted on the same position controlled linear motor that was used in earlier measurements (section 5.1.6, page 84). The procedure for measuring the input and output power was the same as well. Distances z_d are measured between the horn mouths. All surfaces were covered in absorbing foam to counter reflections. A photograph of the setup is shown in figure 6.9.

The electrical load R_L connected to the receiving transducer was varied to find its optimum of $840\,\Omega$ at a distance of $z_d = 10$ cm, for which the horns were optimised.
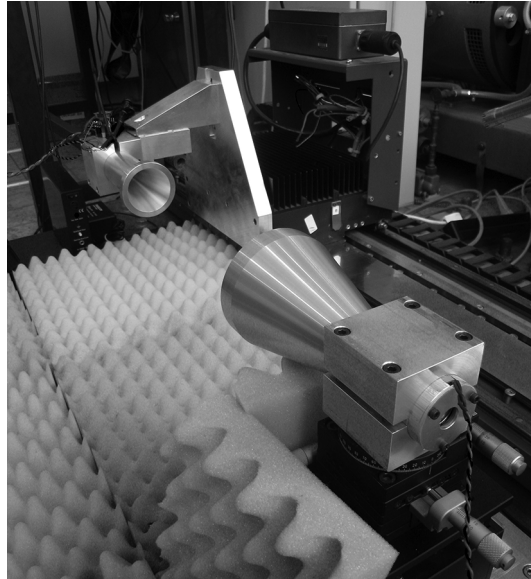
Figure 6.9 The horns were milled out of solid aluminium and mounted on a linear motor with incremental encoder to facilitate accurate position variation.

The electrical capacitance was not compensated, as it did not yield a higher output power. This indicates that the effective internal resistance of the receiver is low in comparison to the reactance of its electrical capacitance.

The power transfer and efficiency of the transducers without horns was measured on the same setup for comparison. A $420\,\Omega$ load proved to be optimal in this case. As before, the distance z_d was measured between the casings of the transducers to allow a fair comparison between the sets of measurements. Although this means that the path lengths between the transducers is shorter by a distance $l_1 + l_2$, arguably leading to a wrong comparison from an acoustic point of view, the distance between the extremities of the transmitter and the receiver is of importance for comparison of the performance of a contactless energy transfer system.

Power transfer and efficiency

The results of the FE simulation and the energy transfer measurements, both with and without horns, are plotted together in figure 6.10 as a function of the distance z_d between the transmitter and the receiver. This distance was incremented in $250\,\mu m$ steps with a $1\,\mu m$ accuracy. It is immediately clear from these graphs that the realised

power transfer and efficiency are much lower than the predictions of the FE model, even after including the transducer losses in the model. Section 6.4.3 will go into more detail about the origin of these differences.

Even though the measured behaviour is different from that of the model, the horns still have a large advantage over the setup without horns. The output power is larger at distances greater than 74 mm, while the efficiency of the hornless setup is already outperformed at a distance of 52 mm. The power transfer and efficiency of the setup without horns is still better in comparison to the case with horns for very small distances, where reflections between the transducers play a large role. Their efficiency and transferred power drops off rather steeply with distance, however, which is something the horns suffer from to a much lesser extent, because of the improved directivity of the transmitter. Furthermore, the increased area of the receiver allows a larger part of the sound wave to be captured and guided towards the piezo transducer.

At $z_d = 10$ cm, the distance for which the horns were optimised, the received electrical power is $\Pi_{out} = 248\,\mu W$, at an energy transfer efficiency of $\eta = 0.68\,\%$. If no horns are used, the same transducers yield an output power of $\Pi_{out} = 79.8\,\mu W$ at an efficiency of $\eta = 0.091\,\%$. The height of the peaks due to reflections does not differ notably from those in the experiment without horns. Only at larger distances, from approximately $z_d = 80$ mm onwards, the height of the peaks in the case without horns is much lower, which is likely caused by larger spreading losses in this case.

If one would look at how the systems compare for equal distances between the diaphragms of the transducers, the horns compare very favourably. Their results in figure 6.10 are then offset by 331.77 mm, which is out of range of the graph, but extrapolation allows us to see that the horns would provide more than an order of magnitude higher output power and efficiency.

6.4.3   Differences between measurements and simulations

There are several possible causes for the experimental results of the power and efficiency measurements with horns to be quite different from the finite element simulations. Firstly, as mentioned earlier, the piezo transducers that are used vary greatly, not only in resonance frequency, but in losses as well. This variation in combination with possible minor deviations in the horn dimensions can lead to large change in the output, since the resonances of the air column in the horn have to be tuned exactly to the resonance of the piezo element. Moreover, section 5.2.1 already indicated that the FE model of the piezoelectric transducers, which was used for optimisation of the horns, deviates from their actual behaviour.
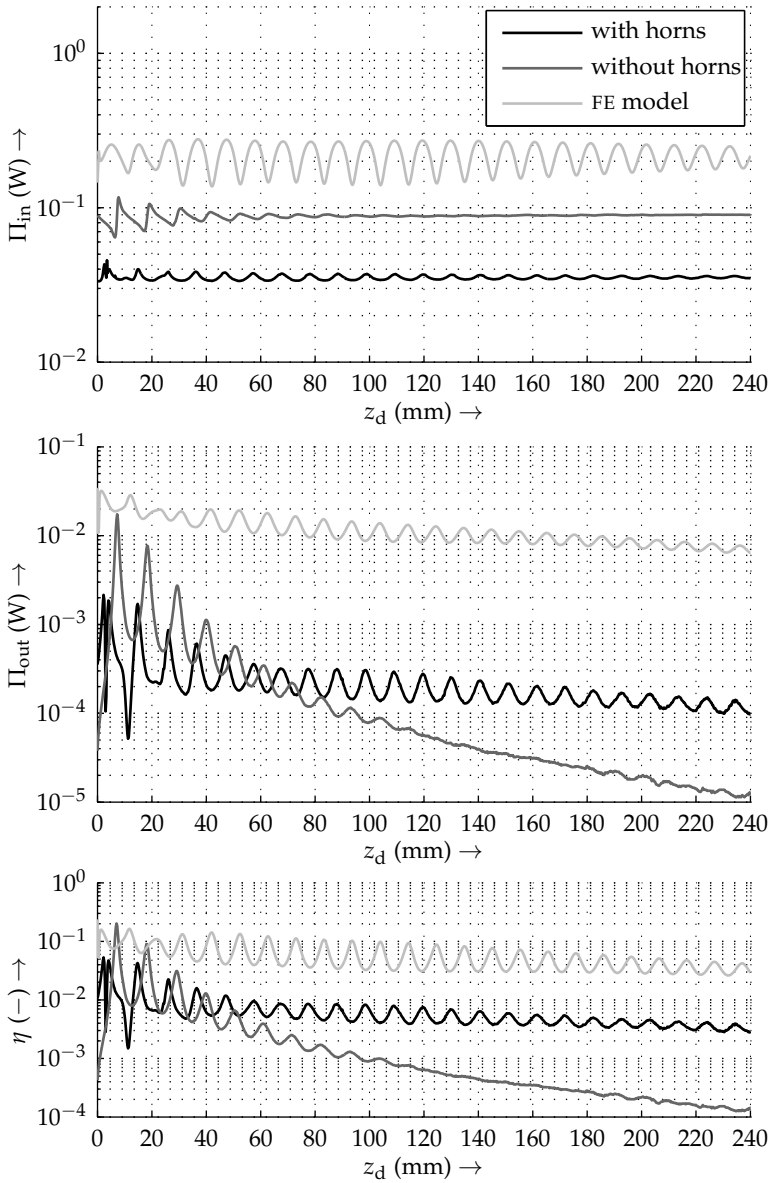
Figure 6.10 Although the horns show a great improvement in energy transfer and efficiency at greater distances, their effect is much smaller than was predicted by the model. The graphs show the electrical input power Π_{in}, the electrical output power Π_{out} and the energy transfer efficiency $\eta = \Pi_{out}/\Pi_{in}$.

Another possible effect that could degrade performance are viscous losses in the small cross-sectional areas of the exponential sections. The viscous and thermal boundary layer thicknesses at $f = 17\,\text{kHz}$ and $20\,^\circ\text{C}$ are respectively [69]

$$d_{\text{vis}} = \sqrt{\frac{2\mu}{\rho_0 \omega}} = 16.9\,\mu\text{m} \tag{6.19a}$$

$$d_{\text{th}} = \sqrt{\frac{2\kappa}{\rho_0 \omega c_p}} = 19.9\,\mu\text{m}\,, \tag{6.19b}$$

with $\mu = 1.8369 \cdot 10^{-5}\,\text{kg}\,\text{m}^{-1}\,\text{s}^{-1}$ being the viscosity, $\kappa = 0.0257\,\text{W}\,\text{m}^{-1}\,\text{K}^{-1}$ the thermal conductivity and $c_p = 1.005 \cdot 10^3\,\text{J}\,\text{kg}^{-1}\,\text{K}^{-1}$ the isobaric mass heat capacity, all of dry air at $20\,^\circ\text{C}$. These correspond to a viscous boundary layer covering 1.1 % and a thermal boundary layer that makes up 1.3 % of the surface area at the narrowest part ($r = r_2$) of the transmitter horn. There will therefore be a small influence due to viscous losses at the walls of the horns and heat exchange between the horn and the air, but it is not expected to play a huge role.

Although nonlinear effects due to excessively high pressure levels are often responsible for reduced performance of horns, it was confirmed by measuring the linearity between the output sound pressure and the input voltage that this is not an issue in the current design.

The influence of several other parameters will be investigated in the remainder of this section. The performance of the horns is judged based on the sensitivity $\mathcal{S}$ of the horn driver (the piezo element-horn combination). It is defined in this case as the on-axis sound pressure amplitude[2] at a distance of 10 cm from the horn mouth, divided by the input voltage amplitude of the transducer. The sensitivity is measured by means of a Stanford Research Systems SR785 dynamic signal analyser using a swept sine measurement. Only the ratio of the pressure and voltage amplitudes is retained, the phase information is discarded. The horns for the transmitting and the receiving transducers are both used in a transmitting configuration for these tests.

Figure 6.11 beautifully illustrates the reason why losses were included in the finite element model, as the sensitivity without is much too high for both transducers. Adding a transducer loss resistance $R'_m = 190\,\Omega$ brings the simulated sensitivity of the receiver down to that of the measurements, but the sensitivity of the transmitter, as predicted by the FE model, is still too large.

Please keep in mind that the sensitivity is only used as a convenient quantity on the basis of which to judge the deviation between the FE model and the measurements.

---

[2]The sound pressure was measured using a G.R.A.S. 40BF microphone, connected to a 26AC preamplifier and a 12AK power module and postamplifier from the same manufacturer. The whole measurement chain is calibrated using a G.R.A.S. 42AA pistonphone.
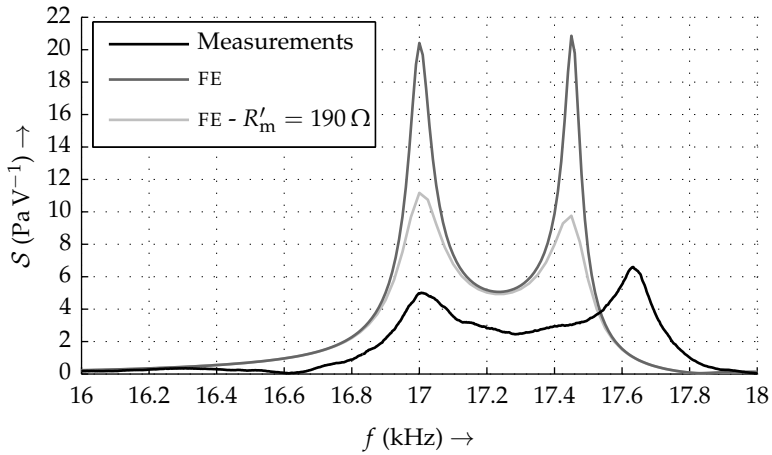
(a)
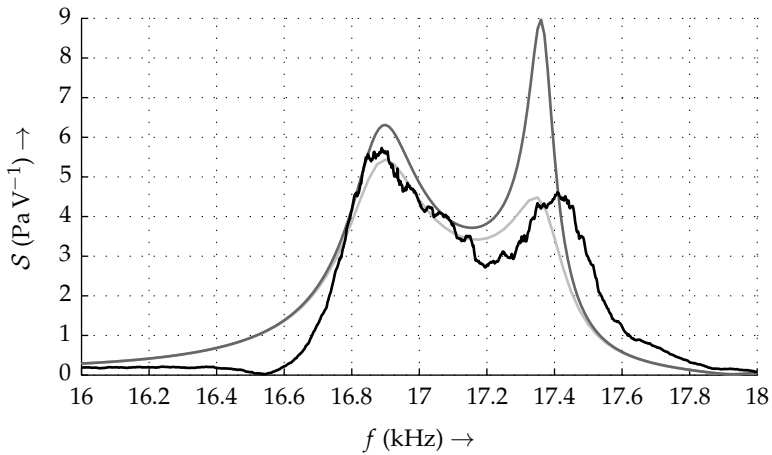
(b)

Figure 6.11   The measured sensitivities of the transmitting (a) and receiving (b) horn drivers are compared with finite element simulations, both with and without transducer losses.

While it bears some information on the performance of the horns, it is not an absolute measure of how well these horns function in an acoustic energy transfer setup, as the sensitivity does not give any information about the directivity, reflections, et cetera.

Horn parameters

The first place to start in the search for the cause of these large deviations is naturally with the influence of the horn dimensions. To this end, the sensitivity at 10 cm from the transmitting horn mouth is simulated again using the finite element model. In these simulations, the horn parameters are varied from their nominal values by plus and minus 4 %; a deviation that they in practice never can have. The results are shown in figures 6.12a-d. These graphs indicate that r_2, r_3 and l_2 have a very limited influence on the on-axis pressure at $z = 10$ cm. The length l_1 of the chamber into which the transducer radiates, however, has an enormous influence on the sensitivity. This is easily explained, as equation (6.3) already shows that it are the reflections in this section that determine the load impedance on the transducer. Lengthening or shortening this section changes the wavelength at which resonance occurs. Therefore the influence of this length is very large. It would not have been odd for the same to apply to the length l_2 of the exponential section, but apparently the reflections in this section play much less of a role in the throat impedance of the horn.

Figure 6.12e shows similar results for a variation of the horn profile. It was changed from its original exponential shape to a conical one in five discrete steps. The intermediate horns are a conical-exponential hybrid. The horn radius as a function of the z-coordinate is given for these horns by

$$r(z) = tr_2 \left(\frac{r_3}{r_2}\right)^{\frac{z-l_1}{l_2}} + (1-t)\left(\frac{r_3 - r_2}{l_2}(z - l_1) + r_2\right), \quad t \in \left\{0, \tfrac{1}{4}, \tfrac{1}{2}, \tfrac{3}{4}, 1\right\}.$$

(6.20)

The figure indicates that the shape of the flaring section of the horn is not important. Surprisingly, at $\mathcal{S} = 11.3$ Pa V^{-1} the on axis pressure is even larger at $f = 17$ kHz for a purely conical section than it is for the originally designed exponential design ($\mathcal{S} = 11.2$ Pa V^{-1}). This renders manufacturing of the horns considerably easier. The best performance at 17 kHz is obtained for $t = \tfrac{1}{2}$, although the sensitivity is only marginally better at $\mathcal{S} = 11.5$ Pa V^{-1}. The differences are not large enough, however, to explain the dissimilarity between the measurements and the simulations.
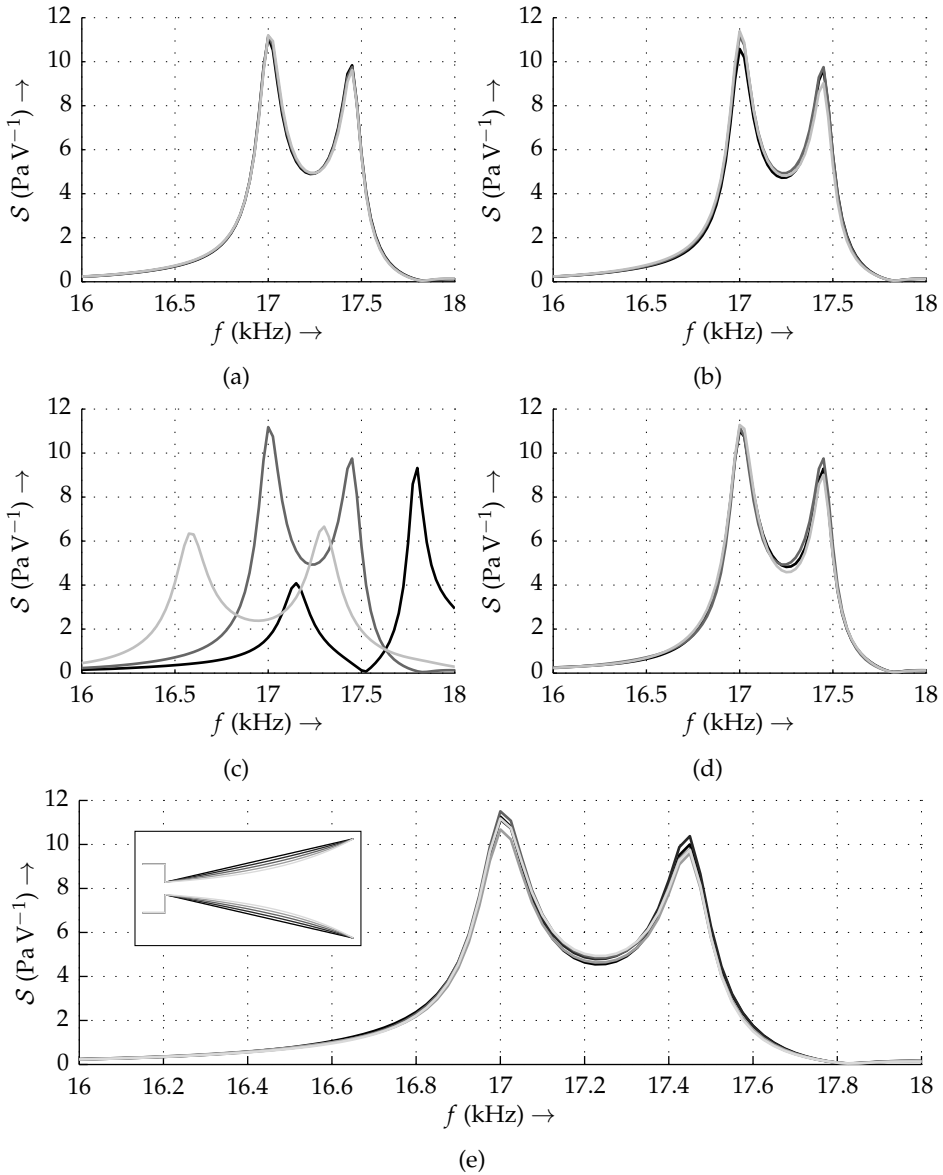
Figure 6.12   Parameter variation of r_2 (a), r_3 (b), l_1 (c), l_2 (d) is investigated by means of FE simulations of the sensitivity S at 10 cm distance from the transmitting horn mouth. The graphs correspond to: nominal value minus 4 % (black), nominal value (dark grey) and plus 4 % (light grey). The influence of the horn profile is shown in (e). It was varied between the original exponential and a conical shape.

Transducer losses

Figure 6.11 already gave a quick first glance at how transducer losses influence the characteristics of the stepped-exponential horn radiators. Understandably, the losses lower the sensitivity, owing to the fact that part of the energy is dissipated in the transducer, rather than radiated.

Figure 6.13 gives a better view of the influence of the transducer losses. The sensitivity indeed decreases when the losses increase. Since the mechanical quality factor Q_{m} of the transducer also decreases (see equation (4.34)), the sharpness of the resonance peaks decreases when the resistance is increased.

As said before, the sensitivity of the receiving horn and transducer match very well with the simulation results for $R'_{\mathrm{m}} = 190\,\Omega$, but those of the transmitting horn do not. They are still more than a factor two off. It is not possible to get both to match only by addition of transducer losses. These losses will therefore play a role in the discrepancy between measurements and model, but will not be the sole cause.

Interestingly enough, especially from figure 6.13b, it appears that the right peak, around 17.4 kHz, is damped much more by the transducer losses than the left one. This effect is much less pronounced for the transmitter (figure 6.13a).

Piezoelectric stress constant

Section 5.2 mentioned that, based on the relative permittivity of the piezoelectric material, it is probable that an incorrect material is used in the finite element model. Let us therefore have a look at how the piezoelectric stress constant influences the sensitivity of the horn drivers, and whether a wrongly chosen value in the FE model can cause the deviations seen in figure 6.11.

The finite element model uses PZT-5A as a piezoelectric material, as was indicated in the previous chapter. The PZT-5A material that is available in the material library in Comsol Mulitphysics has $e_{31} = -5.35\,\mathrm{C\,m^{-2}}$ and $e_{33} = 15.78\,\mathrm{C\,m^{-2}}$. Both values are changed in simulation to investigate their impact on the sensitivity. The 31-component is changed to $-2\,\mathrm{C\,m^{-2}}$ and e_{33} to $5\,\mathrm{C\,m^{-2}}$; first separately, then both components are changed simultaneously. The effect of e_{15} was already shown to be minimal, as one would expect from a bender element, and is therefore not considered.

Figure 6.14 depicts the sensitivity at a 10 cm distance from the horn mouth for these combinations of stress constants. Decreasing the stress constant leads to a lower sensitivity, as is to be expected, since it is the factor relating the stress to the electric field. Altering the stress constant also changes the resonance frequencies of the
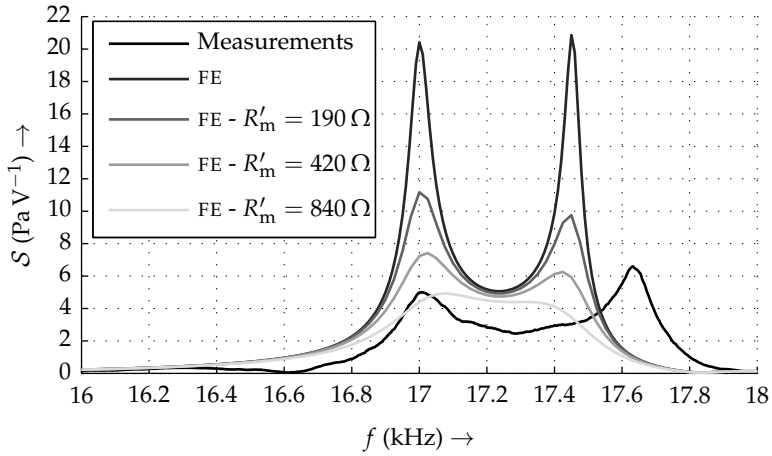
(a)
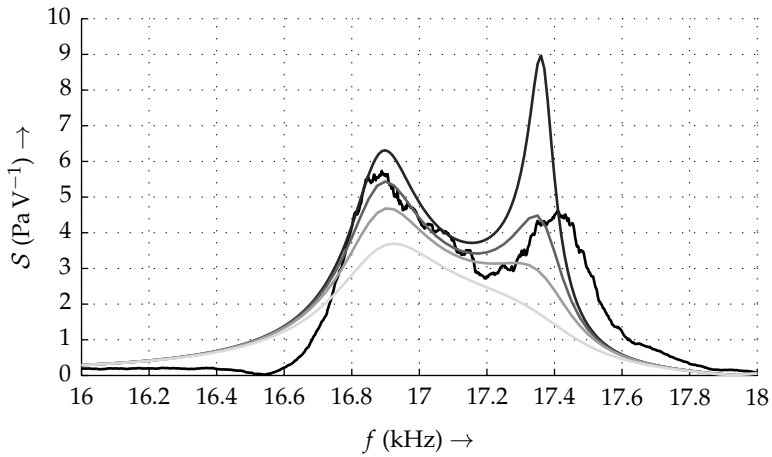
(b)

Figure 6.13 The sensitivity decreases for an increase in transducer losses, as is shown by these finite element simulation results. The sensitivities of the transmitting horn driver (a) and receiving horn driver (b) are shown separately.

Table 6.2 Resonance frequencies of the transducers that are used for component variation analysis.

Transducer	f_0 (kHz)	Transducer	f_0 (kHz)
1	17.0	6	17.1
2	16.8	7	17.0
3	17.0	8	16.8
4	16.8	9	17.1
5	17.0		

system, as is visible, most notably from figure 6.14a. The peaks distinctly shift to a lower frequency for lower stress constants.

Contrarily to the transducer losses, which also lower the sensitivity, as figure 6.13 indicates, the stress constant does not appreciably lower the quality factor in the way that the losses do. It is therefore perfectly reasonable to assume that the stress constant plays a role in the reduced performance of the horns in comparison to the FE simulations.

Component variation

Given the knowledge that the PX051 transducers that drive the horns vary quite substantially from transducer to transducer, the influence of their parameter variation on the sensitivity should be examined as well. To this end the on-axis pressure of the receiving horn is measured for nine different transducers. All transducers were selected on the basis of their resonance frequency f_0 lying in the vicinity of 17 kHz. The exact resonance frequencies are listed in table 6.2.

The sensitivities, again at 10 cm distance, are plotted in figure 6.15. It is immediately clear that there is a huge range of output, depending on the chosen transducer. The peak sensitivity can differ up to approximately a factor 3. Both the shape and the amplitude are subject to variation. The shapes and amplitudes of the sensitivities of transducers 2 and 3, those of 4 and 9, and those of 5 and 7 seem reasonably comparable. The value of the piezo transducer's resonance frequency, from table 6.2, seems to be of little influence, however.

The transducers are fixed to the horns by means of a thin aluminium plate, pressing them firmly against the horn mouth. This plate is fixed onto the horn by means of three M3 bolts, which can be seen in figure 6.9 if one looks closely. It is possible that the force with which they hold the transducer in place influences the performance of the horn driver as a whole. This hypothesis is investigated by fastening the bolts with various torques by means of a Torqueleader TBN2 torquewrench with a range
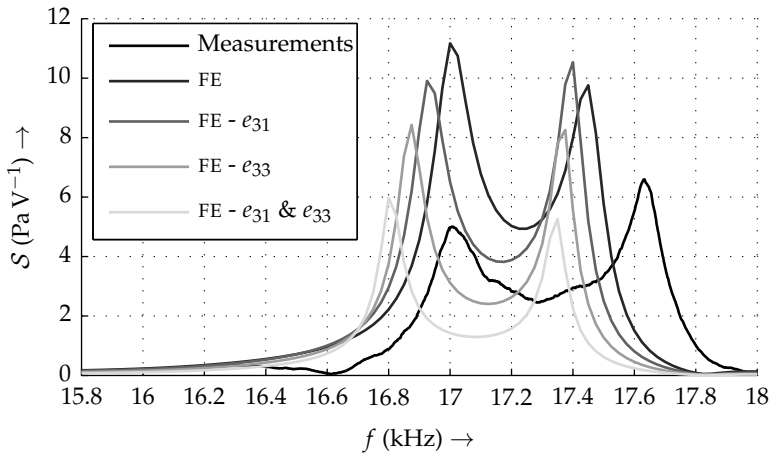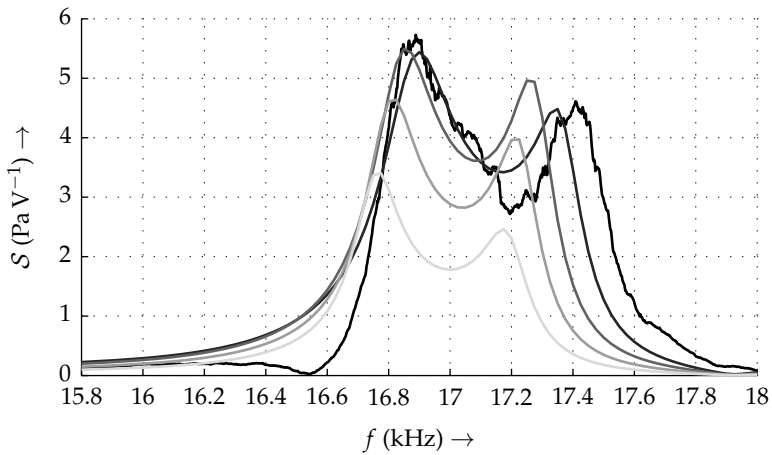
Figure 6.14 The piezoelectric stress constant e has a pronounced influence on the behaviour of both the transmitting transducer-horn combination (a) and the receiving set (b). The graphs show the measured sensitivities and FE simulations using PZT-5A material. The first set of simulations uses unaltered PZT-5A. For the second set e_{31} was changed to $-2\,\mathrm{C\,m^{-2}}$, the third set has $e_{33} = 5\,\mathrm{C\,m^{-2}}$, and the fourth uses both $e_{31} = -2\,\mathrm{C\,m^{-2}}$ and $e_{33} = 5\,\mathrm{C\,m^{-2}}$.
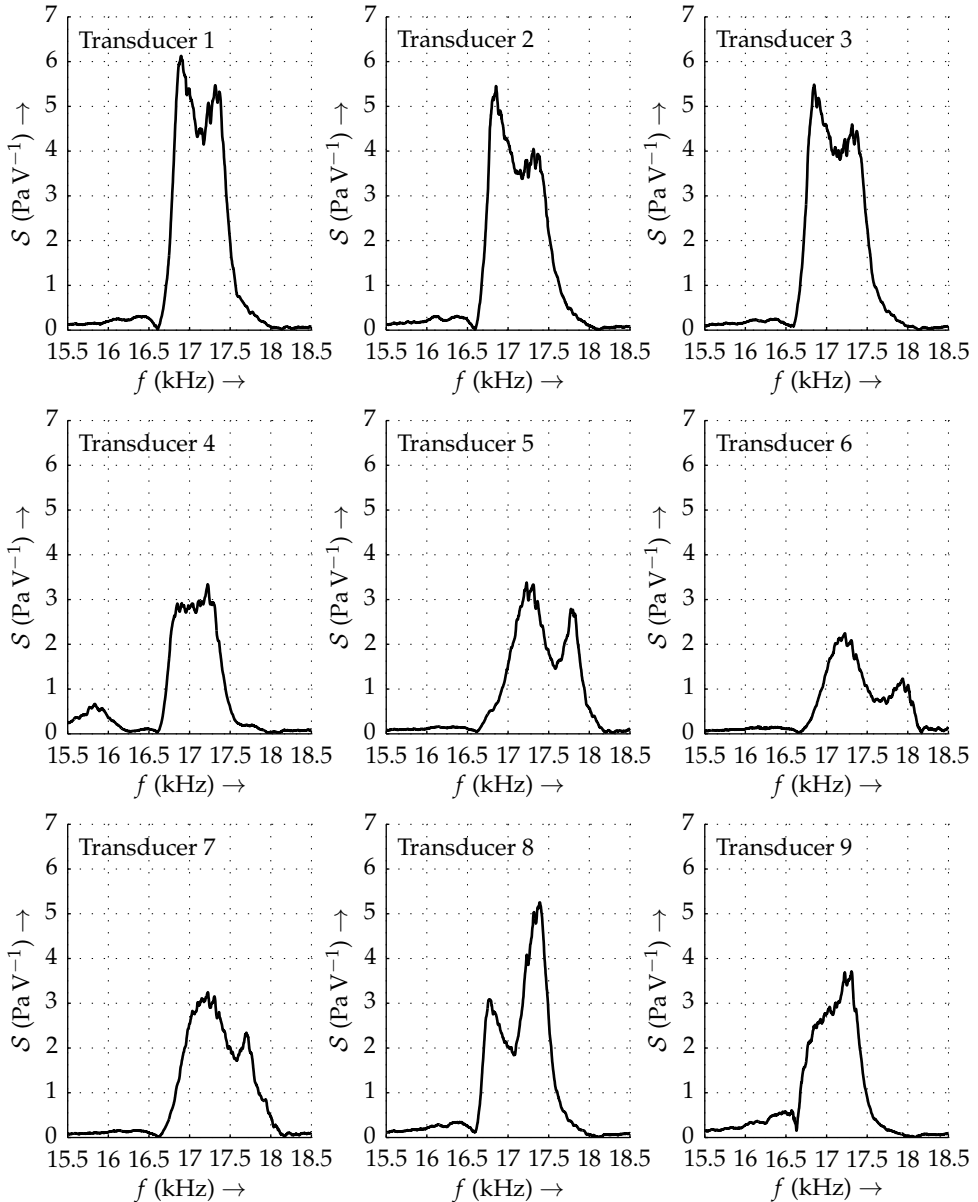
Figure 6.15 The sensitivity of the receiving horn $\mathcal{S}$ using nine different transducers shows the enormous influence that component variation of the driving element has on the output of the horns.
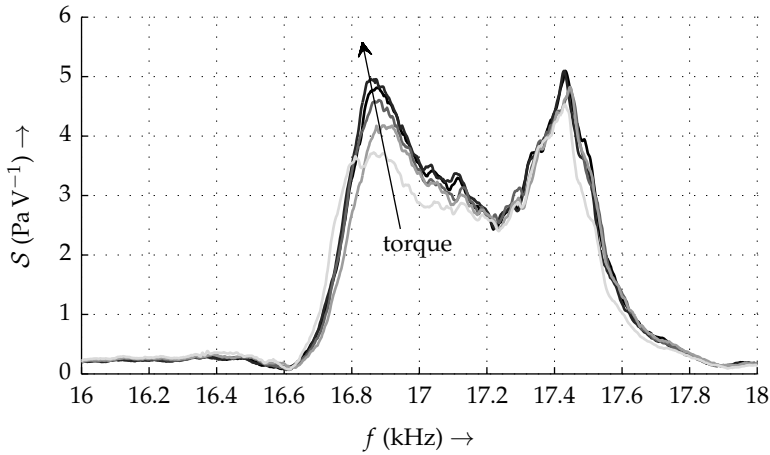
Figure 6.16   The sensitivity of the receiving horn-transducer combination is influenced by the tightening torque of the bolts that keep the transducer in place. The darker the line, the higher this torque.

of 0.2 to 2 N m. The sensitivity of the receiving horn driver is measured as before for a range of fastening torques. Figure 6.16 shows the results. The fastening torque indeed influences the sensitivity, and thus the characteristics of the horn driver. It is mostly the left resonance peak that is affected by tightening of the bolts. The peak not only increases in amplitude, but it also seems to move to a slightly lower frequency.

The results of figure 6.16 can explain the differences in figure 6.15 for a small part, but not completely, since the influence is not large enough to account for a factor 3 increase of the sensitivity. Although the bolts were not tightened using a torque wrench for the experiment of figure 6.15, the actual torque used will not have lain in so great a range as used in these experiments. Moreover, the output does not change considerably for the three highest fastening torques.

Temperature variation

From the horn parameter sensitivity analysis, we know that the most important parameter of the horn is the length l_1 of the first section. Its length is used for setting up a resonance condition, where the output greatly increases through reflections. Exactly like the effect described in the previous chapter, the wavelength plays a crucial part here. When the sound velocity changes, the frequency at which resonance occurs changes along with it. Now, the speed of sound in air is only affected by the temperature of the medium. The effect of all other parameters is

negligible [58]. Since the measurements in this chapter were done in a period were the maximum ambient temperature lay at $25\,°C$ or higher, let us choose this value as a reference value to investigate the influence of the temperature.

The equation of state for a perfect gas is, according to [58], equal to

$$p_t = \rho_t r T_K \tag{6.21}$$

with $r \approx 287.06\,\mathrm{J\,kg^{-1}\,K^{-1}}$ the specific gas constant and T_K the absolute temperature in Kelvins. Combination with (3.7b) allows the sound velocity to be written as

$$c^2 = \gamma r T_K$$
$$= c_0^2 \left(1 + \frac{T}{T_0} \right) \tag{6.22}$$

where c_0 is the sound velocity at $0\,°C$, T is the temperature in $°C$ and $T_0 = 273.15\,K$. From equation (3.7b), and the list of physical constants in A.5, we can calculate the sound velocity at $0\,°C$ to be $c_0 = 331.33\,\mathrm{m\,s^{-1}}$.

To obtain a resonance condition, the length l_1 of the first section of the horn must be approximately half a wavelength. Therefore we have

$$l_1 \approx \frac{1}{2} \frac{c_{20\,°C}}{f_{20\,°C}} = \frac{1}{2} \frac{c_{25\,°C}}{f_{25\,°C}} \,, \tag{6.23}$$

or

$$\frac{f_{25\,°C}}{f_{20\,°C}} = \sqrt{\frac{T_0 + 25\,°C}{T_0 + 20\,°C}}$$
$$\approx 1.00849 \,. \tag{6.24}$$

The horns were designed for a frequency $f_{20\,°C} = 17\,\mathrm{kHz}$, which implies that the shift in resonance frequency is $f_{25\,°C} - f_{20\,°C} \approx 144.3\,\mathrm{Hz}$. Suppose we would choose this to be equal to the $3\,\mathrm{dB}$ bandwidth, or, in other words, that only half the power is available at $17\,\mathrm{kHz}$ and $25\,°C$. In that case the corresponding quality factor is

$$Q = \frac{1}{2} \frac{17\,\mathrm{kHz}}{144.3\,\mathrm{Hz}} \approx 59 \,. \tag{6.25}$$

This is a very low quality factor for a piezoelectric transducer. It is therefore very probable that the temperature is a main contributor to the differences between the measurements and the modelled behaviour.

6.5   Conclusions and discussion

This chapter investigated the use of horns in an acoustic energy transfer system in an attempt to improve the energy throughput in such a system and to reduce the reflections that were shown to be of a large influence. First measurements using a simple nonoptimised horn design indicated that the addition of horns to an existing AET system has enough interesting effects to warrant a further investigation of their influence. Although they did not reduce reflections, they significantly improved the efficiency at greater distances because of the increased directivity of the transmitter and the enlarged surface of the receiver.

Stepped exponential horns were successively designed for the transmitter and the receiver of an acoustic energy transfer system to boost the output power and the energy transfer efficiency. The profile of these horns follows a stepwise change in radius, which is used to boost the throat impedance, followed by a section that flares out exponentially, whose purpose is the optimisation of the directivity of the transmitter and the surface of the receiver. Optimisation of the electrical output power was performed using a global optimisation algorithm in combination with a finite element model of the horns and the piezoelectric transducers.

Initial measurements of the energy transfer showed a significant deviation in power levels from those predicted by the finite element model. Losses in the transducers were therefore added to the model in the form of an equivalent resistance. This resistance alone proved not sufficient to explain the difference, as the measured power transfer and energy transfer efficiency were still much lower than simulations indicated. Still, the effect of the horns is evident, especially at greater distances between the transmitter and the receiver. At $z_d = 10.0$ cm—the distance between the transmitter and receiver for which the horns were designed—the addition of the horns results in an output power that is approximately 3.1 times higher while the efficiency is 7.5 times higher in comparison to measurements without horns.

Various possible sources of the discrepancy between the measured energy transfer and that predicted by simulations were investigated. Losses, as mentioned earlier, are a part of the cause, but it is shown in this chapter that they cannot solely make up for the difference. Bringing the simulated sensitivities of the transducers with horns down to the level of the measurement requires adding so high a loss resistance that resonance peaks completely disappear because of a much reduced quality factor.

It was shown that the piezoelectric stress constant can account for a large variation in output of the order of the observed difference. Unlike the transducer losses, this constant can bring the sensitivities down to the measured amplitudes, without compromising the resonance peaks. Taking into consideration that the piezoelectric material used in the transducers is unknown, and, moreover, already shown to be

different from the material used in simulation (see page 90), there is a fair chance that a large part of the discrepancies is to be attributed to an incorrect transducer model. Again, this goes to show that transducer identification is critical for AET system modelling, and must occur before designing impedance adaptation measures.

Not only are the materials of the piezoelectric transducers unknown, even the component variation between transducers proves to be a large problem. Swapping transducers makes a large difference, not only in output, but in frequency response as well. There is no discernable connection between the transducer's resonance frequency and the obtained sensitivity plot. It was even found that the same transducer could give a slightly different output when remounting. All in all, the poor reproducibility was ultimately the reason why the experiments were stopped.

Of all horn parameters, only the length l_1 of the first section of the horn has a distinct influence on the output. Reflections in this section greatly boost the impedance seen by the transducer. In hindsight this was not necessarily a good choice, as the system's sensitivity to parameter variation is enormous. Especially the combination with temperature variation will influence the output to a large extent. It was shown that a temperature rise of $5\,°C$ implies half the output power is obtained if the horn is coupled to a component with a quality factor of 59. It is therefore expected that the variation of this resonance frequency is one of the main contributors to the observed differences, although, unfortunately, this has not been verified.

It would have been better to investigate the impact of horns on the AET energy transfer using a length l_1 that is very short in comparison to the wavelength, as is conventionally done in horn loudspeaker systems [15]. The disadvantage in this case is that there is no resonance that can be used to boost the impedance, while the advantage is that there is no resonance that can cause mismatch problems. The stepwise change in radius can still be utilised for impedance transformation according to equation (6.2) in this case. If one does choose to work with multiple components that should resonate at the same frequency, adjustability of these resonance frequencies is a must.

Another principle that is used in horns for audio purposes is the addition of a phasing plug [15, 20], that equalises path lengths from different parts of the transducer diaphragm to the throat of the horn. At certain frequencies these path length differences, when unequal, can cause interference when the size of the diaphragm is of the order of a wavelength or larger. Sound waves from the edge of the diaphragm can then (partly) cancel those emitted from the centre. Possibly this leads to a decreased output when the resonance frequency changes. The finite element model did not predict the telltale notches in the frequency response that give away this problem. The principle was therefore not researched further.

A third principle used in horns for loudspeakers is the addition of a compression

chamber behind the diaphragm. Without it, the diaphragm experiences a large opposing pressure from the impedance transformation by the horn when it moves in the forward direction. When it moves backwards, however, it only has to counteract the free air radiation impedance. This can lead to nonlinearity, which in audio applications is of course extremely undesirable. Nonlinearity was found to be not an issue in the experiments so far. If the horns are to be used at larger output levels it may become necessary to add a compression chamber at the back of the transducer, which adds a stiffness component that counteracts this nonlinearity.

Lastly, it was shown that the profile of the section that flares out from a small radius r_2 to a larger horn mouth radius r_3 is not critical at all. A conical horn can be used instead of the chosen exponential shape without problems, and will even result in a higher sensitivity. Such a horn is much easier to manufacture when turning it form metal, just as the the horns in this chapter. It is not a particularly large problem though, as modern 3D printing technology can produce about any desired shape. Keep in mind that the sensitivity does not give any information about the directivity of the horn and the effect it has on reflections. Here an exponential section may still prove to be advantageous.

7

Experiments with bolt-clamped Langevin transducers

LOUDSPEAKERS make use of the high radiation resistance that the large surface of their diaphragms offers. The sound that would be produced by the voice coil alone would be barely noticeable, but the loudspeaker's cone can produce an impressive sound volume. The diaphragm couples the vibrations of the small voice coil to a considerable volume of air, making it a very effective method of impedance matching. This principle of impedance adaptation by means of a change in surface area can also be employed in acoustic energy transfer to match the transmitting and receiving transducers to the medium. It is used in this chapter in an attempt to increase the output power.

Let us suppose that we have a radiator that moves against a counteracting pressure. The force that it has to exert is equal to the product of this pressure and its surface area, $F = pA$. The pressure is, however, not constant, but is linked with the transducer's directivity, which increases with the radiating surface area. Therefore the radiation resistance grows faster than linearly with the surface area of the radiator. This can be seen in figure 4.3.

The experiments that have been discussed up to this point all leave something to be desired, mostly in terms of output power and efficiency, but also in terms of reproducibility. Different transducers are used in this chapter in an attempt to boost the output power and to increase the reproducibility. Bolt-clamped Langevin transducers (BLT) [125] were chosen for this purpose. These are 33-mode piezoelectric actuators, which are comprised of one or more piezoelectric rings, attached to a metal front and back mass that are used for tuning of the transducer's resonance frequency (see figure 7.1). This topology addresses a major issue of piezoelectric
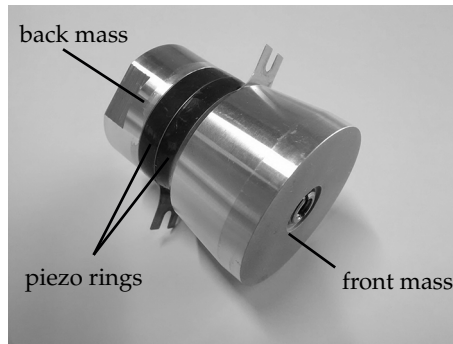
Figure 7.1   The Steiner & Martins SMBLTD45F40H transducers that are used in this chapter consist of two piezoelectric discs between an aluminium front and back mass, held together by a bolt that applies a prestress.

transducers, namely the low power handling capabilities of piezoelectric material. While these materials can stand compressive stress very well, they crack very easily under tensile stress. A bolt that connects the front and back masses is used to apply a prestress in the BLT topology, making it suitable for high power applications. Moreover, the transducer topology is typically very efficient if hard PZT material is used.

All experiments in this chapter make use of Steiner & Martins SMBLTD45F40H bolt-clamped Langevin transducers, a photograph of which can be seen in figure 7.1. Aluminium plates are bolted to the transducers to increase their radiating and receiving surface areas. Plates of various radii and thicknesses are used so that the influence of the plate dimensions can be investigated. The radius of a plate r is either 40 mm, 70 mm or 100 mm, while the thickness d can be 1 mm, 5 mm or 10 mm. A shorthand notation r/d is used in this chapter to indicate specific plates, e.g. a 70/10 plate would be of 70 mm radius and have a thickness of 10 mm. In the experiments, the transmitter and receiver were always fitted with the same plates.

This chapter discusses energy transfer measurements of the transducers with and without plates, as well as peculiarities that were encountered during the measurements.

7.1   Reflections

All previous measurements were done at a fixed driving frequency, while the distance between the transmitter and the receiver was varied. This is a logical approach,

as one wants to work at the frequency that provides the maximum output, but is not necessarily the most insightful. For example, the effect of reflections only becomes truly apparent when both the driving frequency and the distance between the transducers is varied. To illustrate this, an experiment was carried out where the Langevin transducers were mounted on the same linear motor setup that was used in earlier experiments. One transducer was attached to the mover, while the other remained stationary. The transducers were clamped at their rear mass by means of rubber o-rings, to minimise the influence on the transducers' vibrations. The ratio of output voltage amplitude V_{out} to input voltage amplitude V_{in} was measured by means of a Stanford Research Systems SR785 signal analyser. The transmitter was driven by a Toellner TOE7621-40 operational amplifier. The driving voltage amplitude was $V_{in} = 400\,mV$.

Figure 7.2 shows the measured voltage gain from transmitter to receiver in the (z_d, f)-domain, without plates (figure 7.2a), and in case both transmitters are fitted with the $r = 70\,mm$, $d = 5\,mm$ plates (figure 7.2b). The most distinct feature of these figures are the resonance frequencies of the system (and the transducers), which are visible as horizontal lines of high gain at a fixed frequency. Figure 7.2a shows a main resonance frequency of 40 kHz, and several resonance frequencies that yield a slightly lower output, e.g. at approximately 52 kHz, 70 kHz and 80 kHz. Figure 7.2b shows that the plates add a plethora of other resonances, mostly in the low frequency region up to approximately 55 kHz.

The voltage gain plots in figure 7.2 also nicely show the reflections between the transducers. In theory one would expect reflections to form hyperbolical lines (because of a constant wavelength) in the (z_d, f)-domain. Since the output at various frequencies is very different due to the high quality factor of the transducers, these lines are a bit harder to see, although they are quite discernable if one looks closely. The many resonance frequencies that the plates add in figure 7.2b help in this respect. The reflections almost form continuous lines in the frequency range of 30 kHz to 55 kHz. The theoretically expected locations of the reflection induced peaks, i.e.

$$f_r = \frac{nc}{2z_d}, \quad n \in \mathbb{Z},\tag{7.1}$$

are also drawn in figure 7.2 as dashed black lines. The sound velocity was chosen as $c = 344\,m\,s^{-1}$ for figure 7.2a and $c = 347\,m\,s^{-1}$ for figure 7.2b. Clearly, these lines match very well with the measurements.

The reader will undoubtedly have noticed the second set of reflections in figure 7.2b, which are indicated with the solid black hyperbolical lines. These are caused by the clamping discs that are used to attach the radiating plates to the transducer. Figure 7.3 shows that because these discs have a finite thickness $d_d = 3.5\,mm$, a second set of surfaces for reflection exist, a distance $z_d - 2d_d$ apart. Sound waves reflect from
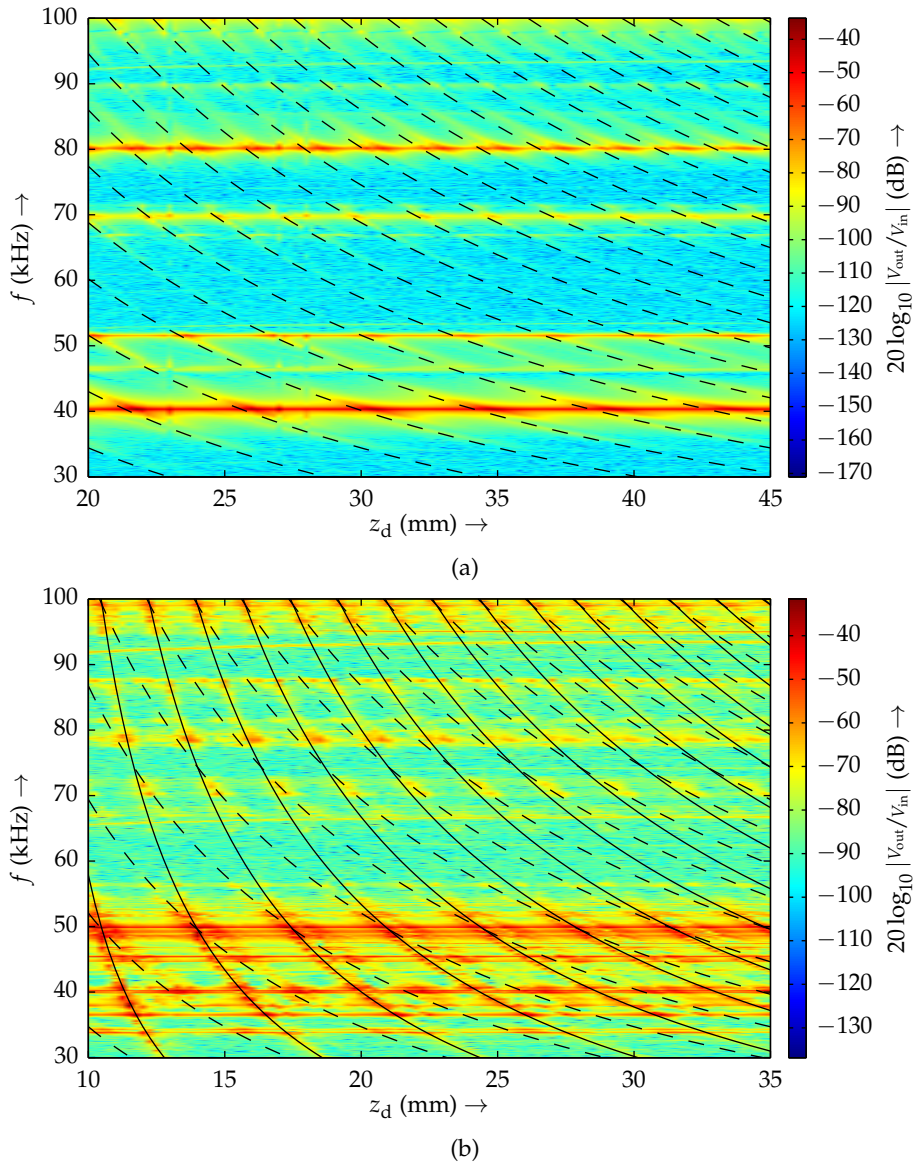
(a)

(b)

Figure 7.2 The voltage transfer ratio of receiver output voltage to transmitter input voltage as a function of the distance z_d between the two and the driving frequency for a system without plates (a) and with 70/5 plates (b). The expected location of the reflections in the (z_d, f)-domain is indicated by the dashed black lines. The solid black lines in (b) correspond to reflections between the discs that affix the plates to the transducers.
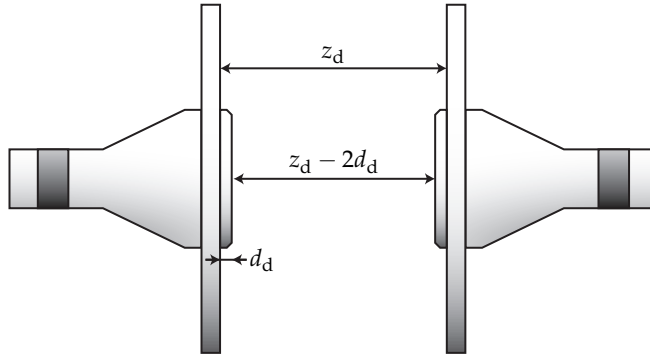
Figure 7.3   The distance z_d between the transducers is measured between their plates. Beside from the plates, reflections also occur from the discs that are used to attach the plates to the transducers.

these surfaces as well, thereby introducing a second resonance condition

$$f_{r,d} = \frac{nc}{2\left(z_d - 2d_d\right)}, \quad n \in \mathbb{Z}. \tag{7.2}$$

The solid black lines in figure 7.2b indicate that this is indeed the case.

7.2   Normal modes

Figure 7.2 not only shows reflections, but also predicts a minimal influence of the plates on the energy transfer. As one can see from the colour of the graph, the output corresponding to the reflections between the discs is much higher than those between the plates, by about 10 to 20 dB. It seems that the plates do not increase the output as expected, but that the majority of the radiation takes place from the centre part of the transducer-plate combination.

An explanation can be found in the vibrational modes of the plates, two examples of which are visualised in figure 7.4. At high frequencies, as the wavelength of the stress waves in the plates becomes comparable to the plate dimensions, the plates can no longer be considered to be rigid objects. The vibrations induce standing wave patterns on the surface of the plate. Its surface therefore moves with alternating zones of positive and negative displacement, thereby reducing the average displacement of the plate. As a result there is a large acoustic short circuit across the surface of the plate. This severely reduces the output of the plates when used as an acoustic radiator.
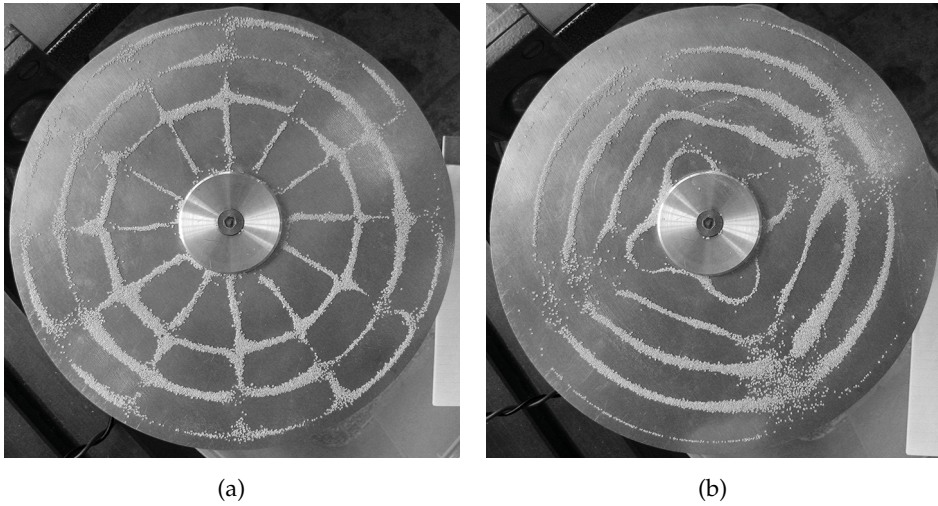
(a) (b)

Figure 7.4 Two of the normal modes of the 100/5 plate visualised using granulated sugar. The shown plate modes occur at 35.81 kHz (a) and 38.14 kHz (b).

The larger the radius and the thinner the plate, the lower the frequency at which the first mode shape appears. These modes of vibration are therefore very difficult to prevent at high frequencies. They can, however, be used advantageously, by adding a half-wavelength path difference to regions that vibrate with a 180° phase difference. This can be achieved by means of plates that have stepwise thickness variations [11, 36–39].

7.3 Load impedance

The optimal load resistance should be determined before the energy transfer is measured. Since it seems that the plates do not significantly contribute to the power transfer, the load resistance was determined for the case without plates. To this end, the voltage gain from transmitter to receiver $G = |\bar{v}_{out}|/|\bar{v}_{in}|$ was again measured as a function of frequency and distance using a Stanford Research RS785 signal analyser for various values of load resistance R_L (measured by means of a four wire resistance measurement and an Agilent 34461A digital multimeter). The normalised output power is then $\Pi'_{out} = G^2/R_L = \Pi_{out}/V_{in}^2$. The input voltage amplitude was $V_{in} = 400\,\text{mV}$.

It is assumed that the maximum output power lies in the 40 to 40.2 kHz range.
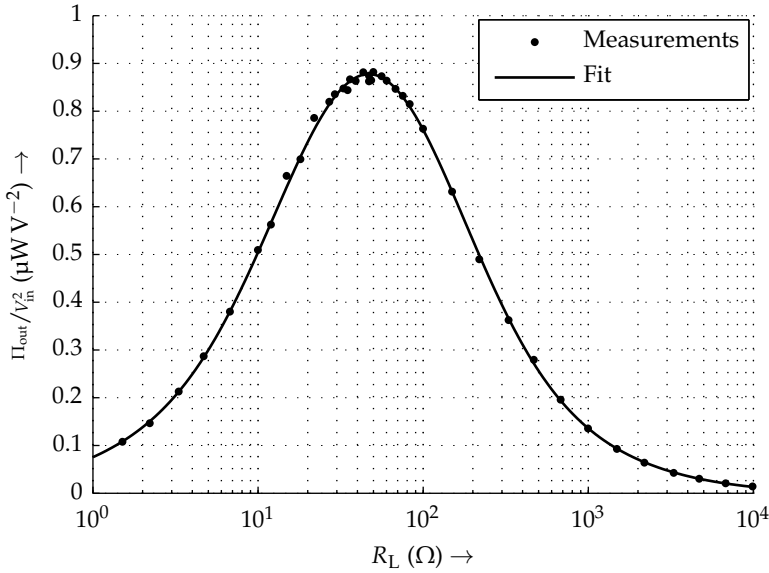
Figure 7.5   The measured normalised output power as a function of the load
resistance shows a distinct optimum. A double Gaussian function is
used to fit the optimal value.

The voltage gain was measured in this range with a frequency resolution of 1 Hz.
The distance between the transducers was varied between 20 and 45 mm to find
the maximum gain. This was repeated for every load impedance. The maximum
occurred at, or very close to 22.960 mm in each case, while the optimal frequency
varied slightly. The measured normalised output power as a function of load
resistance is shown in figure 7.5. The graph also contains a double Gaussian function

$$\Pi'_{\text{out}} = a_1 e^{-\left(\frac{\ln(R_{\text{L}})-b1}{c_1}\right)^2} + a_2 e^{-\left(\frac{\ln(R_{\text{L}})-b2}{c_2}\right)^2} \tag{7.3}$$

that was fitted to the measurement data for easy determination of the optimal load
impedance, which was found to be $R_{\text{L,opt}} = 46.8\,\Omega$. Further experiments are carried
out using a load resistance of $R_{\text{L}} = 46.988\,\Omega$.

The use of an inductance for the compensation of the piezo element's parasitic
capacitance (see section 4.2) is not necessary, as the reflected mechanical resistance
of the transducer must be smaller than $R_{\text{L,opt}}$, which is 46.8 Ω, and its capacitance
is $C_{\text{e}} = 3.41\,\text{nF}$, which at 40 kHz equals a reactance $X_2 = 1.17\,\text{k}\Omega$. The criterion of
equation (4.49) therefore tells us that compensation will not help increase the output
power. This was confirmed through measurements.

7.4 Comparison between plate dimensions

The measurements of figure 7.2b and the plate modes of figure 7.4 strongly indicate that the addition of radiating plates to the transducers does not have the desired effect of increasing the output power. However, this cannot be properly assessed based solely on voltage gain measurements, using a nonoptimally terminated receiver and a single plate size. It is necessary to look at more plate dimensions and to perform proper power measurements before conclusions can be drawn. The effectiveness of the plates will be judged in this section based on the maximum normalised power transfer that can be achieved with them.

The measurements of the voltage transfer in figure 7.2 show that the plates introduce many extraneous resonances to the acoustic energy transfer system. Moreover, the presence of reflections means that it is far from trivial at which frequency and distance the energy transfer is to be measured when one is interested in the maximum output power. It is therefore necessary to scan the entire distance and frequency domain. If the power transfer measurements were to be done in the same fashion as previous measurements, i.e. using an oscilloscope and a multimeter to determine the input and output power, the measurements would take an enormous amount of time, because of the high resolution that is required in both distance and frequency. Therefore it was chosen to measure the power by means of the signal analyser that was also used for the measurements of section 7.1. It again measures the voltage gain G, as well as the input voltage amplitude $|\bar{v}_{\text{in}}|$ and input impedance $\overline{Z}_{\text{in}}^{\text{e}} = \bar{v}_{\text{in}}/\bar{i}_{\text{in}}$ as a function of the driving frequency. The current i_{in} is measured using a Tektronix TCP312 current probe and TCPA300 amplifier. The output power Π_{out} and efficiency η are then found from

$$\Pi_{\text{out}} = \tfrac{1}{2} \frac{G^2 \, |\bar{v}_{\text{in}}|^2}{R_{\text{L}}} \tag{7.4a}$$

$$\eta = G^2 \frac{\left|\overline{Z}_{\text{in}}^{\text{e}}\right|^2}{R_{\text{L}} \, \text{Re}\left(\overline{Z}_{\text{in}}^{\text{e}}\right)} \,. \tag{7.4b}$$

Please note that these measurements assume that all measured signals (v_{in}, i_{in} and v_{out}) are sinusoidal. Therefore only small signal energy transfer behaviour can be measured. However, this was considered to be a good basis on which to compare the power transfer between plate dimensions. A driving voltage amplitude of $|\bar{v}_{\text{in}}| = 400\,\text{mV}$ was used for the measurements. The measurement method was first checked against power measurements with an oscilloscope and digital multimeter as used before. The maximum deviation between the two was found to be smaller than 3 %.

Finding the maximum output power for each plate size is far from trivial. It is sought based on the voltage gain G. As mentioned, the whole frequency and distance range must be surveyed with a high resolution. The analyser is used in FFT-mode (fast Fourier transform) with a chirp source to quickly scan the frequency domain. The distance is increased in 100 μm increments to find the maximum. It is assumed that the optimum lies between 30 kHz and 100 kHz, and at a maximum distance of 40 mm. Once the maximum is found, the input and output power are measured in a swept sine measurement in a $(100 \, \text{Hz}, 500 \, \mu\text{m})$ band around it. The results are shown in figure 7.6 for all plates of 40 mm radius, the 70/5 and 100/5 plates, and the case without plates. The measurement resolution in z_d is a bit low for the quality factor imposed by the reflections, but care was taken that the maximum output power lies on the chosen z_d measurement grid. The resolution therefore does not pose any problems in judging the maximum output power and the corresponding efficiency.

The measured output power levels indeed confirm the suspicion that the plates only degrade the system performance. The maximum output power without plates is at 4.0 μW the highest, only to be followed by the 40/10 plates at $\Pi_\text{out} = 0.26 \, \mu\text{W}$. The efficiency of these plates is better than that achieved by the bare transducers, but it must be pointed out that since the distance is measured between the plates, the extremities of the transducers are actually much closer together for the 40/10 plates, which can possibly explain this difference. The maximum efficiency is very low at 0.24 % for the transducers without plates because of the enormous impedance mismatch between the transducers and the medium.

7.5 Nonlinearity

The output power and efficiency were measured at a low input voltage amplitude in the previous section. Experiments revealed that increasing the input voltage to the transmitter leads to nonlinear behaviour of the AET system. It is not easily noticeable from electrical measurements, as the transducers function as high quality factor filters, but it can be observed as a slight distortion of the transmitter current. The nonlinearity is, however, very apparent from pressure measurements, such as can be seen for instance in figure 7.7 for a transducer fitted with a 70/1 plate. The higher the amplitude of the input voltage, the more the pressure is distorted by higher harmonics. In some cases subharmonics (harmonics of half the driving frequency) were encountered as well. It was asserted that the measured distortion was not due to the microphone measurement system.

Investigation of the nonlinear behaviour of the systems is best done based on
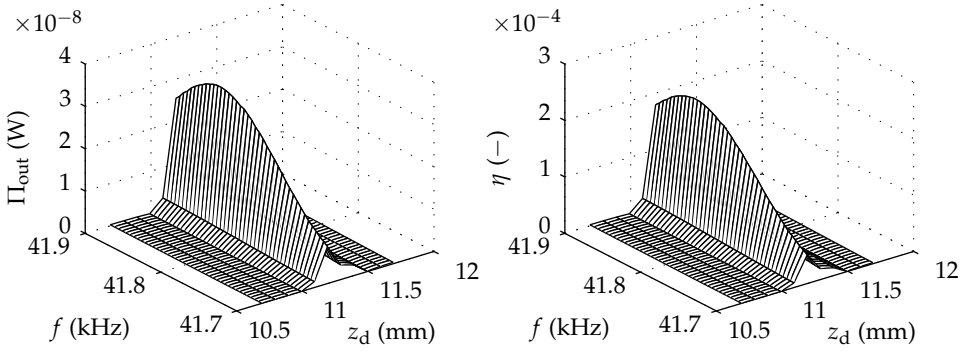
(a) $r = 40\,\text{mm}$, $d = 1\,\text{mm}$
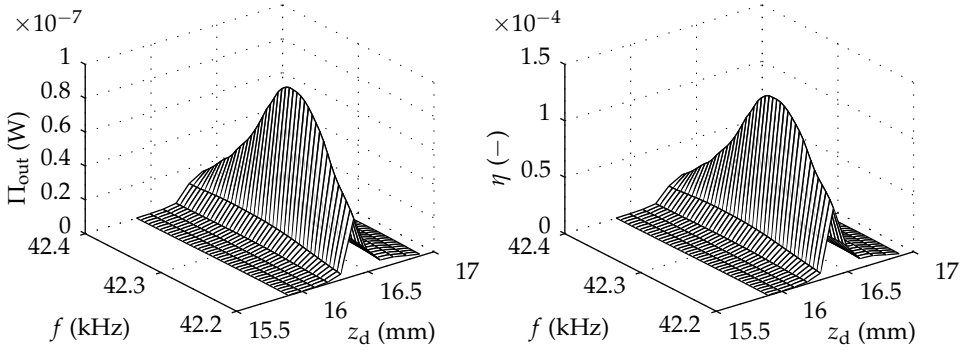
(b) $r = 40\,\text{mm}$, $d = 5\,\text{mm}$
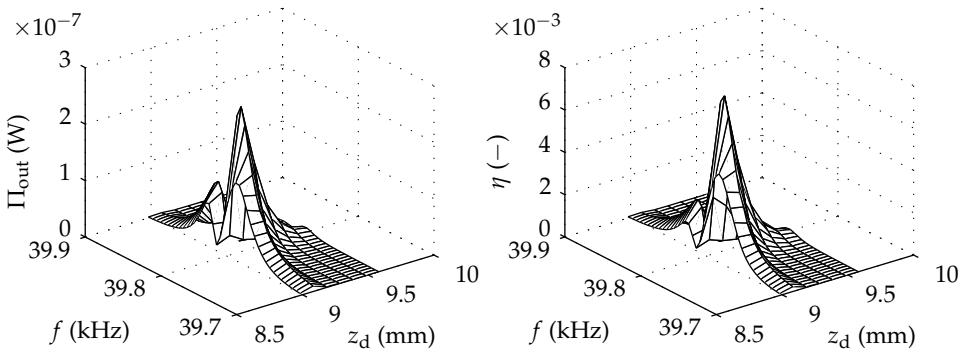
(c) $r = 40\,\text{mm}$, $d = 10\,\text{mm}$
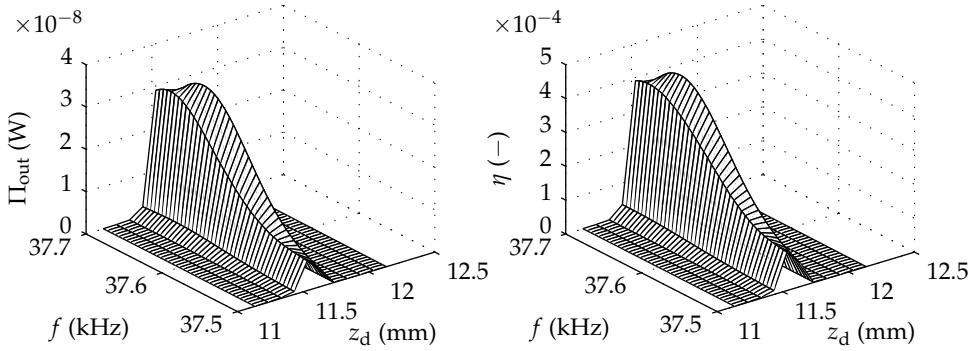
(d) $r = 70\,\text{mm}$, $d = 5\,\text{mm}$
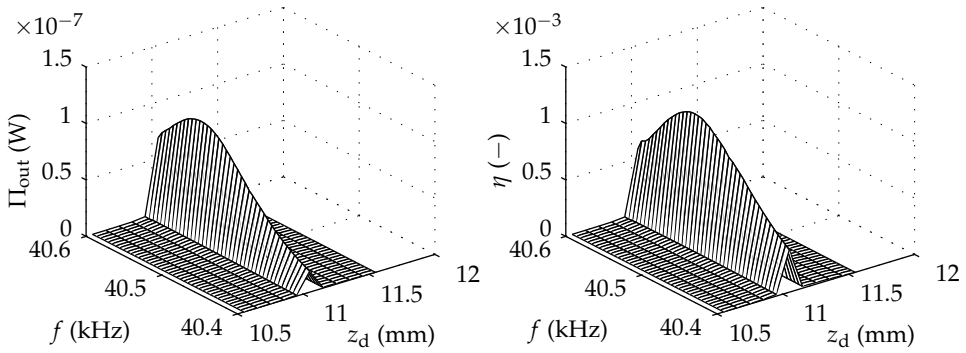
(e) $r = 100\,\text{mm}$, $d = 5\,\text{mm}$
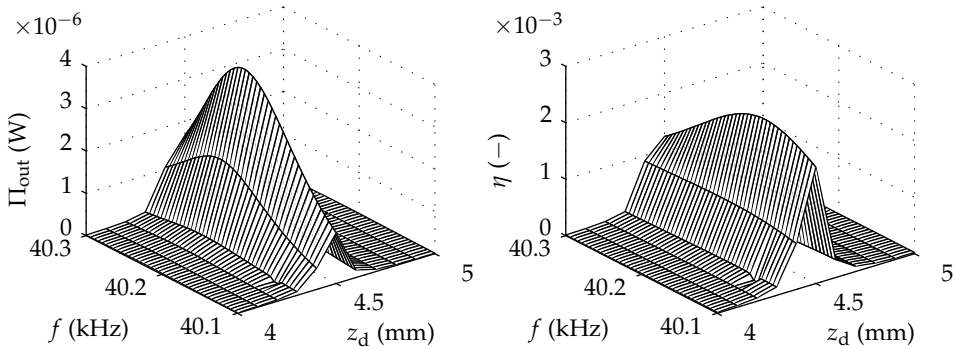
(f) Without plates

Figure 7.6 Output power Π_{out} and efficiency η, measured for various plate dimensions, around the point of maximum output power in the (z_{d}, f)-domain.
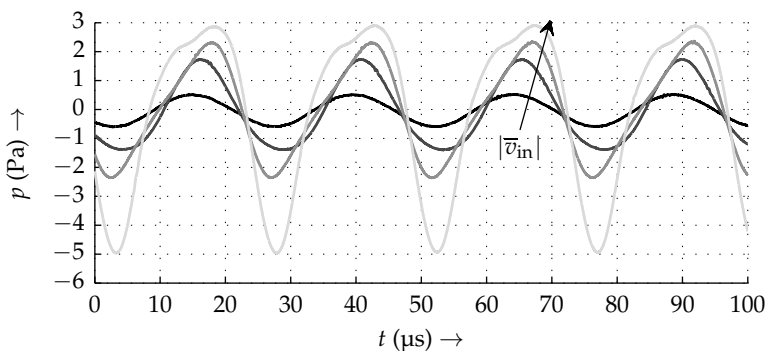
Figure 7.7 Typical examples of pressure waveforms of a Langevin transducer (in this case with 70/1 plate) show distortion that increases with the input voltage amplitude $|\overline{v}_{in}|$.

pressure measurements in the frequency domain. These give a clear picture of the harmonic content of the pressure generated by the transducer. Figure 7.8 shows the pressure produced by a Langevin transducer fitted with a 70/5 plate, which was selected because it nicely illustrates the whole range of nonlinear behaviour that was encountered. The pressure is again measured with a G.R.A.S. 40BF microphone, with 26AC preamplifier and 12AK power module. It was calibrated using a G.R.A.S. 42AA pistonphone. The pressure is measured at a distance of 400 mm on the transducer's axis. The microphone is connected to the Stanford Research Systems signal analyser, which is used in FFT mode. A driving frequency of $f = 42.75$ kHz is used, as it is very close to a major resonance frequency (42.8 kHz) and corresponds exactly to an FFT bin.

At very low input voltages, the pressure spectrum, as one would expect, only contains the fundamental frequency. As the input voltage grows, there is a distinct value of the input voltage amplitude, just shy of 16 V, where a second harmonic component appears. Increasing the input voltage further to 20 V gives us the earlier mentioned subharmonic components at multiples of half the fundamental frequency. At 24 V amplitude, all harmonics and subharmonics gain sideband components, while for even higher frequencies more and more sideband components appear. A sort of runaway, possibly thermal, seems to occur here: while all other components are introduced into the spectrum at distinct input voltages, the continuous sidebands come into existence gradually as the system seems to slowly settle into a steady state.

Measurements of the frequency spectrum of the driving voltage showed, beside the fundamental frequency, a second harmonic component. It is not present at an input voltage amplitude of 800 mV, while for all the other measurements it is 61 dB
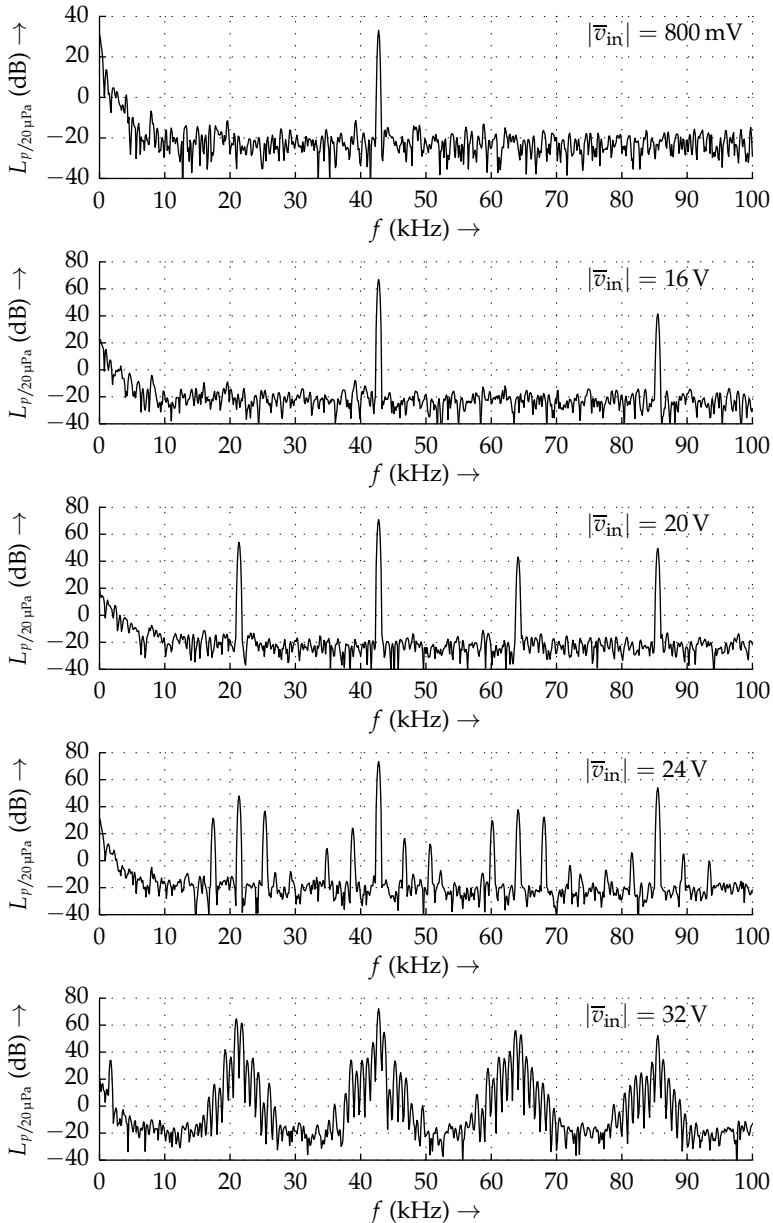
Figure 7.8 Chaotic behaviour is observed when the input voltage amplitude is increased. At first, harmonics and subharmonics appear, followed by spontaneous sidebanding. The sound pressure level was measured 400 mm in front of the transducer, which was fitted with a 70/5 plate.

to 68 dB smaller than the first harmonic component. Moreover, none of the other harmonic components in figure 7.8 are visible in the input voltage spectrum. It can therefore be concluded that the distortion is not introduced by the driving amplifier.

The behaviour that figure 7.8 shows, including subharmonics and spontaneous sidebanding, is sometimes encountered in loudspeakers [14, 29, 86, 95, 129]. Judging from publications on the topic, it seems that it is most commonly encountered in traditional voice coil topologies, where it is often attributed to nonlinearity of compliance components, although sometimes bending waves in the cone are mentioned as a cause. These nonlinearities introduce chaotic behaviour into the system, such as witnessed by the measurements that are shown here. It is therefore reasonable to assume that the nonlinearities are introduced by the transducer, especially since they also occur in the transducers without plates. It seems that the addition of the radiating plates only amplifies the effect. A first hypothesis is that the nonlinear behaviour is caused by the transducer's clamping bolt, which has the effect of a nonlinear compliance term due to its prestress.

7.6   Energy transfer

Since the plates do not have the desired effect, the energy transfer is henceforth investigated using bare Langevin transducers without any plates attached. Energy transfer measurements are carried out to investigate the dependency of the power transfer on the distance as well as the input voltage. The transducers that are used for the remaining experiments were cherry-picked to obtain the largest output power.

7.6.1   Variation of distance

One of the interesting features of a contactless energy transfer system, is how it performs when the distance changes. Therefore similar measurements as in figure 7.6 were performed, but now for a larger distance range. The measurement setup is exactly the same, apart from the different transducers that are used. Measurements are complicated by the nonlinearity of the transducers, necessitating the use of a low input voltage. The normalised power is therefore measured. This allows the results to be extrapolated to predict the energy transfer capabilities of similar transducers that are designed to have a linear response. Because of the low input voltage, the method of power measurement described in section 7.4 can be used.

The measured output power and efficiency are depicted in figure 7.9 as a function of the driving frequency f and the distance z_d between the transducers. The maximum
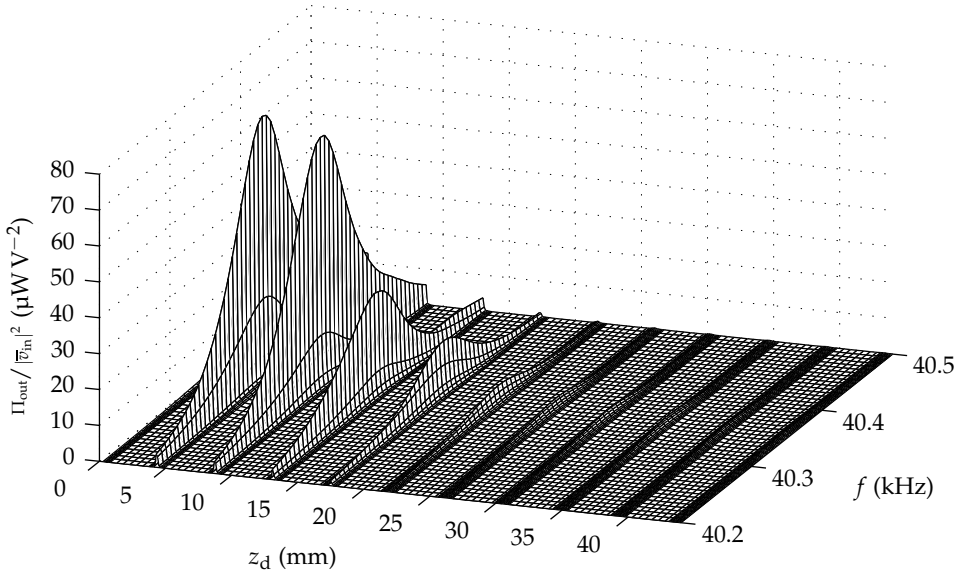
(a)
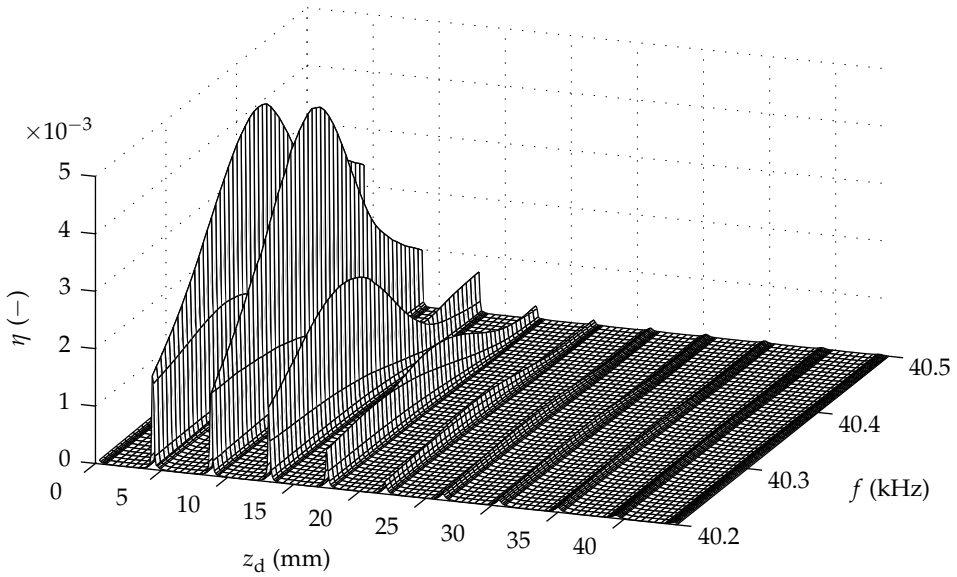
(b)

Figure 7.9 The measured output power Π_{out} (a) and efficiency η (b) decrease rapidly as the distance increases. The resolution in z_{d} is 100 µm in a band of 500 µm around peaks. The resolution elsewhere is reduced to 500 µm to enhance the graphs' clarity.

output power that was measured was 11.9 µW at an input voltage amplitude of 400 mV, corresponding to a normalised output power of 74.3 µW V^{-2}. This value is different from the maximum output power in figure 7.6f, as is the resonance frequency. This difference can be explained by the use of other transducers for these measurements. The maximum efficiency that was obtained in these measurements is very low, at $5.0 \cdot 10^{-3}$.

Figure 7.9 nicely illustrates the difficulty that lies in obtaining an output power and efficiency of any significance. The very large quality factors of the output power and the efficiency, both with respect to f (due to the resonance frequency of the transducer) and z_d (because of reflections), mean that very accurate frequency control and positioning are required. Comparing figures 7.9a and 7.9b, the quality factor of the efficiency with respect to the frequency is slightly lower than that of the output power. A slightly mismatched frequency is therefore less problematic in terms of efficiency than it is powerwise.

The reflections between the two transducers can not only be observed in the output power, but in the power fed to the transmitter as well. Therefore the electrical impedance of the transmitter must contain information about the distance between the transducers. Ideally, it could be used to determine the optimal distance between them. This information can then subsequently be used to position the transmitter so that the energy flow is at its maximum. Figure 7.10 depicts the magnitude of the input impedance $|\overline{Z}_{in}^e|$ of the transmitter as it was obtained in the measurements of figure 7.9. The reflections are visible, although the relative change in impedance is fairly small. The magnitude of the impedance is 9.1 % higher at the first peak at $z_d = 4.3$ mm, than it is halfway between the first and the second peak at $z_d = 6.5$ mm, both at the respective frequencies of maximum output power. This difference rapidly decreases for successive peaks in the direction of higher z_d.

7.6.2 Variation of input voltage

Despite the nonlinearity of the transducers limiting the power transfer, one can still measure the maximum power transfer capabilities of the acoustic energy transfer system as it is. Since the waveforms are in that case no longer sinusoidal, as section 7.5 showed, power measurement using a signal analyser gives incorrect results. Therefore the voltages and currents are measured using a LeCroy HDO6034 oscilloscope. The input voltage is measured directly at the transducer's terminals using a LeCroy ADP305 differential voltage probe. The current through the transducer is measured by means of a Tektronix TCP312 current probe and a TCPA300 amplifier. The delay of the current probe was compensated for in the measurements.

While the transducer's maximum voltage is specified as 500 V, the Toellner opera-
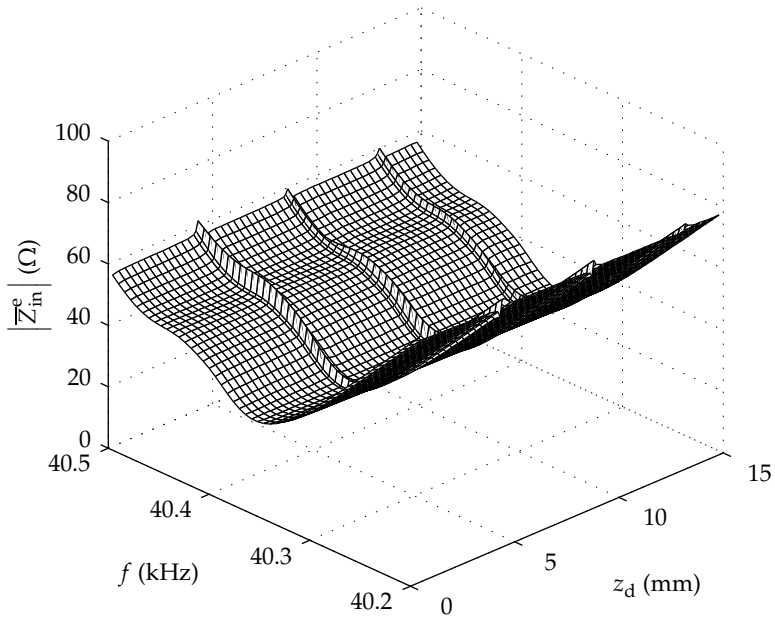
Figure 7.10   The reflections also have an effect on the magnitude of the transmitter impedance. The resolution in z_d is 100 µm in the direct vicinity of the power transfer peaks, and 300 µm elsewhere.

tional amplifier that drives it limits the voltage amplitude to 40 V. A transformer is therefore used to boost the input voltage to a maximum of 190 V.

The input power is calculated as the cyclic mean of the product of v_{in} and i_{in}. The output power is obtained from the RMS (root-mean-square) value of v_{out} and the load resistance. Contrarily to previous measurements, the cyclic mean and RMS value are determined in MATLAB, utilising the autocorrelation to find each signal's period.

Measuring at higher power levels means that the transducers heat up through dissipation. It became clear during measurements that this influences the resonance frequency of the system and the optimal distance between the transducers, as well as significantly decreases the output power. The system seems to reach a steady state after a while. It is likely that this is caused by the thermal characteristics of the transducers. A changing resonance frequency is a known nonlinear effect in piezoelectric materials, that is often attributed to large mechanical deformations and self-heating [8]. To limit the influence of self-heating as much as possible, measurements are done in short bursts.

The energy transfer is measured for different values of the input voltage amplitude. The measured output power and efficiency are shown in figure 7.11. The optimal frequency and distance were determined for each value of input voltage to reduce the influence of temperature, and possibly other nonlinear effects, as much as possible. The burst mode measurements seemed to help in this respect as the optimal distance, unlike for continuous measurements, was constant at $z_d = 4.340$ mm. The optimal frequency varied very slightly between 40.346 kHz and 40.354 kHz.

Figure 7.11a shows that the output power has a bending point around $|\bar{v}_{in}| = 50$ V, after which the output power increases approximately linearly. In a linear system one would expect the output power to increase quadratically with the input voltage amplitude. The efficiency in figure 7.11b initially drops very rapidly as the input voltage increases, but then falls off at an increasingly slower pace. Whether it reaches a steady state or not can unfortunately not be concluded from this graph. The maximum output power that was measured is 36.3 mW at an input voltage amplitude of 190 V.

7.7 Reproducibility

The reproducibility of the described measurements is a cause for concern, just as it was in previous chapters. It is investigated here based on the electrical impedance
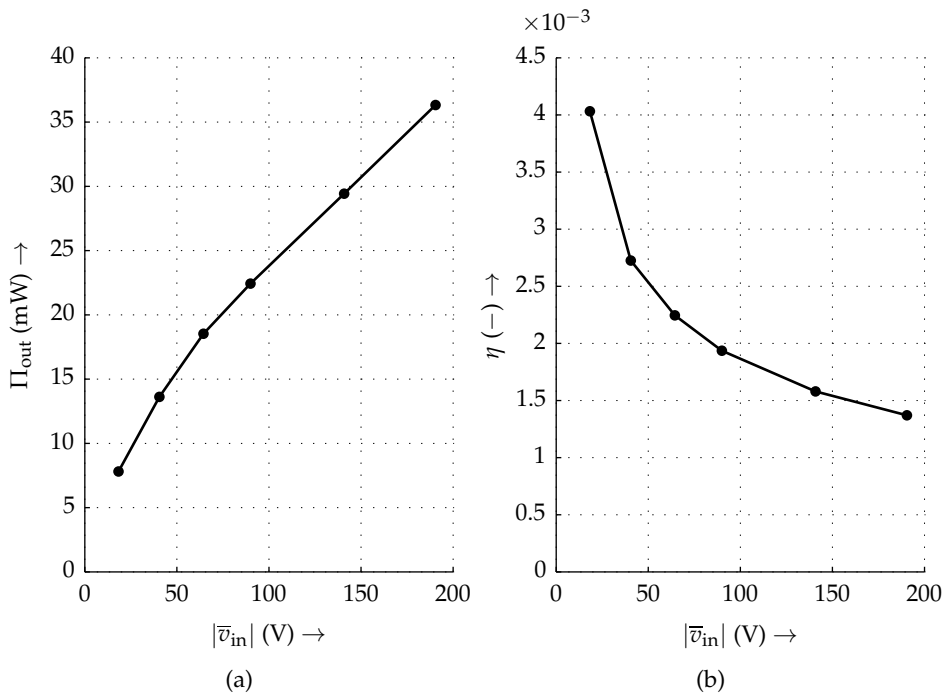
Figure 7.11   The output power Π_{out} as a function of input voltage amplitude $|\overline{v}_{\text{in}}|$ (a) increases approximately linearly after a bending point. The efficiency η (b) decreases rapidly.
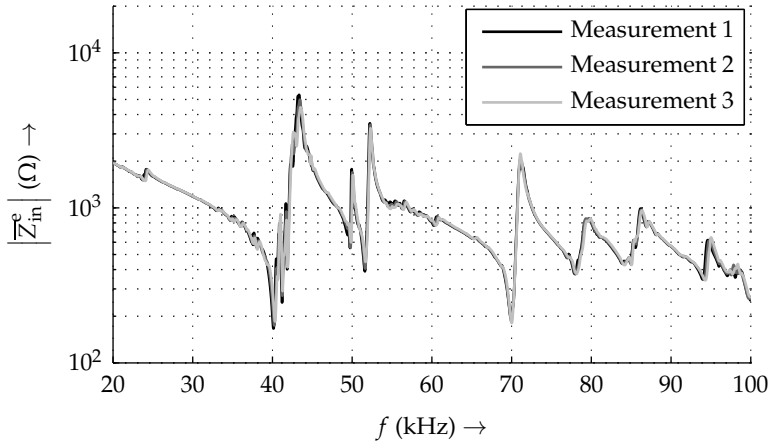
Figure 7.12 The magnitude of the transducer's electrical impedance shows very little variation when the plates are not removed between measurements. The transducer was fitted with a 100/1 plate.

$\overline{Z}_{in}^{e}$ of the transducer. Only the magnitude of the impedance is considered here. It is measured by means of an Agilent 4294A precision impedance analyser.

Impedance measurements of the transducers without plates have a good reproducibility. Impedance curves measured at different instances are virtually indistinguishable. The maximum deviation in the impedance magnitude is 4 %, while the average deviation is $2 \cdot 10^{-7}$. The reproducibility of impedance measurements with plates is, unfortunately, a bit of a different story. Large differences were seen between different impedance measurements of the same transducer with the same plate. Especially the plates of a thickness $d = 1\,\text{mm}$ proved to be problematic. Measuring the impedance multiple times without removing the plates, however, yields impedance curves that match up almost perfectly, as figure 7.12 shows. These impedance measurements were spread out over the course of hours to remove time dependency from the equation. Since these measurements were done with one of the most problematic plates, and the reproducibility issue is virtually nonexistent in these measurements, it must be caused either by the fastening torque of the screw with which the plate is bolted onto the transducer, or by the remounting of the plates.

The influence of the fastening torque T was investigated by remounting the plate a number of times, each time with a fixed torque, and measuring the electrical impedance. Figure 7.13 shows the results for a 70/10 plate. While there is some variation visible for a torque of $T = 1\,\text{N m}$, the impedance agrees much better for higher torques, although there is no complete match (see for example the resonances around 48 kHz and 82 kHz). The 100/1 plate has very different results, however.

Figure 7.14 depicts the impedance for the same three fastening torques. While the results match to some extent for $T = 1\,\mathrm{N\,m}$, the variation is drastically higher for higher torques. Many new resonances appear, and some move to another frequency.

Since the impedance measurements do not necessarily agree better when the plates are fixed with an equal torque, the problems regarding reproducibility must be caused by variation in the positioning of the plates. It turned out that the plates of 1 mm thickness are thin enough to move laterally in the thread of the screw that should hold them in place. The plate is therefore not automatically centred by the screw. This can easily result in very different behaviour, as it makes the transducer asymmetric. Possibly the 70/10 plates are centred better when the torque is increased, which would explain the greater consistency in results for higher fastening torques. At 1 N m both plates are very comparable. This is to be expected, as they are quite loosely attached to the transducer, so there is probably a reduced influence of the radiating plate.

The point to take away from this is that reassembly of the transducers is generally a cause of variation in measurement results, especially for thin plates. All measurement results given in this chapter are therefore a possible set of outcomes. This variation is only increased by the temperature dependency that was already discussed in section 7.6.2. It also shows that modelling of this system for design purposes would not have been very meaningful, as the behaviour in reality may be very different due to reproducibility issues, even if an initial model would show good agreement with measurement results.

7.8   Conclusions and discussion

This chapter set out to investigate impedance adaptation of transducers through enlargement of their radiating surface, in an attempt to reduce reflections, and particularly to increase the output power. Plates of varying radius and thickness that are attached to the transducers were chosen as a solution. Bolt-clamped Langevin transducers were chosen for their large power handling capabilities and their high efficiency. Unfortunately, initial voltage gain measurements indicated that the plates do not increase the output power. These measurements suggest that the largest part of the power is transferred between the centres of the transducers, and not between the plate surfaces.

A subsequent set of energy transfer measurements proves that the plates indeed do not increase the output power; the highest output power was obtained without the use of plates. Although the output power is lower for every plate size, the energy
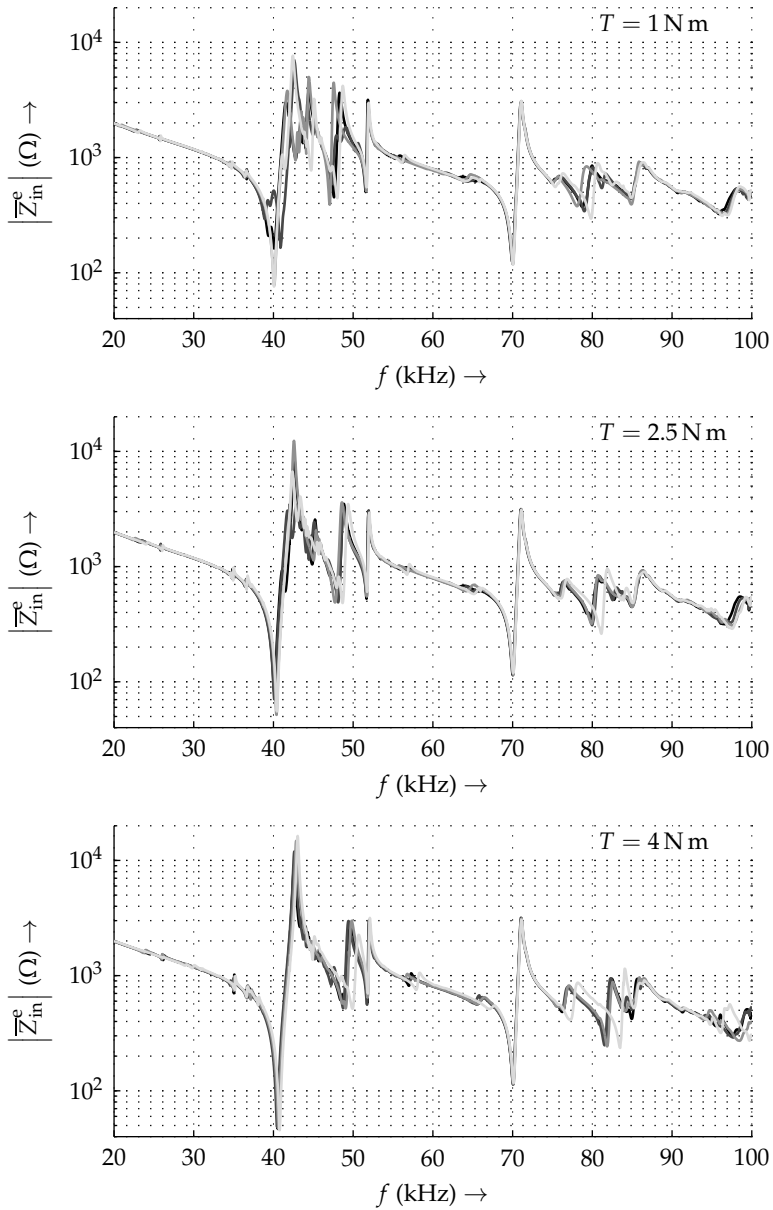
Figure 7.13 Measurements of the magnitude of the transducer impedance show the variation that occurs in remounting the plates. The 70/10 plate that is used for these experiments is fastened with a fixed torque of $1\,\mathrm{N\,m}$, $2.5\,\mathrm{N\,m}$ or $4\,\mathrm{N\,m}$.
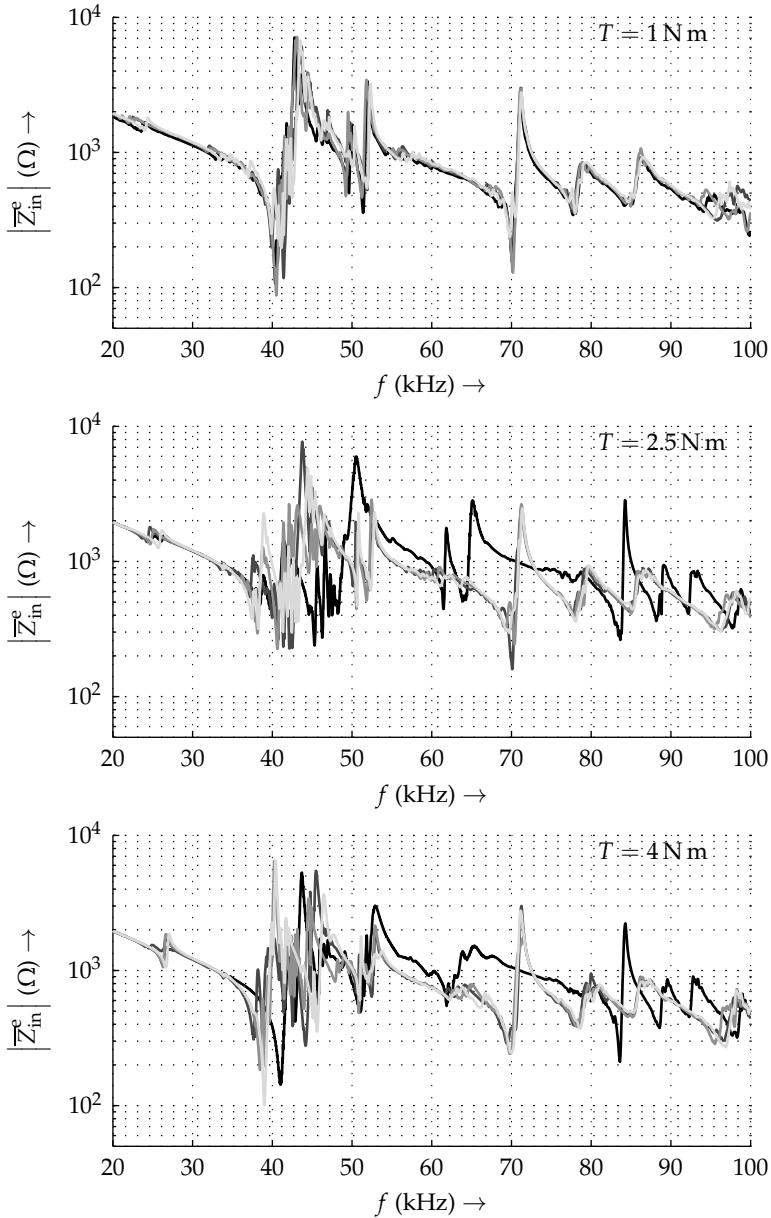
Figure 7.14   The 100/1 plates are subject to much more variation, judging from the transducer impedance. The screw attaching the plate to the transducer is again fastened with a torque of $1\,\mathrm{N\,m}$, $2.5\,\mathrm{N\,m}$ or $4\,\mathrm{N\,m}$.

transfer efficiency is slightly higher with the 40/10 plates attached. This is due to a smaller net distance between the transmitter and the receiver (2 mm, compared to 4.5 mm without plates), because of the discs that clamp the plates to the transducers.

The unsatisfying performance of the radiating plates as impedance matching devices is ascribed to the normal vibration modes of the plates. These result in a partitioning of the plates into small sections that vibrate with opposite phase, causing an acoustic short circuit that severely reduces the radiated power. At high frequencies it is very difficult to prevent these normal modes. It is possible, however, to use plates having local thickness variations, which negate the phase difference that the normal modes introduce.

Matters are complicated further by the nonlinearity of the transducers. It causes their performance at high power levels to significantly deviate from the expected sinusoidal behaviour. Harmonics and subharmonics appear at discrete input voltage amplitudes, and at a certain point spontaneous sidebanding occurs, indicating chaotic behaviour. The same phenomena have been observed in voice coil loudspeakers. Normally they are blamed on nonlinearity of the compliance of the loudspeaker suspension, or on diaphragm modes. It is possible that they are introduced in this AET system because of nonlinearity of the materials, or because of the pretension applied by the transducer's prestress bolt.

Because of the nonlinear behaviour, low power measurements of the energy transfer were done initially. The maximum output power that was measured is 12 µW at an input voltage amplitude of 400 mV. Extrapolation to a voltage of 500 V, which is the maximum voltage that the transducers allow, would yield an output power of $\Pi_{out} = 18.6$ W. Naturally, linearity of both the transducer and the air are assumed. The maximum efficiency that was attained in these measurements is $5 \cdot 10^{-3}$. This low value is a consequence of the very poor impedance matching of the transducers to the medium.

The measurements again illustrate the stringent requirements on the positioning of the transducers imposed by the reflections. The high quality factor that the reflections bring to the system means that a 100 µm displacement is accompanied by a 7 dB drop in output power. Therefore accurate positioning of the transducers is of paramount importance. If an AET system is to transfer any energy, it will be necessary to adjust the position of the transmitter depending on the location of the receiver. Since the distance between consecutive peaks is 4.3 mm for this system (cf. figure 7.9), a maximum variation of the transmitter position of 2.2 mm is required, which is quite acceptable. Information about the optimum position of the transmitter can possibly be obtained from the transmitter impedance, since it gives information about the location of the energy transfer peak. The difference in impedance between an output power maximum and minimum is 9 % at the first peak, making it quite

discernible, but for larger z_d it is barely detectable.

Measurements of the variation of the output power with input voltage revealed an approximately linear relation between the two for high values of input voltage, instead of the expected quadratic relationship. Consequently, the efficiency η decreases rapidly for higher input voltages. The maximum obtained output power is 36.3 mW at 190 V input voltage amplitude. From the measured normalised output power in figure 7.9a, one would have expected an output power of 2.7 W.

The reproducibility of measurement results was judged based on electrical impedance measurements of the transducers. While the reproducibility of these measurements was excellent when the bare transducers were measured, much variation was observed when radiating plates were attached to them. It was deduced through experiments that the most likely cause of this variation is the positioning of the plates with respect to the transducer. The problem seemed to be most prevalent with the plates of 1 mm thickness. These proved difficult to position symmetrically with respect to the axis of the transducer, causing many varying resonances.

Lastly, the experiments in this chapter show that the frequency of optimal power transfer varies not only with distance, but also with ambient temperature. It is therefore important to perform measurements both as a function of distance and frequency. Alternatively, a maximum power tracking algorithm can be used, so that the system always works at its optimal frequency.

Conclusions & recommendations

T HIS THESIS focuses on the contactless transfer of energy from an electrical
source to an electrical load, using sound waves that propagate through air as an
intermediate energy carrier. Its main purpose lies in providing an exploratory
overview of the subject, pointing out the features, opportunities and limitations of
the approach. It investigates a number of peculiarities of the system and describes
various paths that have been followed in the pursuit of optimised system perform-
ance. While the research has answered several questions, it has simultaneously
raised numerous new ones, paving the way—and leaving a couple of direction
signs—for further investigation.

This final chapter briefly summarises the most important conclusions of the work
that has been presented in this dissertation. Furthermore, it lists the main contribu-
tions of the research, and discusses several recommendations for future work on
acoustic energy transfer in air. AET being a quite new field, this list naturally is far
from exhaustive.

8.1   Conclusions

A theoretical limit to the efficiency of acoustic energy transfer has been derived,
based on a model that includes diffraction, attenuation and transducer losses. The
model indicates that, for a maximum transmitter and receiver diameter of 20 cm
and 1 m distance between the two, acoustic energy transfer has the potential to

perform at least 5 to 10 times better than an inductively coupled system of the same dimensions. Optimal electrical loading conditions were derived from this model, which indicate that the receiving element, unfortunately, has an efficiency of 50 % when maximum output power is desired.

The model on which the theoretical limit is based was validated through experiments, showing that energy transfer by means of sound waves is feasible. A maximum output power of 40 mW was demonstrated using piezoelectric transducers. In this case, the output power was limited by the mechanical breakdown of the transmitting transducer. The measurements revealed the occurrence, influence and importance of reflections. These create periodic maxima and minima of energy transfer and efficiency, spaced at half-wavelength intervals, and thus restrict the free placement of a receiving element. Transducer losses were identified from impedance measurements in vacuum, to allow a fair comparison between the measurements and the model. The measured efficiency corresponds very well to the theoretical limit at the first spatial resonance peak, but the decline in efficiency with the distance between both transducers proved to be greater in reality than predicted by the model. This is most likely due to the pressure and particle velocity distribution being altered drastically by the reflections.

Reflections have been modelled both analytically and numerically. The analytical model is based on a transmission line model, assuming plane waves. A lumped element attenuation coefficient accounts for the spreading of sound waves and the absorption in the medium. It is obtained from a circular piston radiator model and depends on the spatial coordinate. Because there are unknowns in the transducer model, parameter fitting is used to bring the model into line with measurement data. Results show a very good agreement between the two, but the obtained transducer parameters are nonphysical. Nevertheless, the results show that the model is not without merits. It is expected that simulation results deviate for distances that lie in the near field of the transducer, due to averaging of the pressure in this region in the calculation of the attenuation constant.

The numerical model describes reflections by means of multiphysical finite element analysis of the transducers in an air domain. Although it is able to predict the effect of reflections on the output power and efficiency, it is unable to do so accurately. The predicted output power is an order of magnitude too high and the variation of the input power with the distance between the two transducers is considerably different from the measurements. This is attributed to an incorrect model of the transducers. Sensitivity analysis identified the most influential parameters, but revealed no extreme sensitivity to changes in their values.

Stepped-exponential horns were designed, optimised and constructed as a means of impedance adaptation for both the transmitting and receiving transducers. Their

profile is comprised of a stepwise change in radius followed by a section that flares out exponentially. Resonance in the horn is used to greatly increase its throat impedance. The horns improved the output power by a factor 3.1, and the efficiency by a factor 7.5 at 10 cm distance between the transmitter and the receiver. The experimental results deviate significantly from the finite element model that was used for their optimisation. This discrepancy is likely caused by a combination of temperature variation, which detunes the horn's resonance frequency, an unknown piezoelectric material and component variation of the transducers. The exact profile of the flaring section was shown to be irrelevant for the output pressure.

Radiating surface enlargement has been investigated as a second means of impedance adaptation. It was applied to bolt-clamped Langevin transducers in the form of aluminium plates that are screwed onto the transducer. Nine different plate sizes were manufactured to investigate the influence of the plate dimensions. It was found that the plates do not increase the output power. This is due to their normal modes, which severely reduce the effective velocity of the radiator. Moreover, the transducers suffer from nonlinear behaviour, manifesting in harmonics, subharmonics and spontaneous sidebanding when the driving voltage is increased. Furthermore, problems were encountered with respect to reproducibility due to difficulty in coaxial placement of plates on transducers. The maximum output power that was measured (without plates), is 36.3 mW. Measurements showed the importance of measuring as a function of the frequency and the distance between the transducers. It was found that optimal positioning of the transmitter is possible based on its electrical impedance.

Essentially, acoustic energy transfer through air is possible. Achieved power levels are adequate for small systems such as sensors, MEMS, et cetera, but are insufficient for implementation in more power hungry applications such as actuators or wireless charging. The transducers are the restricting factor. Proposed models of AET are usable, but they require more research to become accurate enough for design purposes. Throughout this thesis, transducer modelling has been shown to be of critical importance for accurate acoustic energy transfer modelling, since it is the element that connects the electrical, mechanical and acoustic domains. Almost all uncertainty in models can ultimately be traced down to the transducer.

8.2   Thesis contributions

- **Introduction to a broader audience of acoustic energy transfer as a method of contactless transfer of electrical energy.** Contactless energy transfer by means of sound waves was already introduced in its most basic form in

1985 [19]. Unfortunately, it was never picked up as a serious contender to electromagnetic alternatives. The research done for this thesis and publications thereof have helped in bringing the subject to the attention of a broader audience [97].

- **Experimental validation of the principle of contactless energy transfer employing vibration of air as a means of energy transport.** Viability of the principle of AET has been shown through measurements of the electrical energy transfer by means of sound waves on a number of setups. A maximum electrical output power of 40 mW has been achieved.

- **Derivation of a theoretical upper limit to acoustic energy transfer efficiency** A theoretical limit to the efficiency of acoustic energy transfer has been derived. It is based on an analytical model of the energy transfer between two circular transducers, describing diffraction and attenuation losses. The losses in the transducers were estimated from their equivalent electrical circuits. Optimal loading conditions for the receiving transducer have been derived.

- **Analytically and numerically modelling the reflections that occur in an AET system.** Reflections have been shown to be a very essential characteristic of a typical acoustic energy transfer system. They generate a partial standing wave that restricts the placement of the receiver to distinct locations where the energy transfer and efficiency are high. Reflections are therefore of large influence on the energy transfer. This thesis presents two models of reflections: one based on transmission line theory, and the other a finite element model.

- **Design and optimisation of impedance adaptation measures.** Impedance mismatch has been identified as a major factor limiting the performance of an acoustic energy transfer setup. At the receiving side it introduces reflections, thereby limiting the absorbed power and introducing more losses, while a mismatch at the transmitting end limits the power transfer to the medium. Two methods of impedance adaptation have been investigated:

  - Resonant horn structures, comprising a stepwise change in radius followed by an exponentially varying radius profile. Horns have been designed and optimised for both the transmitting and receiving transducers. The energy transfer using these horns has been verified experimentally.

  - Acoustic impedance transformation for bolt-clamped Langevin transducers, consisting of aluminium plates of varying radius and thickness. A setup was built and measurements were done to verify the influence of the plates on the energy transfer, as well as identifying various effects that limit the energy transfer, i.e. nonlinearity and chaos, thermal characteristics and normal vibration modes.

8.3   Recommendations

No research is ever complete, unfortunately, and there is always room for improvement. Especially in a subject that is in its infancy, such as acoustic energy transfer, there is bound to be many a topic left untouched. Many ideas about new research directions, or how to improve results that have been obtained have formed during the course of the research. The most important recommendations are discussed in this section. Some of these have already been treated in the concerning chapters of this dissertation, but they will be repeated here for the sake of completeness.

Modelling   The models that have been presented in this thesis show many similarities with measurements, but generally they are unable to accurately predict the behaviour of the AET systems. A major factor in this respect is the validation of the separate parts of the model. For example, the transmission line model cannot be validated properly because the transducer model contains too many uncertainties. It is therefore advisable to construct models of the separate parts of the system (transducer, wave propagation, reflections), and validate them separately. Once they are found to be accurate enough the system model can be assembled and validated as a whole. In this thesis it was attempted to validate all models through measurements of electrical quantities only. It will be necessary to also measure mechanical quantities for proper validation. One can think of pressure measurements, or velocity profile estimation (for example by means of acoustic holography [4, 42, 83]).

Especially for the purpose of accurately modelling acoustic energy transfer, one should start with acoustic energy in its most basic form. Problematic factors should be eliminated as much as possible from the system, so that the basic mechanisms can be thoroughly researched and understood. One can think of circumventing the problem of reflections using a very small receiver, so that waves diffract around it and reflections are negligible. Other possibilities are using transducers that are sufficiently rigid, or do not vibrate at their normal modes but rather can be considered one-dimensional. This greatly facilitates their modelling and the complexity of their coupling with the medium. A last example is acoustic energy transfer through a wave guide, so that spreading losses can be taken out of the equation. Some of these choices will probably reduce the power level and efficiency, but will allow one to fully understand the system, and from there make choices about how to optimise it.

Transducers   Transducer design for acoustic energy transfer is a whole field of research in itself, or should at least become one in near future. All experiments in this dissertation made use of piezoelectric transducers, and not only this thesis; the use of piezoelectric transducers is prevalent throughout the field of acoustic energy transfer. The only example to date of the use of another type of actuator for AET

is [43], where an electromagnetic acoustic transducer (EMAT) design is evaluated. The authors concluded that piezoelectric transducers are better suited, under the restriction that they are well coupled to the medium. There is, however, no reason not to consider other actuator topologies, such as voice coil or ribbon loudspeakers, electrostatic topologies, magnetostrictive materials, et cetera. The advantage of piezoelectric materials is that they can be used at very high frequencies and high efficiencies. The frequencies used in this research however, are not extremely high (up to 40 kHz). Therefore, different transducer designs may be just as efficient. They can circumvent specific problems of piezoelectric components, such as having to use them at their resonance frequency for any output of significance. This thesis shows that these high quality factor resonances can be very problematic when they have to be matched.

During the research it gradually became clear that impedance matching is not by far as important for the transmitter as it is for the receiver. The underlying problem is depicted graphically in figure 8.1 for a set of bolt-clamped Langevin transducers. A poorly matched transducer implies a reflection coefficient close to one, and a very small transmission coefficient. A wave that arrives at the radiating surface of the transmitter mostly reflects, and only part is transmitted to the air, illustrated by the length of the arrows in figure 8.1. The reflected wave, however, stays confined to the geometry of the transducer. It will reflect from the back of the transducer and return to the radiating face. This is the resonance condition on the basis of which bolt-clamped Langevin transducers work. These reflections do not cause losses per se, as long as the material is relatively lossless. The wave that arrives at the surface of the *receiver*, on the other hand, mostly reflects off it, and only a small part continues as a stress wave in the transducer. The reflections from the receiver travel back to the transmitter, where they reflect again; A process that was amply discussed in chapter 5. As long as the directivity of the transducers is high, this will not cause severe losses, but as soon as diffraction comes into play, the efficiency degrades considerably due to spreading of the reflected wave. This shows that the impedance adaptation of the receiver is much more important than that of the transmitter. A very light receiver, such as a ribbon transducer or electrostatic loudspeaker, will be much more appropriate than a piezoelectric transducer in this case. This also illustrates that optimal designs for the transmitter and reducer may consist of entirely different topologies. The transmitter design should be focused on delivering high power, while the receiver design should focus on a low impedance transducer.

Besides a low impedance, the receiver will have to adhere to a specific design. Suppose a plane wave propagates towards a receiver, as in figure 8.2. Ideally, the ratio between the pressure p_1 and particle velocity u_1 at the face of the receiver is equal to Z_0^a, so that the wave does not reflect. If the receiver is much thinner than a

Figure 8.1   The transmission coefficient at the transducer-medium interface is very small for a poorly matched transducer. The wave that is reflected from the surface of the transmitter stays confined to the transmitter geometry and does not cause losses. The reflections on the receiver do cause losses due to absorption and diffraction.

wavelength, or it is sufficiently rigid, it will move the air at its back with a velocity $u_2 = u_1$. To do so, it has to exert a pressure of approximately $p_2 = Z_0^a u_2 = p_1$. Because the pressure and particle velocity are equal at the front and back face of the receiver, it does not extract any power from the wave, and the wave only passes through it. If it would absorb energy, p_1 would be larger than $Z_0^a u_1$, and the incident wave would reflect. For perfect matching—as well as for reasons of efficiency—it is therefore necessary to prevent the transducer from radiating a wave from its back face, essentially requiring the active sound intensity at the back of the transducer to be equal to zero. This can be accomplished in several manners, for instance:

- A vacuum at the back of the transducer, so that it cannot radiate, i.e. $p_2 = 0$. This can cause nonlinear behaviour because of an uneven loading at the front and back of the transducer.

- A closed back, creating a resonance chamber; in this case a standing wave pattern is created behind the transducer where p_2 and u_2 have a phase difference of 90°. Energy radiated from the back is in that case not lost, save for a small fraction that is dissipated because of damping in the air. This design can, just as with the horns, lead to problems with temperature variation, and should hence be used with caution.

- A fixed back, so that $u_2 = 0$. This requires the wave to be completely attenuated in the transducer material through extraction of its energy. It therefore does not work for a rigid transducer.

Designing specific transducers for AET will be the way forward. Transducers can be designed on the basis of desirable properties, such as a specified acoustic impedance, size, rigidity, resonance frequency, sensitivity, flexural modes, transformation ratio between mechanical and electrical quantities, and electrical characteristics (with respect to the power electronics that have to drive the transducer, respectively extract energy from it).
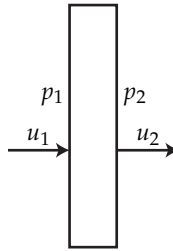
Figure 8.2 A plane pressure wave impinging on a receiver. The pressure in front of the transducer is p_1 and the particle velocity is u_1. The pressure and particle velocity at the back of the receiver are likewise p_2 and u_2.

Reflection models In chapter 5, the characteristic impedance Z_0^a of the transmission line was assumed to be constant. Since the wave propagation in the line is modelled as a plane wave, this is not a strange assumption. The true wave, however, is not a plane wave, and the characteristic impedance it experiences is not constant throughout the medium. The model can possibly be improved by calculating the impedance in the same manner as the lumped element attenuation constant.

It was assumed in the transmission line model that both the wave that emanates from the transmitter and the wave that reflects from the transducer follow the radiation pattern of a circular piston source. This may not be the case, especially so because the radiation pattern will change due to the pressure field that arises as a result of these reflections. Better results may be obtained by accurately modelling the radiation patterns of both the transmitted and reflected waves.

Horns As mentioned in chapter 6, using a resonance chamber in a horn can lead to considerable mismatch problems when using multiple high quality factor resonating systems (multiple transducers, horns, and a resonating air column in between). It is advisable to keep the length of the first section of the horn short in comparison to a wavelength. The corresponding impedance transformation step will be much lower, but there will likely be less influence of the ambient temperature, and therefore less problems in tuning the system. This will allow one to gain a better understanding of the effects at play.

A number of likely causes of the reduced performance of the horns have been indicated, the temperature mentioned above being one of them. Their influence should be investigated through a series of experiments to pinpoint the main cause.

Regarding the design of the horns, it is wise to incorporate a phasing plug to prevent wave cancellation originating from path length differences from the tranducer's radiating surface to the throat of the horn. A compression chamber can be added to

the back to increase linearity. Although this has not been found to be a problem, it may become one when power levels are increased.

Possibly horns can be used advantageously in a hybrid impedance matching topology, where the first step is obtained by means of matching layers, and a second step through application of a horn. Matching layers can be used very well for high to medium-high impedance steps, but are ill-suited for low impedance media (see section 5.3). Horns, on the other hand, are best used for the medium to low impedance step, since they always perform the last step, down to the impedance of the radiating medium. Using this solution they do not have to bridge the entire impedance gap between the transducer and the medium.

Diaphragm design   Normal modes make radiation from a diaphragm inefficient. They are therefore best avoided. This can be challenging when high frequencies and a large radiating surface are amongst the requirements. While in loudspeaker design it is not uncommon to use dissipative diaphragm materials, so that modes are damped [20], this is not a viable option for acoustic energy transfer, as it adds to the losses of the system. A diaphragm hence must be as rigid as possible. Great improvements over the flat plates that were used in chapter 7 can be obtained by using a cone shape for example (as is used in loudspeakers), by using a stiffer material or by dividing the radiating surface into smaller segments by means of a transducer array. Alternatively, the flexural modes can be used advantageously, since the transducers operate at a single frequency. Gallego-Juarez *et al.* designed high efficiency, high directivity transducers where a plate of stepped thickness cancels the phase difference in the radiation due to the plate's normal modes [11,36–39]. These will certainly be useful for AET as a transmitter design.

General considerations   Quite a few problems that had to be dealt with during this research were linked with finite element analysis. They mostly were caused by high quality factor resonances. A small change in mesh parameters can in such a case shift the resonance frequency by several Hertz, which can drastically alter the output of the simulation. Low efficiency systems, such as AET, are also difficult to simulate since the output power can often be of the same order of magnitude as the error in the simulation. It is therefore advisable to decouple the simulation into separate parts, e.g. a transmitter, wave propagation and a receiver. This will improve the accuracy of the simulations. Care should still be taken in matching different resonance frequencies.

On the same topic, when designing a setup, one should make sure that a resonance frequency is adjustable, or a lower quality factor should be used. While this possibly comes at the expense of maximum efficiency and output power, when taking component variation and model inaccuracy into account the power transfer and

efficiency will likely be higher.

All acoustic energy transfer systems that were discussed in this thesis suffered from much higher spreading losses than attenuation losses. In such a case it is beneficial to consider focusing, or diffraction-free beam patterns, as they improve the directivity of the transmitter. They improve the efficiency, especially for larger distances. For very high frequencies the effect will be less pronounced, as in that case spreading losses decrease and absorption losses rise. Phased array transducers can be used to this end, for example capacitive micromachined ultrasonic transducers (CMUT) [67], or piezoelectric transducer arrays such as used in medical ultrasound applications [22]. A phased array has the added advantage of beam steering, which is necessary when the location of the receiver is *a priori* unknown. For large output power one could consider a design consisting of a large surface area filled with small transducers. A possible difficulty lies in tuning all transducers to the same resonance frequency.

One goal of impedance adaptation is to prevent reflections, so that the position of the receiver can be chosen freely, instead of being restricted to multiples of half a wavelength. If all impedance adaptation measures fail, one can opt to adjust the distance between both transducers mechanically to obtain the maximum output power. The required distance variation is of the order of a couple of millimetres for kilohertz waves, which is easily achieved (4.3 mm at 20 kHz, for instance).

Lastly, measurements should preferably be performed at a constant temperature, since the optimal distance (due to reflections), changes as a function of sound velocity, and therefore temperature.

A

Symbols and notation

A.1 Symbols

Symbol	Quantity	Unit
A	Surface area	m^2
B	Magnetic flux density	T
$\mathcal{B}$	Adiabatic bulk modulus	Pa
c	Sound velocity	$m\,s^{-1}$
	Elastic constant	Pa
c_p	Isobaric mass heat capacity of air	$J\,kg^{-1}\,K^{-1}$
D	Electric displacement field	$C\,m^{-2}$
e	Piezoelectric stress constant	$C\,m^{-2}$ or $N\,V^{-1}\,m^{-1}$
E	Electric field	$V\,m^{-1}$
f	Frequency	Hz
F	Force	N
i	Current	A
I	Instantaneous sound intensity	$W\,m^{-2}$
k	Angular wave number	m^{-1}
l	Length	m
m	Horn flare constant	m^{-1}
p	Pressure	Pa
Q	Quality factor	$-$
	Volume velocity	$m^3\,s^{-1}$

Symbol	Quantity	Unit
$\mathcal{R}$	Reflection coefficient	—
$\mathbb{R}$	The set of real numbers	$\star$
S	Strain	—
$\mathcal{S}$	Transmitter sensitivity	$\mathrm{Pa\,V^{-1}}$
T	Stress	Pa
u	Particle velocity	$\mathrm{m\,s^{-1}}$
v	Voltage	V
W	Work	J
z_d	Distance between transmitter and receiver	m
Z^a	Acoustic impedance	$\mathrm{N\,s\,m^{-3}}$
Z^e	Electrical impedance	Ω
$\mathbb{Z}$	The set of integers	$\star$
α	Absorption coefficient	$\mathrm{m^{-1}}$
ε	Permittivity	$\mathrm{F\,m^{-1}}$
η	Energy transfer efficiency	—
ξ	Particle displacement	m
κ	Thermal conductivity	$\mathrm{W\,m^{-1}\,K^{-1}}$
λ	Wavelength	m
μ	Viscosity	$\mathrm{kg\,m^{-1}\,s^{-1}}$
Π	Power	W
ρ	Density	$\mathrm{kg\,m^{-3}}$
ω	Radial frequency	$\mathrm{s^{-1}}$

A.2   Subscripts and superscripts

Subscript	Quantity
a	Active sound intensity
att	Attenuation
c	Cutoff
dif	Diffraction
e	Pertaining to the electrical domain
L	Load
m	Mouth
	Pertaining to the mechanical domain
p	Point source
r	Received
t	Throat
	Total

Subscript	Quantity
tr	Transducer
x, y, z	Component in x, y or z direction
0	Equilibrium
	Offset
	Source amplitude

Superscript	Quantity
a	Acoustic
e	Electrical
E	Value for constant electric field
S	Value for constant strain

A.3   Notation

Operator	Quantity
$\bar{a}$	Complex representation
$\vec{a}$	Vector
$\hat{a}$	Unit vector in the direction of $\vec{a}$: $\hat{a} = \vec{a}/\|\vec{a}\|$
$\vec{a} \cdot \vec{b}$	Dot product of vectors $\vec{a}$ and $\vec{b}$
$\vec{a} \times \vec{b}$	Cross product of vectors $\vec{a}$ and $\vec{b}$
∇a	Gradient of a
$\nabla \cdot \vec{a}$	Divergence of $\vec{a}$
$\nabla \times \vec{a}$	Curl of $\vec{a}$
$\mathrm{Re}(\bar{a})$	Real part of $\bar{a}$
$\mathrm{Im}(\bar{a})$	Imaginary part of $\bar{a}$
$\bar{a}^*$	Complex conjugate of $\bar{a}$
$|\bar{a}|$	Absolute value of $\bar{a}$
$\|\vec{a}\|$	Euclidian norm of $\vec{a}$

A.4   Acronyms

Acronym	Meaning
AC	Alternating current
AET	Acoustic energy transfer

Acronym	Meaning
BLT	Bolt-clamped Langevin transducer
CET	Contactless energy transfer
CMUT	Capacitive micromachined ultrasonic transducer(s)
DC	Direct current
EM	Electromagnetic
EMF	Electromotive force
FE	Finite element
FFT	Fast Fourier transform
MEMS	Microelectromechanical system(s)
PZT	Lead zirconate titanate
RF	Radio frequency
RMS	Root-mean-square

A.5 Physical constants

Constant	Value		Unit	Quantity
c	3.4326	$\cdot\,10^2$	$\mathrm{m\,s^{-1}}$	Sound velocity at $20\,°\mathrm{C}$
c_{EM}	2.9979	$\cdot\,10^8$	$\mathrm{m\,s^{-1}}$	Speed of light in vacuum
c_{P}	1.005	$\cdot\,10^3$	$\mathrm{J\,kg^{-1}\,K^{-1}}$	Isobaric mass heat capacity of air at $20\,°\mathrm{C}$
p_0	1.01325	$\cdot\,10^5$	Pa	Atmospheric pressure
Z_0^{a}	4.1332	$\cdot\,10^2$	rayl	Characteristic impedance of air at $20\,°\mathrm{C}$
γ	1.400		—	Ratio of specific heats of air
ε_0	8.8542	$\cdot\,10^{-12}$	$\mathrm{F\,m^{-1}}$	Permittivity of free space
κ	0.0257		$\mathrm{W\,m^{-1}\,K^{-1}}$	Thermal conductivity of air at $20\,°\mathrm{C}$
μ	1.8369	$\cdot\,10^{-5}$	$\mathrm{kg\,m^{-1}\,s^{-1}}$	Viscosity of air at $20\,°\mathrm{C}$
ρ_0	1.2922		$\mathrm{kg\,m^{-3}}$	Air density at $0\,°\mathrm{C}$
	1.2041		$\mathrm{kg\,m^{-3}}$	Air density at $20\,°\mathrm{C}$

B

Coordinate systems

B.1 Coordinate transformations

B.1.1 Spherical coordinates

This thesis uses a spherical coordinate system in which the polar angle θ is the angle between the positive z-axis and the vector. The azimuthal angle φ is the counterclockwise angle between the x-axis and the vector's projection in the xy-plane. By definition $r \geq 0$, $0 \leq \theta \leq \pi$, $0 \leq \varphi \leq 2\pi$. The conversion between Cartesian and spherical coordinates is given by

$$
\begin{aligned}
x &= r\,\sin\theta\cos\varphi\,, & r &= \sqrt{x^2 + y^2 + z^2}\,, \\
y &= r\,\sin\theta\sin\varphi\,, & \theta &= \arccos\left(\frac{z}{r}\right)\,, \\
z &= r\,\cos\theta\,, & \varphi &= \arctan\left(\frac{y}{x}\right)\,.
\end{aligned}
$$

B.1.2 Cylindrical coordinates

A point in a cylindrical coordinate system is defined by a radial distance r, a height z and an azimuthal angle φ, which is defined in the same manner as for the spherical coordinate system. Here again $r \geq 0$, $0 \leq \varphi \leq 2\pi$, and $z \in \mathbb{R}$. The coordinate

transformation between Cartesian and cylindrical coordinates is given by

$$x = r \cos \varphi, \qquad\qquad r = \sqrt{x^2 + y^2},$$

$$y = r \sin \varphi, \qquad\qquad \varphi = \arctan\left(\frac{y}{x}\right).$$

The z-coordinate is equal in both systems.

B.2 Gradient

Let us assume we have a coordinate system with coordinates x_1, x_2 and x_3 and corresponding unit vectors $\hat{x}_1$, $\hat{x}_2$ and $\hat{x}_3$, in which a function f is defined in a point $\vec{x} = x_1\hat{x}_1 + x_2\hat{x}_2 + x_3\hat{x}_3$. The gradient of f is then according to [51] equal to

$$\nabla f = \frac{1}{h_1}\frac{\mathrm{d}f}{\mathrm{d}x_1}\hat{x}_1 + \frac{1}{h_2}\frac{\mathrm{d}f}{\mathrm{d}x_2}\hat{x}_2 + \frac{1}{h_3}\frac{\mathrm{d}f}{\mathrm{d}x_3}\hat{x}_3, \tag{B.1}$$

in which the scale factors h_1, h_2 and h_3 are given by

$$h_1 = \left\|\frac{\partial\vec{x}}{\partial x_1}\right\|, \qquad h_2 = \left\|\frac{\partial\vec{x}}{\partial x_2}\right\|, \qquad h_3 = \left\|\frac{\partial\vec{x}}{\partial x_3}\right\|. \tag{B.2}$$

B.2.1 Gradient in spherical coordinates

Deriving the gradient in spherical coordinates boils down to calculating the scale factors in (B.2), with $x_1 = r$, $x_2 = \theta$ and $x_3 = \varphi$. They are easily found from the definition of the coordinate transformation in section B.1.1:

$$h_1 = \left\|\frac{\partial\vec{x}}{\partial r}\right\| = 1, \tag{B.3a}$$

$$h_2 = \left\|\frac{\partial\vec{x}}{\partial \theta}\right\| = |r| = r, \tag{B.3b}$$

$$h_3 = \left\|\frac{\partial\vec{x}}{\partial \varphi}\right\| = |r \sin(\theta)| = r \sin(\theta). \tag{B.3c}$$

Substituting these coefficients in equation (B.1) results in the definition of the gradient in spherical coordinates:

$$\nabla f = \frac{\mathrm{d}f}{\mathrm{d}r}\hat{r} + \frac{1}{r}\frac{\mathrm{d}f}{\mathrm{d}\theta}\hat{\theta} + \frac{1}{r \sin(\theta)}\frac{\mathrm{d}f}{\mathrm{d}\varphi}\hat{\varphi}. \tag{B.4}$$

B.2.2   Gradient in cylindrical coordinates

The gradient in cylindrical coordinates is found from (B.2) and section B.1.2. The scale factors are given by

$$h_1 = \left\| \frac{\partial \vec{x}}{\partial r} \right\| = 1 , \tag{B.5a}$$

$$h_2 = \left\| \frac{\partial \vec{x}}{\partial \varphi} \right\| = |r| = r , \tag{B.5b}$$

$$h_3 = \left\| \frac{\partial \vec{x}}{\partial z} \right\| = 1 . \tag{B.5c}$$

The gradient is found from these scale factors as

$$\nabla f = \frac{\mathrm{d} f}{\mathrm{d} r} \, \hat{r} + \frac{1}{r} \frac{\mathrm{d} f}{\mathrm{d} \varphi} \, \hat{\varphi} + \frac{\mathrm{d} f}{\mathrm{d} z} \, \hat{z} . \tag{B.6}$$

References

[1] "Tesla's tower," *New York American*, 22 May 1904.

[2] R. M. Aarts, "Optimally sensitive and efficient compact loudspeakers," *Journal of the Acoustical Society of America*, vol. 119, no. 2, pp. 890–896, Feb. 2006.

[3] R. M. Aarts and A. J. E. M. Janssen, "Approximation of the Struve function $\mathbf{H}_1$ occurring in impedance calculations," *Journal of the Acoustical Society of America*, vol. 113, no. 5, pp. 2635–2637, May 2003.

[4] R. M. Aarts and A. J. E. M. Janssen, "Acoustic holography for piston sound radiation with non-uniform velocity profiles," in *Proceedings of the 17th International Congress on Sound & Vibration*, Jul. 2010, pp. 1–6.

[5] M. Abramowitz and I. A. Stegun, Eds., *Handbook of mathematical functions*, 10th ed. Washington D.C.: US Government Printing Office, 1972.

[6] T. E. G. Álvarez-Arenas, "Acoustic impedance matching of piezoelectric transducers to the air," *IEEE Transactions on Ultrasonics, Ferroelectrics, and Frequency Control*, vol. 51, no. 5, pp. 624–633, May 2004.

[7] T. E. G. Álvarez-Arenas and L. Díez, "Novel impedance matching materials and strategies for air-coupled piezoelectric transducers," in *Sensors*, Nov. 2013.

[8] T. Andersen, M. A. E. Andersen, O. C. Thomsen, M. P. Foster, and D. A. Stone, "Non-linear effects in piezoelectric transformers explained by thermal-electric model based on a hypothesis of self-heating," in *Proceedings of IECON 2012 - 38th Annual Conference of the IEEE Industrial Electronics Society*, Oct. 2012, pp. 596–601.

[9] S. Arra, J. Leskinen, J. Heikkilä, and J. Vanhala, "Ultrasonic power and data link for wireless implantable applications," in *Proceedings of the 2nd International Symposium on Wireless Pervasive Computing ISWPC '07*, Feb. 2007, pp. 567–571.

[10] X. Bao, W. Biederman, S. Sherrit, M. Badescu, Y. Bar-Cohen, C. Jones, J. Aldrich, and Z. Chang, "High-power piezoelectric acoustic-electric power feedthru for metal walls," in *Proceedings of SPIE*, ser. Industrial and Commercial Applications of Smart Structures

Technologies, L. Porter Davis, B. K. Henderson, and M. Brett McMickell, Eds., vol. 6930, no. 69300Z, Apr. 2008, pp. 1–8.

[11] A. Barone and J. A. Gallego Juárez, "Flexural vibrating free-edge plates with stepped thicknesses for generating high directional ultrasonic radiation," *The Journal of the Acoustical Society of America*, vol. 51, no. 3B, pp. 953–959, 1972.

[12] H. E. Bass, L. C. Sutherland, and A. J. Zuckerwar, "Atmospheric absorption of sound: Update," *Journal of the Acoustical Society of America*, vol. 88, no. 4, pp. 2019–2021, Oct. 1990.

[13] H. E. Bass, L. C. Sutherland, A. J. Zuckerwar, D. T. Blackstock, and D. M. Hester, "Atmospheric absorption of sound: further developments," *Journal of the Acoustical Society of America*, vol. 97, no. 1, pp. 680–683, Jan. 1995.

[14] F. Bolaños, "Measurement and analysis of subharmonics and other distortions in compression drivers," in *Audio Engineering Society Convention 118*, May 2005, pp. 1–16.

[15] J. Borwick, Ed., *Loudspeaker and headphone handbook*, 2nd ed. Oxford, U.K.: Focal Press, 1994.

[16] W. C. Brown, "The history of power transmission by radio waves," *IEEE Transactions on Microwave Theory and Techniques*, vol. 32, no. 9, pp. 1230–1242, Sep. 1984.

[17] M. Castillo, P. Acevedo, and E. Moreno, "KLM model for lossy piezoelectric transducers," *Ultrasonics*, vol. 41, no. 8, pp. 671–679, Nov. 2003.

[18] A. Charych, "System and method for wireless electrical power transmission," U.S. Patent 6 798 716 B1, Sep. 28, 2004.

[19] G. V. B. Cochran, M. W. Johnson, M. P. Kadaba, F. Vosburgh, M. W. Ferguson-Pell, and V. R. Palmeiri, "Piezoelectric internal fixation devices: A new approach to electrical augmentation of osteogenesis," *Journal of Orthopaedic Research*, vol. 3, no. 4, pp. 508–513, 1985.

[20] A. B. Cohen, *Hi-Fi loudspeakers and enclosures*. London, U.K.: Newnes-Butterworths, 1968.

[21] I. B. Crandall, *Theory of vibrating systems and sound*. New York, NY: D. Van Nostrand Company, 1926.

[22] L. Curiel, F. Chavrier, R. Souchon, A. Birer, and J. Y. Chapelon, "1.5-D High intensity focused ultrasound array for non-invasive prostate cancer surgery," *IEEE Transactions on Ultrasonics, Ferroelectrics, and Frequency Control*, vol. 49, no. 2, pp. 231–242, Feb. 2002.

[23] J. de Boeij, E. Lomonova, J. L. Duarte, and A. J. A. Vandenput, "Contactless power supply for moving sensors and actuators in high-precision mechatronic systems with long-stroke power transfer capability in x-y plane," *Sensors and Actuators A: Physical*, vol. 148, no. 1, pp. 319–328, Nov. 2008.

[24] J. L. Delany, "Bender transducer design and operation," *Journal of the Acoustical Society of America*, vol. 109, no. 2, pp. 554–562, Feb. 2001.

[25] A. Denisov and E. Yeatman, "Ultrasonic vs. inductive power delivery for miniature biomedical implants," in *Proceedings of the IEEE International Conference on Body Sensor Networks*, Jun. 2010, pp. 84–89.

[26] A. Denisov and E. M. Yeatman, "Micromechanical actuators driven by ultrasonic power transfer," *IEEE/ASME Journal of Microelectromechanical Systems*, vol. 23, no. 3, pp. 750–759, Jun. 2014.

[27] A. A. Denisov and E. M. Yeatman, "Battery-less microdevices for body sensor/actuator networks," in *Proceedings of the IEEE International Conference on Body Sensor Networks*, 2013, pp. 1–5.

[28] R. M. Dickinson, "Wireless power transmission technology state of the art - The first Bill Brown lecture," *Acta Astronautica*, vol. 53, no. 4-10, pp. 561–570, Aug. 2003.

[29] I. Djurek, D. Djurek, and A. Petosic, "Chaotic state in an electrodynamic loudspeaker," *Acta Acustica united with Acustica*, vol. 94, no. 4, pp. 629–635, Jul.-Aug. 2008.

[30] J. Durnin, "Exact solutions for nondiffracting beams. I. The scalar theory," *Journal of the optical society of America A*, vol. 4, no. 4, pp. 651–654, 1987.

[31] J. Durnin, J. J. Miceli, and J. H. Eberly, "Diffraction-free beams," *Physical Review Letters*, vol. 58, no. 15, pp. 1499–1501, Apr. 1987.

[32] EMCT SA. Electronic buzzer catalogue. [Online]. Available: http://www.emct.ch/files/buzzer.pdf

[33] L. B. Evans, H. E. Bass, and L. C. Sutherland, "Atmospheric absorption of sound: Theoretical predictions," *Journal of the Acoustical Society of America*, vol. 51, no. 5B, pp. 1565–1575, 1972.

[34] F. Fahy, *Foundations of engineering acoustics*. London, U.K.: Academic press, 2001.

[35] F. J. Fahy, *Sound intensity*. London, U.K.: Elsevier applied science, 1989.

[36] J. A. Gallego Juárez, "Axisymmetric vibrations of circular plates with stepped thickness," *Journal of Sound and Vibration*, vol. 26, no. 3, pp. 411–416, Feb. 1973.

[37] J. A. Gallego Juárez and G. Rodriguez Corral, "Piezoelectric transducer for air-borne ultrasound," *Acta Acustica united with Acustica*, vol. 29, no. 4, pp. 234–239, Oct. 1973.

[38] J. A. Gallego-Juárez, G. Rodriguez-Corral, and L. Gaete-Garreton, "An ultrasonic transducer for high power applications in gases," *Ultrasonics*, vol. 16, no. 6, pp. 267–271, Nov. 1978.

[39] J. A. Gallego Juárez, G. Rodriguez, J. L. San Emeterio, P. T. Sanz, and J. C. Lázaro, "An acoustic transducer system for long-distance ranging applications in air," *Sensors and Actuators A: Physical*, vol. 37–38, pp. 397–402, Jun.-Aug. 1993.

[40] T. Gerrits, D. C. J. Krop, L. Encica, and E. A. Lomonova, "Development of a linear position independent inductive energy transfer system," in *Proceedings of the IEEE International Electric Machines & Drives Conference (IEMDC)*, May 2011, pp. 1445–1449.

[41] J. H. Goll, "The design of broad-band fluid-loaded ultrasonic transducers," *IEEE Transactions on Sonics and Ultrasonics*, vol. 26, no. 6, pp. 385–393, Nov. 1979.

[42] J. W. Goodman, *Introduction to Fourier optics*, 2nd ed.   London, U.K.: McGraw-Hill, 1996.

[43] D. J. Graham, J. A. Neasham, and B. S. Sharif, "Investigation of methods for data communication and power delivery through metals," *IEEE Transactions on Industrial Electronics*, vol. 58, no. 10, pp. 4972–4980, Oct. 2011.

[44] C. R. Hanna and J. Slepian, "The function and design of horns for loud speakers," *Transactions of the American Institute of Electrical Engineers*, vol. 43, pp. 393–411, Jan. 1924.

[45] R. Henderson and K. Schulmeister, *Laser safety*.   Bristol & Philadelphia: Institute of Physics Publishing, 2004.

[46] R. Hooke and T. A. Jeeves, ""Direct search" solution of numerical and statistical problems," *Journal of the ACM*, vol. 8, no. 2, pp. 212–229, Apr. 1961.

[47] H. Hu, Y. Hu, and C. Chen, "Wireless energy transmission through a thin metal wall by shear wave using two piezoelectric transducers," in *Proceedings of the 2008 IEEE Ultrasonics Symposium*, Nov. 2008, pp. 2165–2168.

[48] Y. Hu, X. Zhang, J. Yang, and Q. Jiang, "Transmitting electric energy through a metal wall by acoustic waves using piezoelectric transducers," *IEEE Transactions on Ultrasonics, Ferroelectrics, and Frequency Control*, vol. 50, no. 7, pp. 773–781, Jul. 2003.

[49] T. Ikeda, *Fundamentals of piezoelectricity*.   Oxford, U.K.: Oxford University Press, 1990.

[50] T. Ishiyama, Y. Kanai, J. Ohwaki, and M. Mino, "Impact of a wireless power transmission system using an ultrasonic air transducer for low-power mobile applications," in *Proceedings of the 2003 IEEE Symposium on Ultrasonics*, vol. 2, Oct. 2003, pp. 1368–1371.

[51] A. Jeffrey, *Handbook of mathematical formulas and integrals*.   London, U.K.: Academic press, 1995.

[52] J. Johansson, P.-E. Martinsson, and J. Delsing, "Simulation of absolute amplitudes of ultrasound signals using equivalent circuits," *IEEE Transactions on Ultrasonics, Ferroelectrics, and Frequency Control*, vol. 54, no. 10, pp. 1977–1983, Oct. 2007.

[53] A. Karalis, J. D. Joannopoulos, and M. Soljačić, "Efficient wireless non-radiative mid-range energy transfer," *Annals of Physics*, vol. 323, no. 1, pp. 34–48, Jan. 2008.

[54] H. Kawanabe, T. Katane, H. Saotome, O. Saito, and K. Kobayashi, "Power and information transmission to implanted medical device using ultrasonic," *Japanese Journal of Applied Physics*, vol. 40, no. 5B, pp. 3865–3866, May 2001.

[55] M. P. Kazmierkowski and A. J. Moradewicz, "Unplugged but connected: Review of contactless energy transfer systems," *IEEE Industrial Electronics Magazine*, vol. 6, no. 4, pp. 47–55, Dec. 2012.

[56] G. E. Keiser, *Optical fiber communications*, 3rd ed.   London, U.K.: McGraw-Hill, 2000.

[57] G. S. Kino, *Acoustic waves: devices, imaging, and analog signal processing*.   Englewood Cliffs, NJ: Prentice Hall, 1987.

[58] L. E. Kinsler, A. R. Frey, A. B. Coppens, and J. V. Sanders, *Fundamentals of acoustics*, 3rd ed.   New York, NY: John Wiley & Sons, 1982.

[59] M. Kluge, T. Becker, J. Schalk, and T. Otterpohl, "Remote acoustic powering and data transmission for sensors inside of conductive envelopes," in *Proceedings of IEEE Sensors*, Oct. 2008, pp. 41–44.

[60] V. Klymko, M. Roes, J. van Duivenbode, and E. Lomonova, "Phased transducer array for acoustic energy harvesting inside an MRI machine," in *Proceedings of the 2013 IEEE International Ultrasonics Symposium*, Jul. 2013, pp. 1979–1982.

[61] B. Kolbrek, "Horn theory: An introduction, part 1," *Audio Xpress*, pp. 1–9, 2008.

[62] B. Kolbrek, "Horn theory: An introduction, part 2," *Audio Xpress*, pp. 1–8, 2008.

[63] H. Kolsky, *Stress waves in solids*.   Oxford, U.K.: Clarendon press, 1953.

[64] G. Kossoff, "The effects of backing and matching on the performance of piezoelectric ceramic transducers," *IEEE Transactions on Sonics and Ultrasonics*, vol. 13, no. 1, pp. 20–30, Mar. 1966.

[65] R. Krimholtz, D. A. Leedom, and G. L. Matthaei, "New equivalent circuits for elementary piezoelectric transducers," *Electronics Letters*, vol. 6, no. 13, pp. 398–399, Jun. 1970.

[66] J. Kritz, "A high-efficiency transducer for transmission to air," *IRE Transactions on Ultrasonic Engineering*, vol. 8, no. 1, pp. 14–18, Mar. 1961.

[67] M. Kupnik, M.-C. Ho, S. Vaithilingam, and B. T. Khuri-Yakub, "CMUTs for air coupled ultrasound with improved bandwidth," in *Proceedings of the 2011 IEEE International Ultrasonics Symposium*, Oct. 2011, pp. 592–595.

[68] A. Kurs, A. Karalis, R. Moffatt, J. D. Joannopoulos, P. Fisher, and M. Soljačić, "Wireless power transfer via strongly coupled magnetic resonances," *Science*, vol. 317, no. 5834, pp. 83–86, Jul. 2007.

[69] H. Kuttruff, *Acoustics*.   Abbingdon, U.K.: Taylor & Francis, 2007.

[70] P. J. Larson and B. C. Towe, "Miniature ultrasonically powered wireless nerve cuff stimulator," in *International IEEE/EMBS Conference on Neural Engineering*, Apr. 2011, pp. 265–268.

[71] T. J. Lawry, G. J. Saulnier, J. D. Ashdown, K. R. Wilt, H. A. Scarton, S. Pascarelle, and J. D. Pinezich, "Penetration-free system for transmission of data and power through solid metal barriers," in *Proceedings of the Military Communications Conference - MILCOM 2011*, Nov. 2011, pp. 389–395.

[72] K. L. Lee, C.-P. Lau, H.-F. Tse, D. S. Echt, D. Heaven, W. Smith, and M. Hood, "First human demonstration of cardiac stimulation with transcutaneous ultrasound energy delivery: Implications for wireless pacing with implantable devices," *Journal of the American College of Cardiology*, vol. 50, no. 9, pp. 877–883, Aug. 2007.

[73] S. Q. Lee, W. Youm, and G. Hwang, "Biocompatible wireless power transferring based on ultrasonic resonance devices," in *Proceedings of Meetings on Acoustics*, ser. 030030, vol. 19, Jun. 2013, pp. 1–9.

[74] H. F. Leung, B. J. Willis, and A. P. Hu, "Wireless electric power transfer based on acoustic energy through conductive media," in *Proceedings of the 9th IEEE Conference on Industrial Electronics and Applications*, Jun. 2014, pp. 1555–1560.

[75] S. Lin, "Equivalent circuits and directivity patterns of air-coupled ultrasonic transducers," *Journal of the Acoustical Society of America*, vol. 109, no. 3, pp. 949—957, Mar. 2001.

[76] C. F. Lü, J. S. Yang, J. Wang, and W. Q. Chen, "Power transmission through a hollow cylinder by acoustic waves and piezoelectric transducers with radial polarization," *Journal of Sound and Vibration*, vol. 325, no. 4-5, pp. 989–999, Sep. 2009.

[77] B. G. Lucas and T. G. Muir, "The field of a focusing source," *Journal of the Acoustical Society of America*, vol. 72, no. 4, pp. 1289–1296, Oct. 1982.

[78] T. Maleki, N. Cao, S. H. Song, C. Kao, S.-C. A. Ko, and B. Ziaie, "An ultrasonically powered implantable micro-oxygen generator (IMOG)," *IEEE Transactions on Biomedical Engineering*, vol. 58, no. 11, pp. 3104–3111, Nov. 2011.

[79] P. Maréchal, F. Levassort, L.-P. Tran-Huu-Hue, and M. Lethiecq, "Lens-focused transducer modeling using an extended KLM model," *Ultrasonics*, vol. 46, no. 2, pp. 155–167, May 2007.

[80] F. Mazzilli, M. Peisino, R. Mitouassiwou, B. Cotté, P. Thoppay, C. Lafon, P. Favre, E. Meurville, and C. Dehollain, "In-vitro platform to study ultrasound as source for wireless energy transfer and communication for implanted medical devices," in *Proceedings of the Annual International Conference of the IEEE on Engineering in Medicine and Biology Society (EMBC)*, Aug.-Sep. 2010, pp. 3751–3754.

[81] J. O. McSpadden and J. C. Mankins, "Space solar power programs and microwave wireless power transmission technology," *IEEE Microwave Magazine*, vol. 3, no. 4, pp. 46–57, Dec. 2002.

[82] H. Medwin and J. D. Hagy Jr., "Helmholtz-Kirchhoff theory for sound transmission through a statistically rough plane interface between dissimilar fluids," *Journal of the Acoustical Society of America*, vol. 51, pp. 1083–1090, 1972.

[83] E. M. T. Moers, I. Lopez Arteaga, P. L. van Dalen, R. Scholte, and H. Nijmeijer, "Detection of plate vibration modes by means of near-field acoustic holography in the presence of reflective surfaces," in *Proceedings of ISMA*, Sep. 2012, pp. 3571–3584.

[84] J. O. Mur-Miranda, G. Fanti, Y. Feng, K. Omanakuttan, R. Ongie, A. Setjoadi, and N. Sharpe, "Wireless power transfer using weakly coupled magnetostatic resonators," in *Proceedings of the IEEE Energy Conversion Congress and Exposition*, Sep. 2010, pp. 4179–4186.

[85] H. F. Olson, *Elements of acoustical engineering*. New York, NY: D. Van Nostrand Company, 1940.

[86] H. F. Olson, "The action of a direct radiator loudspeaker with a non-linear cone suspension system," *Journal of the Acoustical Society of America*, vol. 16, no. 1, pp. 1–4, 1944.

[87] H. F. Olson, "Loudspeakers," *Proceedings of the IRE*, vol. 50, no. 5, pp. 730–737, May 1962.

[88] S. Ozeri and D. Shmilovitz, "Ultrasonic transcutaneous energy transfer for powering implanted devices," *Ultrasonics*, vol. 50, no. 6, pp. 556–566, May 2010.

[89] S. Ozeri and D. Shmilovitz, "Simultaneous backward data transmission and power harvesting in an ultrasonic transcutaneous energy transfer link employing acoustically dependent electric impedance modulation," *Ultrasonics*, vol. 54, no. 7, pp. 1929–1937, Sep. 2014.

[90] S. Ozeri, D. Shmilovitz, S. Singer, and C.-C. Wang, "Ultrasonic transcutaneous energy transfer using a continuous wave 650 kHz Gaussian shaded transmitter," *Ultrasonics*, vol. 50, no. 7, pp. 666–674, Jun. 2010.

[91] S. Ozeri, B. Spivak, and D. Shmilovitz, "Non-invasive sensing of the electrical energy harvested by medical implants powered by an ultrasonic transcutaneous energy transfer link," in *Proceedings of the IEEE International Symposium on Industrial Electronics*, May 2012, pp. 1153–1157.

[92] Z. Popović and B. D. Popović, *Introductory electromagnetics*. Upper Saddle River, NJ: Prentice Hall, Inc., 2000.

[93] D. E. Raible, D. Dinca, and T. H. Nayfeh, "Optical frequency optimization of a high intensity laser power beaming system utilizing VMJ photovoltaic cells," in *Proceedings of the International Conference on Space Optical Systems and Applications (ICSOS)*, May 2011, pp. 232–238.

[94] M. Redwood, "Transient performance of a piezoelectric transducer," *Journal of the Acoustical Society of America*, vol. 33, no. 4, pp. 527–536, Apr. 1961.

[95] J. D. Reiss, I. Djurek, A. Petosic, and D. Djurek, "Verification of chaotic behavior in an experimental loudspeaker," *Journal of the Acoustical Society of America*, vol. 124, no. 4, pp. 2031–2041, Oct. 2008.

[96] M. G. L. Roes, J. L. Duarte, M. A. M. Hendrix, and E. Lomonova, "Acoustic Energy Transfer: A review," *IEEE Industrial Electronics Technology News*, 10 Oct. 2013, invited presentation.

[97] M. G. L. Roes, J. L. Duarte, M. A. M. Hendrix, and E. A. Lomonova, "Acoustic Energy Transfer: A review," *IEEE Transactions on Industrial Electronics*, vol. 60, no. 1, pp. 242–248, Jan. 2013.

[98] M. G. L. Roes, M. A. M. Hendrix, and J. L. Duarte, "Contactless energy transfer through air by means of ultrasound," in *Proceedings of IECON 2011 - 37th Annual Conference of the IEEE Industrial Electronics Society*. IEEE, Nov. 2011, pp. 1238–1243.

[99] M. G. L. Roes, M. A. M. Hendrix, and J. L. Duarte, "The effect of reflections on the performance of an acoustic energy transfer system," in *Proceedings of the Energy Conversion Congress and Exposition*, Sep. 2012, pp. 388–393.

[100] M. G. L. Roes, J. L. Duarte, and M. A. M. Hendrix, "Design of stepped exponential horns for acoustic energy transfer systems," in *Proceedings of the 2013 IEEE International Ultrasonics Symposium*, Jul. 2013, pp. 306–309.

[101] M. Rossi, *Acoustics and electroacoustics*. Norwood, MA: Artech house, 1988.

[102] S. Ruschin, "Modified Bessel nondiffracting beams," *Journal of the Optical Society of America A*, vol. 11, no. 12, pp. 3224–3228, 1994.

[103] A. Safari and E. K. Akdoğan, Eds., *Piezoelectric and acoustic materials for transducer applications*. New York, NY: Springer, 2008.

[104] A. Sahai and D. Graham, "Optical wireless power transmission at long wavelengths," in *Proceedings of the International Conference on Space Optical Systems and Applications (ICSOS)*. IEEE, May 2011, pp. 164–170.

[105] V. Salmon, "A new family of horns," *Journal of the Acoustical Society of America*, vol. 17, no. 3, pp. 212–218, Jan. 1946.

[106] V. Salmon, "Generalized plane wave horn theory," *Journal of the Acoustical Society of America*, vol. 17, no. 3, pp. 199–211, Jan. 1946.

[107] A. P. Sample, D. A. Meyer, and J. R. Smith, "Analysis, experimental results, and range adaptation of magnetically coupled resonators for wireless power transfer," *IEEE Transactions on Industrial Electronics*, vol. 58, no. 2, pp. 544–554, Feb. 2011.

[108] A. Sanni, A. Vilches, and C. Toumazou, "Inductive and ultrasonic multi-tier interface for low-power, deeply implantable medical devices," *IEEE Transactions on Biomedical Circuits and Systems*, vol. 6, no. 4, pp. 297–308, Aug. 2012.

[109] S. Shahab and A. Erturk, "Contactless ultrasonic energy transfer: Acoustic-piezoelectric structure interaction modeling and performance enhancement," in *Proceedings of the ASME International Design Engineering Technical Conferences and Computers and Information in Engineering Conference*, vol. 8: 26th Conference on Mechanical Vibration and Noise, Aug. 2014, pp. 1–13.

[110] S. Shahab, M. Gray, and A. Erturk, "An experimentally validated contactless acoustic energy transfer model with resistive-reactive electrical loading," in *Proceedings of SPIE*, ser. Active and Passive Smart Structures and Integrated Systems, W.-H. Liao, G. Park, and A. Erturk, Eds., vol. 9431, no. 943105, Apr. 2015, pp. 1–14.

[111] S. Shahab, M. Gray, and A. Erturk, "Ultrasonic power transfer from a spherical acoustic wave source to a free-free piezoelectric receiver: Modeling and experiment," *Journal of Applied Physics*, vol. 117, no. 10, pp. 1–8, 2015.

[112] S. Shahab, S. Leadenham, F. Guillot, K. Sabra, and A. Erturk, "Ultrasound acoustic wave energy transfer and harvesting," in *Proceedings of SPIE*, ser. Active and Passive Smart Structures and Integrated Systems, W.-H. Liao, Ed., vol. 9057, no. 90570F, Apr. 2014, pp. 1–9.

[113] S. Sherrit, B. Doty, M. Badescu, X. Bao, Y. Bar-Cohen, J. Aldrich, and Z. Chang, "Studies of acoustic-electric feed-throughs for power transmission through structures," in *Proceedings of the Smart Structures and Materials Symposium*, Feb. 2006.

[114] P.-J. Shih and W.-P. Shih, "Design, fabrication, and application of bio-implantable acoustic power transmission," *IEEE/ASME Journal of Microelectromechanical Systems*, vol. 19, no. 3, pp. 494–502, Jun. 2010.

[115] D. Shmilovitz, S. Ozeri, C.-C. Wang, and B. Spivak, "Noninvasive control of the power transferred to an implanted device by an ultrasonic transcutaneous energy transfer link," *IEEE Transactions on Biomedical Engineering*, vol. 61, no. 4, pp. 995–1004, Apr. 2014.

[116] D. A. Shoudy, G. J. Saulnier, H. A. Scarton, P. K. Das, S. Roa-Prada, J. D. Ashdown, and A. J. Gavens, "An ultrasonic through-wall communication system with power harvesting," in *Proceedings of the IEEE Ultrasonics Symposium*, Oct. 2007, pp. 1848–1853.

[117] R. H. Small, "Direct-radiator loudspeaker system analysis," *IEEE Transactions on Audio and Electroacoustics*, vol. 19, no. 4, pp. 269–281, Dec. 1971.

[118] J. P. C. Smeets, T. T. Overboom, J. W. Jansen, and E. A. Lomonova, "Modeling framework for contactless energy transfer systems for linear actuators," *IEEE Transactions on Industrial Electronics*, vol. 60, no. 1, pp. 391–399, Jan. 2013.

[119] C. L. W. Sonntag, J. L. Duarte, and A. J. M. Pemen, "Load position detection and validation on variable-phase contactless energy transfer desktops," in *Proceedings of the IEEE Energy Conversion Congress and Exposition*, Sep. 2009, pp. 1818–1825.

[120] G. W. Stewart and R. B. Lindsay, *Acoustics*. New York, NY: D. Van Nostrand Company, 1930.

[121] B. D. H. Tellegen, "The gyrator, a new electric network element," *Philips research reports*, vol. 3, no. 81–101, pp. 388–409, Apr. 1948.

[122] M. P. Theodoridis and S. V. Mollov, "Improved gate driver for a 13.56 MHz resonant inverter," in *2nd International Conference on Power Electronics, Machines and Drives (PEMD 2004)*, vol. 1, Mar.-Apr. 2004, pp. 143–148.

[123] H. A. C. Tilmans, "Equivalent circuit representation of electromechanical transducers: I. lumped-parameter systems," *Journal of Micromechanics and Microengineering*, vol. 6, no. 1, pp. 157–176, 1996.

[124] H. A. C. Tilmans, "Equivalent circuit representation of electromechanical transducers: II. distributed-parameter systems," *Journal of Micromechanics and Microengineering*, vol. 7, pp. 285–309, 1997.

[125] J. Van Randeraat and R. E. Setterington, Eds., *Piezoelectric ceramics*, 2nd ed.   London, U.K.: Mullard Limited, Jan. 1974.

[126] D. van Wageningen and T. Staring, "The Qi wireless power standard," in *Proceedings of 14th International Power Electronics and Motion Control Conference EPE-PEMC 2010*, ser. S15, Sep. 2010, pp. 25–32.

[127] E. Waffenschmidt and T. Staring, "Limitation of inductive power transfer for consumer application," in *Proceedings of the European Conference Power Electronics and Applications*, vol. 1, Sep. 2009, pp. 1–10.

[128] A. G. Webster, "Acoustical impedance and the theory of horns and of the phonograph," *Proceedings of the National Academy of Sciences of the United States of America*, vol. 5, no. 7, pp. 275–282, Jul. 1919.

[129] R. Wei, Q. Tao, and W. Ni, "Bifurcation and chaos of direct radiation loudspeaker," *Chinese Physics Letters*, vol. 3, no. 10, pp. 469–472, 1986.

[130] Z.-t. Yang, S.-h. Guo, Y.-t. Hu, and J.-s. Yang, "Modeling of power transmission through an elastic wall by piezoelectric transducers and acoustic waves," in *Proceedings of the Symposium on Piezoelectricity, Acoustic Waves, and Device Applications*, Dec. 2008, pp. 93–97.

[131] Z. Yang, S. Guo, and J. Yang, "Transmitting electric energy through a closed elastic wall by acoustic waves and piezoelectric transducers," *IEEE Transactions on Ultrasonics, Ferroelectrics, and Frequency Control*, vol. 55, no. 6, pp. 1380–1386, Jun. 2008.

[132] T. Yano, M. Tone, and A. Fukumoto, "Range finding and surface characterization using high-frequency air transducers," *IEEE Transactions on Ultrasonics, Ferroelectrics, and Frequency Control*, vol. 34, no. 2, pp. 232–236, Mar. 1987.

Acknowledgements

E INDELIJK is het dan zover: mijn proefschrift is af. Terwijl ik dit schrijf beginnen buiten de bladeren aan de bomen voorzichtig te kleuren. Het einde van een seizoen past wel een beetje bij het afsluiten van een periode van hard werken. Want dat is promoveren wel, maar gelukkig staan er ook de nodige leuke momenten tegenover. Een groot aantal mensen heeft, allemaal op hun eigen manier, hetzij bewust of onbewust, een steentje bijgedragen aan dit proefschrift. Zonder hen zou dit proefschrift er zeker niet gekomen zijn. Ik wil hen hier dan ook graag bedanken.

Firstly, Elena, many thanks for giving me the opportunity to pursue a PhD degree in the EPE group. I am grateful for the confidence that you always have placed in me and my capabilities, and for your support throughout the years.

Ongeveer zes jaar geleden, toen ik nog druk bezig was met mijn afstudeerproject, deden mijn toenmalige begeleiders hun best om mij te overtuigen om te gaan promoveren. Het kostte heel wat overredingskracht, maar het is ze uiteindelijk gelukt. Dezelfde twee mensen zijn tijdens mijn promotie mijn dagelijks begeleiders geweest; een rol die ze met verve hebben vervuld. Jorge en Marcel, hartelijk bedankt voor al het enthousiasme, alle discussies en gesprekken, zowel over mijn onderzoek, als over de meest uiteenlopende onderwerpen, alle ondersteuning, maar ook voor de opbeurende woorden wanneer resultaten weer eens tegen bleken te vallen.

A special word of thanks goes to the committee members, prof. Ronald Aarts, prof. Mario Kupnik, prof. Ines Lopez Arteaga and prof. Eric Yeatman for reading my thesis and supplying comments and valuable advice.

Ik wil ook graag de rest van mijn (huidige en oud-) collega's van EPE bedanken voor de leuke sfeer in de groep, alle gezelligheid en de interesse in mijn onderzoek. Speciale dank ben ik verschuldigd aan Marijn, voor alle praktische hulp en technische ondersteuning in het lab, maar ook voor de goede gesprekken van tijd tot tijd. Nancy en Monica, hartelijk bedankt voor alle administratieve hulp door

de jaren heen. Twee andere EPE-ers die een speciaal bedankje verdienen zijn mijn oud-collega's, vrienden en medebestuursleden van ⬛ The*BruceDickinson* productions: Thomas en Jan. Jongens, bedankt voor alle gezelligheid in IM0.06a en daarbuiten: de ALV's, zowel de zinvolle als de zinloze discussies, cowbellmomenten, de support, en de nodige humor.

Ik ben blij met de ontzettend leuke club vrienden om me heen. Zonder de nodige ontspanning van tijd tot tijd zou dit boekje er zeker niet gekomen zijn. Weet dus dat jullie hebben bijgedragen aan het eindresultaat. Op de eerste plaats zijn daar mijn paranimfen: Remco en Mark. Jongens, ontzettend bedankt voor alles de afgelopen jaren, van ons Wervingsdagenjaar, etentjes, avondjes in de kroeg, tot de reisjes die we hebben gemaakt (ook al kon ik niet altijd mee, maar daar hadden jullie dan gelukkig ruim begrip voor). Bedankt voor de lol die we altijd hebben. Een andere groep vrienden die voor de nodige ontspanning hebben gezorgd zijn de Hoc Habet Ouwe Lolly's Alke, Bente, Harm, Jeroen, Joost, Jos, Marloes, Martijn, Peter en Stef. Ik heb jammer genoeg niet meer veel geschermd tijdens mijn promotietijd, maar de overige activiteiten waren een prima vervanging daarvoor. Ik hoop overigens dat ik zeer binnenkort eindelijk niet meer badjasloos door het leven hoef! Mijn nog niet genoemde quizmaatjes van de SSZE, Gilbère, Marloes en Robin, verdienen ook een bedankje. De avondjes pubquizen waren altijd fijne momenten om even de zinnen te verzetten, vooral als we wonnen (meestal weliswaar geheel tegen onze eigen verwachtingen in, maar daarom des te leuker).

Pap en mam, ik kan jullie niet genoeg bedanken voor alle onvoorwaardelijke steun en liefde die jullie altijd hebben gegeven. Het is fijn om te weten dat jullie altijd achter me staan. Herbert en Werner, dank jullie wel voor alle support, interesse, gezelligheid en de fijne band die we hebben.

De laatste pagina's van dit boekje zijn gevuld. Vijf en een half jaar van hard werk zijn ten einde. Wat een eeuwigheid leek toen ik net begon, is werkelijk omgevlogen. En zo begint het volgende hoofdstuk in mijn leven. Maar dáár zal ik waarschijnlijk geen boek over schrijven.

<div align="right">

Maurice Roes
Eindhoven, september 2015

</div>

About the author

MAURICE ROES was born on 22 January 1984 in Breukelen, The Netherlands. He attended Sg. Sophianum in Gulpen for secondary education. After receiving his diploma in 2002, he started studying electrical engineering at Eindhoven University of Technology. He received his MSc (ir.) degree in 2010, specialising in control of power electronics. His master of science thesis dealt with the subject of "Disturbance observer-based control of a dual-output LLC converter for solid state lighting applications". In February 2010 he started as a PhD student in the Electromechanics and Power Electronics group of the Electrical Engineering department of Eindhoven University. His research in the group focused on the contactless transmission of energy through the use of sound waves. This dissertation is the result of his research during this period.